Correlations between the Mineralogy and Recovery Behavior of Rare Earth Elements (REEs) in Coal Waste

Bin Ji

Dissertation submitted to the faculty of the Virginia Polytechnic Institute and State University in partial fulfillment of the requirements for the degree of

Doctor of Philosophy
In
Mining Engineering

Wencai Zhang, Chair
Erik Westman
Cheng Chen
Xinbo Yang

December 02, 2022

Blacksburg, Virginia

Keywords: Coal waste, Rare earth elements, Recovery, Calcination, Mineralogy, Acid leaching, Florencite

Copyright 2022, Bin Ji

Correlations between the Mineralogy and Recovery Behavior of Rare Earth Elements (REEs) in Coal Waste

Bin Ji

ACADEMIC ABSTRACT

Many literatures have been published recently regarding the recovery of REEs from coal-related materials, such as coal waste, acid mine drainage, and coal combustion ash. The recovery of REEs from coal waste has been investigated by the author in recent years, and it was found that after calcination at 600 °C for 2 h, a significant improvement in REE recovery can be achieved. In order to reveal the mechanisms of the enhanced REE recovery after calcination, coal waste samples from two different seams, i.e., Western Kentucky No. 13 and Fire Clay, were selected to investigate the modes of occurrence of REEs.

Scanning electron microscopy- and transmission electron microscopy-energy dispersive X-ray spectroscopy (SEM-EDS and TEM-EDS) analyses were conducted to investigate the mineralogy of REEs in two coal waste samples. Totally, 49 and 50 REE-bearing particles were found from the SEM specimens of Western Kentucky No. 13 and Fire Clay coal waste samples, respectively. Based on the elemental composition analyses and TEM-EDS characterization, it was found that apatite, monazite, and crandallite-group minerals were the major light REE (LREE) carriers, while the heavy REEs (HREE) primarily occurred in zircon and xenotime in these two coal waste samples. Further analyzing the REE content and number of REE-bearing particles, it was confirmed that monazite, xenotime, and crandallite-group minerals were the dominant contributors to the total REE (TREE) contents in both materials. In addition to the mineralogy of REEs, the morphology of REE-bearing particles was also investigated. The SEM images suggested that the particle size of most REE-bearing particles was less than 5 μm. Moreover, not only completely liberated particles, but particles encapsulated by the host minerals present in the two coal waste samples.

To identify the changes of mineralogy of REEs after recovery, the leaching solid residues of the raw and calcined coal waste samples were also characterized by SEM-EDS analysis. After REE recovery, the same REE mineralogical results were observed from the leaching residues of the raw coal waste samples. However, as for the calcined samples, the

crandallite-group minerals disappeared. These results suggested that the crandallite-group minerals were decomposed into easy-to-leach forms after calcination at 600 ℃, thus leading to the improved REE recovery. Moreover, the number of REE-bearing particles (*N*) found from per area of the calcined leaching residue was confirmed to be larger compared to that of the raw ones. A combination analysis of these results indicated that two mechanisms of the enhanced REE recovery after calcination can be confirmed: (1) decomposing the crandallite-group minerals into more soluble species; and (2) promoting the liberation of the REE-bearing particles encapsulated in the host minerals.

The thermal decomposition of crandallite-group minerals was mainly responsible for the enhanced REE recovery from coal waste. However, as a result of the complex isomorphic substitutions and association characteristics, it is difficult to collect a pure endmember of crandallite-group mineral for characterization. Therefore, florencite-(Ce) was synthesized in this study. X-ray diffraction (XRD), SEM-EDS, TEM, thermogravimetric and differential thermal analyses (TGA-DTA), and acid leaching tests were conducted on the synthesized product. The results showed that the variation in Ce leaching recovery corresponded to the phase transformation of florencite. The gradual transformation of florencite from a crystalline mineral into an amorphous phase resulted in the increases in the solubility of Ce. In addition, the thermal transformation of florencite was an independent reaction, which was not interfered by the host materials, such as kaolinite and coal waste.

Correlations between the Mineralogy and Recovery Behavior of Rare Earth Elements (REEs) in Coal Waste

Bin Ji

GENERAL AUDIENCE ABSTRACT

Coal waste has been identified as a promising alternative source of rare earth elements (REEs). This study showed that calcination can significantly improve the REE recovery from coal waste materials. Scanning electron microscopy- and transmission electron microscopy-energy dispersive X-ray spectroscopy (SEM-EDS and TEM-EDS) analyses were conducted to investigate the mineralogy of REEs in two coal waste samples. The results indicated that the REEs mainly present as apatite, zircon, monazite, xenotime, and crandallite-group minerals in the coal waste samples. However, after REE recovery, the crandallite-group minerals disappeared from the calcined coal waste samples. Therefore, it can be confirmed that the calcination treatment resulted in the solubility improvement of crandallite-group minerals in coal waste samples. In order to further investigate the crandallite-group minerals, florencite was synthesized and subjected to a series of characterizations. The results suggested that the thermal phase transformation of florencite from crystalline into amorphous state resulted in the solubility improvement.

Acknowledgements

Time sure does fly when I look back on my entire Ph.D. journey. I can still remember clearly when I first set foot on the Virginia Tech after fifteen hours of flight from Beijing to Roanoke. It feels like yesterday. All my laughter, struggle, and endless effort at Blacksburg will become an unforgettable memory throughout my whole life. Obtaining a Ph.D. degree is a challenging but enjoyable experience for me, and it is impossible to reach the end without the help and encouragement from others.

I would like to take this opportunity to thank and acknowledge my advisor Dr. Wencai Zhang. Without his guidance and support, none of the research and discussion presented throughout this dissertation would be possible. Being a part of Dr. Zhang's first batch and helping build the lab with him over these three years has been an incredible experience that has improved my understanding and admiration of the operations of lab development. He has always been available for support and discussion in my academic and personal life and has helped lift me up from slumps and roadblocks.

My sincerest thanks are extended to Dr. Erik Westman, Dr. Cheng Chen, and Dr. Xinbo Yang for dedicating their time and support to serve as my committee members. The valuable suggestions from my qualifying, and preliminary examinations helped me to better understand and look deeper into this work. Thank you all for always being open to discussion and provide excellent guidance and ideas.

I really appreciate the assistances from the faculty and staff members in our department and other departments. Many thanks to Dr. Emily Sarver, and Lori Andrews, who helped me a lot in Ph.D. study plan, organizing preliminary examination, administrative paperwork, and daily packages. I would also like to acknowledge Dr. Weinan Leng, Stephen McCartney, and especially Dr. Rituraj Borgohain, who trained me instrument operations, and cared about my research progress.

Furthermore, I want to thank all the members of our research group led by Dr. Zhang: Qi Li, Zhongqing Xiao, Sharon Escalante, Shiyu Li, Hao Li, and Viking Zhou. They always spared no effort to help me when I have difficulties, thank you all for your tremendous support during these years.

Lastly, I would like to express my deepest thanks to my parents and family members for their unconditional love and encouragement, which is always my strong backing and motivation to move forward. Without their support and care about, this journey cannot be completed!

All my achievements today should be attributed to the encouragement and strong support from my advisor, my family members, my dear friends, and the Virginia Tech community. I hope I make all of you proud during and after these three years.

Thank you, Virginia Tech! Once a Hokie, always a Hokie.

Table of Contents

Chapter 1 Brief Introduction 1

1.1 Background 1

1.2 Research Objectives 4

1.3 Dissertation Outline 4

Chapter 2 The Mineralogical Characterization of Rare Earth Elements (REEs) from Coal Waste 5

Abstract 5

2.1 Introduction 5

2.2 Materials and Methods 7

2.2.1 Materials 7

2.2.2 Methods 7

2.3 Results and Discussion 10

2.3.1 REE Contents in the Coal Waste 10

2.3.2 REE Mineralogy in the Western Kentucky No. 13 Coal Waste 11

2.3.3 Physical Association Characteristics of REEs in the Western Kentucky No. 13 Coal Waste 15

2.3.4 Mineralogy and Physical Association Characteristics of REEs in the Fire Clay Coal Waste 18

2.4 Conclusions 24

Chapter 3 The Effect of Calcination on the Leaching Recovery and Mineralogical Characterization of Rare Earth Elements (REEs) from Coal Waste 26

Abstract 26

3.1 Introduction 26

3.2 Materials and Methods 28

3.2.1 Materials 28

3.2.2 Calcination 28

3.2.3 Acid Leaching 28

3.2.4 SEM-EDS Analysis 29

3.3 Results and Discussion 31

3.3.1 Effects of Calcination on the Leaching Characteristics of REEs and Major Elements 31
3.3.2 REE Mineralogy in the Leaching Solid Residue of the Western Kentucky No. 13 Coal Waste 34
3.3.3 REE Mineralogy in the Leaching Solid Residue of the Fire Clay Coal Waste 40
3.3.4 Discussion on the Recovery of REEs from Coal Waste 44
3.4 Conclusions 46
Chapter 4 Thermal Transformation Behavior of Florencite and Implications on the Leaching Recovery of Rare Earth Elements (REEs) 48
Abstract 48
4.1 Introduction 48
4.2 Materials and Methods 51
4.2.1 Materials 51
4.2.2 Synthesis of Florencite 51
4.2.3 Calcination 52
4.2.4 Acid Leaching 52
4.2.5 Sample Characterization 53
4.3 Result and Discussion 54
4.3.1 Sample Characterization 54
4.3.2 Phase Transformation of Florencite 58
4.3.3 Leaching Characteristics of Florencite 62
4.3.4 Mixed Calcination and Leaching Characteristics 65
4.4 Conclusions 71
Chapter 5 Summary and Perspectives 73
5.1 Summary 73
5.2 Perspectives 74
Reference 76
Appendices 91
Appendix A Supporting materials for Chapter 2 92
Appendix B Supporting materials for Chapter 3 111
Appendix C Supporting materials for Chapter 4 152

List of Figures

Figure 1.1 The distribution of global REO production in 2021..... 1
Figure 2.1 Procedures used to find REEs-rich particles from the coal waste specimens (BED and SED represent backscattered electron detector and secondary electron detector, respectively)..... 9
Figure 2.2 SEM-BED image (left) and EDS spectrum (right) of Particle 1 found from the Western Kentucky No. 13 coal waste..... 11
Figure 2.3 EDS spectra of Particle 2 (left) and Particle 3 (right) found from the Western Kentucky No. 13 coal waste..... 12
Figure 2.4 EDS spectra of Particle 25 (left) and Particle 6 (right)..... 14
Figure 2.5 Elemental compositions of the Group I and Group II particles found from the Western Kentucky No. 13 coal waste..... 15
Figure 2.6 SEM images of selected REE-bearing particles found from the Western Kentucky No. 13 coal waste: (a) Particle 4, monazite; (b) Particle 6, monazite; (c) Particle 21, crandallite group mineral; and (d) Particle 26, crandallite group mineral. (The REE-bearing particles are marked with red circles.)..... 17
Figure 2.7 SEM-BED images of a xenotime particle taken with different accelerating voltages: (a) 20 kV and (b) 10 kV. (The xenotime particle is marked with red circles.) . 18
Figure 2.8 SEM-BED images of a monazite particle taken with different accelerating voltages: (a) 20 kV and (b) 10 kV. (The monazite particle is marked with red circles.).. 18
Figure 2.9 SEM-BED images and EDS spectra of a zircon (FCP 1) and an apatite (FCP 6) particle found from the Fire Clay coal waste..... 19
Figure 2.10 Elemental compositions of the Group I and Group II particles found from the Fire Clay coal waste..... 23
Figure 2.11 SEM image and EDS spectra of FCP 22 found from the Fire Clay coal waste. 23
Figure 2.12 SEM image and EDS spectra of FCP 29 found from the Fire Clay coal waste. 24
Figure 3.1 Procedures used to find REE-rich particles from the coal waste specimens (BED and SED represent backscattered electron detector and secondary electron detector, respectively) (Ji et al., 2022c)..... 30

Figure 3.2 Leaching characteristics of REEs and major elements from the raw and calcined coal wastes. 32
Figure 3.3 Leaching characteristics of major elements from the raw and calcined coal wastes. 34
Figure 3.4 Elemental compositions of the Group I and Group II particles found in the leaching solid residue of the Western Kentucky No. 13 raw coal waste. 36
Figure 3.5 Elemental compositions of the REE-bearing particles found in the leaching solid residue of the Western Kentucky No. 13 calcined coal waste. 38
Figure 3.6 Numbers of REE-bearing apatite, zircon, crandallite group, and monazite/xenotime particles per area in the Western Kentucky No. 13 specimens. 40
Figure 3.7 Elemental compositions of the Group I and Group II particles found in the leaching solid residue of the Fire Clay raw coal waste. 42
Figure 3.8 Elemental compositions of the REE-bearing particles found in the leaching solid residue of the Fire Clay calcined coal waste. 43
Figure 3.9 Numbers of REE-bearing apatite, zircon, crandallite group, and monazite/xenotime particles per area in the Fire Clay specimens. 44
Figure 3.10 Potential flowsheets that can be used to improve the recovery of REEs from coal waste. 46
Figure 4.1 XRD pattern of the raw synthesized product. 54
Figure 4.2 SEM images of the synthesized florencite-(Ce) (a-c), a liberated florencite-(Ce) particle (d), and the corresponding EDS analysis (e) and elemental mapping of oxygen (f), cerium (g), aluminum (h), and phosphorus (i) of the liberated particle. 57
Figure 4.3 Low-magnification TEM image of a synthesized florencite-(Ce) particle (a), high-resolution TEM image from a thin region located on the right edge of the particle (b), and its corresponding FFT pattern (c). 58
Figure 4.4 XRD patterns of the raw synthesized florencite-(Ce) and samples calcined at different temperatures for 2 h (a), and the changes of peak intensity of selected crystal planes (b). 60
Figure 4.5 TGA-DTA curve of the raw synthesized florencite-(Ce). 61
Figure 4.6 The effect of calcination on the leaching characteristics of (a) Ce, (b) Al, and (c) P from florencite-(Ce). (Note: The standard deviations of the recovery values were ±

3%; therefore, error bars were not added in this figure to maintain the readability of the data.)..... 64
Figure 4.7 XRD patterns of the kaolinite sample (Kao) and mixed materials with different mass ratios (a), calcined products of 700 °C (b), calcined products of 1000 °C (c), and the DTA curves of florencite-(Ce), kaolinite, and the mixed materials with different mass ratios (d). (K-kaolinite; F-florencite-(Ce); M-muscovite; A-anatase; C-$CePO_4$; M1-mullite)... 68
Figure 4.8 XRD patterns of the coal coarse refuse sample (CR) and mixed materials with different mass ratios (a), calcined products of 700 °C (b), calcined products of 1000 °C (c), and the DTA curves of florencite-(Ce), coal coarse refuse, and the mixed materials with different mass ratios (d). (K-kaolinite; F-florencite-(Ce); M-muscovite; Q-quartz; P-pyrite; H-hematite; C-$CePO_4$). 70
Figure 4.9 The leaching characteristics of Ce from mixed samples, and the corresponding 700 °C- and 1000 °C-calcined products: (a) florencite-(Ce) and kaolinite mixtures; and (b) florencite-(Ce) and coal coarse refuse mixtures. (Note: The standard deviations of the recovery values were ± 3%; therefore, error bars were not added in this figure to maintain the readability of the data.) 71
Figure A.1 EDS spectra of the particles containing REEs found from the Western Kentucky No. 13 (WK No. 13) coal waste. (The spectra are labelled as Particle # (Specimen #. Site #. Spectrum #))..... 93
Figure A.2 SEM images of the particles containing REEs found from the Western Kentucky No. 13 (WK No. 13) coal waste. (The images are labelled as # Particle (Specimen #. Site #))..... 96
Figure A.3 EDS spectra of the particles containing REEs found from the Fire Clay coal waste. (The spectra are labelled as # Particle (Specimen #. Site #. Spectrum #)) 102
Figure A.4 SEM images of the particles containing REEs found from the Fire Clay coal waste. (The images are labelled as # Particle (Specimen #. Site #)) 106
Figure B.1 EDS spectra of the particles containing REEs found from the raw Western Kentucky No. 13 (WK No. 13) coal waste leaching residue. (The spectra are labelled as WRL # (Specimen #. Site #. Spectrum #)) 112

Figure B.2 SEM images of the particles containing REEs found from the raw Western Kentucky No. 13 (WK No. 13) coal waste leaching residue. (The images are labelled as WRL # (Specimen #. Site #)) 116
Figure B.3 EDS spectra of the particles containing REEs found from the calcined Western Kentucky No. 13 (WK No. 13) coal waste leaching residue. (The spectra are labelled as WCL # (Specimen #. Site #. Spectrum #)) 121
Figure B.4 SEM images of the particles containing REEs found from the calcined Western Kentucky No. 13 (WK No. 13) coal waste leaching residue . (The images are labelled as WCL # (Specimen #. Site #)) 125
Figure B.5 EDS spectra of the particles containing REEs found from the the raw Fire Clay (FC) coal waste leaching residue. (The spectra are labelled as FRL # (Specimen #. Site #. Spectrum #)) 130
Figure B.6 SEM images of the particles containing REEs found from the the raw Fire Clay (FC) coal waste leaching residue. (The images are labelled as FRL # (Specimen #. Site #)) 135
Figure B.7 EDS spectra of the particles containing REEs found from the the calcined Fire Clay (FC) coal waste leaching residue. (The spectra are labelled as FCL # (Specimen #. Site #. Spectrum #)) 143
Figure B.8 SEM images of the particles containing REEs found from the the calcined Fire Clay (FC) coal waste leaching residue . (The images are labelled as FCL # (Specimen #. Site #)) 147
Figure C.1 SEM images, EDS spectra, and elemental mapping of the synthesized florencite-(Ce) under various magnifications. 153
Figure C.2 The FFT patterns of selected symmetrical diffraction spots in red color (a)(c)(e), and the corresponding IFFT images (b)(d)(f). 153

List of Tables

Table 2.1 REEs contents of the coal waste samples (whole sample basis, mg/kg). 10
Table A.1 Elemental compositions of the particles containing REEs found from the Western Kentucky No. 13 coal waste through SEM-EDS analysis..... 92
Table A.2 Elemental compositions of the particles containing REEs found from the Fire Clay coal waste through SEM-EDS analysis. 101
Table B.1Elemental compositions of the particles containing REEs found from the raw Western Kentucky No. 13 (WK No. 13) coal waste leaching residue through SEM-EDS analysis. 111
Table B.2 Elemental compositions of the particles containing REEs found from the calcined Western Kentucky No. 13 (WK No. 13) coal waste leaching residue through SEM-EDS analysis. 120
Table B.3 Elemental compositions of the particles containing REEs found from the raw Fire Clay (FC) coal waste leaching residue through SEM-EDS analysis. 129
Table B.4 Elemental compositions of the particles containing REEs found from the calcined Fire Clay (FC) coal waste leaching residue through SEM-EDS analysis. 142
Table C.1 The chemical composition of the completely recrystallized product..... 153

Preface

This dissertation is submitted as a completion of the degree of Doctor of Philosophy at Virginia Polytechnic Institute and State University. This research was conducted by the author, Bin Ji, under the supervision of Dr. Wencai Zhang in the Department of Mining and Minerals Engineering.

This dissertation is established based on three manuscripts. Altogether, the dissertation includes, three peer-reviewed journal articles, and one journal article to be submitted for review.

The content of Chapter 1 comes from two published papers, including "Ji, B., Li, Q., Zhang, W., 2022. Leaching recovery of rare earth elements from the calcination product of a coal coarse refuse using organic acids. J. Rare Earths 40, 318–327.", and "Ji, B., Li, Q., Zhang, W., 2022. Rare earth elements (REEs) recovery from coal waste of the Western Kentucky No. 13 and Fire Clay Seams. Part I: Mineralogical characterization using SEM-EDS and TEM-EDS. Fuel 307, 121854."

Chapter 2 has been published as "Ji, B., Li, Q., Zhang, W., 2022. Rare earth elements (REEs) recovery from coal waste of the Western Kentucky No. 13 and Fire Clay Seams. Part I: Mineralogical characterization using SEM-EDS and TEM-EDS. Fuel 307, 121854."

Chapter 3 has been published as "Ji, B., Li, Q., Tang, H., Zhang, W., 2022a. Rare earth elements (REEs) recovery from coal waste of the Western Kentucky No. 13 and Fire Clay seams. Part II: Re-investigation on the effect of calcination. Fuel 315, 123145."

Chapter 4 is to be submitted for peer review. The experiments and data processing were conducted by Bin Ji under the supervision of Dr. Wencai Zhang.

Chapter 1 Brief Introduction

1.1 Background

Rare earth elements (REEs) are a group of 15 elements referred to as the lanthanide series in the periodic table of elements. Scandium (Sc) and yttrium (Y) are normally included in this categorization because of their similar properties and occurrence in the same ore bodies as the lanthanides (Balaram, 2019). REEs are generally classified into two sub-groups according to their atomic weights and locations in the periodical table (Binnemans et al., 2013; Massari and Ruberti, 2013), namely light rare earth elements (LREEs) and heavy rare earth elements (HREEs). Promethium (Pm) is produced by radioactive decay and considered as the only element listed in the periodical table without stable isotopes (Elkina and Kurushkin, 2020; Zhang et al., 2015b). The global production of REEs was estimated to 280,000 metric tons of REO in 2021 (Sangine, 2020). Figure 1.1 The distribution of global REO production in 2021.shows REE production by different countries. REEs have been coded as critical materials by several international institutions and governments due to their supply risks and importance to the clean energy industry, advanced military applications, and many commodity items in high-tech industries (Binnemans et al., 2013; Chu, 2011; DoI, 2018; European Commission, 2015). The criticality of REEs has led to increasing interests and studies in the recovery from alternative resources, such as waste electrical and electronic equipment, permanent magnets, and lamp phosphors (Binnemans et al., 2013; Di Piazza et al., 2017).

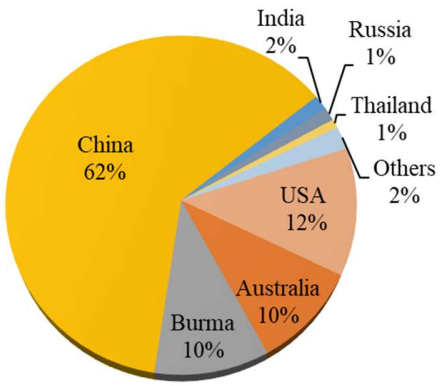


Figure 1.1 The distribution of global REO production in 2021.

Rare earth elements (REEs) recovery from coal-related materials, including coal, coal waste, coal combustion ash, and acid coal mine drainage, has been extensively studied in recent years (Mahandra et al., 2021; Peiravi and Dehghani, 2021; Sreenivas and Moudgil, 2021; Vass et al., 2019; Zhang et al., 2020). Several different methods have been tested to obtain satisfactory recovery of REEs from the coal-related materials. Physical and physico-chemical separation methods, such as size fractionation, density separation, magnetic separation, and froth flotation, have been used to concentrate REEs from coal, coal waste, and coal combustion ash (Gupta et al., 2017; Huang et al., 2018; Lin et al., 2017; Pan et al., 2020; Yoon et al., 2016; Zhang et al., 2015a; W. Zhang et al., 2017; Zhang et al., 2018). For example, using froth flotation, a concentrate containing 2300 mg/kg of total REEs was obtained from a coal waste derived from the Fire Clay coal seam (W. Zhang et al., 2017). REE contents in a fly ash sample were elevated from 782 mg/kg to 1025 mg/kg by combining size fractionation and magnetic separation (Pan et al., 2020). Therefore, the physical and physico-chemical methods are effective for the pre-concentration of REEs to obtain a higher-grade feedstock for downstream recovery and purification processes.

Hydrometallurgical methods, such as salt, acid, and alkaline leaching, have been employed to extract REEs from the coal-related materials (Cao et al., 2018; King et al., 2018; Laudal et al., 2018; Yang et al., 2019; Yang and Honaker, 2020; Zhang et al., 2018). Satisfactory recoveries have been obtained from low-rank coals with mild leaching conditions, for example, nearly 90% of the total REEs existing in a lignite were leached using 0.5 mol/L H_2SO_4 (Laudal et al., 2018). However, for high-rank coals and coal waste materials, much lower recovery values were normally obtained even using more concentrated acid solutions at higher temperatures (e.g., 1.2 mol/L H_2SO_4 at 75°C) (Honaker et al., 2017; Yang et al., 2019). Due to the glassy structure formed during combustion process, REE recovery from coal fly ash and bottom ash is more challengeable relative to pre-combustion coal and coal waste. As suggested by sequential chemical extraction studies reported in the literature (Lin et al., 2018; Pan et al., 2019), more than 80% of the REEs in the coal fly ash samples occurred as silicate and aluminosilicate forms, which can only be dissolved through digestion. In order to improve REE recovery from coal combustion ash, pyrometallurgical methods, such as roasting with the addition of

alkalis, were carried out before leaching to destroy the glassy structure (Taggart et al., 2018; Tang et al., 2019).

The REE-containing minerals are mainly grouped into halides, carbonates, oxides, phosphates, and silicates. Bastnaesite, monazite, and xenotime are the most economically viable REE-bearing minerals that are worth mining and processing (Kanazawa and Kamitani, 2006; Peiravi et al., 2017). Many metallurgical processes have been developed to achieve the maximum extraction of REEs. In general, the oxidization roasting will be conducted on the bastnasite to decompose the fluorocarbonate and oxidize the cerium to tetravalent state, which is then subjected to acid leaching to dissolve the non-cerium rare earths. The obtained leaching residue, which mainly composes of CeO_2, is further digested with caustic soda followed by HCl leaching to achieve the selective separation of individual rare earths. (Wang et al., 2017). Both monazite and xenotime are chemically and thermally stable, which normally require concentrated alkali- or acid-baking to destruct the crystal structure before extraction (Franken, 1995; Kumari et al., 2015a). In addition, preconcentration steps, such as flotation, gravity and magnetic separations, are normally indispensable to reject significant amount of gangue minerals and generate REE concentrates which are conducive for the downstream metallurgical treatments. (Abaka-Wood et al., 2019a, 2019b). The developments in green technologies and high-tech applications are driving unprecedented demand for REEs, and the gradual depletion of high grade REE-bearing minerals has stimulated intensive research on REE recovery from alternative sources to ensure adequate supply for present and future use (Swain and Mishra, 2019).

The authors have been focusing on REE recovery from kaolinite and coal-related materials for years, and it was found that the recovery of REEs, especially light REEs (LREEs), was significantly improved after calcination pretreatment at 600-700 °C for 2 h without adding any additives (Ji et al., 2022a; Zhang and Honaker, 2020, 2019a). For example, the leaching recovery of LREEs from a natural kaolinite sample was increased from less than 15% to over 90% after calcination at 600 °C for 2 h, and the same phenomenon was also observed in coal coarse refuse.

1.2 Research Objectives

It has been verified that calcination has a positive impact on REE recovery from coal waste. However, the mechanisms of the enhanced REE recovery after calcination was still unclear. Considering the complex occurrence modes of REEs, it is essential to identify the types, contents, and association characteristics of REE-bearing phases present in the coal waste. Therefore, the major objective of this study is to investigate the mineralogy of REEs in the coal waste. By comparing the changes of REE mineralogy before and after REE recovery, the mechanisms of the significantly improved REE recovery after calcination pretreatment can be confirmed.

1.3 Dissertation Outline

This dissertation comprises of five chapters, the outline of each chapter is as follows:

Chapter 1 gives a brief introduction of rare earth elements (REEs), an overview of REE recovery from coal-related materials, and current research progress. The research objectives as well as the outline of the dissertation are also present.

In the Chapter 2, two coal waste samples were selected as the research object, and REE mineralogy was studied systematically through SEM-EDS and TEM-EDS analyses. The mineralogy and the association characteristics of REEs occurred in the coal waste were determined.

Chapter 3 mainly focuses on the characterization of REE mineralogy in the leaching residues, i.e., the raw leaching residue, and the calcined leaching residue. By comparing the REE mineralogy changes before and after REE recovery, the mechanisms of the enhanced REE recovery as a result of calcination pretreatment can be concluded.

The characterization of pure endmember of crandallite-group minerals was conducted in Chapter 4. A combination analysis indicated a detailed thermal phase transformation process of florencite. In addition, the florencite was mixed with the host minerals, such as kaolinite and coal waste to detect potential reactions during calcination.

Chapter 5 summarizes this dissertation and provides perspectives for further improvement of the current study.

Chapter 2 The Mineralogical Characterization of Rare Earth Elements (REEs) from Coal Waste

Abstract

The mineralogy of rare earth elements (REEs) in the Western Kentucky No. 13 and Fire Clay coal waste was studied using scanning electron microscopy – energy dispersive spectroscopy (SEM-EDS). A total of 49 and 50 REE-bearing particles were found from the SEM-EDS specimens of the two materials, respectively. For both materials, light REEs were found in apatite, monazite, and crandallite group minerals, while heavy REEs primarily existed in zircon and xenotime. Based on the number and REE contents of the REE-bearing mineral particles, it was concluded that monazite, xenotime, and crandallite group minerals were major contributors to the total REE contents in both materials. The number of crandallite group mineral particles found from the Western Kentucky No. 13 material was more than that of monazite and xenotime particles, while the number of these two types of REE-bearing mineral particles found from the Fire Clay material was close. Since the monazite and xenotime particles contained more REEs relative to the crandallite group mineral particles, it was inferred that the majority of the REEs, especially the light REEs, present in the Fire Clay coal waste occurred as monazite and xenotime. In addition, comparing with the Western Kentucky No. 13 material, a larger portion of the heavy REEs in the Fire Clay material were comprised in zircon. SEM images of the REE-bearing particles indicated that both liberated particles and particles locked by dominant minerals appeared in the two materials. A few of the particles found from the Western Kentucky No. 13 material were completely encapsulated within the dominant minerals. Findings from the current study will promote REE recovery from coal-related materials, particularly coal waste.

2.1 Introduction

Actually, a considerable amount of research has been completed on the mineralogy of REEs in coal. Four main genetic modes of REE enrichment in coal have been identified: terrigeous, tuffaceous, infiltrational, and hydrothermal (Dai and Finkelman, 2018; Seredin and Dai, 2012). For coals with normal REE contents, these elements are mainly

concentrated in accessary minerals, resistate minerals, and/or clay minerals; whereas, for coals with high REEs contents, these elements typically occur as authigenic minerals and/or organically-bound phases (Seredin and Dai, 2012; Zhang et al., 2015b). Using scanning electron microscopy - and transmission electron microscopy – energy dispersive spectroscopy (SEM-EDS and TEM-EDS), many different types of REE-bearing minerals have been found in coal, which include but are not limited to zircon ($ZrSiO_4$), crandallite ($CaAl_3(PO_4)_2(OH)_5{\cdot}H_2O$), florencite ($REEAl_3(PO_4)_2(OH)_6$), apatite ($Ca_5(PO_4)_3(OH,F,Cl)$), monazite ($REEPO_4$), xenotime ($YPO_4$), bastnaesite ($REECO_3F$), kimuraite ($CaY_2(CO_3)_4{\cdot}6(H_2O)$), lanthanite ($(REE)_2(CO_3)_3{\cdot}8(H_2O)$), rhabdophane ($REEPO_4{\cdot}H_2O$), cherchite ($Y(PO4){\cdot}2H_2O$), and rare earth oxides (Dai et al., 2016; Hower et al., 2018, 2016; Seredin and Dai, 2012; Zhang and Noble, 2020). Moreover, sequential chemical extraction tests were also performed on coals to quantify the occurrence modes of REEs. For example, based on the test results of 20 coal samples, it has been concluded that the REEs predominantly occurred as phosphate minerals in the bituminous coals while as clays in the low rank coals (Finkelman et al., 2018).

Although there have been a lot of research on the mineralogy of REEs in coal, the correlation between the REE mineralogy and REE recovery has not been well established. Moreover, by analyzing REE contents in the process streams generated by a group of 20 coal preparation plants located in the eastern USA, it was found that around 73% of the REEs in the run-of-mine coals reported to coal waste after coal preparation (Luttrell et al., 2019). Therefore, REE recovery from coal waste is more promising relative to other coal-related materials from the perspective of total amount of REEs. Unfortunately, the mineralogy of REEs in coal waste has rarely been investigated, and existing findings reported in the literature are insufficient to provide guidance for the selection of efficient recovery methods and the design of advanced recovery processes (P. Zhang et al., 2017; Zhang and Honaker, 2019a, 2020). Recently, the authors did a systematic study on the mineralogy and recovery of REEs from the coal waste of two different seams: Western Kentucky No. 13 and Fire Clay. Characterization methods, results, and findings relevant to the mineralogy are presented in the current paper.

2.2 Materials and Methods

2.2.1 Materials

Representative plant feed samples were collected from two coal preparation plants located in Kentucky, USA, which processed the Western Kentucky No. 13 (WK) and Fire Clay (FC) seam coals, respectively. The samples were air-dried and the materials coarser than 10 mm were obtained by dry sieving. The oversize fractions were density fractionated using a dense medium bath of 2.2 specific gravity (SG), which was prepared by mixing magnetite powder finer than 48 μm with tap water. After separation, the resultant sink materials were rinsed with tap water to remove the entrained magnetite particles, and then air-dried at room temperature and finally pulverized to a top particle size of 0.18 mm using a jaw crusher and a hammer mill. REE mineralogy of the pulverized materials originating from the two different seams was characterized in the current study. In a typical coal preparation process, the 2.2 SG sink fraction is normally abandoned as coal waste. Therefore, findings from this study will contribute to REE recovery from coal waste.

2.2.2 Methods

Comprehensive mineralogical characterizations of REEs existing in the coal waste of the two different seams were conducted through SEM-EDS. SEM-EDS specimens were prepared by sprinkling the solid particles onto double-sided carbon tape mounted on a SEM stub. A layer of Au/Pd of 5 nm thickness was coated on the specimens using a desktop sputter coater (208HR, Cressington Scientific Instrument, England, UK). The characterization was performed using a JSM-IT500HR SEM (JEOL, MA, USA) equipped with an Ultim Max EDS detector (Oxford Instruments, Abington, UK). The EDS detector was controlled and the EDS data was analyzed using AZtech software (Oxford Instruments, Abington, UK). The software provides several different scanning modes for elemental analysis. Point & ID mode and Map mode were employed in the current study. The Point & ID mode enables a quick elemental composition analysis at a specific point or across a region of interest, while the Map mode is able to tell the distribution of elements in an area of interest by developing elemental maps. If there is a brighter color at a specific location in the map, it means a higher concentration of the corresponding element is present. The Point & ID mode enables elemental composition analysis to be performed in points,

rectangles, circles, and polygons. In the present study, several points on the same REE-bearing particle were analyzed, and the highest REE content obtained from the analyses in the different points was used to evaluate REE mineralogy. This method will minimize the interference of dominant mineral particles (e.g., clays).

The procedures used to find REEs-rich particles from the specimens are presented in Figure 2.1. An area was first selected from a specimen using the SEM at a magnification of 1,200x followed by elemental mapping using the EDS in the Map mode. Cerium, yttrium, and phosphate were selected as predefined elements during the EDS analysis, while the other elements existing in the area were automatically identified by the software. After elemental mapping, the maps of the three elements were observed with naked eye to find regions with a brighter color relative to the overall maps. If a brighter region was found, elemental composition of the region was analyzed using the EDS in the Point & ID mode. Otherwise, another area will be selected from the specimen to repeat the procedures. After elemental composition analysis, the peaks in the spectra were carefully checked by comparing with the standard peaks of corresponding metals. If REEs were confirmed to exist, SEM images of the region were taken at much higher magnifications (e.g., 10,000x), and a more detailed elemental analysis was conducted in this region using the EDS in the Point & ID mode. If REEs did not exist, another area will be selected from the specimen to repeat the whole procedures. Rather than random selection, the areas were gradually selected from one side of the specimen to the other side to avoid repeated analysis of the same area. Four and two SEM-EDS specimens were prepared and analyzed for the Western Kentucky No. 13 and the Fire Clay samples, respectively. Reliable conclusions relevant to the mineralogical characteristics of the REEs were reached by analyzing the REE-bearing particles found from the specimens.

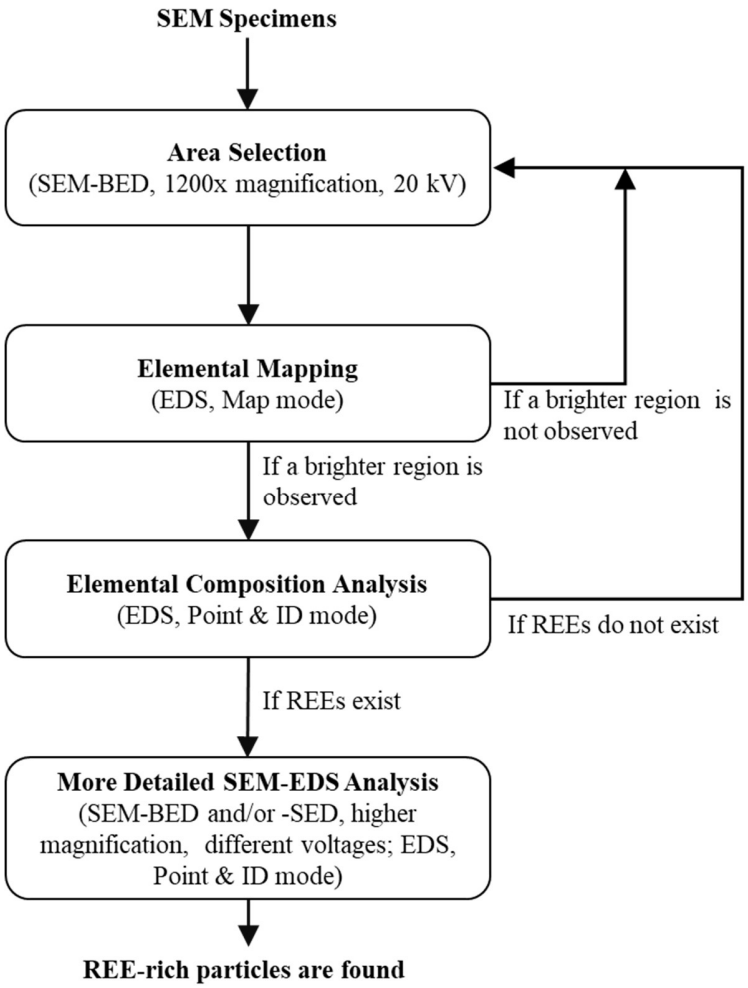


Figure 2.1 Procedures used to find REEs-rich particles from the coal waste specimens (BED and SED represent backscattered electron detector and secondary electron detector, respectively).

To measure elemental composition, the coal waste samples of 0.1 g were digested following a modified ASTM D6357-11 method (Zhang and Honaker, 2020). Elemental concentrations in the solutions obtained from the solid digestion were measured using an inductively coupled plasma - optical emission spectrometry (ICP-OES) unit manufactured by Thermo Fisher Scientific, USA. The unit was calibrated using six standards prepared at the following concentrations: 0 ppm, 0.05 ppm, 0.5 ppm, 1 ppm, 5 ppm and 10 ppm. The calibration was verified by two independently sourced check standards, i.e., continuing calibration verification (CCV) and continuing calibration blank (CCB), every 10 samples. The REE recovery for these check standards was ±10% RSD.

2.3 Results and Discussion

2.3.1 REE Contents in the Coal Waste

REE contents of the coal waste samples of the two different seams are presented in Table 2.1. The Western Kentucky No. 13 coal waste contained 309 mg/kg of total REEs, which is close to that of the Fire Clay coal waste (312 mg/kg). Moreover, the contents of light and heavy REEs in the two different materials were also similar, as suggested by the nearly same light to heavy REEs ratios (4.8 versus 4.7). The total REE contents were higher than the content of upper continent crust (UCC, 179 mg/kg; (Taylor and McLennan, 1985)) and the average content of world coals (72.4 mg/kg; (Ketris and Yudovich, 2009)). However, comparing with commercial rare earth ores, such as monazite and xenotime ores, the content levels were much lower. Moreover, the content levels were below the detection limit of commonly used mineralogical characterization methods, such as X-ray diffraction (around 1%), thus causing difficulties in understanding the mineralogical characteristics of the REEs, which are critical for designing efficient recovery processes. In the current study, mineralogical characteristics of the REEs were systematically investigated through SEM-EDS analysis following the procedures described in Section 2.2.

Table 2.1 REEs contents of the coal waste samples (whole sample basis, mg/kg).

Seam	Sc	Y	La	Ce	Pr	Nd	Sm	Eu	Gd	Tb
WK	17.7	22.6	49.9	107.7	13.5	53.7	13.8	2.1	8.9	1.7
FC	14.6	26.8	52.2	109.3	13.6	55.2	11.8	1.4	9.1	1.0
Seam	Dy	Ho	Er	Tm	Yb	Lu	TREEs	LREEs	HREEs	L/H
WK	6.2	0.4	4.8	0.7	3.8	1.7	309	256	52.9	4.8
FC	5.9	1.2	4.9	0.5	3.4	0.7	312	257	55.0	4.7

Note: WK and FC represent Western Kentucky No. 13 and Fire Clay seams, respectively; TREEs: total REEs (Sc, Y, plus lanthanides); LREEs: light REEs (Sc plus La through Sm); HREEs: heavy REEs (Y plus Eu through Lu); H/L: the ratio of LREEs to HREEs.

2.3.2 REE Mineralogy in the Western Kentucky No. 13 Coal Waste

A total of 49 REE-bearing particles referred to as Particle 1-Partcle 49 were found from the Western Kentucky No. 13 specimens. Elemental compositions, EDS spectra, and SEM images of the particles are provided in the Appendix. All the particles except Particle 1 contained certain amounts of phosphor, therefore the REEs existing in the Western Kentucky No. 13 coal waste primarily occurred as phosphate minerals. Based on the elemental compositions of Particle 1 shown in Figure 2.2, it can be concluded that zircon ($ZrSiO_4$) was the REE-bearing mineral, and the REEs contained in the mineral were yttrium and scandium. Among the remaining 48 particles, two particles (i.e., Particles 2 and 3) had extremely high calcium and phosphor contents. The EDS spectra shown in Figure 2.3 suggested that the particles were apatite, and cerium is the only REE detected in the mineral. It has to be mentioned that several zircon and many apatite particles were found from the specimens, whereas REEs were detected in only three of those particles (i.e., Particles 1-3). Given these findings, it can be inferred that although REE-bearing zircon and apatite were found from the specimens, these two types of minerals only contributed to a small portion of the total REEs comprised in the Western Kentucky No. 13 coal waste.

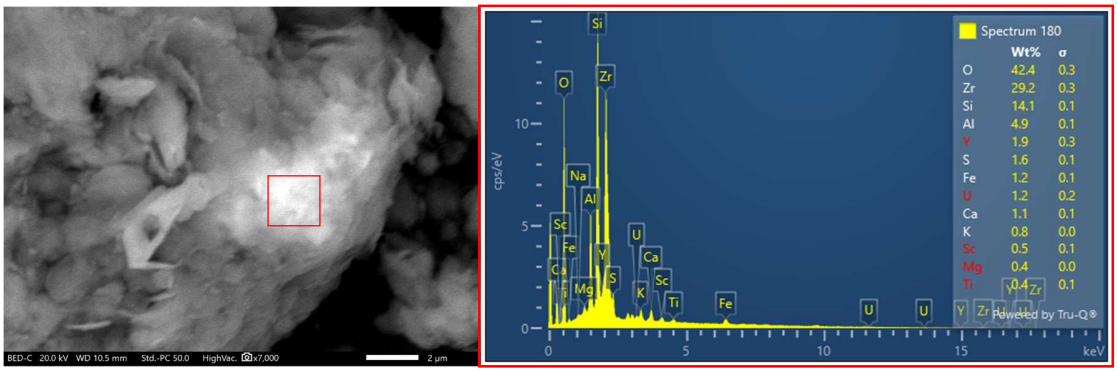


Figure 2.2 SEM-BED image (left) and EDS spectrum (right) of Particle 1 found from the Western Kentucky No. 13 coal waste.

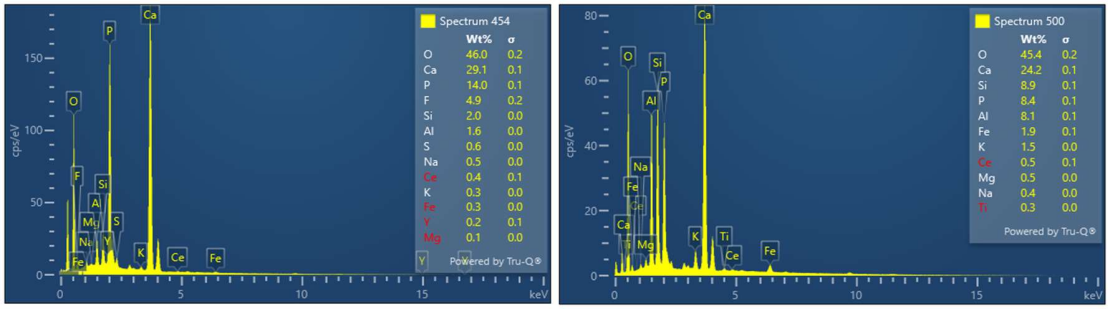


Figure 2.3 EDS spectra of Particle 2 (left) and Particle 3 (right) found from the Western Kentucky No. 13 coal waste.

Based on the EDS spectra and elemental compositions, the remaining 46 REE-bearing particles were tentatively classified into two groups: Group I (Particles 11-49) and Group II (Particles 4-10). Figure 2.4 shows the EDS spectra of Particle 25 and Particle 6, which represent the Group I and Group II particles, respectively. Comparisons between the two spectra suggested that Particle 6 contained less aluminum than Particle 25, however, Particle 6 was more enriched in REEs. Moreover, the ratio of total REEs to phosphor content (TREE/P) of Particle 25 was much lower than that of Particle 6 (0.36 versus 4.35). All the comparisons between the two particles suggested that their REE-bearing minerals are different. Figure 2.5 presents more systematic comparisons between the Group I and II particles in terms of the elemental composition. As Figure 2.5 (a) and (b) show, the Group II particles except Particle 7 contained less aluminum than the Group I particles, however, the majority of the Group I particles contained less REEs relative to the Group II particles. Moreover, TREE/P ratios of the Group I particles were less than those of the Group II particles (Group I < 2 while Group II > 2). These contrasts agreed with the differences observed between Particles 25 and 6. Particle 7 had an aluminum content of 12.9%, which is similar to the contents of the Group I particles; whereas, given the relatively higher total REE content and larger TREE/P ratio, this particle was classified into Group II.

From the scattered data points shown in Figure 2.5, it can be observed that for the Group I particles, as the phosphor content increased, the aluminum content remained at high levels, and the calcium content showed an increasing trend, while the content of silicon, iron, and potassium gradually decreased. Moreover, as Figure 2.5(f) and (g) show, several Group I particles also contained strontium and barium, and the content of these two

elements showed an increasing trend with increases in the phosphor content. Therefore, aluminum, phosphor, calcium, strontium, and barium are the constituent elements of the REE-bearing minerals existing in the Group I particles. Crandallite group minerals normally contain these elements, such as crandallite itself ($CaAl_3(PO_4)_2(OH)_5{\cdot}H_2O$), goyazite ($SrAl_3(PO_4)_2(OH)_5{\cdot}H_2O$), gorceixite ($BaAl_3(PO_4)_2(OH)_5{\cdot}H_2O$), and florencite ($REEAl_3(PO_4)_2(OH)_6$) (Mordberg, 2004a; Rasmussen, 1996; Sejkora et al., 2001). Therefore, it can be inferred that crandallite group minerals are likely the REE-bearing phases in the Group I particles. As Figure 2.5(b) shows, considerable differences in REE content existed among the Group I particles. For example, as presented in the Appendix, Particle 11 contained 19.3% of total REEs, while the content of calcium, strontium, and barium was minimal. However, as compared with Particle 11, Particle 40 had a much lower total REE content of 1% but a higher strontium content of 5.6%. Therefore, florencite and goyazite were likely the REE-bearing minerals in the Particles 11 and 40, respectively.

For the Group II particles, the content of aluminum, silicon, iron, and potassium decreased with increases in the phosphor content, while the calcium content was not correlated with the phosphor content. Moreover, all the particles did not contain strontium and barium. Therefore, REE mineralogy of the Group II particles is different from that of the Group I particles. Comparisons among the different figures of Figure 2.5 suggested that a positive correlation only existed between the total REEs and phosphor content. Therefore, the REE-bearing minerals existing in the Group II particles were likely monazite and xenotime. Based on the types of REEs comprised in the particles, it can be inferred that four of the particles were monazite, while the other three were xenotime (see the Appendix). The sum of the number of the monazite and xenotime particles is much less than that of the crandallite group mineral particles (i.e., 7 versus 39), however, total REE contents of the monazite and xenotime particles are much higher. Therefore, based on the SEM-EDS data obtained from the current study, it is difficult to determine which REE-bearing mineral dominated in the coal waste material. Elemental compositions shown in the Appendix suggested that the crandallite group minerals only contained light REEs, while xenotime and zircon contained certain amounts of heavy REEs.

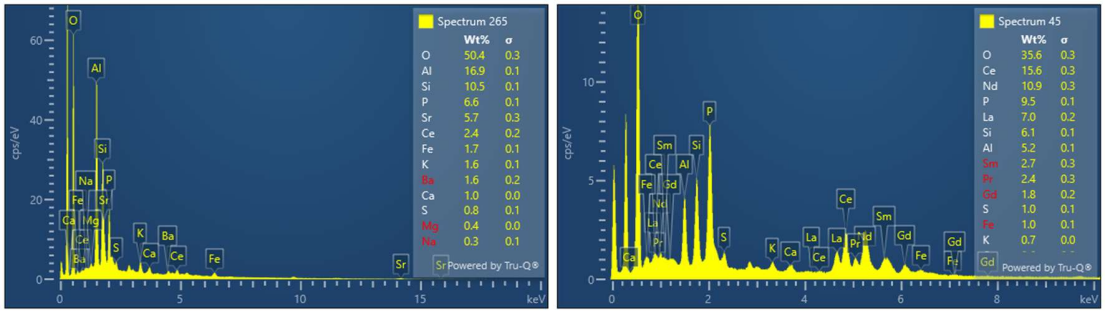
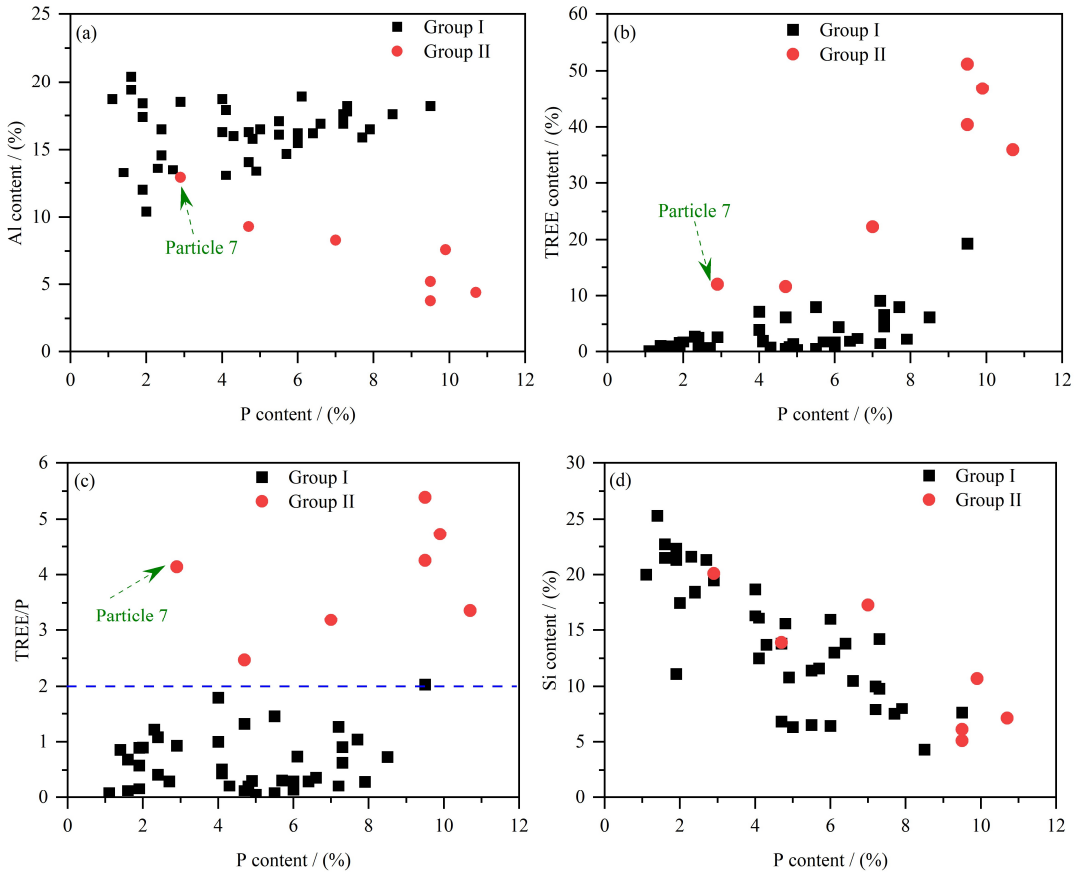


Figure 2.4 EDS spectra of Particle 25 (left) and Particle 6 (right).



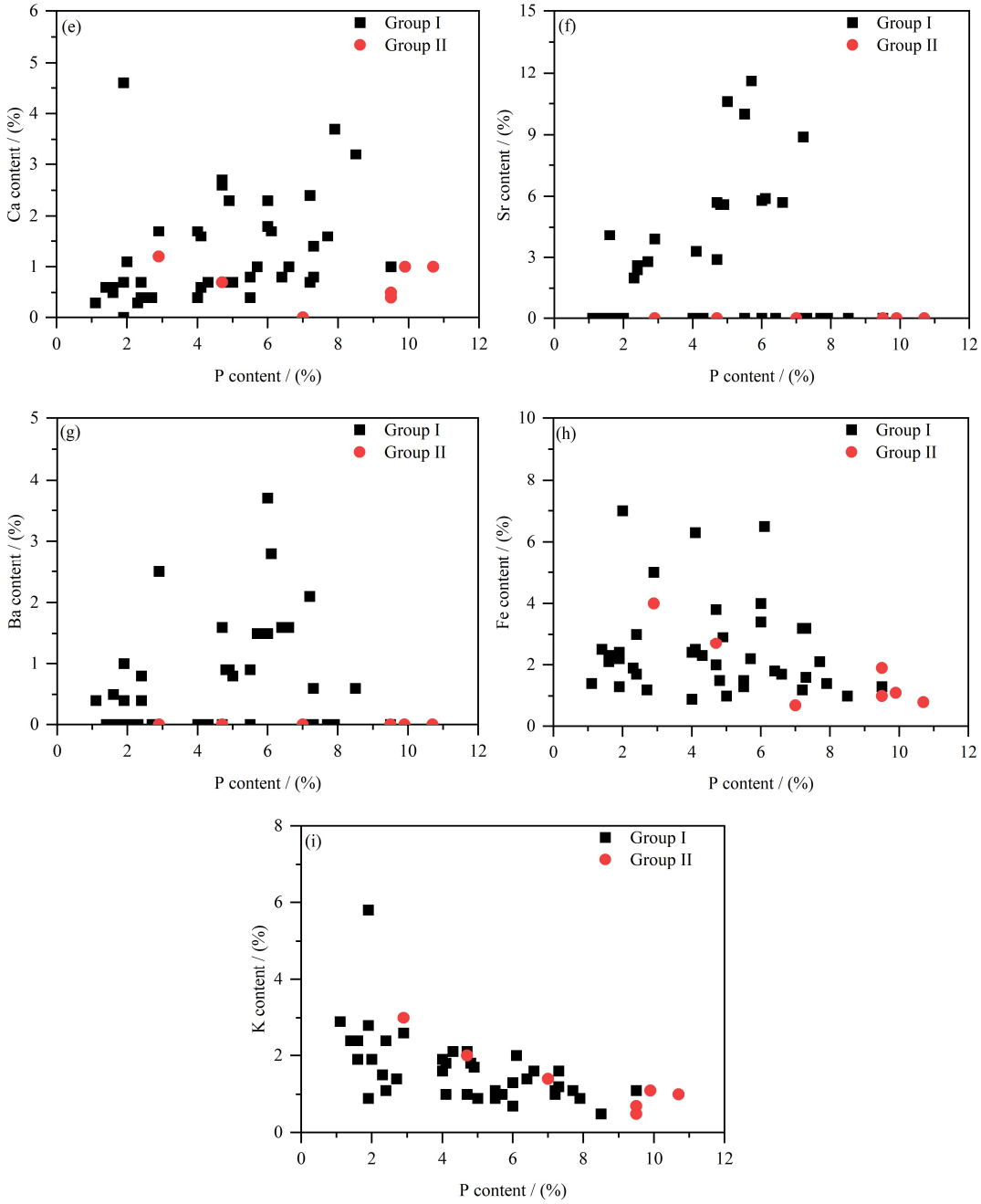


Figure 2.5 Elemental compositions of the Group I and Group II particles found from the Western Kentucky No. 13 coal waste.

2.3.3 Physical Association Characteristics of REEs in the Western Kentucky No. 13 Coal Waste

The SEM-EDS characterization results presented in Section 3.2 suggested that REEs existing in the Western Kentucky No. 13 coal waste sample primarily occurred as

crandallite group minerals, monazite, and xenotime. Meanwhile, a small portion of the REEs were also comprised in a few zircon and apatite particles. These findings are critical for REE recovery from the material, however, in order to design efficient recovery processes, physical association characteristics of the REE-bearing particles with dominant mineral particles also need to be studied.

SEM images of the REE-bearing particles presented in Figure 2.6 and the Appendix A were employed to study the physical association characteristics. It can be observed from the images that for the same type of REE-bearing minerals, both liberated particles and particles locked by the dominant minerals existed in the material. For example, as Figure 2.6(a) and (b) show, although both Particle 4 and Particle 6 were monazite, the former particle was locked by an aluminum silicate particle, while the latter existed as a liberated particle. Moreover, per the SEM images of all the REE-bearing particles shown in the Appendix, it can be concluded that the particle size of these particles was very fine, typically less than 5 μm. Moreover, for selected particles, such as Particles 10, 18, and 25, the particle size was less than 1 μm. These characteristics limit the application of physical separation methods, such as gravity separation and froth flotation, to efficiently beneficiate REEs from the material, since those methods normally require sufficient liberation and have a relatively coarser bottom size limit.

Different locking statuses were observed by comparing the SEM-BED images taken at different accelerating voltages. As Figure 2.7 shows, the region corresponding to a locked xenotime particle was bright when using 20 kV, however, as the voltage decreased to 10 kV, no noticeable difference in brightness was observed between the region and the overall image. The difference of using different voltages was likely due to that the penetration depth and interaction volume of electrons decrease with the decrease in the accelerating voltage. Therefore, this phenomenon indirectly confirmed that the xenotime particle was completely encapsulated by the dominant mineral particle. Unlike the xenotime particle, the bright region corresponding to a locked monazite particle presented in Figure 2.8 shrunk but not disappeared as the accelerating voltage decreased from 20 kV to 10 kV. Therefore, rather than being completely encapsulated, a portion of the monazite particle surface was exposed. The complete and incomplete encapsulation statuses may lead to different REEs recovery characteristics. For example, in order to dissolve the completely

encapsulated xenotime particle through hydrometallurgical methods, such as acid leaching, the dominant mineral particle needs to be destructed first, whereas for the partially encapsulated monazite particle, the REEs can be leached regardless whether the dominant mineral particle is destructed or not.

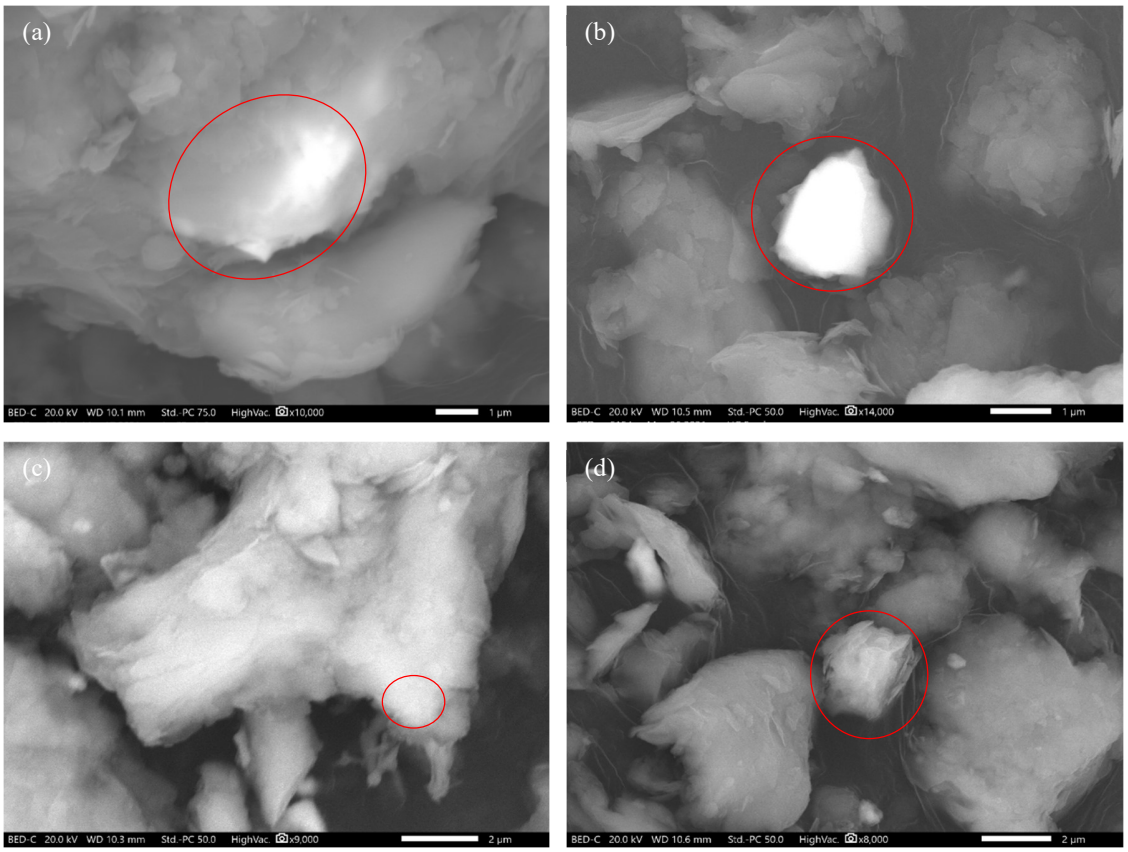


Figure 2.6 SEM images of selected REE-bearing particles found from the Western Kentucky No. 13 coal waste: (a) Particle 4, monazite; (b) Particle 6, monazite; (c) Particle 21, crandallite group mineral; and (d) Particle 26, crandallite group mineral. (The REE-bearing particles are marked with red circles.)

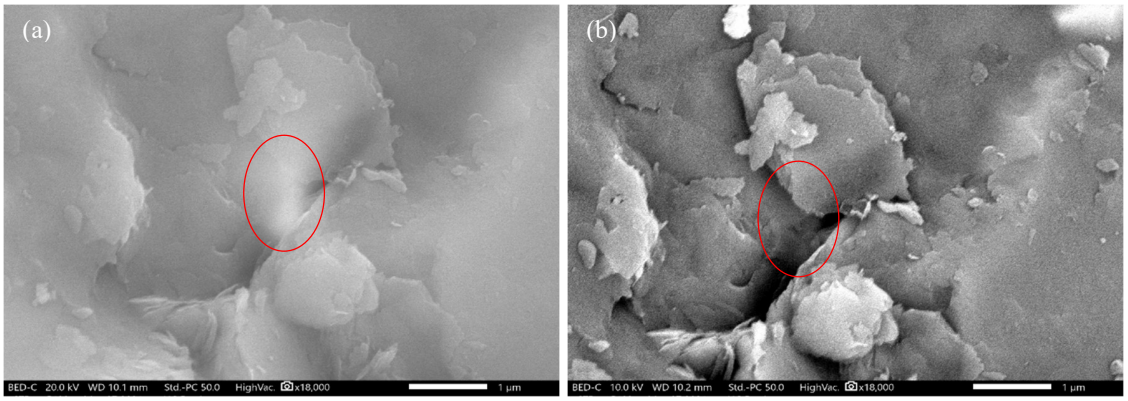


Figure 2.7 SEM-BED images of a xenotime particle taken with different accelerating voltages: (a) 20 kV and (b) 10 kV. (The xenotime particle is marked with red circles.)

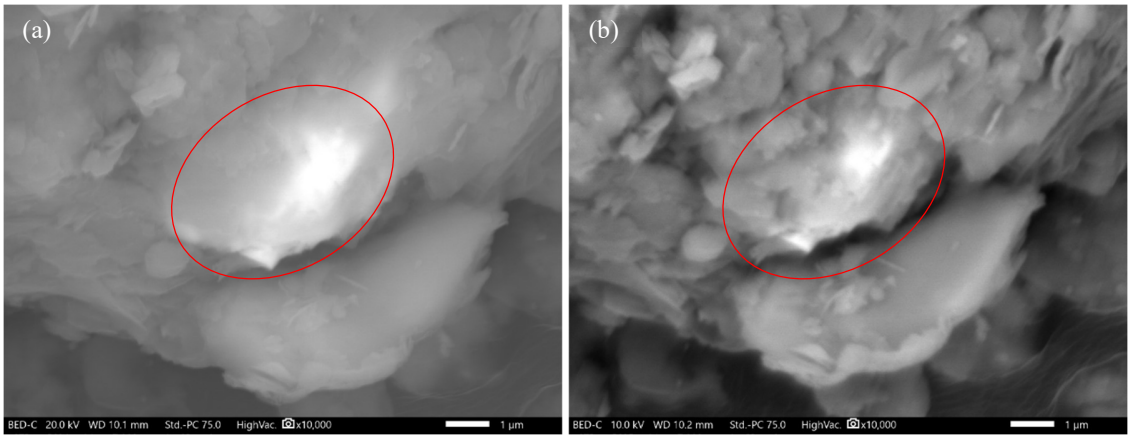


Figure 2.8 SEM-BED images of a monazite particle taken with different accelerating voltages: (a) 20 kV and (b) 10 kV. (The monazite particle is marked with red circles.)

2.3.4 Mineralogy and Physical Association Characteristics of REEs in the Fire Clay Coal Waste

A total of 50 REE-bearing particles referred to as FCP 1-FCP 50 were found from the Fire Clay specimens, which is close to the number of particles found from the Western Kentucky No. 13 specimens (i.e., 50 versus 49). Elemental compositions, EDS spectra, and SEM images of the Fire Clay particles are provided in the Appendix. More REE-bearing zircon particles (FCP 1-5) were found from the Fire Clay specimens relative to the Western Kentucky No. 13 specimens (i.e., 5 versus 1). In addition, REEs contained in the zircon particles of the Fire Clay specimens were primarily yttrium and scandium. This finding is consistent with the phenomenon observed from the Western Kentucky No. 13 specimens.

Therefore, comparing with the Western Kentucky No. 13 coal waste, a greater portion of the heavy REEs especially yttrium in the Fire Clay coal waste were associated with zircon. The REE-bearing mineral of FCP 6 is apatite since the calcium and phosphor content is extremely high. Similar to the apatite particles found from the Western Kentucky No. 13 specimens, the apatite particle from the Fire Clay specimens primarily contained cerium. SEM images and EDS spectra of selected zircon and apatite particles found from the Fire Clay material are presented in Figure 2.9.

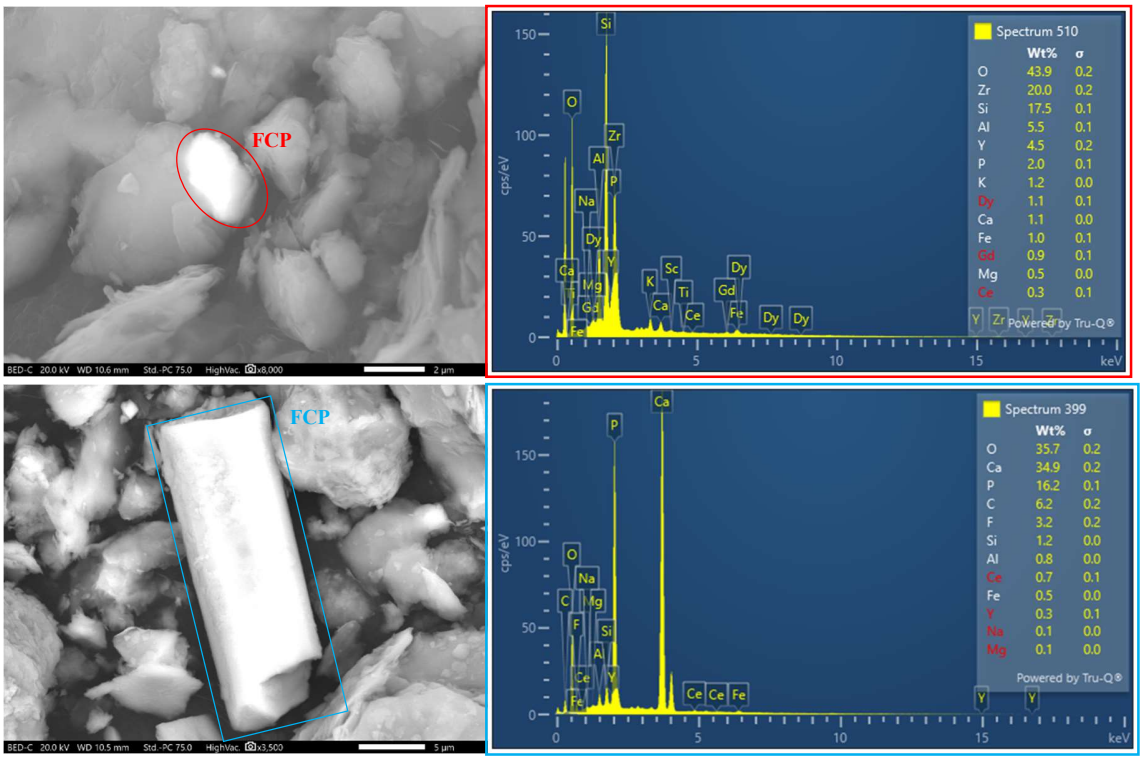


Figure 2.9 SEM-BED images and EDS spectra of a zircon (FCP 1) and an apatite (FCP 6) particle found from the Fire Clay coal waste.

Based on aluminum contents, phosphor contents, and TREE/P ratios, the remaining 44 particles were classified into two groups: Group I (FCP 27-50) and Group II (FCP 7-26). The method of classification is the same as that used for the REE-bearing particles found from the Western Kentucky No. 13 specimens. As Figure 2.10 shows, the aluminum content of Group I particles remained at high levels as the phosphor content increased, and a few of the particles also contained strontium and barium. Therefore, it can be concluded that REEs comprised in the Group I particles primarily existed as crandallite group

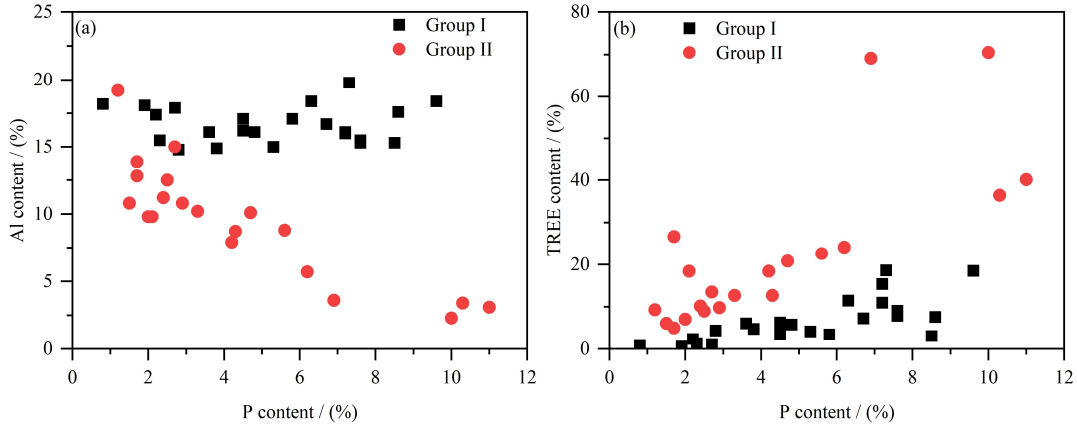
minerals. Moreover, comparing with the Group I particles of the Western Kentucky No. 13 specimens, the particles of the Fire Clay specimens contained less calcium, and a positive correlation between the calcium and phosphor content did not exist (see Figure 2.5(e) and Figure 2.10(e)). Therefore, crandallite itself was unlikely the dominant REE-bearing crandallite group mineral in the Fire Clay coal waste. The REE-bearing crandallite group minerals were more likely florencite, goyazite, and gorceixite.

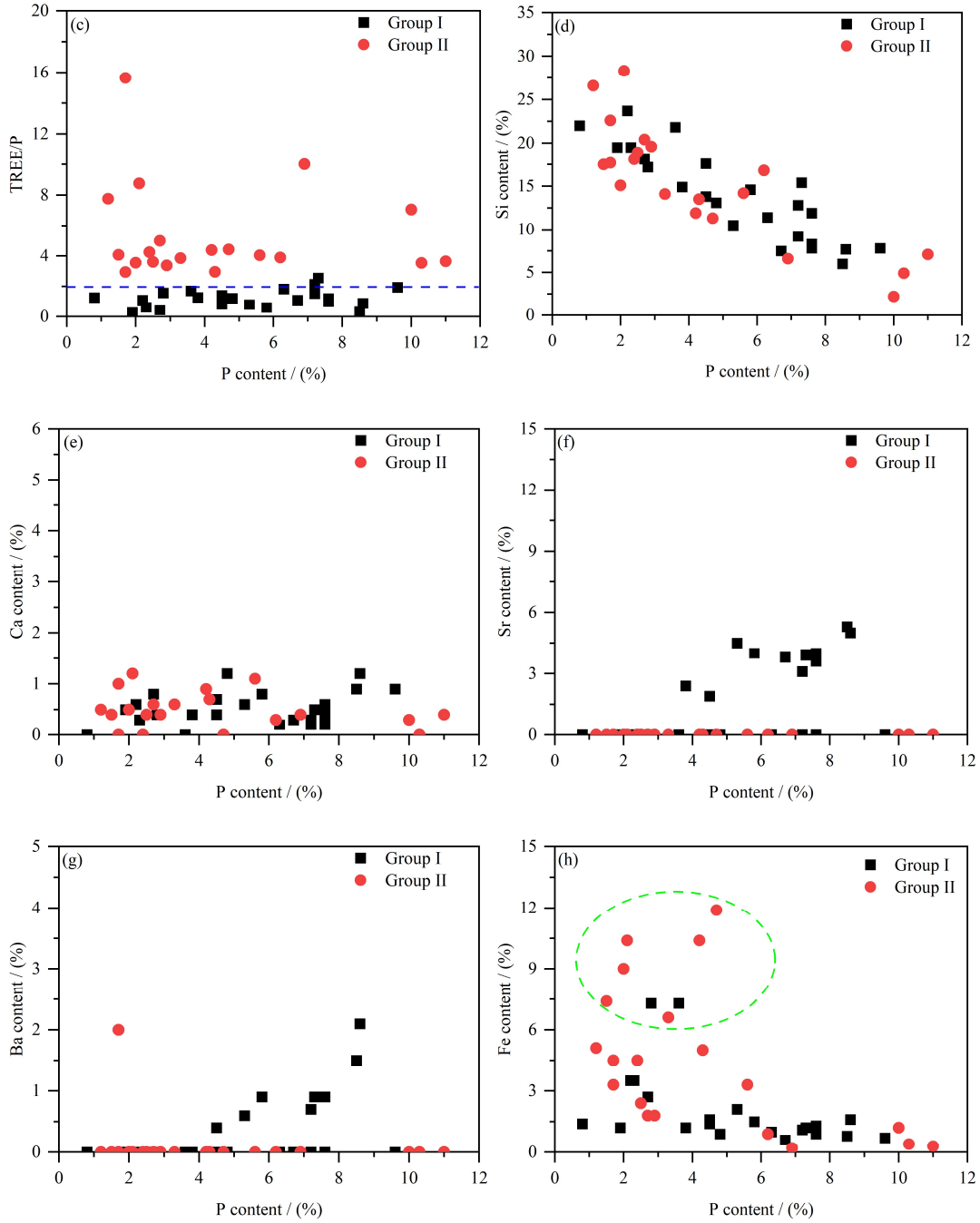
Comparing with the Group I particles, the Group II particles were characterized with relatively lower aluminum but higher TREE contents. Moreover, TREE/P ratios of the majority of the Group II particles were larger than those of the Group I particles (Group I < 2 while Group II > 2). The differences between the two groups of the Fire Clay particles were similar to those observed from the Western Kentucky No. 13 particles. Therefore, REE-bearing minerals of the Group II particles were monazite and xenotime. Based on the types of REEs comprised in the particles, it can be concluded that 18 Group II particles (FCP 7-24) were monazite while the remaining two particles (FCP 25 and 26) were xenotime. The sum of the number of the monazite and xenotime particles were close to that of the crandallite group mineral particles (i.e., 20 versus 24). Given the finding that the Group II particles contained more REEs than the Group I particles, it can be inferred that the majority of the REEs existing in the Fire Clay coal waste were associated with monazite and xenotime. As presented in Section 3.2, only 7 out of the 49 REE-bearing particles found from the Western Kentucky No. 13 specimens were monazite and xenotime. Therefore, a greater portion of the REEs in the Fire Clay coal waste occurred as monazite and xenotime relative to the Western Kentucky No. 13 coal waste.

As the phosphor content increased, the silicon and potassium content gradually decreased for both the Group I and Group II particles. Therefore, the dominant silicon- and potassium-bearing minerals, such as clays, unlikely contained REEs. Moreover, as Figure 2.10(h) shows, a negative correlation existed between the iron and phosphor content, suggesting that the contribution of iron minerals to the total REEs content was minimal. However, a few of the particles had extremely high iron contents, for example, a monazite particle (FCP 22) contained as high as 9% of iron. This phenomenon was likely due to the physical association of REE-bearing particles with iron mineral particles. For example, as Figure 2.11 shows, a monazite particle (FCP 22) contained 7.1% TREE (cerium plus

lanthanum plus neodymium) and 9% iron, and the particle is locked by a dominant mineral particle containing more iron (e.g., 14.1%, spectrum 237). A similar association of monazite and iron minerals (e.g., iron spinels) has been observed from the Fire Clay coal by Hower et al. (Hower et al., 2018). In addition to the monazite particle, an anatase particle containing 14.5% titanium (spectrum 235) was also locked in the iron mineral particle.

Based on the SEM images of the REE-bearing particles presented in the Appendix, it can be observed that both liberated particles and particles locked by the dominant minerals existed in the Fire Clay material. Besides iron mineral particles, several REE-bearing particles were also locked by the particles of other dominant minerals, such as aluminum silicates (e.g., clays, see Figure 2.12). Similar to the Western Kentucky No. 13 material, the particle size of REE-bearing particles found from the Fire Clay material was also normally finer than 5 μm, and a few particles were even finer than 1 μm. These physical association characteristics will largely limit the application of physical separation methods to beneficiate the REE-bearing minerals. It has to be mentioned that completely encapsulated REE-bearing particles were not found from the Fire Clay specimens by comparing the SEM-BED images taken at different accelerating voltages. Therefore, the REE-bearing particles were partially encapsulated by the dominant mineral particles.




(c)
Group I
Group II
TREE/P
P content / (%)
(d)
Group I
Group II
Si content / (%)
P content / (%)
(e)
Group I
Group II
Ca content / (%)
P content / (%)
(f)
Group I
Group II
Sr content / (%)
P content / (%)
(g)
Group I
Group II
Ba content / (%)
P content / (%)
(h)
Group I
Group II
Fe content / (%)
P content / (%)

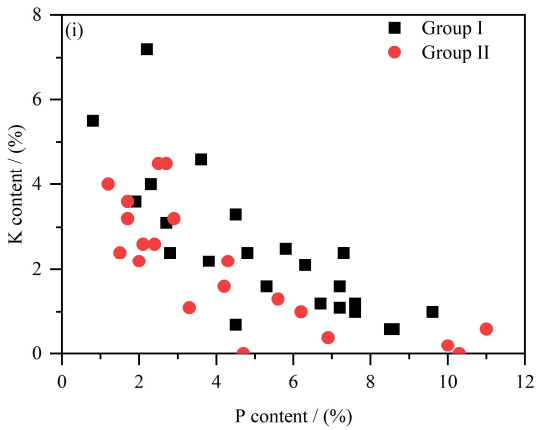


Figure 2.10 Elemental compositions of the Group I and Group II particles found from the Fire Clay coal waste.

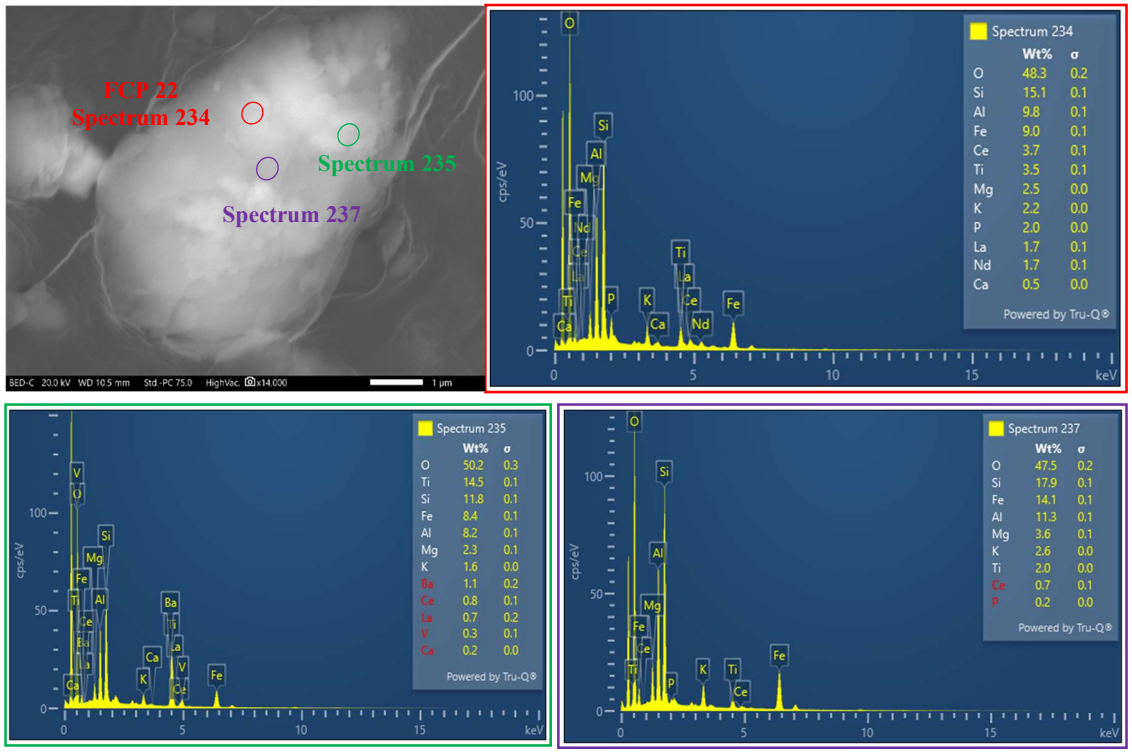


Figure 2.11 SEM image and EDS spectra of FCP 22 found from the Fire Clay coal waste.

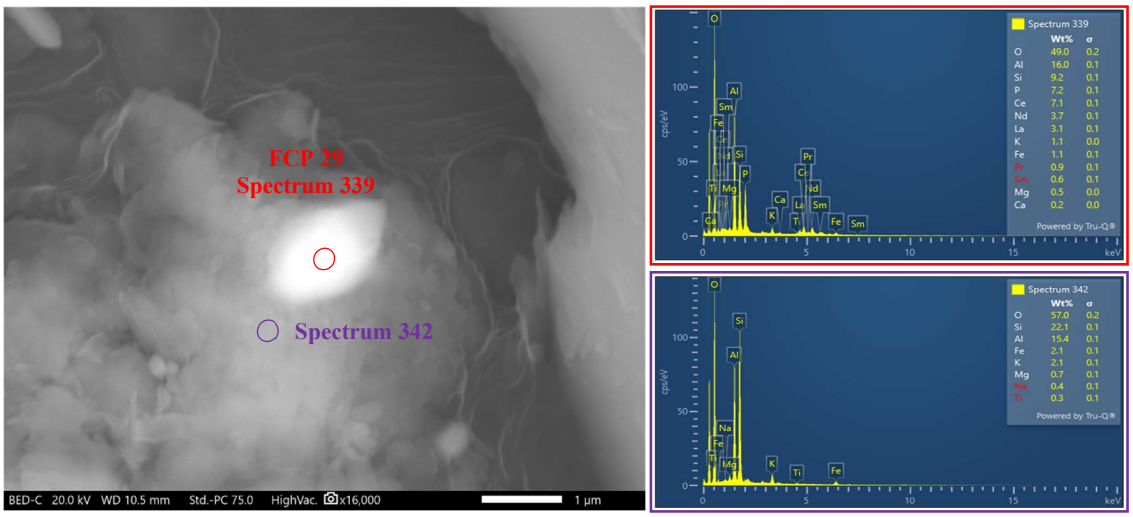


Figure 2.12 SEM image and EDS spectra of FCP 29 found from the Fire Clay coal waste.

2.4 Conclusions

The mineralogy and physical association characteristics of REEs existing in the Western Kentucky No. 13 and Fire Clay coal waste were systematically studied through SEM-EDS analysis. A total of 49 REE-bearing particles were found from the SEM-EDS specimens of the Western Kentucky No. 13 sample. Based on the compositional analysis data obtained by EDS, REE-bearing mineral particles were zircon, apatite, monazite, xenotime, and crandallite group minerals. Among these minerals, light REEs were detected in the apatite, monazite, and crandallite group minerals, while the other two minerals only contained heavy REEs. Zircon and apatite accounted for a small portion of the REEs since only one zircon and two apatite particles were found to contain REEs. The majority of the REEs occurred as monazite, xenotime, and crandallite group minerals. Based on the SEM images of the particles, it was observed that both liberated REE-bearing particles and particles locked by the dominant minerals existed in the West Kentucky No. 13 coal waste. Moreover, a few locked particles were completely encapsulated within the dominant mineral particles. All the REE-bearing particles have a particle size of less than 5 µm, while a few particles were less than 1 µm.

A total of 50 REE-bearing particles were found from the SEM-EDS specimens of the Fire Clay coal waste. REE-bearing minerals of the Fire Clay coal waste were the same as those of the Western Kentucky No. 13 coal waste. A greater portion of the heavy REEs in

the Fire Clay material occurred as zircon since more zircon particles were found. Moreover, the number of monazite and xenotime particles was close to that of the crandallite group mineral particles (20 versus 24), however, the monazite and xenotime particles contained much more REEs. Therefore, it was concluded that the majority of the REEs existing in the Fire Clay coal waste occurred as monazite and xenotime. The physical association characteristics and particle size of the REE-bearing particles in the Fire Clay material were similar to those in the Western Kentucky No. 13 material, while completely encapsulated particles were not found.

Chapter 3 The Effect of Calcination on the Leaching Recovery and Mineralogical Characterization of Rare Earth Elements (REEs) from Coal Waste

Abstract

In previous studies, the authors found that the leaching recovery of rare earth elements (REEs) from coal waste can be improved by calcination without adding any additives. Two potential mechanisms were proposed to explain the enhanced recovery: (1) decomposition of difficult-to-dissolve REE-bearing minerals into soluble forms; and (2) liberation of REE-bearing minerals encapsulated in clays after calcination due to the dehydration and disintegration of the layered clay structure. Unfortunately, no direct evidence was obtained to confirm the mechanisms. In the present study, the mineralogy of REEs existing in the leaching solid residue of raw and calcined coal wastes of the Western Kentucky No. 13 and Fire Clay seams was systematically characterized through scanning electron microscopy-energy dispersive X-ray spectroscopy (SEM-EDS) analysis. Characterization results showed that crandallite-group minerals still existed in the leaching solid residue of the raw coal wastes but disappeared in the leaching solid residue of the calcined products. Therefore, calcination decomposed crandallite-group minerals into easy-to-leach forms and thereby enhanced the leaching recovery of REEs. Moreover, the numbers of REE-bearing particles (*N*) found per area under SEM were calculated. Larger *N* values were obtained from the leaching solid residue of the calcined coal wastes relative to the raw coal wastes and the leaching solid residue of the raw coal wastes. Therefore, calcination promoted the liberation of REE-bearing particles. Overall, findings from the present study confirmed the two mechanisms that explain the positive effect of calcination on the recovery of REEs from coal waste.

3.1 Introduction

In the extractive metallurgical process of commercial rare earth minerals, such as monazite and xenotime (Kumari et al., 2015b; Sun et al., 2007; Wu et al., 2006, 2007; Xing et al., 2010; Yu et al., 2009; Yuan et al., 2017; Zhu et al., 2003), thermal treatment, normally referred to as calcination or roasting, is frequently applied to improve the leaching

performance of these minerals. However, due to the high stability of the crystal structure of monazite and xenotime, chemical reagents, such as NaOH (Kumari et al., 2015b), CaO plus NaCl plus $CaCl_2$ (Wu et al., 2007), and CaO plus carbon (Yuan et al., 2017), are required during the thermal treatment to convert monazite and xenotime into more leachable forms (e.g., rare earth hydroxides/oxides). In addition to the commercial rare earth minerals, the recovery of rare earth elements (REEs) from alternative resources has become a hot topic because of the increasing criticality of REEs (Chu, 2011; Petty, 2018). Coal-based materials have been reported as promising feedstocks for REE recovery due to the large reserves of coal and the relatively high REE contents in coal (Dai et al., 2018; Dai and Finkelman, 2018; Fu et al., 2022; Seredin and Dai, 2012). Many studies have been performed to improve the recovery performance of REEs from coal-based materials, which have been comprehensively summarized in several review articles (Eterigho-Ikelegbe et al., 2021; Zhang et al., 2020, 2015b).

The authors have been focusing on REE recovery from coal waste for several years (Honaker et al., 2020; Zhang and Honaker, 2019a, 2020). One of the most important findings is that calcination pretreatment without adding any chemicals can largely improve the leaching recovery of REEs from coal waste; for example, the leaching recovery of total REEs from the Western Kentucky No. 13 coal waste was enhanced from around 25% to greater than 80% after calcination at 750 ºC (Zhang and Honaker, 2020). By comparing the leaching characteristics of REEs with those of the major elements comprised in coal waste, and evaluating mineralogical changes as a function of calcination temperature, two possible mechanisms were proposed to explain the enhanced recovery: (1) decomposition of difficult-to-dissolve REE-bearing minerals into soluble forms; and (2) liberation of REE-bearing minerals encapsulated in clays after calcination due to the dehydration and disintegration of the layered clay structure. However, no direct evidence has been obtained to confirm the two mechanisms. Ji et al. (Ji et al., 2022c) found that monazite, xenotime, and crandallite-group minerals are major contributors to the total REE contents in the coal waste of both the Western Kentucky No. 13 and Fire Clay seams. As introduced in the previous paragraph, thermal decomposition of monazite and xenotime requires chemical reagents; however, the enhancements in the recovery of REEs from coal waste were obtained by calcination without adding any additives. To confirm the two mechanisms and

explain the inconsistent findings obtained in the thermal treatment of coal waste and monazite/xenotime minerals, the authors re-investigated the effect of calcination on REE recovery from coal waste. Experimental methods and results are presented and discussed in the following sections.

3.2 Materials and Methods

3.2.1 Materials

The Western Kentucky No. 13 and Fire Clay coals were collected from coal preparation plants located in Kentucky, USA. The coals were air-dried and then sieved using a screen of 10-mm aperture size. The oversized materials were density fractionated using a dense medium bath of 2.2 specific gravity (SG), and the sink fractions were washed, air-dried, and finally pulverized to a top particle size of 0.18 mm (80 mesh). In a typical coal preparation process, 2.2-SG sink fractions are normally rejected as coal wastes. Proximate analysis showed that the pulverized materials had an ash content of 88.47% (Western Kentucky No. 13) and 92.08% (Fire Clay), respectively. The materials have been investigated in the study by Ji et al. (Ji et al., 2022c), which presents more details about the sample collection, preparation, and analysis procedures. Trace metal grade HCl (37 wt.%), HNO_3 (67 wt.%), and HF (50 wt.%) were purchased from Thermo Fisher Scientific, USA, and used for acid leaching tests and solid digestions. Type I deionized water with a resistivity of 18.2 MΩ·cm at room temperature was used for all the tests.

3.2.2 Calcination

Calcination of the coal waste materials was performed in a temperature-controllable muffle furnace (EW-33858-80, Cole-Parmer, USA). A known weight of the solids was placed in porcelain crucibles (around 5 g per crucible), which were then transferred into the furnace. The temperature in the furnace was elevated from room temperature to 600 ˚C at a ramping rate of 20 ºC/min. After 2 h of calcination, the furnace was automatically cooled to room temperature, and the calcined materials were emptied from the crucibles and used as feeds for acid leaching tests and REE mineralogy analyses.

3.2.3 Acid leaching tests

Both the raw and calcined coal wastes were subjected to acid leaching tests to evaluate the effect of calcination on the leaching performance of REEs and other elements. The tests were conducted in three-neck round-bottom flasks of 0.5-L maximum volumetric capacity. The flasks were connected to thermometers and condensers to measure temperature and reduce water loss due to evaporation, respectively. The reaction temperature was controlled using a water bath, while solid/liquid mixing was achieved using a magnetic stirrer. Detailed descriptions of the leaching apparatus have been published previously (Ji et al., 2020; Zhang and Honaker, 2020). For each test, 2.5-g solid was mixed with 250-mL HCl solution of 1.2 M, and the reaction temperature was fixed at 75 ºC. The leaching conditions were consistent with those used in the authors' prior studies on REE recovery from coal refuse (Zhang and Honaker, 2020, 2019b, 2019a). During the reaction, to evaluate the leaching characteristics of REEs and other elements, representative samples were collected from the slurry at different time intervals from the start of the leaching process up to a total period of 2 h (i.e., 5 min, 15 min, 30 min, 60 min, 90 min, and 120 min). Solid and liquid fractions of the samples were obtained through centrifuging at 4000 rpm. The liquid fractions were diluted using 5 v/v% HNO_3 and then subjected to elemental concentration analysis using inductively coupled plasma mass spectrometry (ICP-MS). The solid fractions were dried, ashed, and digested following a scenario modified from the ASTM D6357-11 method. The digestion solutions were analyzed using ICP-MS, and the analysis results were used to back-calculate the elemental contents of the solids. Leaching recovery was calculated based on elemental concentrations in the liquid fractions and elemental contents of the solid fractions. Three duplicates were performed on the raw coal wastes, and standard deviations in the leaching recovery were less than 3%.

3.2.4 SEM-EDS Analysis

REE mineralogy in the leaching solid residue of the raw and calcined coal wastes was characterized through SEM-EDS analysis, following the same procedures used by Ji et al. (Ji et al., 2022c). Several SEM specimens of the leaching solid residues were prepared by sprinkling the solid particles onto double-sided carbon taps mounted on SEM stubs. Then, the specimens were coated with a layer of Au/Pd of 5 nm thickness. A JSM-IT500 HRE SEM (JEOL, MA, USA) instrument with an Ultim Max EDS detector (Oxford Instruments,

Abingdon, UK) was used for the analysis. The EDS detector was controlled and the EDS data was analyzed using AZtech software (Oxford Instruments, Abingdon, UK). The procedures used to find REE-rich particles from the specimens are presented in Figure 3.1. Detailed explanations of the procedures can be referred to the last chapter. Many REE-rich particles were found in the specimens through the SEM-EDS analysis, and REE mineralogy in the coal wastes was evaluated based on the EDS elemental composition data.

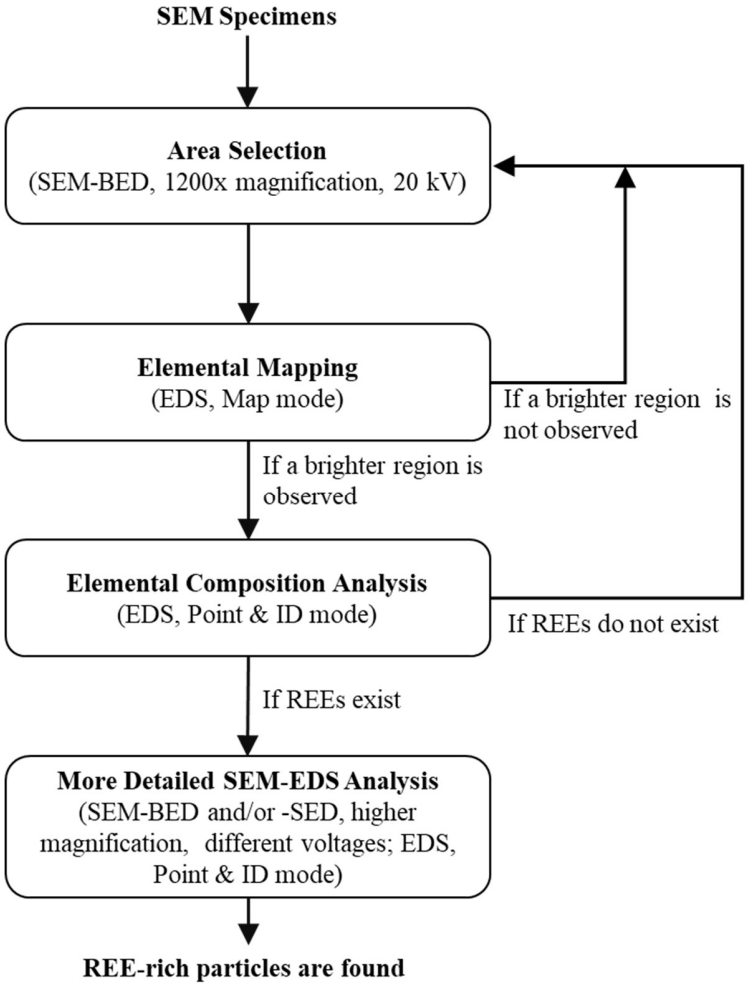
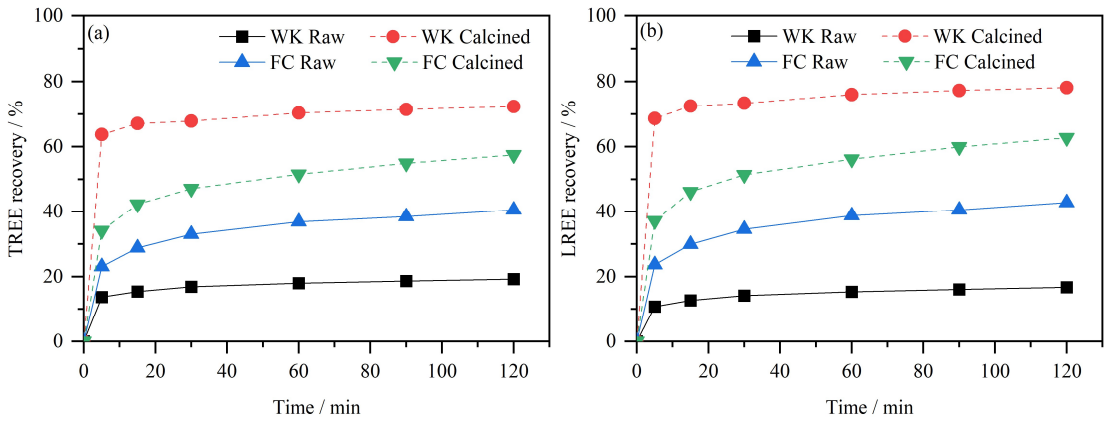


Figure 3.1 Procedures used to find REE-rich particles from the coal waste specimens (BED and SED represent backscattered electron detector and secondary electron detector, respectively) (Ji et al., 2022c).

3.3 Results and Discussion

3.3.1 Effects of Calcination on the Leaching Characteristics of REEs and Major Elements

Acid leaching tests were performed on the raw and calcined coal wastes to evaluate the effect of calcination on the leaching characteristics of REEs and major elements. As Figure 3.2 shows, leaching recoveries of REEs from the raw coal wastes were low; for example, after 2 h of reaction, only around 20% and 40% of total REEs (TREEs) were leached from the Western Kentucky No. 13 and Fire Clay raw coal wastes, respectively. Calcination pretreatment of the coal wastes at 600 ˚C for 2 h had positive effects on the recovery. After 2 h of reaction, around 72% and 57% of TREEs were leached from the calcined coal waste of the two different seams, respectively (Figure 3.2(a)). Comparisons between the recovery values of light REEs (LREEs) and heavy REEs (HREEs) suggested that the positive effect of calcination on the recovery of LREEs is more significant than that of the HREEs (Figure 3.2(b) and (c)). For example, after the calcination pretreatment, the 2 h leaching recovery of LREEs from the Western Kentucky No. 13 coal waste increased from around 17% to 78%; whereas, under the same conditions, the recovery of HREEs only increased from around 32% to 43%. The effects of calcination on the leaching recovery of REEs from the coal wastes are consistent with the findings from previous studies (Zhang and Honaker, 2020, 2019a).



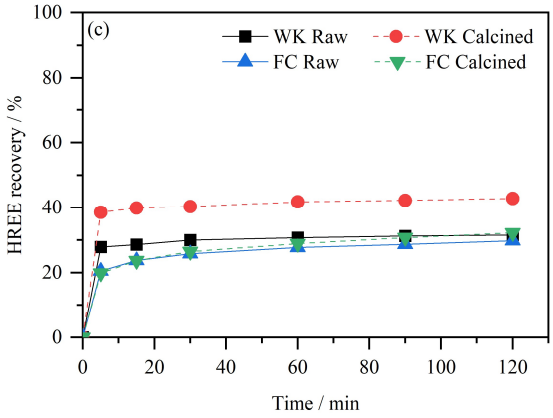


Figure 3.2 Leaching characteristics of REEs and major elements from the raw and calcined coal wastes.

REEs often associate with other minerals through isomorphic substitutions (Chen et al., 2019; Enkhbayar et al., 2016), and in this case, the leaching characteristics of REEs are related to the leaching characteristics of the constituent elements of the other minerals. In order to assess whether the positive effects of calcination on the REE recovery were due to mineralogical changes of the dominant minerals existing in the coal wastes, the leaching characteristics of several major elements comprised in the coal wastes were investigated. The major elements were selected based on the elemental composition of the coal wastes, in order to reflect the leaching behavior of the dominant minerals existing in the coal wastes (Ji et al., 2022d). As shown in Figure 3.3, leaching recoveries of Si and Ti from both the raw and calcined coal wastes were negligible, indicating that the dominant Si- and Ti-bearing minerals, such as quartz and rutile, did not contribute to the positive effects of calcination. Unlike Si and Ti, Ca was more leachable than the REEs, and Ca recoveries of greater than 70% were achieved from the raw coal wastes. Therefore, the dominant Ca-bearing minerals, such as calcite, dolomite, and gypsum, did not contain a significant amount of REEs. The recovery of Al was considerably improved after calcination, primarily due to the dehydration and disintegration of clay interlayers (Ji and Zhang, 2021a; Okada et al., 1998). However, the leaching kinetics of Al was much lower than that of the REEs; for example, by prolonging the reaction time from 5 min to 2 h, the recovery of Al from the Western Kentucky No. 13 calcined coal waste increased from around 21% to 74%, while the recovery of REEs only increased by around eight absolute percentage points.

Therefore, the dominant Al-bearing minerals, such as kaolinite, did not contain significant amounts of REEs.

For the Western Kentucky No. 13 seam, around 32% of Fe was leached from both the raw and calcined coal wastes after 2 h of reaction, but the leaching kinetics of Fe was noticeably reduced after calcination. The decrease in the leaching kinetics can be explained by the conversion of pyrite into hematite during the calcination process (Zhang and Honaker, 2019a). For the Fire Clay seam, higher recovery values of around 46% and 68% were obtained from the raw coal waste after 5 min and 2 h of reaction, respectively, suggesting that a larger portion of the Fe in the Fire Clay coal waste existed as relatively easy-to-leach forms. After calcination, the leaching kinetics of Fe in the Fire Clay coal waste was also reduced, likely due to the same reason as the Western Kentucky No. 13 coal waste. For the coal waste of both seams, calcination did not noticeably enhance the leaching recovery of Fe after 2 h of reaction. This phenomenon is different from that observed from the leaching characteristics of REEs, indicating that the contribution of dominant Fe-bearing minerals, such as pyrite, to the positive effects of calcination on the REE leaching recovery was minimal.

Based on the contrasts in the leaching characteristics of REEs and major elements, it can be concluded that the positive effects of calcination on the leaching recovery of REEs cannot be explained by the mineralogical changes of the dominant minerals comprised in the coal wastes. To reveal the mechanisms of the positive effects, SEM-EDS analyses were performed on the leaching solid residue of the raw and calcined coal wastes, following the procedures described in section 2.2.3. The analysis results were compared with those of the raw coal wastes, as described by Ji et al. (Ji et al., 2022d).

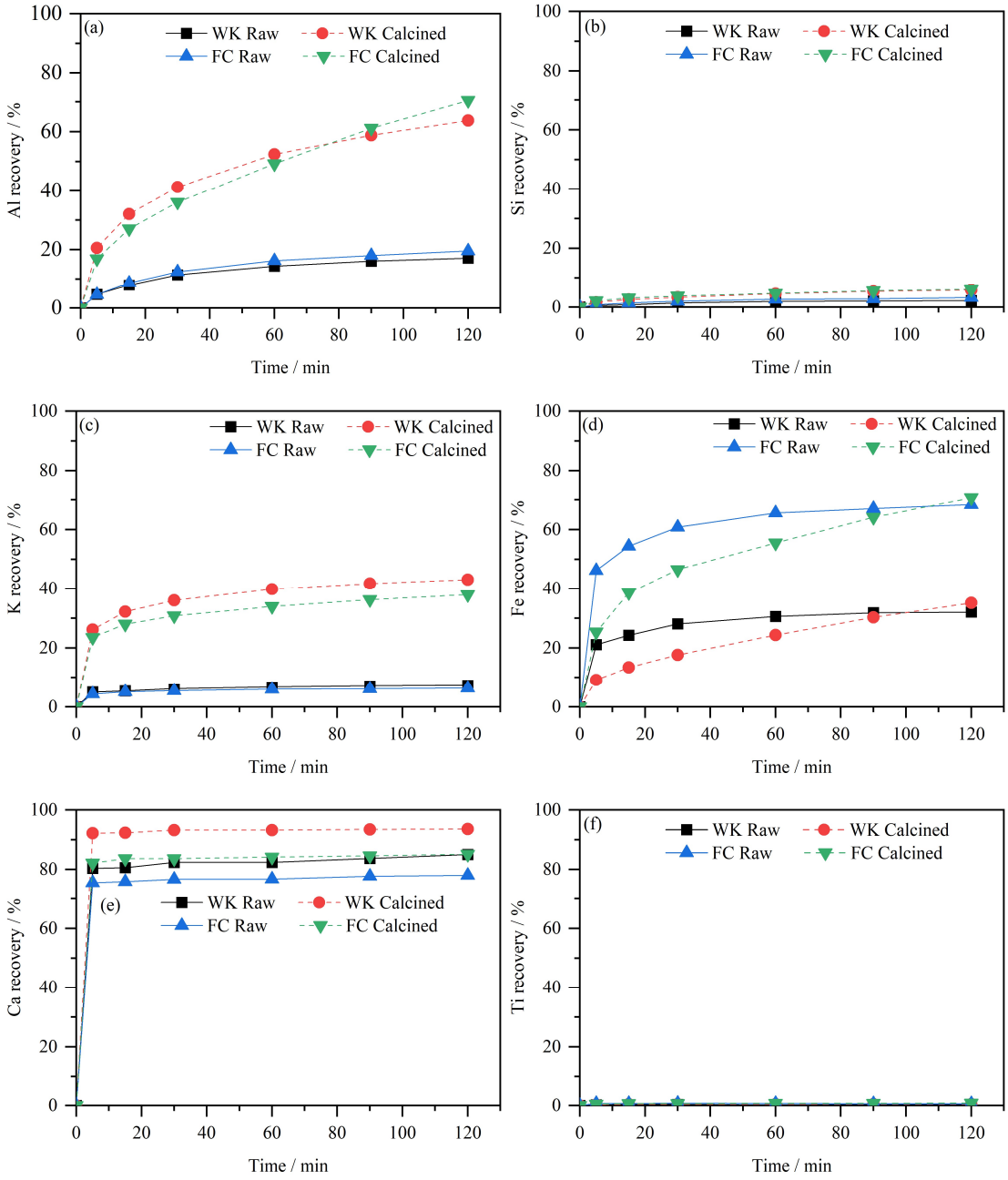


Figure 3.3 Leaching characteristics of major elements from the raw and calcined coal wastes.

3.3.2 REE Mineralogy in the Leaching Solid Residue of the Western Kentucky No. 13 Coal Waste

A total of 49 REE-bearing particles, referred to as WRL 1 – WRL 49, were found in the leaching solid residue of the Western Kentucky No. 13 raw coal waste through SEM-

EDS analysis. Among those particles, WRL 1 and WRL 2 were rich in Zr and Si, suggesting that the REE-bearing mineral was zircon. In addition, because only Y was detected in these two particles, it can be concluded that zircon primarily contributed to the HREEs found in the coal waste. It needs to be clarified that only Y detected in the particles does not necessarily mean the particles only contained Y. Some other REEs might also be contained in the particles, but their contents were too low to be detected by the EDS software. This phenomenon also likely occurred in the other REE-bearing minerals found in the coal waste. While Ji et al. (Ji et al., 2022c) found several REE-enriched apatite particles in the raw coal waste; in this investigation, apatite was not found in the leaching solid residue of the coal waste. The contrast indicated that the apatite existing in the raw coal waste was leached. Therefore, REE recoveries obtained from the raw coal waste presented in Figure 3.2 were partially attributable to the leaching of apatite.

The remaining REE-bearing particles can be classified into two groups based on the ratio of TREE to P content (TREE/P; Group I < 2 while Group II >2). This method has been used by Ji et al. (Ji et al., 2022d), and it has been confirmed that Group I particles are crandallite-group minerals, while Group II particles are predominantly monazite and xenotime (Ji et al., 2022d). Among the remaining particles, 34 and 13 particles were classified into the two groups, respectively (Figure 3.4(a)). As Figure 3.4(b) shows, the Al content of Group I particles remained at high levels, while the Al content of Group II particles gradually decreased with increases in the P content. In addition, as Figure 3.4(c) shows, the TREE content of Group II particles gradually increased with increases in the P content, while the TREE content of Group I particles was uncorrelated with the P content. These phenomena are consistent with those observed from the Western Kentucky No. 13 raw coal waste (Ji et al., 2022d). Therefore, among the remaining 47 REE-bearing particles, there were 34 crandallite-group mineral particles and 13 monazite/xenotime particles. As Figure 3.4(d)-(f) show, several Group I particles also contained certain amounts of Ca, Sr, and Ba, agreeing with the elemental composition of crandallite [$CaAl_3(PO_4)_2(OH)_5 \cdot H_2O$], goyazite [$SrAl_3(PO_4)_2(OH)_5 \cdot H_2O$], and gorceixite [$BaAl_3(PO_4)_2(OH)_5 \cdot H_2O$], respectively.

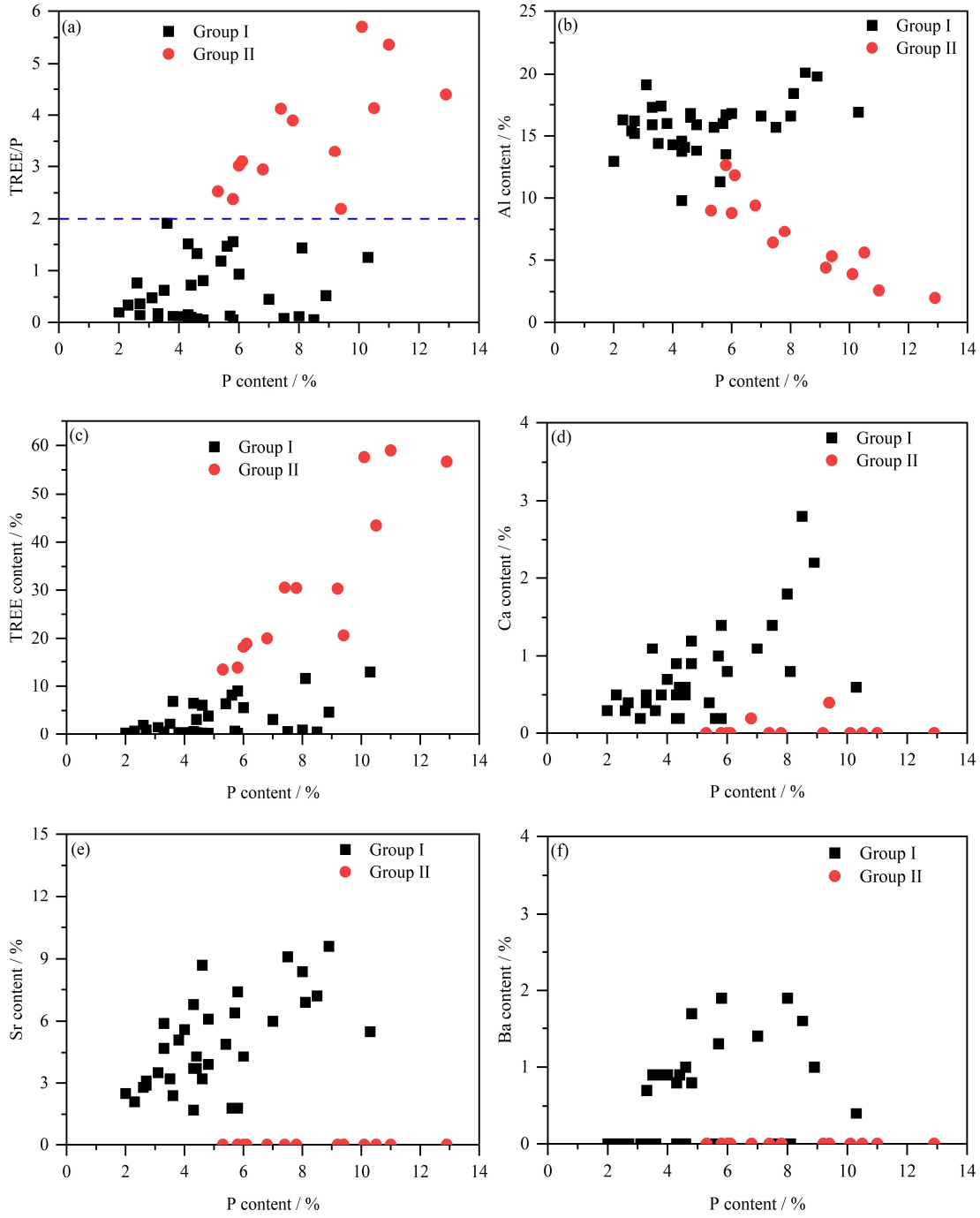
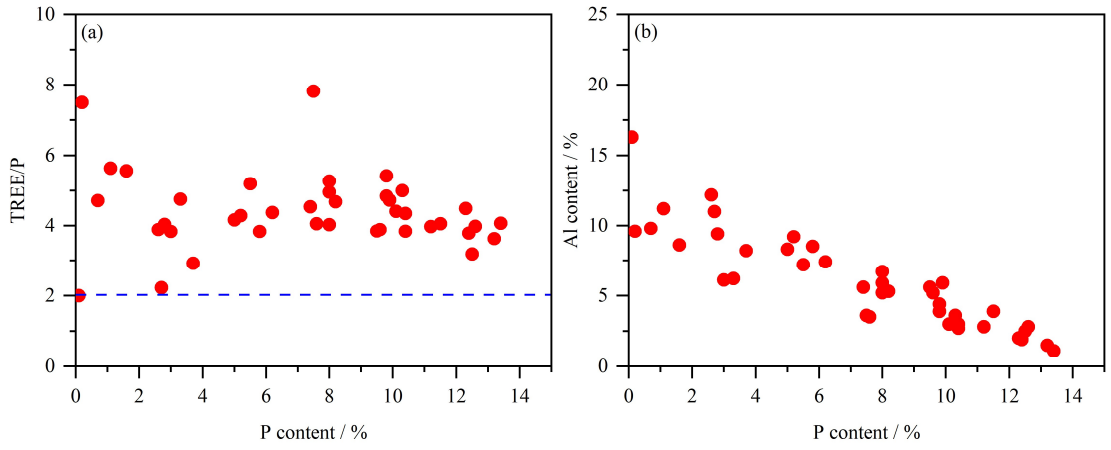


Figure 3.4 Elemental compositions of the Group I and Group II particles found in the leaching solid residue of the Western Kentucky No. 13 raw coal waste.

Using the same SEM-EDS analysis method as the leaching solid residue of the raw coal waste, a total of 47 REE-bearing particles, referred to as WCL 1 – WCL 47, were found in the leaching solid residue of the calcined coal waste. Based on elemental

compositions shown in the supplementary spreadsheet, seven of the 47 particles (i.e., WCL 1 – WCL 7) were zircon. Changes in the TREE/P ratio, the Al content, and the TREE content of the remaining 40 particles as a function of the P content are shown in Figure 3.5. TREE/P values of almost all the 40 particles were greater than 2; meanwhile, with increases in the P content, the Al and TREE content gradually decreased and increased, respectively. These phenomena indicated that all the particles belonged to Group II, and the REE-bearing minerals were monazite and xenotime. Therefore, only zircon, monazite, and xenotime were found in the leaching solid reside of the calcined coal waste; however, in addition to these three REE-bearing minerals, crandallite-group minerals were also found in the leaching solid residue of the raw coal waste. The contrast suggested that calcination increased the leachability of crandallite-group minerals, which explains the considerable increases in the REE leaching recovery after calcination.

Based on the SEM-EDS analysis results of the leaching residue of the raw and calcined coal wastes, it can be concluded that the leaching of apatite contributed to the recovery of REEs from the raw coal waste, while after the calcination pretreatment, crandallite-group minerals were decomposed into easy to leach forms, thus causing considerable increases in the REE recovery. In addition, as shown in the supplementary spreadsheet, the crandallite-group mineral particles predominantly contained LREEs, and as such, the positive effect of calcination on the recovery of LREEs is more significant than that of the HREEs (see Figure 3.2).



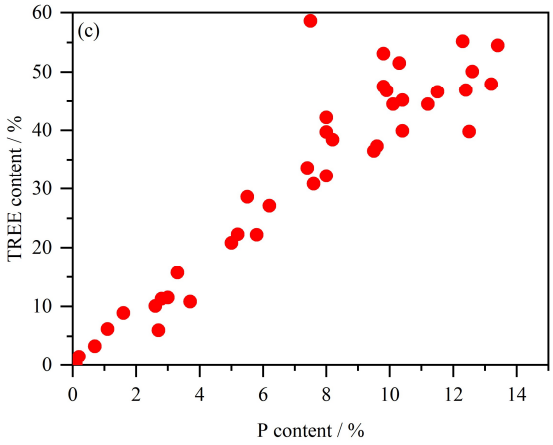


Figure 3.5 Elemental compositions of the REE-bearing particles found in the leaching solid residue of the Western Kentucky No. 13 calcined coal waste.

As presented in Figure 3.1, several SEM-EDS specimens were prepared for the same material, and for each specimen, elemental mapping was performed on many areas. During the analysis, not only the number of REE-bearing particles found in each specimen was recorded, but also the number of analyzed areas. Therefore, the number of REE-bearing particles per area (N) can be calculated for each specimen; meanwhile, by counting the number of REE-bearing particles found in all the SEM specimens of the same material as well as the number of areas analyzed, N can also be calculated for each material. Figure 3.6 shows N values of apatite, zircon, crandallite-group, and monazite/xenotime particles for different materials, including the raw coal waste, the raw coal waste leaching residue, and the calcined coal waste leaching residue. For each SEM specimen, the N value of each type of REE-bearing mineral was calculated and based on N values of all the specimens of the same material, standard deviations were calculated, which are reported as error bars in Figure 3.6. The REE-bearing particle numbers and area numbers of the leaching residues can be found from the supplementary spreadsheet, while those of the raw coal waste have been published by Ji et al. (Ji et al., 2022d). The same magnification of 1200x was used for the different materials when conducting elemental mapping in areas. In addition, based on the SEM images of REE-bearing particles found in the three materials, it can be concluded that after calcination and leaching, the particle size of REE-bearing particles remained almost unchanged: the REE-bearing particles were very fine, typically less than 5 μm, and

for selected particles, the particle size was less than 1 μm. Given these facts, it is reasonable to compare the *N* value of the three materials.

As shown in Figure 3.6, the *N* value of apatite and crandallite-group minerals reduced to zero in the raw coal waste leaching residue and the calcined coal waste leaching residue, respectively, suggesting that these minerals were completely leached. Because the solubility of zircon and monazite/xenotime is low, it is expected that the *N* value of zircon and monazite/xenotime in the three materials would remain unchanged or be slightly reduced; however, as shown in the figure, the *N* value of zircon and monazite/xenotime noticeably increased in the leaching residues, particularly the leaching residue of the calcined coal waste. Ji et al. (Ji et al., 2022d) found that several REE-bearing particles were completely encapsulated within clays. In addition, due to limitations of the electron penetration depth, it is expected that many REE-bearing particles in the raw coal waste were deeply encapsulated within clays, which cannot be found using SEM-EDS. Therefore, the increases in the *N* value of zircon and monazite/xenotime indicated that after calcination and leaching, a portion of the deeply encapsulated zircon and monazite/xenotime particles in the raw coal waste were liberated.

As suggested by the increases in the leaching recovery of Al after calcination (Figure 3.3(a)), the interlayers of kaolinite in the coal waste were dehydrated and disintegrated during calcination, and as a result, the kaolinite particles were expanded. This phenomenon has been previously reported (Abdullah et al., 2018; Ji and Zhang, 2021b; Liew et al., 2012; San Cristóbal et al., 2010). During the acid leaching process, the calcined coal waste was mixed with an acid solution through magnetic stirring. Under the function of chemical leaching and mechanical stirring, the kaolinite particles were expected to disintegrate, leading to the liberation of encapsulated REE-bearing particles. Although thermal decomposition is the direct reason for the increased leachability of crandallite-group minerals, the disintegration of kaolinite during the calcination and leaching process indirectly promoted the recovery of REEs by liberating the completely encapsulated crandallite-group particles.

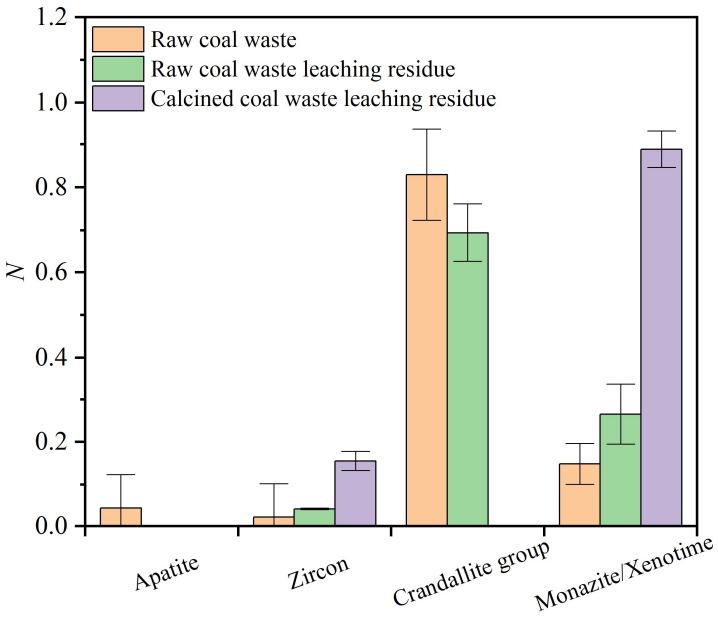


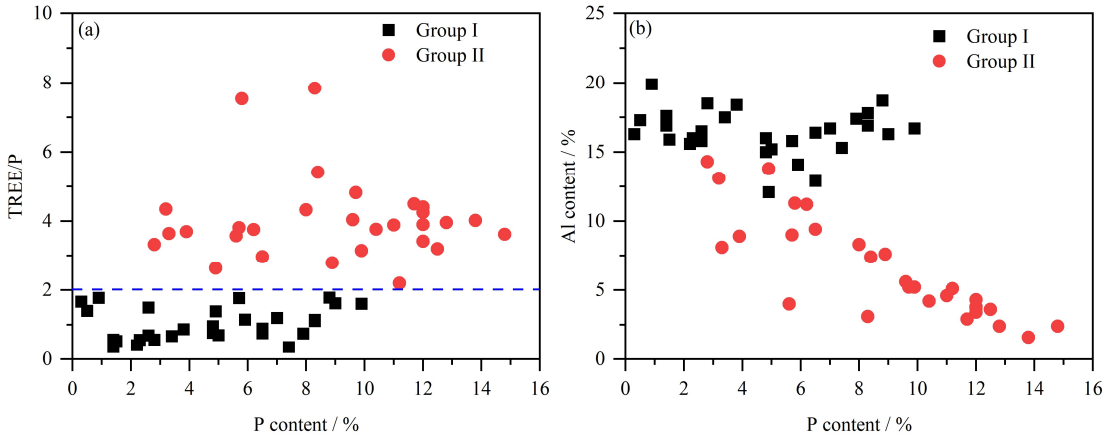
Figure 3.6 Numbers of REE-bearing apatite, zircon, crandallite group, and monazite/xenotime particles per area in the Western Kentucky No. 13 specimens.

3.3.3 REE Mineralogy in the Leaching Solid Residue of the Fire Clay Coal Waste

A total of 64 REE-bearing particles, referred to as FRL 1 – FRL 64, were found in the leaching solid residue of the Fire Clay raw coal waste. Ji et al. (Ji et al., 2022d) found REE-bearing apatite particles in the Fire Clay raw coal waste; however, no apatite was found in the leaching solid residue of the coal waste. This phenomenon is the same as that observed from the SEM-EDS analysis of the Western Kentucky No. 13 materials. The REE recoveries obtained from the Fire Clay raw coal waste presented in Figure 3.2 were partially attributable to the leaching of apatite. Among the 64 particles, six particles were zircon based on their high Zr and Si contents shown in the supplementary spreadsheet. Only HREEs, such as Y and Dy, were detected in the zircon particles using EDS, suggesting that zircon primarily contributed to the HREEs comprised in the Fire Clay coal waste. Similar to the Western Kentucky No. 13 coal waste, only HREEs detected in the zircon particles does not necessarily mean the particles only contained HREEs. Some LREEs might also existed in the particles, but their contents were too low to be detected by the EDS software. The other REE-bearing minerals found in the Fire Clay materials might also contain some REEs that cannot be detected due to their low contents.

Using the same method as the leaching residue of the Western Kentucky No. 13 coal waste (Figure 3.4), the remaining 58 particles can be classified into two groups (Figure 3.7). For the Group I particles, the TREE/P values were less than 2, and the Al content remained at high levels with increases in the P content; whereas, for the Group II particles, the TREE/P values were greater than 2, and as the P content increased, the Al content gradually decreased while the TREE content gradually increased. In addition, several Group I particles also contained certain amounts of Ca, Sr, and Ba. These phenomena were similar to those observed from the leaching residue of the Western Kentucky No. 13 raw coal waste. It can be concluded that the Group I particles were mainly crandallite-group minerals, while the Group II particles were mainly monazite and xenotime.

A total of 62 REE-bearing particles were found from the leaching residue of the Fire Clay calcined coal waste. Among the 62 particles, 11 particles were zircon based on elemental compositions shown in the supplementary spreadsheet. As Figure 3.8 shows, for the remaining 51 particles, only one particle was classified into the Group I, suggesting that most crandallite-group particles were decomposed into easy-to-leach forms after calcination, thus leading to considerable increases in the leaching recovery of REEs. In addition, because only LREEs were detected in the crandallite-group particles, the positive effect of calcination on the leaching recovery of LREEs is more significant than that of the HREEs (see Figure 3.2). These findings are consistent with those from the SEM-EDS analysis of the Western Kentucky No. 13 coal waste and leaching residues.



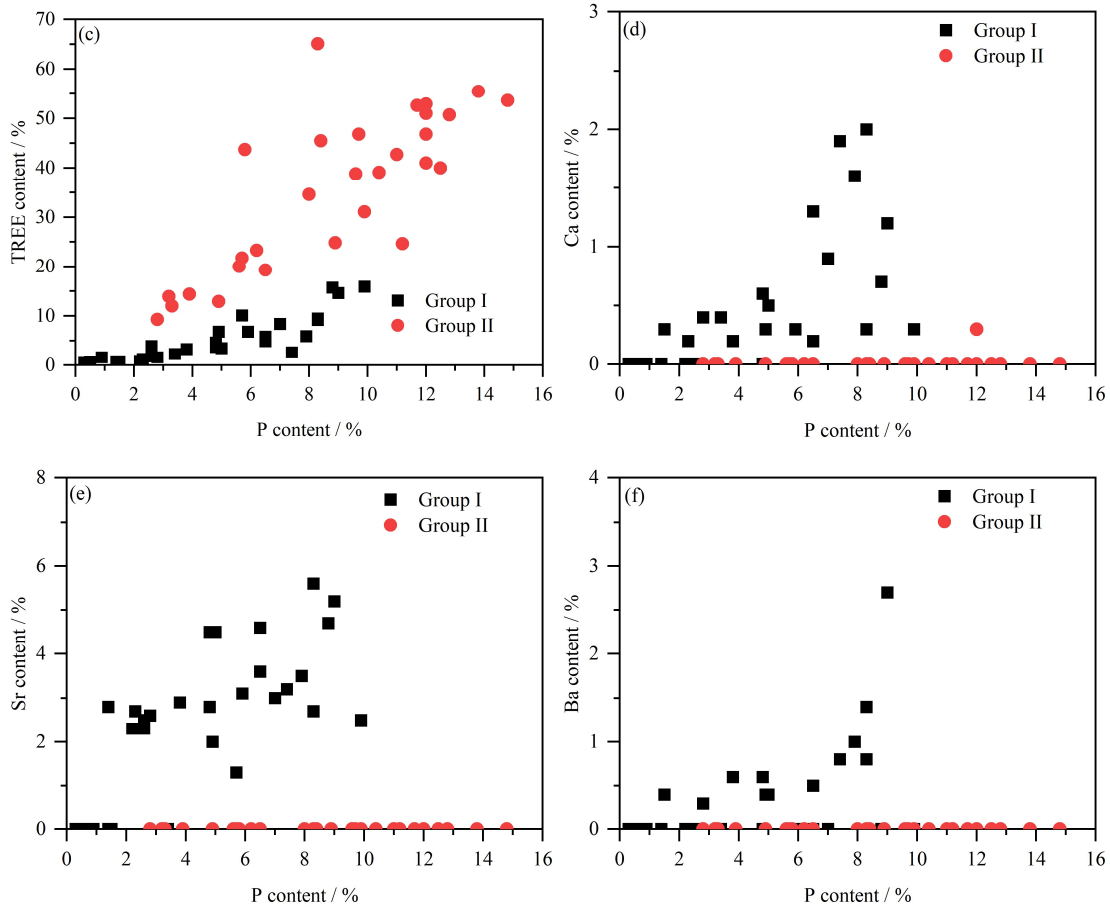
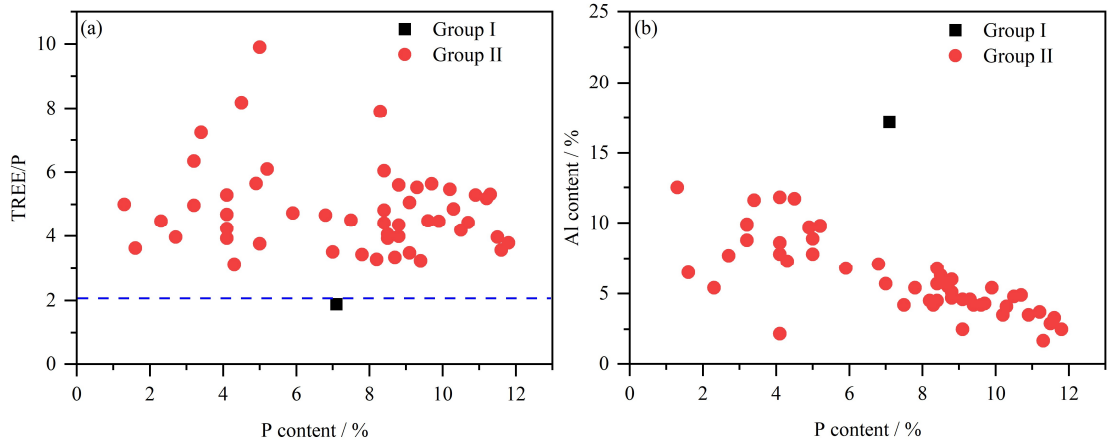


Figure 3.7 Elemental compositions of the Group I and Group II particles found in the leaching solid residue of the Fire Clay raw coal waste.



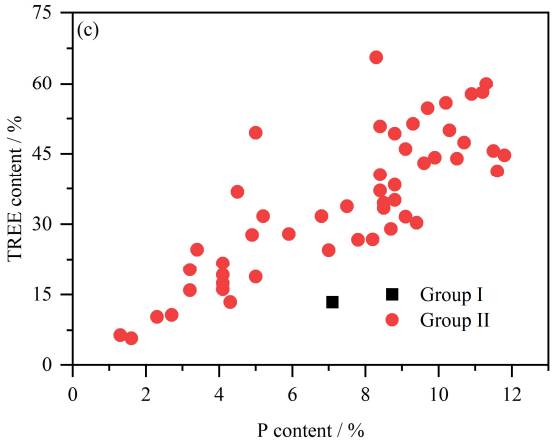


Figure 3.8 Elemental compositions of the REE-bearing particles found in the leaching solid residue of the Fire Clay calcined coal waste.

Using the same method as the Western Kentucky No. 13 materials, *N* values of the apatite, zircon, crandallite-group, and monazite/xenotime minerals existing in the Fire Clay materials were calculated. As Figure 3.9 shows, the *N* value of zircon and monazite/xenotime increased after calcination and leaching. This phenomenon is the same as that observed in the Western Kentucky No. 13 materials (see Figure 3.6). In addition, similar to the Western Kentucky No. 13 coal waste, the recovery of Al from the Fire Clay coal waste was also enhanced after the calcination pretreatment (Figure 3.3(a)). These findings suggested that completely encapsulated REE-bearing particles in the Fire Clay coal waste were liberated after calcination and leaching due to the disintegration of clay particles. This effect indirectly promoted the recovery of REEs by liberating the completely encapsulated crandallite-group particles.

The *N* value of crandallite-group minerals in the raw coal waste and the raw coal waste leaching residue of the Fire Clay seam was around 0.49 and 0.46, respectively (Figure 3.9); however, for the raw coal waste and the raw coal waste leaching residue of the Western Kentucky No. 13 seam, the *N* value of crandallite-group minerals was around 0.83 and 0.70, respectively (Figure 3.6). Unlike the crandallite-group minerals, the *N* value of monazite/xenotime in the raw coal waste and raw coal waste leaching residue of the Fire Clay seam is larger than the Western Kentucky No. 13 seam; for example, in the raw coal waste of the Fire Clay and Western Kentucky No. 13 seams, the *N* value of monazite/xenotime was around 0.41 and 0.15, respectively. The smaller *N* values of

crandallite-group minerals but larger *N* values of monazite/xenotime in the Fire Clay coal waste suggested that a larger portion of the REEs in the Fire Clay coal waste, especially the LREEs, occurred as monazite and xenotime relative to the Western Kentucky No. 13 coal waste. This contrast explained the relatively smaller increases in the recovery of LREEs from the Fire Clay coal waste after the calcination pretreatment relative to the Western Kentucky No. 13 coal waste (see Figure 3.2).

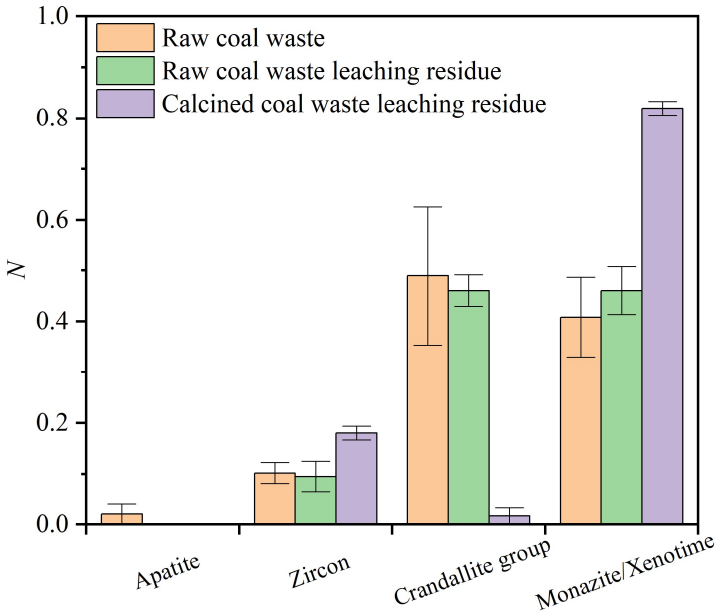


Figure 3.9 Numbers of REE-bearing apatite, zircon, crandallite group, and monazite/xenotime particles per area in the Fire Clay specimens.

3.3.4 Discussion on the Recovery of REEs from Coal Waste

Based on the SEM-EDS analysis results obtained by Ji et al. (Ji et al., 2022d) and in the current study, it has been confirmed that apatite, zircon, crandallite-group minerals, monazite, and xenotime are major REE-bearing minerals in the coal waste of the Western Kentucky No. 13 and Fire Clay seams. Apatite can be leached under weakly acidic conditions (e.g., 0.1 M HCl, corresponding final pH of around 1.5-2.0 (Ji et al., 2021)); however, zircon, crandallite-group minerals, monazite, and xenotime are difficult to leach even under strongly acidic conditions (e.g., 1.2 M HCl in the present study). In addition, a large portion of the REE-bearing minerals in the coal wastes are encapsulated in clay

particles and, thereby, have no access to hydrogen ions during the leaching reaction. Due to these factors, it is challenging to achieve a satisfactory recovery of REEs from the raw coal wastes. Experimental results of the present study suggested that calcination without adding any additives can partially address this dilemma by destroying the structure of clays and decomposing crandallite-group minerals. For example, REE recovery from the Western Kentucky No. 13 coal waste was improved from around 20% to 72% after calcination at 600 ˚C for 2 h (see Figure 3.2). Unfortunately, because the crystal structure of zircon, monazite, and xenotime is very stable and cannot be easily decomposed, calcination without adding any additives failed to noticeably improve the recovery of HREEs from the Western Kentucky No. 13 and Fire Clay coal wastes as well as the recovery of LREEs from the Fire Clay coal waste. To address this issue, the authors proposed several potential flowsheets, which are referred to as Flowsheets A-D and presented in Figure 3.10.

In Flowsheet A, after calcination and acid leaching, physical beneficiation is employed to concentrate the undissolved REE-bearing minerals (i.e., monazite, xenotime, and zircon), which can be further processed as a high-grade concentrate. The viability of this flowsheet can be confirmed based on the finding that most of the REE-bearing minerals were liberated after calcination and leaching (see Figure 3.6 and Figure 3.9). Because the REE-bearing particles were ultrafine (i.e., typically less than 5 μm), physical beneficiation methods with lower particle size limits are required, such as enhanced gravity separation and nanobubble flotation (Zhang et al., 2015b). In Flowsheet B, chemical reagents, such as NaOH and CaO plus carbon, are added during calcination to promote the thermal decomposition of the REE-bearing minerals ((Kumari et al., 2015b; Yuan et al., 2017)). In addition to calcination, the coal wastes can also be treated in a high-concentration alkaline solution at high temperature to decompose the REE-bearing minerals (Flowsheet C) (Abdel-rehim, 2005; Kumari et al., 2015a). Acid baking with 98% sulfuric acid at high temperature can provide exceedingly harsh leaching conditions and, thereby, has been used to leach monazite and xenotime (Demol et al., 2019; Kumari et al., 2015a). Therefore, acid baking can also be employed to improve the recovery of REEs from the coal wastes (Flowsheet D).

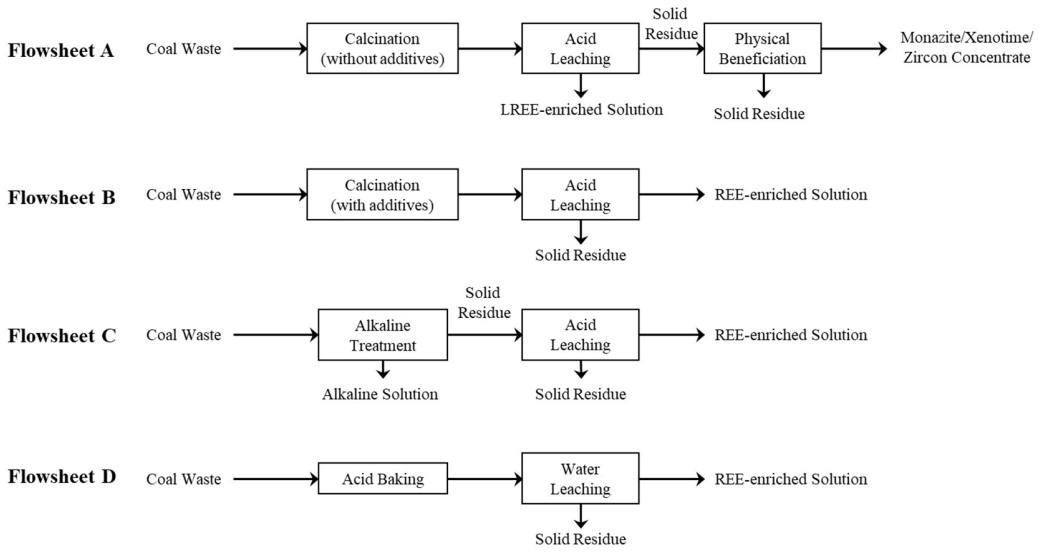


Figure 3.10 Potential flowsheets that can be used to improve the recovery of REEs from coal waste.

3.4 Conclusions

In this study, calcination, acid leaching, and SEM-EDS characterization tests were conducted to confirm the mechanisms of enhanced REE recovery from the Western Kentucky No. 13 and Fire Clay coal wastes caused by calcination at 600 ºC without adding any additives. Acid leaching test results showed that after the calcination pretreatment, the recovery of TREEs from the coal waste of the two different seams increased by 52 and 17 absolute percentage points, respectively; however, the increases were primarily attributable to the LREEs, and the recovery of HREEs was only slightly increased. In the study by Ji et al. (Ji et al., 2022d), several different types of REE-bearing minerals, including apatite, zircon, monazite, xenotime, and crandallite-group minerals, were found in the raw coal wastes through SEM-EDS analysis. In the present study, by comparing the leaching characteristics of REEs and major elements comprised in the coal wastes, it was confirmed that the proportion of REEs associated with major minerals as isomorphic substitutions is minimal. All the REE-bearing minerals except apatite were found in the leaching solid residue of the raw coal wastes, suggesting that most of the REE-bearing minerals were difficult to leach under the experimental conditions of 1.2 M HCl and 75 ºC leaching temperature. Unlike the leaching solid residue of the raw coal wastes, crandallite-group particles were rarely found in the leaching solid residue of the calcined coal wastes. The

contrast suggested that calcination led to the decomposition of crandallite-group minerals into easy-to-leach forms, which explains the increases in the leaching recovery of REEs. Moreover, based on the numbers of REE-bearing particles found per area under SEM-EDS, it was concluded that calcination promoted the liberation of REEs-bearing particles and thus the leaching recovery of REEs.

Among all the REE-bearing minerals, HREEs were only detected in xenotime and zircon using SEM-EDS, and xenotime and zircon were frequently found in the leaching solid residue of the calcined coal wastes. These phenomena suggested that calcination without adding any chemical reagents cannot decompose the HREE-bearing minerals; therefore, only slight increases in the recovery of HREEs were achieved. Similar to xenotime and zircon, monazite also remained undecomposed during the calcination pretreatment. Additionally, compared with the Western Kentucky No. 13 coal waste, more LREEs existed in monazite in the Fire Clay coal waste. Therefore, the calcination pretreatment is less efficient in improving the recovery of LREE from the Fire Clay coal waste and the recovery of HREEs from both coal wastes. Based on findings from this study, several flowsheets were proposed to further enhance the recovery of REEs from the coal wastes, particularly HREEs.

Chapter 4 Thermal Transformation Behavior of Florencite and Implications on the Leaching Recovery of Rare Earth Elements (REEs)

Abstract

Pure florencite-(Ce), an endmember of crandallite-group minerals, was synthesized using a hydrothermal method. To investigate the thermal phase transformation behavior of florencite, the raw synthesized material was calcined at various temperatures followed by X-ray diffraction analysis (XRD). Results showed that florencite-(Ce) started to dehydroxylate in the temperature range of 400-500 °C, and the crystal structure was decomposed at 600-700 °C, while further elevating the calcination temperature to over 900 °C resulted in the recrystallization of $CePO_4$. Thermogravimetric and differential thermal analyses (TGA-DTA) showed that the thermal phase transformation of florencite followed three stages, and the complete decomposition of florencite-(Ce) and the recrystallization of $CePO_4$ occurred at around 677 °C and 971 °C, respectively. Acid leaching tests were performed on the raw synthesized and calcined materials to investigate the effect of calcination on the leaching characteristics of Ce from florencite-(Ce). It was found that the variation in Ce leaching recovery corresponded to the phase transformation of florencite. The gradual transformation of florencite from a crystalline mineral into an amorphous phase resulted in the increases in the solubility of Ce. To reveal the potential effects of kaolinite and coal coarse refuse on the thermal phase transformation of florencite, the synthesized florencite-(Ce) was mixed with these materials with different mass ratios. The mixtures were calcined at 700 °C and 1000 °C, respectively. XRD, DTA, and acid leaching test results showed that kaolinite and coal coarse refuse had no effect on the thermal phase transformation behavior of florencite.

4.1 Introduction

Minerals of crandallite-group are known in a variety of rock types, including shear zone (Chakraborty et al., 2014), carbonatites (McKie, 1962a), placers (Lefebvre and Gasparrini, 1980), hydrothermal deposits (Gaudin et al., 2020), and granitic pegmatites (Dill et al., 2006). Crandallite ($CaAl_3(PO_4)_2(OH)_6$), goyazite ($SrAl_3(PO_4)_2(OH)_6$), gorceixite ($BaAl_3(PO_4)_2(OH)_6$), florencite ($REEAl_3(PO_4)_2(OH)_6$) and plumbogummite

($PbAl_3(PO_4)_2(OH)_6$) are the most important endmembers of crandallite-group minerals (Dill, 2001; Stanley, 2000). As a result of their high capacity for ionic substitutions, a crandallite-group mineral rarely occurs on its own, which is normally found as mixtures or solid-solutions with varying chemical compositions (Mordberg, 2004b; Schwab et al., 2004). For example, authigenic crandallite, gorceixite, and goyazite were identified in Athabasca Group sediments, however, it was challenging to make a clear distinction among them due to the occurrence of solid-solution state and the varying amounts of the distinguishing elements (Ca, Ba, and Sr) present in the minerals (Wilson, 1985). Crandallite-group minerals with complicated chemical compositions were also found from the Schugorsk bauxite deposit (Stanley, 2000). This deposit were mainly composed of crandallite itself with other elements, such as Sr, Pb, Ce, and Nd as admixtures. In addition, crandallite-group minerals are normally dispersed and scattered as accessory phases in the form of ultrafine particles throughout host materials. Poly-mineral aggregates of crandallite-group minerals were confirmed to be closely associated with iron and manganese oxides and hydroxides, with a grain size of less than 5 microns (Ozhogina et al., 2019). It was reported that florencite of minute crystal size (<0.1-10 μm in width) and trace concentration (0.0379 wt. % in average) were present in marine sandstones. The florencite crystals were only visible using an optical microscope under high magnifications (Rasmussen, 1996). Therefore, the general content of crandallite-group minerals is normally low in the host materials.

Due to the high capacity of ionic substitutions and the existence in the form of finely dispersed particles, it is challenging to collect and separate pure endmembers of crandallite-group minerals. As a result, hydrothermal methods were developed for the artificial synthesis of crandallite-group minerals, providing great opportunities to explore their special physio-chemical properties. Ignatobva et al. reported the first attempt to synthesize pure crandallite, which was then improved by a hydrothermal treatment of amorphous reaction products (Gilkes and Palmer, 1983; Ignatova et al., 1965). Schwab et al. synthesized goyazite, gorceixite, plumbogummite, and florencite-(La, Ce, Pr) using hydroxides of the desired cations, freshly precipitated $Al(OH)_3$, and H_3PO_4 (Schwab et al., 1990a, 1990b). This method avoided the incorporation of foreign ions, such as Na^+ or Cl^-, into the mineral lattice, and the formation of contaminant phases, like boehmite or

hydroxyapatites. The synthesized pure endmembers of crandallite-group minerals were applied to determine their X-ray data, lattice constants, and morphological properties, which cannot be obtained from the naturally occurred materials. By analyzing the chemical and physical properties of the pure endmembers, it is reasonable to deduce the corresponding properties of the mixed crystals commonly found in nature. Actually, it has been pointed that the synthesized pure endmembers of crandallite-group minerals exhibited hexagonal unit cells with similar lattice constants, and shared comparable thermal behaviors (Hikichi et al., 1989).

However, these studies were usually conducted decades ago, and mainly focused on the characterization of the whole mineral group, rather than a specific endmember. In addition, the increasing demand for valuable metals drives great interests in exploring alternative resources, as valuable metals-bearing minerals, the recovery of Sr, Ba, Pb, and REEs, contained in the crandallite-group minerals was not taken into consideration, and limited research has been reported to date. Despite the relatively low grade of valuable metals, the exploitation cost can be largely offset by the low cost, high abundance, and wide applications of the host materials (Moldoveanu and Papangelakis, 2016). For example, after obtaining the high-purity REE leaching solution from the acid treatment of florencite-bearing kaolinite, the residue solid can be used to prepare porous material or zeolite-based adsorbent, which utilizes the resources comprehensively and makes the process economically viable (Ji and Zhang, 2022, 2021c). Therefore, it is essential to investigate the valuable metal recovery from crandallite-group minerals as well as its host materials.

In this study, florencite-(Ce), a pure endmember of crandallite-group minerals, was synthesized by a hydrothermal method, followed by XRD, SEM-EDS, and TEM analyses. The results indicate that high-purity and well-crystallized florencite-(Ce) was formed. The synthesized materials were calcined under various temperatures to investigate the phase transformation as a result of calcination, and the thermal behavior was further evaluated by TGA-DTA analysis. Acid leaching tests were performed on the raw synthesized and calcined materials to determine the changes of Ce solubility with the phase transformation. After that, to detect if any reactions occur between the florencite and host materials during calcination, the synthesized florencite-(Ce) was mixed with kaolinite, and coal coarse

refuse materials, respectively, with different mass ratios. The XRD, DTA, and acid leaching tests were conducted on the raw mixed and calcined materials.

4.2 Materials and Methods

4.2.1 Materials

The chemicals used for florencite synthesis, including cerium (III) nitrate hexahydrate ($Ce(NO_3)_3 \cdot 6H_2O$), sodium hydroxide (NaOH), phosphoric acid (H_3PO_4, 85 wt.%), and aluminum hydroxide ($Al(OH)_3$), were of certified ACS grade and purchased from Thermo Fisher Scientific (USA). Analytical grade NaOH and HCl were used for pH adjustment. Type I deionized water with a resistivity of 18.2 MΩ·cm at room temperature was used for all experiments.

4.2.2 Synthesis of Florencite

Florencite was synthesized by a hydrothermal process, a modified method previously reported elsewhere (Schwab et al., 1990b). Typically, 0.01 M of $Ce(NO_3)_3 \cdot 6H_2O$ was dissolved in a beaker containing 50 mL of deionized water. The initial pH of the prepared solution was measured to be 3.85 at 25 °C. Then, 5 M NaOH was added dropwise into the solution under magnetic stirring until a pH of 11 was reached. The gradual increase of pH led to the formation of cerium (III) hydroxide ($Ce(OH)_3$) precipitate (Abellan et al., 2017), which served as the Ce source for florencite synthesis. After 5 min of stirring, the $Ce(OH)_3$ precipitate with a light brown color was collected by centrifugation followed by 3 times of washing with deionized water. Then, the freshly precipitated $Ce(OH)_3$ was mixed with 50 mL of deionized water under vigorous magnetically stirring before the addition of 0.03 M freshly precipitated $Al(OH)_3$ and 20 mL of 1 M H_3PO_4 solution. The reaction mixture gradually converted into homogenous white colloids under constant stirring for 10 min. After that, the colloids were transferred into a Teflon-lined stainless-steel autoclave vessel of 0.1 L maximum volumetric capacity. The autoclave was tightly sealed and placed in a drying oven (AT09-UL, Across International, USA) for hydrothermal treatment at 200 °C for 3 months. The reaction can be described by Equation (1):

$$Ce(OH)_3\ (l) + 3Al(OH)_3\ (s) + 2H_3PO_4\ (l) = CeAl_3(PO_4)_2(OH)_6\ (s) + 6H_2O\ (l) \quad (1)$$

After the reaction completed, the autoclave was naturally cooled down to room temperature. Precipitates with a white color were formed in the autoclave. The precipitates were collected by centrifugation and then washed several times with deionized water and absolute alcohol to remove impurities. The final synthesized products were obtained after drying overnight at 60 °C.

4.2.3 Calcination

Calcination tests were carried out in a temperature-controlled muffle furnace manufactured by Cole-Parmer, USA. For each batch of calcination, 1.0 g of the synthesized material was weighted and put in a porcelain crucible, which was then placed into the furnace chamber. The synthesized material was calcined under static air condition at 300 °C, 400 °C, 500 °C, 600 °C, 700 °C, 800 °C, 900 °C, and 1000 °C, respectively, at a ramping rate of 20 °C/min from room temperature. After 2 h of calcination at the desired temperatures, the calcined products were automatically cooled down to room temperature and collected for subsequent leaching and characterization tests.

4.2.4 Acid Leaching

To evaluate the effect of calcination on the leaching characteristics of Ce from florencite-(Ce), both the raw synthesized and calcined materials were subjected to acid leaching tests. The tests were conducted in a three-neck round bottom flask of 100 mL maximum volumetric capacity. Detailed descriptions of the experimental setup used for the acid leaching tests have been reported in the authors' previous publications (Ji et al., 2020). For each test, 50 mL of 1.2 M HCl solution was preheated to 75 °C before the addition of 0.5 g of the sample. During the leaching process, to investigate the leaching kinetics of Ce, representative samples of 1 mL was taken from the slurry at different time intervals from the beginning of the reaction up to a total period of 2 h (i.e., 5 min, 15 min, 30 min, 60 min, 90 min, and 120 min). Immediately upon the collection, the samples were subjected to centrifugation at 4000 rpm for solid/liquid separation. The residual solids were washed with deionized water several times to completely remove the remaining leach solutions. After drying at 60 °C overnight, the solid residues were digested following the procedures reported by the authors (Zhang and Honaker, 2020). The digestion solutions as well as the leach solutions generated from the leaching tests were diluted 100 times in 5 v/v% HNO_3

for elemental concentration analysis using inductively coupled plasma mass spectrometry (ICP-MS). The leaching recovery of Ce was calculated based on the elemental concentration in the leach solutions and the solid residues.

4.2.5 Sample Characterization

The crystallinity of the raw and calcined materials was evaluated using X-ray diffraction (XRD). A Bruker D8 Advance Twin diffractometer manufactured by Bruker Corporation was used for the analysis along with monochromatized radiation source of Cu-Kα (λ = 1.5418 Å). Approximately 1.0 g of the sample was packed into a sample holder with a flat upper surface being made. XRD patterns were recorded at room temperature over a 2θ range of 10–70° with a step size of 0.02°, operating at 40 kV and 40 mA. MDI Jade Version 6.0 software was used to analyze the XRD data.

Thermogravimetric and differential thermal analyses (TGA-DTA) were conducted using a thermogravimetric analyzer (TGA 5500, TA Instrument, USA) equipped with a high-temperature furnace. In brief, around 50 mg of the material was weighted and placed onto a platinum pan before inserting into the high-temperature furnace. The analysis was conducted with a ramping rate of 10 °C/min and a nitrogen flow rate of 10 mL / min to determine the thermal stability of the synthesized material in the temperature range of 50 – 1000 °C.

The morphology of the synthesized material was evaluated using a scanning electron microscopy (SEM, JSM-IT500, JEOL, USA) capable of operating at accelerating voltages ranging from 3.0 kV to 20 kV, and the elemental composition was determined by the equipped energy dispersive X-ray spectroscopy detector (EDS, Ultim Max, Oxford Instruments, UK). A high-resolution transmission electron microscopy (TEM, JEM-2100, JEOL, Japan) operated at 200 kV was used to analyze the detailed crystal structure of the synthesized material. The material was first dispersed in ethanol and sonicated for 15 min, after that, a few microliters of the obtained colloidal solution were dropped onto lacey formvar coated 200 mesh Cu grids before drying by evaporation at room temperature. The resulting images were analyzed by Digital Micrograph software (GMS 3, Gatan, USA) and CrysTbox program (Klinger, 2017).

4.3 Result and Discussion

4.3.1 Sample Characterization

The phase purity and crystal structure of the synthesized product were examined by XRD analysis. All the diffraction peaks of the XRD pattern shown in Figure 4.1 were perfectly indexed to the hexagonal phase of florencite-(Ce), and the calculated lattice constants (a=b= 6.966 Å, c= 16.254 Å) were very close to the unit cell of the standard florencite-(Ce) (a=b=6.972 Å, c=16.262 Å) referenced from the JCPDS card No. 43-0673. The well-defined sharp peaks and the absence of other crystalline phases indicate the excellent crystallinity and high purity of the synthesized florencite-(Ce).

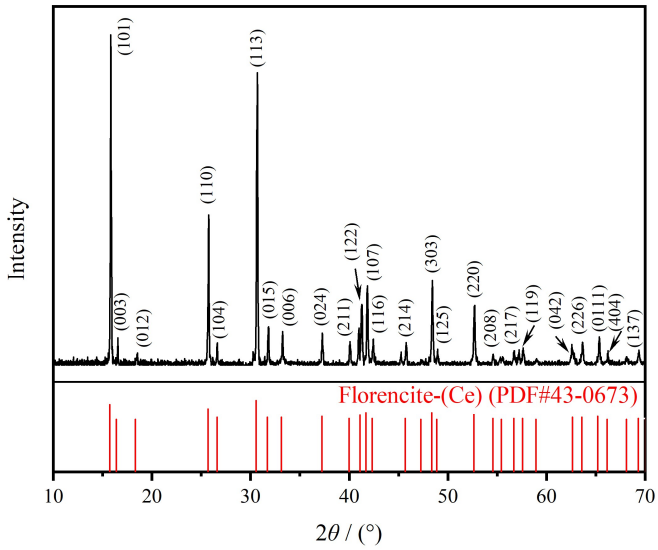


Figure 4.1 XRD pattern of the raw synthesized product.

Several studies have reported that rhombohedral, pseudo-rhombohedral, and pseudo-cubic crystals and their mixtures, as well as the agglomerates and clusters of the crystals were present in both natural and synthesized florencite specimens (J.J. Lefebvre and Patterson, 1982; McKie, 1962b; Nickel and Temperly, 1987; Pouliot and Hofmann, 1981; Repina et al., 2011). The morphology and surface characteristics of the synthesized florencite-(Ce) were evaluated by SEM-EDS analysis. As shown in Figure 4.2(a), the synthesized florencite-(Ce) comprised of isolated rhombohedra, irregularly shaped crystals, and crystal agglomerates of inhomogeneous size. The higher-magnification image (Figure 4.2(b)) showed a flower-like crystal agglomerate with faces growing outward from

the center. The agglomerate had a diameter of around 25 μm and consisted of many little crystals. The same phenomenon was observed in pharmaceutical ingredient crystallization and vanadium pentoxide synthesis processes (Gielen et al., 2017; Zheng et al., 2018). At the early stage of crystallization, individual crystals link each other by liquid bridges and orient around a central core that cements the crystals together, forming a star or flower shape. Then, the stabilization of these aggregated crystals occurs as a result of the attractive forces, such as Van der Waals interaction (Gielen et al., 2017). Solid bridges formed by molecular growth in the final stage of crystallization result in the appearance of crystal agglomerates. In addition, if interactions or collision frequency between individual crystals were insufficient, the aggregates will disintegrate into smaller fragments (Nichols et al., 2002), thus leading to a variety of shapes and sizes as depicted by Figure 4.2(c). Figure 4.2(d) showed the SEM image of a typical rhombohedral florencite crystal with sharp edges and an equilateral length of around 2 μm. The surface elemental composition and distribution of the synthesized florencite-(Ce) were further characterized by EDS analysis. The EDS spectrum shown in Figure 4.2(e) confirmed the existence of O, Ce, Al, and P in the synthesized florencite-(Ce). The atomic ratio of O:Ce:Al:P determined by the EDS spectrum was 3.4:2.1:1.4:1, which is close to the theoretical ratio of 3.6:2.2:1.3:1 calculated from the chemical formula of florencite-(Ce) [$CeAl_3(PO_4)_2(OH)_6$]. Furthermore, the elemental mapping shown in Figure 4.2(f)-(i) indicated that O, Ce, Al, and P were homogenously distributed in the crystal. Figure S1 in the Appendix shows the SEM images, EDS spectra, and elemental mapping of the synthesized florencite-(Ce) at various magnifications, which indicate very similar chemical compositions and elemental distributions regardless of crystal shape.

The SEM results indicated that the morphology of the synthesized material was complex, and most of the particles had a thickness of a few microns, which were too large to obtain a clear microstructure by TEM imaging even with high accelerating voltages. However, in some cases, the thinner edge of such particles can still provide sufficient evidence for the microstructural characterization (S'Ari et al., 2021; Stawski et al., 2019). In order to obtain further insights into the crystal structure, TEM analysis was conducted on the synthesized florencite-(Ce). Figure 4.3(a) showed the presence of an adjacent particle attached with connective interfaces having irregular polygon shape and thinner

edge. The dark color in the central area indicated the impossibility of being transmitted by electrons to generate high resolution images. It is a usual practice to move the focus to particle edges which are thin and thus represent the true texture of the particle (Sharma et al., 2000). As depicted by Figure 4.3(b), the thinner area of the particle was subjected to high-resolution TEM imaging, and continuous lattice fringes were observed from an edge selected from the particle. To obtain a clear observation of the crystal lattice arrangement, inverse fast Fourier transform (IFFT) was performed on the symmetrical diffraction spots, and the detailed calculation results can be referred to Figure S2 in the Appendix. The lattice spacings were determined as 0.219, 0.269, and 0.293 nm, which are consistent with the interplanar spacings of the (122), (006), and (013) planes of florencite-(Ce) (Figure 4.3(c)). Based on the XRD, SEM-EDS, and TEM analyses results, it can be concluded that high-purity florencite-(Ce) with high crystallinity was synthesized by the hydrothermal method.

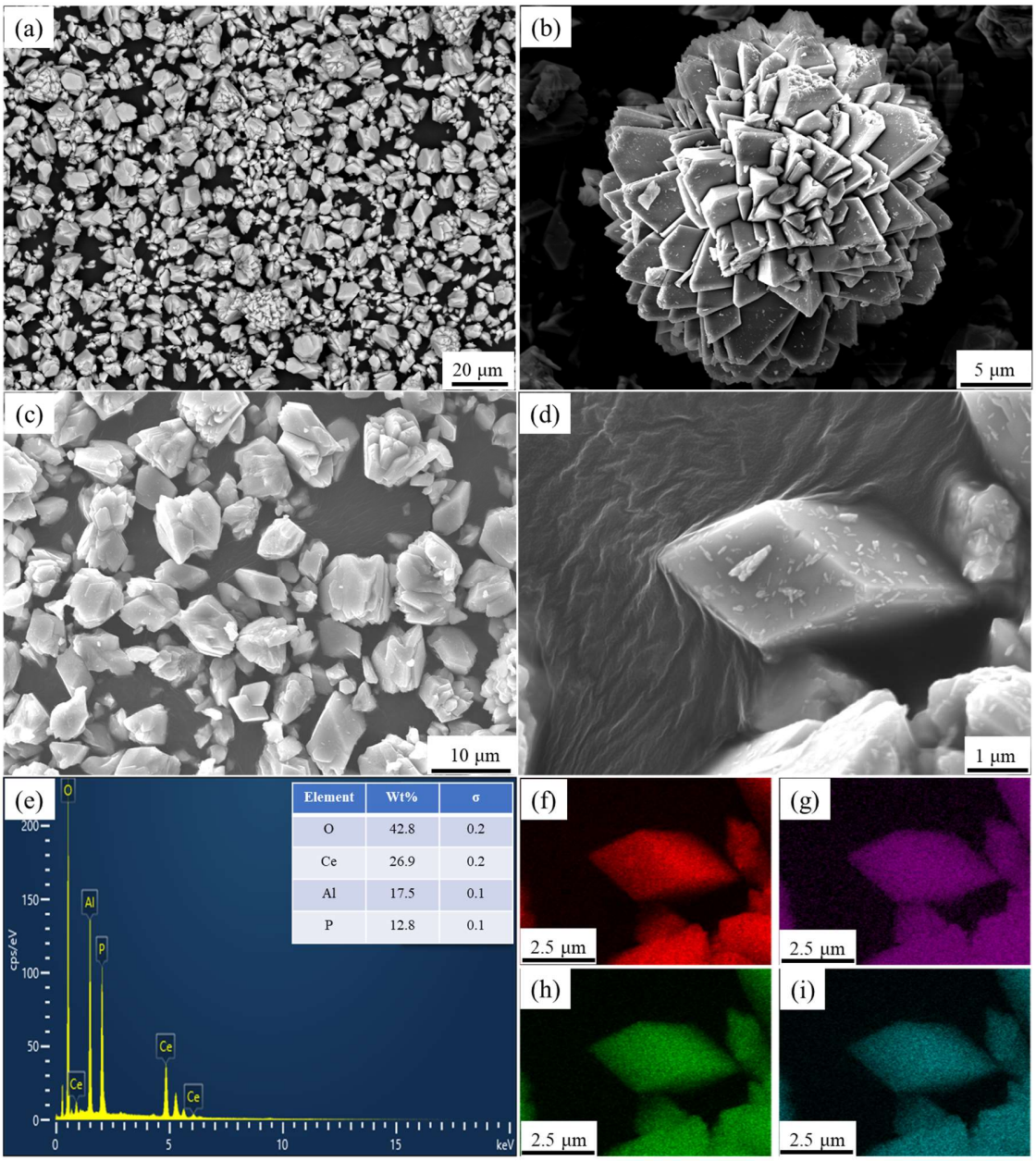


Figure 4.2 SEM images of the synthesized florencite-(Ce) (a-c), a liberated florencite-(Ce) particle (d), and the corresponding EDS analysis (e) and elemental mapping of oxygen (f), cerium (g), aluminum (h), and phosphorus (i) of the liberated particle.

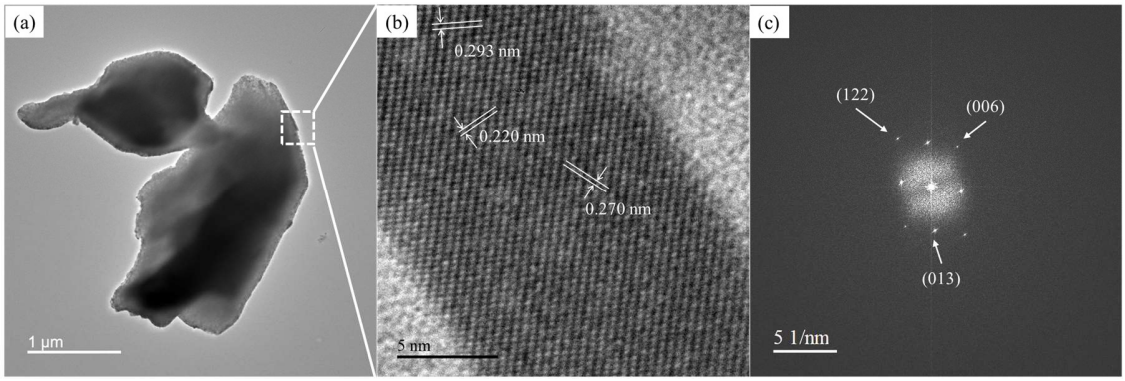


Figure 4.3 Low-magnification TEM image of a synthesized florencite-(Ce) particle (a), high-resolution TEM image from a thin region located on the right edge of the particle (b), and its corresponding FFT pattern (c).

4.3.2 Phase Transformation of Florencite

XRD, SEM-EDS, and TEM analyses proved the high purity of the florencite-(Ce) synthesized by the hydrothermal method. In order to investigate the thermal phase transformation of florencite-(Ce), XRD analysis was performed on the raw synthesized sample as well as the products calcined at various temperatures for 2 h. As shown in Figure 4.4(a), the well-defined sharp peaks of florencite-(Ce) were observed in the raw synthesized sample and the 300 °C-, 400 °C-, and 500 °C-calcined products. However, the intensity of the reflection peaks of florencite-(Ce) was noticeably decreased when the calcination temperature was elevated to 600 °C. All the reflection peaks disappeared from the XRD pattern of the 700 °C-calcined product, suggesting that the crystallized structure was transformed into an amorphous phase, and the florencite-(Ce) was completely decomposed.

In order to present the crystal structure alterations more intuitively at temperatures lower than 700 °C, major diffraction peaks at 2θ of 15.82°, 25.74°, 30.67°, 41.85°, 48.42°, and 52.71°, which represent the (101), (110), (113), (107), (303), and (220) crystal planes of florencite-(Ce), respectively, were selected to quantify the peak intensity changes as a result of calcination. As shown in Figure 4.4(b), compared with the raw synthesized sample, after 2 h of calcination at 300 °C, the peak intensity of all the selected planes increased, and slight improvements were still observed when elevating the calcination temperature to 400 °C. These results suggested that calcination at 300-400 °C enhanced

the crystal intensity of florencite-(Ce) instead of decomposing it. Earlier studies reported that the removal of adsorbed water and strongly physically bound water from inorganic materials can be achieved in the temperature range of 100-400 °C (Longhi et al., 2019; Nergis et al., 2020; Wuddivira et al., 2012). Therefore, after calcination at 300-400 °C for 2 h, the free and physically bound water molecules were removed, thus leading to the increases in relative content of florencite-(Ce) in calcined product, which explains the enhancement of peak intensities of major planes. However, significant decreases in the peak intensity of all selected planes were noticed when increasing the calcination temperature to 500 °C, and only faint peak signals were observed after calcination at 600 °C for 2 h. These results indicated florencite-(Ce) started to dehydroxylate in the temperature range of 400-500 °C, and the crystal structure was completely destructed in the temperature range of 600-700 °C. Further elevating the calcination temperature to 800 °C, broad and weak peaks centered at 2θ of around 21.1°, 28.5°, 30.8°, and 41.9° appeared in the XRD pattern (Figure 4.4(a)), and when the sample was treated at 900 °C for 2 h, the intensity of these diffraction peaks was further improved accompanied by the appearance of an additional weak peak at 2θ of 48.3°. This finding indicated that calcination at temperatures higher than 700 °C led to the evolution of the amorphous phase into a poorly crystallized structure, despite the reflections were difficult to be clearly indexed. However, the intensity of these difficult-to-index reflections was noticeably improved when increasing the calcination temperature to 1000 °C, and the well-defined diffraction peaks present in the XRD pattern were characteristic of $CePO_4$ (JCPDS card No. 32-0199) with the monoclinic system. These results indicated that the broad peaks of low intensity at 800 °C and 900 °C corresponded to the germination of $CePO_4$, and the complete crystallization into an ordered $CePO_4$ structure occurred at 900-1000 °C.

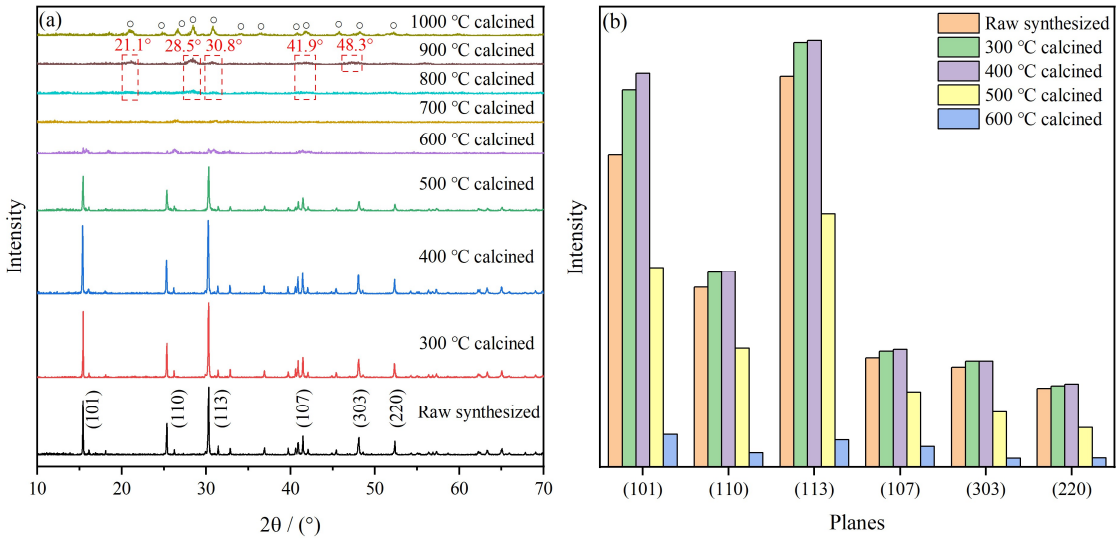


Figure 4.4 XRD patterns of the raw synthesized florencite-(Ce) and samples calcined at different temperatures for 2 h (a), and the changes of peak intensity of selected crystal planes (b).

The XRD analysis confirmed the decomposition of florencite-(Ce) occurs between 600 °C to 700 °C, and complete recrystallization into $CePO_4$ takes place at temperatures higher than 900 °C. In order to reveal the phase transformation process of florencite-(Ce) more precisely, the thermal behavior of the raw synthesized florencite-(Ce) was evaluated by TGA-DTA, and the obtained curves are shown in Figure 4.5. The weight loss and the corresponding DTA curves demonstrated the thermal reactions of the raw synthesized florencite-(Ce) took place following three defined stages in the temperature range of 50-1000 °C, i.e., Stage I, Stage II, and Stage III, respectively. Stage I occurred in the temperature range of 50-200 °C with a weight loss of 0.27%, which was assigned to the removal of free and physically bound water molecules (Longhi et al., 2019; Nergis et al., 2020). After that, a dramatic weight loss of 11.51% (Stage II) took place between 200 °C and 900 °C, resulting from the removal of chemically bound water. The weight loss is very close to the water content (10.5%) of florencite-(Ce) calculated from its theoretical chemical formula $[CeAl_3(PO_4)_2(OH)_6]$. A corresponding endothermic peak was observed at 677.3 °C, which can be ascribed to the dehydroxylation of hydroxyl groups, thus resulting in the decomposition of the raw synthesized florencite-(Ce) into an amorphous phase (Yariv, 2005). Further elevating the temperature to 1000 °C (Stage III) led to a

minimal weight loss of 0.27%, however, an exothermic peak of low intensity appeared at 970.8 °C, which corresponds to the recrystallization of the amorphous phase into $CePO_4$. In the light of the XRD and TGA-DTA results from this work, and combined with findings from previous studies (Frank N.Blanchard, 1971; Frost et al., 2012; Hikichi et al., 1989; Schwab et al., 1990b, 1990a), it can be concluded that the thermal phase transformation of florencite-(Ce) follows the process represented below:

$$CeAl_3(PO_4)_2(OH)_6 \xrightarrow{Decomposition} CeO \cdot 1.5Al_2O_3 \cdot P_2O_5 \xrightarrow{Recrystallization} CePO_4 + AlPO_4 + Al_2O_3 \qquad (2)$$

The decomposition of florencite-(Ce) crystals occurs in the temperature range of 650-700 °C, followed by the recrystallization of the amorphous phase to form $CePO_4$, $AlPO_4$, and Al_2O_3. However, only weak reflections of $CePO_4$ were present in the XRD pattern of the 1000 °C-calcined product (Figure 4.4(a)). The absence of reflections corresponding to $AlPO_4$ and Al_2O_3 can be explained by two potential reasons: (1) the relative content of $AlPO_4$ and Al_2O_3 is lower compared with that of $CePO_4$ after recrystallization (Table C.1), and (2) higher temperatures are required for the formation of $AlPO_4$ and Al_2O_3 with ordered structure (Frank N.Blanchard, 1971; Hikichi et al., 1989).

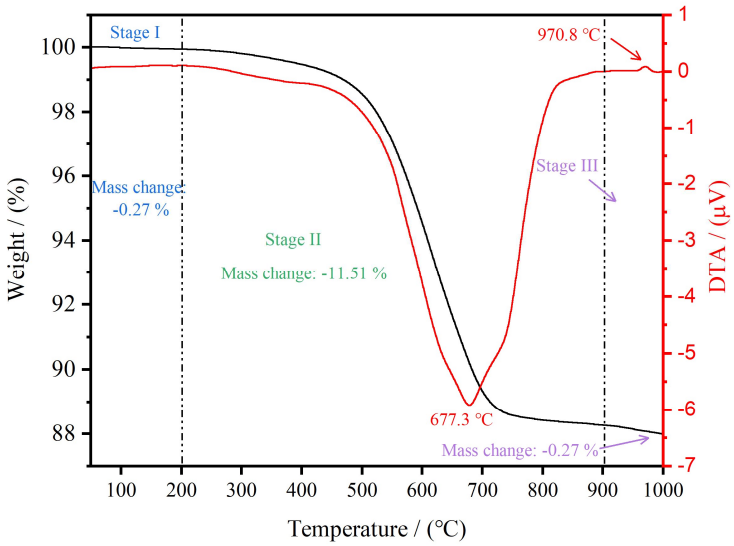


Figure 4.5 TGA-DTA curve of the raw synthesized florencite-(Ce).

4.3.3 Leaching Characteristics of Florencite

To determine the effect of calcination on the leaching characteristics of Ce from florencite-(Ce), acid leaching tests were performed on the raw synthesized sample as well as the samples calcined at various temperatures. The leaching conditions of 10 g/L solids concentration, 1.2 mol/L HCl solution, and 75 °C leaching temperature were employed, which are consistent with the previous studies of recovering REEs from florencite-bearing materials (Ji et al., 2022b; Ji and Zhang, 2021b). As Figure 4.6 shows, the raw synthesized florencite-(Ce), 300 °C- and 400 °C-calcined products exhibited similar leaching behavior, with less than 10% of Ce being extracted after the completion of the reaction, suggesting that calcination at 300 °C or 400 °C for 2 h has negligible effect on the solubility of Ce compared with the synthesized sample.

The leaching recovery of Ce increased remarkably with the further elevation of the calcination temperature. Around 30% of Ce was released from the 500 °C-calcined product after 2 h of reaction, and the leaching recovery increased by 45 absolute percentage points under the same leaching conditions when the sample was treated at 600 °C for 2 h. The highest Ce leaching recovery of up to 98% was obtained from the 700 °C-calcined product, which means an almost complete dissolution of Ce. In addition to the significant recovery improvement resulted from the calcination at 700 °C, a faster leaching kinetics of Ce was also observed. As shown in Figure 4.6, over 87% of Ce was leached within the first 5 min of the reaction, and a recovery gain of only around 10 absolute percentage points was obtained by prolonging the reaction time to 2 h. This result indicated that calcination at 700 °C significantly improves the solubility of Ce from florencite-(Ce). As presented in Figure 4.4 and Figure 4.5, calcination at 300-400 °C had no effect on the structural decomposition of florencite-(Ce), and partial destruction was observed from 500 °C-calcined product. When the calcination temperature increased to 600 °C, the hydroxyl groups within the lattice structure of florencite-(Ce) were remarkably dehydroxylated. The complete decomposition of florencite-(Ce) occurred at the temperature of 677.3 °C, therefore, the crystallized structure is fully transformed into an amorphous phase after 2 h of calcination at 700 °C. It is worth mentioning that the phase transformation of florencite-(Ce) corresponds to the variations in Ce leaching recovery as a function of calcination temperature: no recovery improvement was obtained from 300 °C- or 400 °C-calcined

products, a slight recovery increase occurred at 500 °C, a considerable gain in recovery was realized at 600 °C, and 700 °C of calcination led to the nearly complete dissolution of Ce. It has been reported that the solubility of a compound in the amorphous form is higher than the more stable crystalline form because of a higher Gibbs free energy (Gurunath et al., 2013). The same phenomenon can also be observed from the kaolinite. As a result of the presence of Al–O–Si bonds and shielding of aluminum cation by the siliconoxygen network, the raw kaolinite has low solubility in acids (Tantawy and Ali Alomari, 2019). However, after the dehydroxylation, the aluminum can be easily dissolved from the dehydroxylated aluminosilicate phase except for the silica. Therefore, it is reasonable to conclude that the gradual transformation of the crystallized structure into an amorphous phase results in the increases in solubility of Ce from florencite-(Ce).

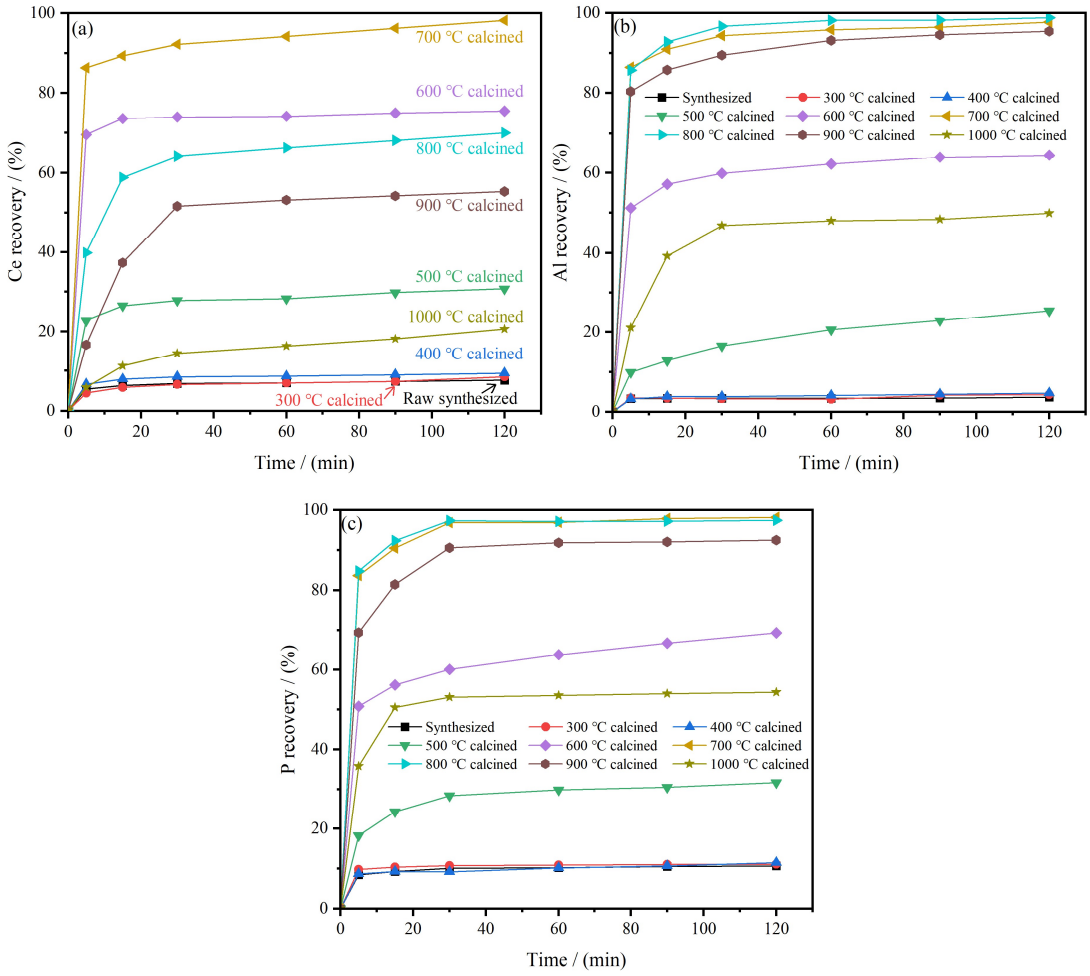


Figure 4.6 The effect of calcination on the leaching characteristics of (a) Ce, (b) Al, and (c) P from florencite-(Ce). (Note: The standard deviations of the recovery values were ± 3%; therefore, error bars were not added in this figure to maintain the readability of the data.)

Further elevating the calcination temperature to higher than 700 °C led to noticeable reductions in both the leaching kinetics and the recovery of Ce from florencite-(Ce). For example, the final leaching recovery of Ce was less than 70% when the calcination temperature increased to 800 °C, and the value decreased further by 15 absolute percentage points after calcination at 900 °C for 2 h. A recovery of only 20% was obtained after 2 h of reaction when increasing the calcination temperature to 1000 °C. In addition, the leaching kinetics of Ce from the samples calcined at temperatures higher than 800 °C was much lower than that of the 500-700 °C-calcined products. After the first 5 min of the leaching reaction, less than 16 % of Ce was released from the 900 °C-calcined product, and around 60 min was required for the reaction to reach equilibrium. The XRD and TGA-DTA analyses showed that the transformation of the amorphous phase into $CePO_4$ begins at around 800 °C, and the formation of an ordered $CePO_4$ structure occurs at 970.8 °C. It has been proved that crystallized $CePO_4$ possesses high chemical resistance and thereby normally requires concentrated sulfuric acid baking at high temperature to decompose (Demol et al., 2019; Kim and Osseo-Asare, 2012). The gradual evolution of $CePO_4$ from amorphous to crystalline phases definitely reduced the solubility of Ce from the calcined products.

Figure 4.6(b)(c) displays the effect of calcination on the leaching characteristics of Al and P from florencite-(Ce). As shown, both the leaching recoveries and kinetics of Al and P were increased with the increasing of calcination temperature, which reached the highest values after calcination at 700 °C for 2 h. For example, the leaching recoveries of Al and P were over 97% from the 700 °C-calcined product after the completion of the reaction. This result indicates that the solubility of florencite-(Ce) increased with the decomposition degree of crystal structure. However, different from that of Ce, minimal differences could be observed from the leaching recoveries of Al and P when elevating the calcination temperatures to 800 °C and 900 °C, respectively. Further increasing the calcination temperature to 1000 °C, both the leaching recoveries of Al and P decreased to the same

level of around 50 %, which were higher than that of Ce at the same leaching conditions (20.5 %).

The XRD and DTA analyses conclude that the recrystallization of $CePO_4$ results in the significant reduction of Ce leaching recovery, and the exothermic peak centered at 970.8 ℃ corresponds to the formation of ordered crystal structure of $CePO_4$. As reported in the literature, the final recrystallization products of amorphous florencite-(Ce) include $CePO_4$, $AlPO_4$, and Al_2O_3, but the crystal reflections as well as the thermal peaks of $AlPO_4$ and Al_2O_3 were not present in the XRD and DTA signals within the studied temperature range. It has been reported that the solubility of $AlPO_4$ in HCl is relatively low compared with amorphous phases (Drüppel et al., 2007; Kolb et al., 1981). Therefore, a combination analyses of XRD, DTA, and leaching characteristics indicate that 1000 ℃ calcination results in the formation of ordered $CePO_4$ structure, while ordered $AlPO_4$ and Al_2O_3 structure formation may need much higher temperatures, and the reduction in the leaching recoveries of Al and P may be related to the germination of $AlPO_4$ at 1000 ℃.

4.3.4 Mixed Calcination and Leaching Characteristics

The phase transformation of florencite-(Ce) as a result of calcination and its impact on the solubility of Ce were investigated in previous section. The solubility of Ce from florencite-(Ce) positively correlated with the degree of structural decomposition in the temperature range of 500-700 °C, while a negative correlation was observed between the leaching recovery of Ce and the recrystallization of the amorphous phase into $CePO_4$ at temperatures higher than 700 °C. Florencite has been reported to be an accessory phase disseminated and scattered throughout the host materials as micro particles, such as chlorite, kaolinite, leucophyllite, quartzite, and coal coarse refuse (Gabudianu Radulescu et al., 2009; Gaudin et al., 2020; Janeczek and Ewing, 1996; Ji et al., 2022b; Nagy et al., 2002). The authors have systematically investigated the effect of calcination on the leaching recovery of REEs from kaolinite and coal coarse refuse, and significant improvements of light REE recovery were obtained after the materials were calcined in the temperature range of 600-800 °C, while the leaching recovery decreased when further increasing the calcination temperature to 900 °C (Ji et al., 2022a; Zhang and Honaker, 2020). Although the leaching characteristics of light REEs from kaolinite and coal coarse

refuse were comparable with those of the raw synthesized florencite-(Ce), there is also a possibility that some chemical reactions may occur between florencite and host materials during calcination, which accelerate or hinder the phase transformation of florencite-(Ce).

However, due to the trace amount of naturally occurred florencite (~ 200 ppm of light REEs) as well as its finely disseminated characteristics, it is impossible to detect any potential reactions between florencite and host materials during calcination. To make possible reactions detectable, the synthesized florencite-(Ce) (Flo) was mixed with kaolinite (Kao) and coal coarse refuse (CR) with different mass ratios (i.e., 1:1, 1:5, 1:10, 1:20). The Kao and CR have been investigated previously by the authors (Ji et al., 2022a, 2022c). Each mixture with a certain mass ratio was then grinded for 10 min to get a homogeneous sample, followed by pellet preparation using a hydraulic press and 25 mm evaluable pellet die set. The mixed sample was pressed at 12 tons/cm^2 for 2 min, resulting in a pellet of 2 cm diameter and 1 mm thickness, to ensure the close association between the florencite-(Ce) and host materials. The pellets were then calcined at 700 °C and 1000 °C, respectively, which are critical temperatures for the phase transformation of florencite-(Ce). XRD and DTA analyses were performed on the raw mixed and the calcined samples to understand the potential reactions, and the effect of calcination on the leaching recovery of Ce was evaluated by acid leaching tests.

As shown in Figure 4.7(a), the Kao sample shows a high purity and crystallinity with all well-defined reflections being indexed to kaolinite. After mixing with florencite-(Ce), combined reflections of florencite-(Ce) and kaolinite were present in the XRD spectrum, and the peak intensities of florencite-(Ce) decreased with the increase in the relative content of kaolinite, suggesting that these two phases were evenly mixed. The complete decomposition temperature for both the kaolinite and florencite-(Ce) is 700 °C. After calcination at 700 °C for 2 h, weak peaks were observed from the XRD pattern of the 700 °C-calcined kaolinite sample, which result from the improved relative contents of anatase and muscovite (Reli et al., 2012). Regardless of the various mass ratios, negligible differences were observed in XRD patterns among the mixtures and the Kao sample, indicating no newly formed crystallized phase was present in the mixtures after 2 h of calcination at 700 °C (Figure 4.7(b)). As shown in Figure 4.7(c), increasing the calcination temperature to 1000 °C, the muscovite was decomposed while the anatase still existed in

the XRD pattern of Kao sample. Three weak and broad peaks located at 2θ of around 26.32°, 33.84°, and 67.15° were identified as mullite germination, which was due to the recrystallization of amorphous metakaolinite. This result indicated that calcination at 1000 °C led to the germination of mullite phase, which is in accordance with previous studies on thermal phase transformation of kaolinite (Chakraborty, 2014; Chargui et al., 2018; Salvador, 1995). It was observed that the reflections of $CePO_4$ dominated in the XRD pattern of 1000 °C calcined product with a mass ratio of 1:1, and the peak intensities decreased with the reduction of florencite-(Ce) mass ratio. Similar to that of the 700 °C-calcined samples, no additional diffraction peaks emerged in the XRD patterns of the 1000 °C-calcined mixed materials with various mass ratios, indicating that calcination does not produce new crystallized phases in the mixtures of kaolinite and florencite-(Ce).

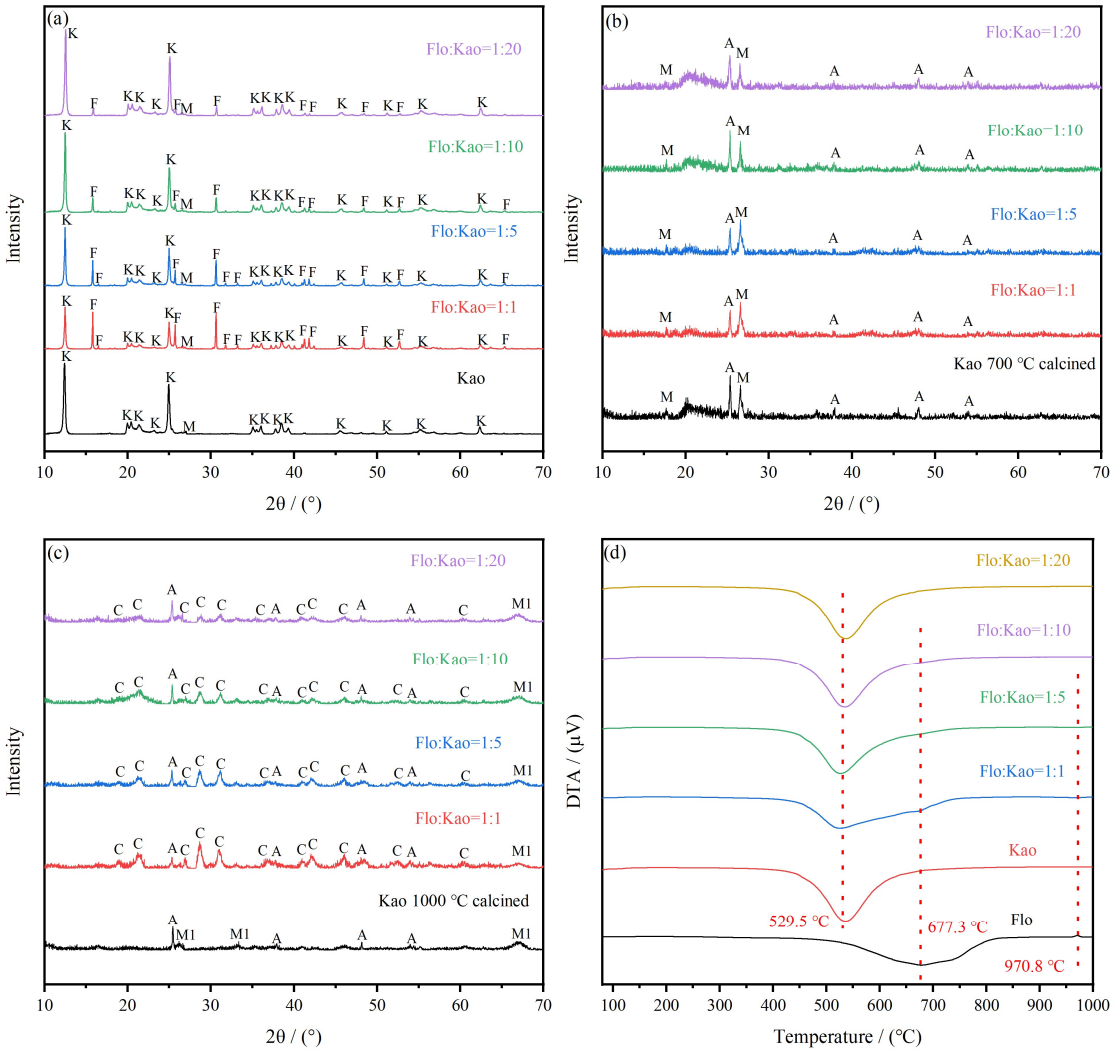


Figure 4.7 XRD patterns of the kaolinite sample (Kao) and mixed materials with different mass ratios (a), calcined products of 700 °C (b), calcined products of 1000 °C (c), and the DTA curves of florencite-(Ce), kaolinite, and the mixed materials with different mass ratios (d). (K-kaolinite; F-florencite-(Ce); M-muscovite; A-anatase; C-$CePO_4$; M1-mullite).

In order to further identify potential reactions precisely, DTA was conducted to analyze the thermal behavior of the mixed materials, and the result is shown in Figure 4.7(d). The Kao sample showed an endothermic peak centered at 529.5 °C due to the structural decomposition, while no DTA peaks appeared when elevating the temperature up to 1000 °C. The germination of mullite as indicated by the XRD pattern of 1000 °C-calcined kaolinite (Figure 4.7(c)) was not reflected by a corresponding exothermic DTA peak, which may be related to the incomplete recrystallization reaction or the composition of the raw kaolinite used (Chen et al., 2004; Katayama et al., 2014; Redaoui et al., 2018). Differences in endothermic peak intensities between kaolinite and florencite-(Ce) can be observed from the DTA curves, which likely result from the differences in thermal reaction intensities as well as the particle size, packing density, and weight of the loaded samples (Devi et al., 2021; Grim, Ralph, 1947). After mixing with florencite-(Ce) at various mass ratios, the DTA curve of 1:1 mass ratio mixture shows two endothermic peaks. The intensive peak located at around 529.5 °C corresponded to kaolinite dehydroxylation, while the broad peak centered at 677.3 °C was the indicator of florencite-(Ce) decomposition. With increases in the relative content of kaolinite, the DTA curves in the temperature range of 500-700 °C became narrow, and the curve of 1:20 mass ratio mixture was comparable with that of the Kao. The exothermic peak of florencite-(Ce) at 970.8 °C was not detected from the DTA curves of the mixtures, which was mainly caused by the reduced mass ratio of florencite-(Ce) and the low reactivity of the thermal reaction. Furthermore, no additional thermal peaks were detected by the DTA during the calcination process, indicating no thermal reactions occurred between the kaolinite and florencite-(Ce) within the studied temperature range.

The phase transformation and thermal behavior of the mixtures of florencite-(Ce) (Flo) and coal coarse refuse (CR) are present in Figure 4.8. As shown, after calcination at 700 °C for 2 h (Figure 4.8(b)), the crystallized kaolinite in the coal coarse refuse was decomposed, and hematite appeared in the calcined product as a result of the pyrite

oxidation (Ji et al., 2022e; Zhang and Honaker, 2019a). When the calcination temperature rose to 1000 °C, the amorphization of muscovite into siliceous or silicon-alumina phases occurred, thus only the reflections of quartz and hematite were present in the pattern (Figure 4.8(c)) (Zhou et al., 2013). Similar to the XRD patterns shown in Figure 4.7, the reflections of florencite-(Ce) appeared and the peak intensities decreased with the increases in the mass ratio of coal coarse refuse. All the florencite-(Ce) peaks disappeared in the 700 °C-calcined mixtures, and the formation of $CePO_4$ was observed when elevating the calcination temperature to 1000 °C. As indicated by the XRD patterns of the raw mixtures as well as the calcined products, no additional phases were formed or recrystallized when the samples were treated at 700 °C and 1000 °C, respectively. The thermal behavior of the florencite-(Ce), coal coarse refuse, and their mixtures is shown in Figure 4.8(d). The DTA curve of coarse refuse showed endothermic peaks at 109.1 °C, 519.4 °C, and 874.5 °C, which corresponded to the removal of adsorbed water, the dehydroxylation of clay minerals, and the decomposition and amorphization of muscovite, respectively (Ptáček et al., 2010; Wang et al., 2022). After mixing with florencite-(Ce) at a mass ratio of 1:1, a pronounced endothermic peak indicating the amorphization of florencite-(Ce) appeared in the DTA curve. When increasing the mass ratio of coal coarse refuse, the intensity of the thermal characteristic peak of florencite-(Ce) were gradually weaken, and the peak is hardly visible in the DTA curve of 1:20 mass ratio. Except for the thermal characteristic peaks of the florencite-(Ce) and coal coarse refuse themselves, no newly formed endothermic or exothermic peaks appeared within the studied temperature range.

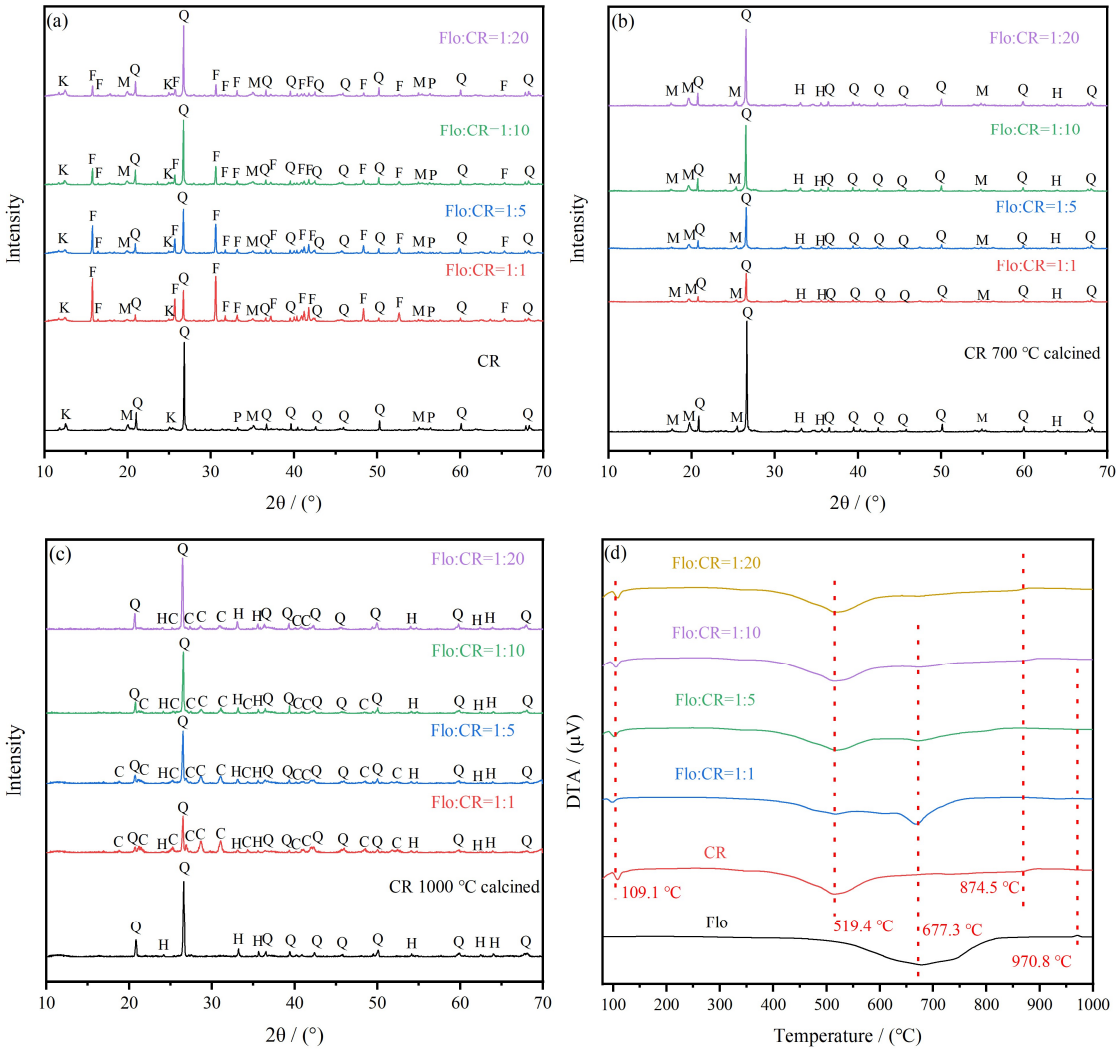


Figure 4.8 XRD patterns of the coal coarse refuse sample (CR) and mixed materials with different mass ratios (a), calcined products of 700 °C (b), calcined products of 1000 °C (c), and the DTA curves of florencite-(Ce), coal coarse refuse, and the mixed materials with different mass ratios (d). (K-kaolinite; F-florencite-(Ce); M-muscovite; Q-quartz; P-pyrite; H-hematite; C-$CePO_4$).

Acid leaching tests were conducted to investigate the effect of calcination on the leaching recovery of Ce from the raw mixtures and calcined products. As shown in Figure 4.9(a), the leaching recovery of Ce from mixtures of various mass ratios without calcination showed the same characteristics, which less than 10% of Ce being leached after the completion of the leaching reaction. After calcination at 700 °C for 2 h, the leaching kinetic as well as the recovery of Ce increased significantly for all the mixed samples, and a final

recovery value of 97-98% was obtained. Further elevating the calcination temperature to 1000 °C led to remarkable reductions in the solubility of Ce, and the recovery curves of the samples with different mass ratio of florencite-(Ce) overlapped. Moreover, the leaching characteristics of Ce from the raw mixtures and calcined products agreed well with those of the florencite-(Ce) itself shown in Figure 6, that is, minimal amount of Ce was leached from the raw florencite-(Ce), and Ce solubility increased significantly after the decomposition of florencite-(Ce) structure, however, the recrystallization of $CePO_4$ sharply reduced the solubility of Ce. The same phenomenon was also found in the case of florencite-(Ce) and coal coarse refuse mixtures (Figure 4.9(b)).

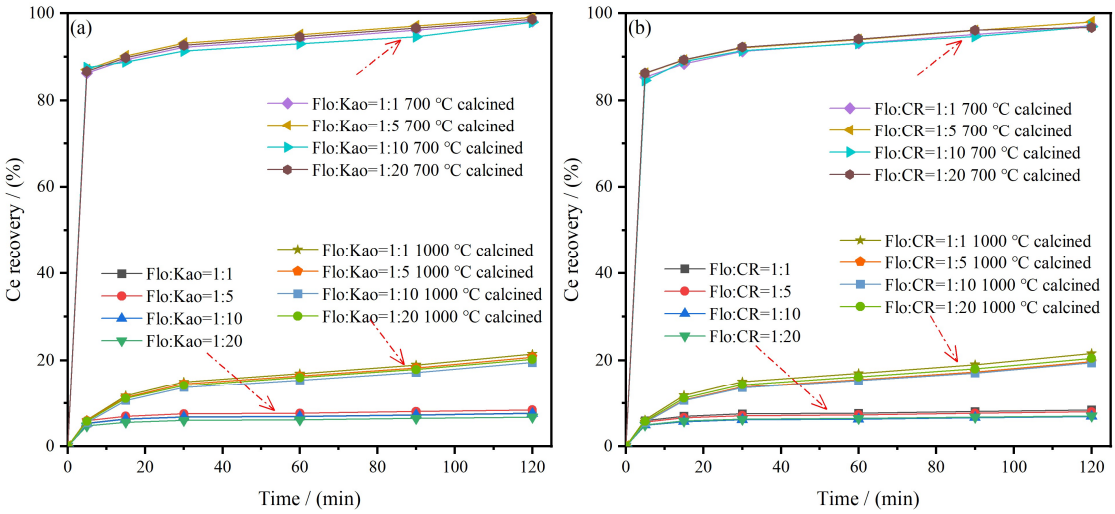


Figure 4.9 The leaching characteristics of Ce from mixed samples, and the corresponding 700 °C- and 1000 °C-calcined products: (a) florencite-(Ce) and kaolinite mixtures; and (b) florencite-(Ce) and coal coarse refuse mixtures. (Note: The standard deviations of the recovery values were ± 3%; therefore, error bars were not added in this figure to maintain the readability of the data.)

4.4 Conclusions

In the present study, pure florencite-(Ce), an endmember of crandallite-group minerals, was synthesized using a hydrothermal method. The XRD SEM-EDS, and TEM analyses suggested the formation of high purity florencite-(Ce) with well-crystallized structure. The synthesized florencite-(Ce) was then calcined under different temperatures to investigate its thermal phase transformation behavior. The results showed that calcination at 300-400

°C enhanced the crystallinity of florencite-(Ce) as a result of the removal of free and physically bound water. After that, the crystal structure decomposed gradually with the increase in the calcination temperature, and the amorphous phase was formed after calcination at 700 °C for 2 h. However, further elevating the calcination temperature led to the evolution of $CePO_4$, and the complete crystallization of ordered $CePO_4$ structure occurred in the temperature range of 900-1000 °C. TGA-DTA analysis presented three weight loss stages between 50 °C and 1000 °C, and the complete decomposition of florencite-(Ce) structure occurred at 677.3 °C, while the exothermic peak at 970.8 °C indicated the recrystallization of ordered $CePO_4$.

Acid leaching tests were applied to investigate the effect of calcination on the leaching characteristics of Ce from florencite-(Ce). The results showed that the leaching recovery of Ce correlated positively with the degree of structure decomposition of florencite-(Ce), and the highest value was obtained from the 700 °C-calcined product which was an amorphous phase. After that, the solubility of Ce decreased gradually as a result of the recrystallization of $CePO_4$. To identify any potential reactions between florencite and host materials during calcination, the florencite-(Ce) was mixed with kaolinite and coal coarse refuse materials, respectively, with different mass ratios, which were then calcined at 700 °C and 1000 °C. Both the raw and calcined mixtures were subjected to XRD analysis and acid leaching tests. By combining the result of DTA analysis, it can be concluded that the phase transformation of florencite-(Ce) was an independent reaction, which was not interfered by the kaolinite and coal coarse refuse.

Chapter 5 Summary and Perspectives

5.1 Summary

In this work, two different coal waste samples were selected to investigate the correlations between the mineralogy and recovery behavior of rare earth elements (REEs). SEM-EDS, TEM-EDS, acid leaching, XRD, and TGA analyses were conducted on both the coal waste samples as well as the synthetic product. Based on the findings from this study, the conclusions can be drawn as follows:

1. REEs mainly occur as zircon, apatite, monazite, xenotime, and crandallite-group minerals in both the Western Kentucky No. 13 and Fire Clay coal waste. Among these minerals, apatite, monazite, and crandallite-group minerals were the major host materials for light REEs, while heavy REEs were normally found in zircon and xenotime.

2. By comparing the number and REE contents of particles found from these two coal waste samples, the majority of the REEs occurred as monazite, xenotime, and crandallite-group minerals in the Western Kentucky No. 13 coal waste, while monazite and xenotime were the major REE carriers found from Fire Clay coal waste. The SEM images showed that both liberated REE-bearing particles and particles locked by dominant minerals existed in these two coal waste samples.

3. Calcination pretreatment at 600 ℃ without adding any additives can improve the REE recovery from coal waste samples, and the increases were primarily attributable to light REEs. SEM-EDS analysis showed that various REE-bearing minerals still existed in the leaching residue of raw coal waste samples, while crandallite-group minerals were rarely found in the leaching solid residue of the calcined coal waste samples.

4. The thermal decomposition of crandallite-group minerals led to the improvement of REE recovery from coal waste samples, especially light REEs. In addition, more crandallite-group mineral particles were found from Western Kentucky No. 13 coal waste, which resulted in a higher recovery increase relative to that of Fire Clay coal waste.

5. Florencite, as a pure endmember of crandallite-group minerals, was synthesized in this study. The XRD and TGA-DTA analyses showed that the complete decomposition of florencite structure occurred between 600-700 ℃, leading to the significant increase in

REE solubility. Further increasing the calcination temperature resulted in the evolution of $CePO_4$, which lowered the REE recovery from florencite.

6. The synthesized florencite was mixed with coal waste samples and kaolinite to identify if any reactions occur between them during calcination. By analyzing the XRD, DTA, and acid leaching results, it can be concluded that the phase transformation of florencite was an independent reaction, which was not interfered by its host materials.

5.2 Perspectives

In this research dissertation, comprehensive investigations have been conducted on the correlations between the mineralogy and recovery behavior of REEs in coal waste. The significant improvement of light REE recovery can be attributed to the thermal decomposition of crandallite-group minerals. However, as a result of the complicated REE mineralogy and the promising recovery potential, more efforts ought to be devoted to achieving the maximum utilization of coal waste. The perspectives of this study were suggested as follows:

1. The present study investigated the mineralogy of REEs occurred in the coal waste samples, and it was concluded that the thermal decomposition of crandallite-group minerals was responsible for the significant increase in light REEs. Despite this, there are still a portion of REEs existed in the form of monazite, apatite, zircon, and especially xenotime which is the major carrier of heavy REEs. It is suggested to design a circuit to reach the maximum recovery of REEs from coal waste, especially the heavy REEs.

2. In addition to the REEs, coal waste materials can also be regarded as promising sources of strategically important elements, such as Ga, Ge, Ag, and Re, etc. The characterization and utilization of these elements will mitigate the supply limitations and reduce the environmental issues of disposing of coal wastes. The extraction and recovery of more valuable metals from coal waste should be considered in the future work.

3. In this study, the REEs were rarely extracted from the raw coal waste, however, the solubility increased significantly after the thermal pretreatment at 600 ℃. The thermal pretreatment definitely increases the operational cost, thus impairing the economic feasibility. Actually, the calcined coal waste can be applied to the fields of construction materials, and water treatment, etc. More efforts need to be devoted to combining the REE

recovery and the subsequent utilization of the calcined coal waste, which can realize the maximum benefit and comprehensive utilization.

4. Florencite was synthesized and characterized by XRD, SEM, TEM, and TGA-DTA analyses in this study. However, as a rarely reported mineral, there are some investigations still need to be done. For example, how to identify the molecular cleavage of florencite, the formation of each phase, the decomposition rate, and the hexagonal decomposition steps during calcination process.

Reference

Abaka-Wood, G.B., Zanin, M., Addai-Mensah, J., Skinner, W., 2019a. Recovery of rare earth elements minerals from iron oxide–silicate rich tailings – Part 1: Magnetic separation. Miner. Eng. 136, 50–61. https://doi.org/10.1016/J.MINENG.2019.02.026

Abaka-Wood, G.B., Zanin, M., Addai-Mensah, J., Skinner, W., 2019b. Recovery of rare earth elements minerals from iron oxide–silicate rich tailings – Part 2: Froth flotation separation. Miner. Eng. 142, 105888. https://doi.org/10.1016/J.MINENG.2019.105888

Abdel-rehim, A.M., 2005. A new technique for extracting zirconium form Egyptian zircon concentrate 76, 234–243. https://doi.org/10.1016/j.minpro.2005.02.004

Abdullah, M.M.A.B., Ming, L.Y., Yong, H.C., Tahir, M.F.M., 2018. Clay-Based Materials in Geopolymer Technology, in: Cement Based Materials. https://doi.org/10.5772/intechopen.74438

Abellan, P., Moser, T.H., Lucas, I.T., Grate, J.W., Evans, J.E., Browning, N.D., 2017. The formation of cerium(III) hydroxide nanoparticles by a radiation mediated increase in local pH. RSC Adv. 7, 3831–3837. https://doi.org/10.1039/C6RA27066B

Balaram, V., 2019. Rare earth elements: A review of applications, occurrence, exploration, analysis, recycling, and environmental impact. Geosci. Front. 10, 1285–1303. https://doi.org/10.1016/j.gsf.2018.12.005

Binnemans, K., Jones, P.T., Blanpain, B., Van Gerven, T., Yang, Y., Walton, A., Buchert, M., 2013. Recycling of rare earths: A critical review. J. Clean. Prod. https://doi.org/10.1016/j.jclepro.2012.12.037

Cao, S., Zhou, C., Pan, J., Liu, C., Tang, M., Ji, W., Hu, T., Zhang, N., 2018. Study on Influence Factors of Leaching of Rare Earth Elements from Coal Fly Ash. Energy and Fuels 32, 8000–8005. https://doi.org/10.1021/acs.energyfuels.8b01316

Chakraborty, A.K., 2014. Phase transformation of kaolinite clay, Phase Transformation of Kaolinite Clay. https://doi.org/10.1007/978-81-322-1154-9

Chakraborty, M., Biswas, S., Sengupta, N., Sengupta, P., 2014. First Report of Florencite from the Singhbhum Shear Zone of the East Indian Craton. Int. J. Mineral. 2014, 1–8. https://doi.org/10.1155/2014/978793

Chargui, F., Hamidouche, M., Belhouchet, H., Jorand, Y., Doufnoune, R., Fantozzi, G.,

2018. Mullite fabrication from natural kaolin and aluminium slag. Bol. la Soc. Esp. Ceram. y Vidr. 57, 169–177. https://doi.org/10.1016/J.BSECV.2018.01.001

Chen, X., Guo, F., Chen, Q., Liu, X., Zhao, Z., 2019. Dissolution behavior of the associated rare-earth elements in scheelite using a mixture of sulfuric and phosphoric acids. Miner. Eng. 144, 106057. https://doi.org/10.1016/j.mineng.2019.106057

Chen, Y.F., Wang, M.C., Hon, M.H., 2004. Phase transformation and growth of mullite in kaolin ceramics. J. Eur. Ceram. Soc. 24, 2389–2397. https://doi.org/10.1016/S0955-2219(03)00631-9

Chu, S., 2011. Critical materials strategy. DIANE Publishing.

Dai, S., Finkelman, R.B., 2018. Coal as a promising source of critical elements: Progress and future prospects. Int. J. Coal Geol. 186, 155–164. https://doi.org/10.1016/j.coal.2017.06.005

Dai, S., Liu, J., Ward, C.R., Hower, J.C., French, D., Jia, S., Hood, M.M., Garrison, T.M., 2016. Mineralogical and geochemical compositions of Late Permian coals and host rocks from the Guxu Coalfield, Sichuan Province, China, with emphasis on enrichment of rare metals. Int. J. Coal Geol. 166, 71–95. https://doi.org/10.1016/j.coal.2015.12.004

Dai, S., Yan, X., Ward, C.R., Hower, J.C., Zhao, Lei, Wang, X., Zhao, Lixin, Ren, D., Finkelman, R.B., 2018. Valuable elements in Chinese coals: a review. Int. Geol. Rev. 60, 590–620. https://doi.org/10.1080/00206814.2016.1197802

Demol, J., Ho, E., Soldenhoff, K., Senanayake, G., 2019. The sulfuric acid bake and leach route for processing of rare earth ores and concentrates: A review. Hydrometallurgy 188, 123–139. https://doi.org/10.1016/J.HYDROMET.2019.05.015

Devi, N., Srivastava, S., Yogi, B., Kumar Gupta, S., 2021. A Review on Differential Thermal Analysis. Chem. Res. J. 6, 71–80.

Di Piazza, S., Cecchi, G., Cardinale, A.M., Carbone, C., Mariotti, M.G., Giovine, M., Zotti, M., 2017. Penicillium expansum Link strain for a biometallurgical method to recover REEs from WEEE. Waste Manag. 60, 596–600. https://doi.org/10.1016/j.wasman.2016.07.029

Dill, H.G., 2001. The geology of aluminum phosphate and sulphates of the alunite group minerals: A review. Earth Sci. Rev. 53, 35–93. https://doi.org/10.1016/S0012-

8252(00)00035-0

Dill, H.G., Melcher, F., Füßl, M., Weber, B., 2006. Accessory minerals in cassiterite: A tool for provenance and environmental analyses of colluvial-fluvial placer deposits (NE Bavaria, Germany). Sediment. Geol. 191, 171–189. https://doi.org/10.1016/J.SEDGEO.2006.03.022

DoI, U.S., 2018. Final List of Critical Minerals 2018. Fed. Regist. 83, 23295–23296.

Drüppel, K., Hösch, A., Franz, G., 2007. The system Al2O3-P2O5-H2O at temperatures below 200 °C: Experimental data on the stability of variscite and metavariscite AlPO4·2H2O. Am. Mineral. 92, 1695–1703. https://doi.org/10.2138/am.2007.2487

Elkina, V., Kurushkin, M., 2020. Promethium: To Strive, to Seek, to Find and Not to Yield. Front. Chem. 8, 1–8. https://doi.org/10.3389/fchem.2020.00588

Enkhbayar, D., Seo, J., Choi, S., Lee, Y.J., 2016. Mineral Chemistry of REE-Rich Apatite and Sulfur-Rich Monazite from the Mushgai Khudag , Alkaline Volcanic-Plutonic Complex , South Mongolia 2016. https://doi.org/10.4236/ijg.2016.71003

Eterigho-Ikelegbe, O., Harrar, H., Bada, S., 2021. Rare earth elements from coal and coal discard – A review. Miner. Eng. 173, 107187. https://doi.org/10.1016/j.mineng.2021.107187

European Commission, 2015. Report on critical raw materials for the eu.

Finkelman, R.B., Palmer, C.A., Wang, P., 2018. Quantification of the modes of occurrence of 42 elements in coal. Int. J. Coal Geol. 185, 138–160. https://doi.org/10.1016/j.coal.2017.09.005

Frank N.Blanchard, 1971. Thermal analysis of crandallite, in: QUARTERLY JOURNAL of the FLORIDA ACADEMY OF SCIENCES. pp. 1–9.

Franken, K.M., 1995. A roast-leach process for extraction of rare earths from complex monazite-xenotime concentrates. Sep. Sci. Technol. 30, 1941–1949. https://doi.org/10.1080/01496399508010386

Frost, R.L., Palmer, S.J., Pogson, R.E., 2012. Thermal stability of crandallite CaAl3(PO4) 2(OH)5·(H2O): A “Cave” mineral from the Jenolan Caves. J. Therm. Anal. Calorim. 107, 905–909. https://doi.org/10.1007/s10973-011-1578-6

Fu, B., Hower, J.C., Zhang, W., Luo, G., Hu, H., Yao, H., 2022. A review of rare earth elements and yttrium in coal ash : content , modes of occurrences , combustion

behavior , and extraction methods. Prog. Energy Combust. Sci. 88, 100954. https://doi.org/10.1016/j.pecs.2021.100954

Gabudianu Radulescu, I., Rubatto, D., Gregory, C., Compagnoni, R., 2009. The age of HP metamorphism in the Gran Paradiso Massif, Western Alps: A petrological and geochronological study of “silvery micaschists.” Lithos 110, 95–108. https://doi.org/10.1016/j.lithos.2008.12.008

Gaudin, A., Ansan, V., Lorand, J.P., Pont, S., 2020. Genesis of a florencite-bearing kaolin deposit on ordovician schists at Saint-Aubin-des-Châteaux, Armorican Massif, France. Ore Geol. Rev. 120. https://doi.org/10.1016/j.oregeorev.2020.103445

Gielen, B., Jordens, J., Thomassen, L.C.J., Braeken, L., Van Gerven, T., 2017. Agglomeration control during ultrasonic crystallization of an active pharmaceutical ingredient. Crystals 7. https://doi.org/10.3390/cryst7020040

Gilkes, R.J., Palmer, B., 1983. Synthesis, properties, and dehydroxylation of members of the crandallite-goyazite series. Mineral. Mag. 47, 221–227. https://doi.org/10.1180/minmag.1983.047.343.13

Grim, Ralph, E., 1947. Differential Thermal Curves of Prepared Mixtures of Clay Minerals. Am. Mineral. 32, 493–501.

Gupta, T., Ghosh, T., Akdogan, G., Bandopadhyay, S., 2017. Maximizing REE enrichment by froth flotation using Box-Behnken design in Alaskan coal. SME Annu. Conf. Expo 2017 Creat. Value a Cyclical Environ. 408–412.

Gurunath, S., Pradeep Kumar, S., Basavaraj, N.K., Patil, P.A., 2013. Amorphous solid dispersion method for improving oral bioavailability of poorly water-soluble drugs. J. Pharm. Res. 6, 476–480. https://doi.org/10.1016/J.JOPR.2013.04.008

Hikichi, Y., Ohsato, H., Miyamoto, M., 1989. Syntheses and thermal changes of plumbogummite-group phosphate minerals. J. Mineral. Soc. Japan 19, 67–78. https://doi.org/10.2465/gkk1952.19.67

Honaker, R.Q., Groppo, J., Yoon, R.H., Luttrell, G.H., Noble, A., Herbst, J., 2017. Process evaluation and flowsheet development for the recovery of rare earth elements from coal and associated byproducts. Miner. Metall. Process. 34, 107–115. https://doi.org/10.19150/mmp.7610

Honaker, R.Q., Zhang, W., Werner, J., Noble, A., Luttrell, G.H., Yoon, R.-H., 2020.

Enhancement of a process flowsheet for recovering and concentrating critical materials from bituminous coal sources. Mining, Metall. Explor. 37, 3–20.

Hower, J.C., Berti, D., Hochella, M.F., Mardon, S.M., 2018. Rare earth minerals in a “no tonstein” section of the Dean (Fire Clay) coal, Knox County, Kentucky. Int. J. Coal Geol. 193, 73–86. https://doi.org/10.1016/j.coal.2018.05.001

Hower, J.C., Eble, C.F., Dai, S., Belkin, H.E., 2016. Distribution of rare earth elements in eastern Kentucky coals: Indicators of multiple modes of enrichment? Int. J. Coal Geol. 160–161, 73–81. https://doi.org/10.1016/j.coal.2016.04.009

Huang, Q., Noble, A., Herbst, J., Honaker, R., 2018. Liberation and release of rare earth minerals from Middle Kittanning, Fire Clay, and West Kentucky No. 13 coal sources. Powder Technol. 332, 242–252. https://doi.org/10.1016/j.powtec.2018.03.063

Ignatova, L.I., Karpova, L.I., Zhil’tsova, I.G., 1965. Synthesis of the Aluminophosphate Minerals. Geokhimiya 11, 1355–1363.

J.J. Lefebvre, Patterson, L.E., 1982. Hydrothermal assemblages of aluminian serpentine, florencite and kyanite in the Zairian Copperbelt. Ann. la Société géologique Belgique 105, 51–71.

Janeczek, J., Ewing, R.C., 1996. Florencite-(La) with fissiogenic REEs from a natural fission reactor at Bangombé, Gabon. Am. Mineral. 81, 1263–1269. https://doi.org/10.2138/AM-1996-9-1024

Ji, B., Li, Q., Honaker, R., Zhang, W., 2022a. Acid leaching recovery and occurrence modes of rare earth elements (REEs) from natural kaolinites. Miner. Eng. 175, 107278. https://doi.org/10.1016/J.MINENG.2021.107278

Ji, B., Li, Q., Huang, Q., Zhang, W., 2021. Enhanced leaching recovery of rare earth elements from a phosphatic waste clay through calcination pretreatment. J. Clean. Prod. 319, 128654. https://doi.org/10.1016/J.JCLEPRO.2021.128654

Ji, B., Li, Q., Tang, H., Zhang, W., 2022b. Rare earth elements (REEs) recovery from coal waste of the Western Kentucky No. 13 and Fire Clay seams. Part II: Re-investigation on the effect of calcination. Fuel 315, 123145. https://doi.org/10.1016/J.FUEL.2022.123145

Ji, B., Li, Q., Zhang, W., 2022c. Rare earth elements (REEs) recovery from coal waste of the Western Kentucky No. 13 and Fire Clay Seams. Part I: Mineralogical

characterization using SEM-EDS and TEM-EDS. Fuel 307, 121854. https://doi.org/10.1016/J.FUEL.2021.121854

Ji, B., Li, Q., Zhang, W., 2022d. Rare earth elements (REEs) recovery from coal waste of the Western Kentucky No. 13 and Fire Clay Seams. Part I: Mineralogical characterization using SEM-EDS and TEM-EDS. Fuel 307, 121854. https://doi.org/10.1016/J.FUEL.2021.121854

Ji, B., Li, Q., Zhang, W., 2022e. Leaching recovery of rare earth elements from the calcination product of a coal coarse refuse using organic acids. J. Rare Earths 40, 318–327. https://doi.org/10.1016/j.jre.2020.11.021

Ji, B., Li, Q., Zhang, W., 2020. Leaching Recovery of Rare Earth Elements from Calcination Product of a Coal Coarse Refuse Using Organic Acids. J. Rare Earths. https://doi.org/10.1016/j.jre.2020.11.021

Ji, B., Zhang, W., 2022. Chemosphere Adsorption of cerium (III) by zeolites synthesized from kaolinite after rare earth elements (REEs) recovery. Chemosphere 303, 134941. https://doi.org/10.1016/j.chemosphere.2022.134941

Ji, B., Zhang, W., 2021a. Rare earth elements (REEs) recovery and porous silica preparation from kaolinite. Powder Technol. 391, 522–531. https://doi.org/10.1016/j.powtec.2021.06.028

Ji, B., Zhang, W., 2021b. The effect of mechanical grinding and thermal treatment on the recovery of rare earth elements (REEs) from kaolinite. Powder Technol. 394, 622–631. https://doi.org/10.1016/J.POWTEC.2021.08.077

Ji, B., Zhang, W., 2021c. Rare earth elements (REEs) recovery and porous silica preparation from kaolinite. Powder Technol. 391, 522–531. https://doi.org/10.1016/J.POWTEC.2021.06.028

Kanazawa, Y., Kamitani, M., 2006. Rare earth minerals and resources in the world. J. Alloys Compd. 408–412, 1339–1343. https://doi.org/10.1016/J.JALLCOM.2005.04.033

Katayama, M., Kawai, Y., Mizuno, Y.H., Mizuno, K., Aoyama, M., Kobayashi, Y., 2014. Preparation of dense mullite polycrystals by reaction sintering of kaolin materials and alumina and their microstructure. J. Ceram. Soc. Japan 122, 300–306. https://doi.org/10.2109/JCERSJ2.122.300

Ketris, M.P., Yudovich, Y.E., 2009. Estimations of Clarkes for Carbonaceous biolithes: World averages for trace element contents in black shales and coals. Int. J. Coal Geol. 78, 135–148. https://doi.org/10.1016/j.coal.2009.01.002

Kim, E., Osseo-Asare, K., 2012. Aqueous stability of thorium and rare earth metals in monazite hydrometallurgy: Eh-pH diagrams for the systems Th-, Ce-, La-, Nd- (PO 4)-(SO 4)-H 2O at 25 °c. Hydrometallurgy 113–114, 67–78. https://doi.org/10.1016/J.HYDROMET.2011.12.007

King, J.F., Taggart, R.K., Smith, R.C., Hower, J.C., Hsu-Kim, H., 2018. Aqueous acid and alkaline extraction of rare earth elements from coal combustion ash. Int. J. Coal Geol. 195, 75–83. https://doi.org/10.1016/j.coal.2018.05.009

Klinger, M., 2017. More features, more tools, more CrysTBox. J. Appl. Crystallogr. 50, 1226–1234. https://doi.org/10.1107/S1600576717006793

Kolb, E.D., Grenier, J.C., Laudise, R.A., 1981. Solubility and growth of AlPO4 in a hydrothermal solvent: HCl. J. Cryst. Growth 51, 178–182. https://doi.org/10.1016/0022-0248(81)90299-2

Kumari, A., Panda, R., Jha, M.K., Kumar, J.R., Lee, J.Y., 2015a. Process development to recover rare earth metals from monazite mineral: A review. Miner. Eng. 79, 102–115. https://doi.org/10.1016/j.mineng.2015.05.003

Kumari, A., Panda, R., Jha, M.K., Lee, J.Y., Kumar, J.R., Kumar, V., 2015b. Thermal treatment for the separation of phosphate and recovery of rare earth metals (REMs) from Korean monazite. J. Ind. Eng. Chem. 21, 696–703. https://doi.org/10.1016/j.jiec.2014.03.039

Laudal, D.A., Benson, S.A., Addleman, R.S., Palo, D., 2018. Leaching behavior of rare earth elements in Fort Union lignite coals of North America. Int. J. Coal Geol. 191, 112–124. https://doi.org/10.1016/j.coal.2018.03.010

Lefebvre, J.J., Gasparrini, C., 1980. Florencite, an occurrence in the Zairian copperbelt. Can. Mineral. 18, 301–311.

Liew, Y.M., Kamarudin, H., Mustafa Al Bakri, A.M., Luqman, M., Khairul Nizar, I., Ruzaidi, C.M., Heah, C.Y., 2012. Processing and characterization of calcined kaolin cement powder. Constr. Build. Mater. 30, 794–802. https://doi.org/10.1016/j.conbuildmat.2011.12.079

Lin, R., Howard, B.H., Roth, E.A., Bank, T.L., Granite, E.J., Soong, Y., 2017. Enrichment of rare earth elements from coal and coal by-products by physical separations. Fuel 200, 506–520. https://doi.org/10.1016/j.fuel.2017.03.096

Lin, R., Stuckman, M., Howard, B.H., Bank, T.L., Roth, E.A., Macala, M.K., Lopano, C., Soong, Y., Granite, E.J., 2018. Application of sequential extraction and hydrothermal treatment for characterization and enrichment of rare earth elements from coal fly ash. Fuel 232, 124–133. https://doi.org/10.1016/j.fuel.2018.05.141

Longhi, M.A., Zhang, Z., Rodríguez, E.D., Kirchheim, A.P., Wang, H., 2019. Efflorescence of alkali-activated cements (geopolymers) and the impacts on material structures: A critical analysis. Front. Mater. 6, 89. https://doi.org/10.3389/FMATS.2019.00089/BIBTEX

Luttrell, G.H., Kiser, M.J., Yoon, R.H., Noble, A., Rezaee, M., Bhagavatula, A., Honaker, R.Q., 2019. A Field Survey of Rare Earth Element Concentrations in Process Streams Produced by Coal Preparation Plants in the Eastern USA. Mining, Metall. Explor. 36, 889–902. https://doi.org/10.1007/s42461-019-00124-5

Mahandra, H., Hubert, B., Ghahreman, A., 2021. Recovery of Rare Earth and Some Other Potential Elements from Coal Fly Ash for Sustainable Future. Clean Coal Technologies: Beneficiation, Utilization, Transport Phenomena and Prospective. https://doi.org/10.1007/978-3-030-68502-7

Massari, S., Ruberti, M., 2013. Rare earth elements as critical raw materials: Focus on international markets and future strategies. Resour. Policy 38, 36–43. https://doi.org/10.1016/j.resourpol.2012.07.001

McKie, D., 1962a. Goyazite and florencite from two African carbonatites. Mineral. Mag. J. Mineral. Soc. 33, 281–297. https://doi.org/10.1180/MINMAG.1962.033.259.03

McKie, D., 1962b. Goyazite and florencite from two African carbonatites. Mineral. Mag. J. Mineral. Soc. 33, 281–297. https://doi.org/10.1180/MINMAG.1962.033.259.03

Moldoveanu, G.A., Papangelakis, V.G., 2016. An overview of rare-earth recovery by ion-exchange leaching from ion-adsorption clays of various origins. Mineral. Mag. 80, 63–76. https://doi.org/10.1180/minmag.2016.080.051

Mordberg, L.E., 2004a. Thorium in crandallite-group minerals: an example from a Devonian bauxite deposit, Timan, Russia. Mineral. Mag. 68, 489–497.

https://doi.org/10.1180/0026461046830200

Mordberg, L.E., 2004b. Thorium in crandallite-group minerals: an example from a Devonian bauxite deposit, Timan, Russia. Mineral. Mag. 68, 489–497. https://doi.org/10.1180/0026461046830200

Nagy, G., Draganits, E., Demény, A., Pantó, G., Árkai, P., 2002. Genesis and transformations of monazite, florencite and rhabdophane during medium grade metamorphism: Examples from the Sopron Hills, Eastern Alps. Chem. Geol. 191, 25–46. https://doi.org/10.1016/S0009-2541(02)00147-X

Nergis, D.D.B., Abdullah, M.M.A.B., Sandu, A.V., Vizureanu, P., 2020. XRD and TG-DTA study of new alkali activated materials based on fly ash with sand and glass powder. Materials (Basel). 13. https://doi.org/10.3390/MA13020343

Nichols, G., Byard, S., Bloxham, M.J., Botterill, J., Dawson, N.J., Dennis, A., Diart, V., North, N.C., Sherwood, J.D., 2002. A review of the terms agglomerate and aggregate with a recommendation for nomenclature used in powder and particle characterization. J. Pharm. Sci. 91, 2103–2109. https://doi.org/10.1002/jps.10191

Nickel, E.H., Temperly, J.E., 1987. Arsenoflorencite-(Ce): a new arsenate mineral from Australia. Mineral. Mag. 51, 605–609. https://doi.org/10.1180/MINMAG.1987.051.362.16

Okada, K., Shimai, A., Takei, T., Hayashi, S., Yasumori, A., MacKenzie, K.J.D., 1998. Preparation of microporous silica from metakaolinite by selective leaching method. Microporous Mesoporous Mater. 21, 289–296. https://doi.org/10.1016/S1387-1811(98)00015-8

Ozhogina, E., Rogozhin, A., Yakushina, O., Astakhova, Y., Likhnikevich, E., Sycheva, N., Iospa, A., Zhukova, V., 2019. Modern Methods of Technological Mineralogy in Assessing the Quality of Rare Metal Raw Materials, in: Springer Proceedings in Earth and Environmental Sciences. Springer Nature, pp. 119–122. https://doi.org/10.1007/978-3-030-22974-0_27

Pan, J., Nie, T., Vaziri Hassas, B., Rezaee, M., Wen, Z., Zhou, C., 2020. Recovery of rare earth elements from coal fly ash by integrated physical separation and acid leaching. Chemosphere 248, 126112. https://doi.org/10.1016/j.chemosphere.2020.126112

Pan, J., Zhou, C., Tang, M., Cao, S., Liu, C., Zhang, N., Wen, M., Luo, Y., Hu, T., Ji, W.,

2019. Study on the modes of occurrence of rare earth elements in coal fly ash by statistics and a sequential chemical extraction procedure. Fuel 237, 555–565. https://doi.org/10.1016/j.fuel.2018.09.139

Peiravi, M., Ackah, L., Guru, R., Mohanty, M., Liu, J., Xu, B., Zhu, X., Chen, L., 2017. Chemical extraction of rare earth elements from coal ash. Miner. Metall. Process. 34, 170–177. https://doi.org/10.19150/MMP.7856

Peiravi, M., Dehghani, F., 2021. A Review of Rare-Earth Elements Extraction with Emphasis on Non-conventional Sources : Coal and Coal Byproducts , Iron Ore Tailings , Apatite , and Phosphate Byproducts. Min. Sci. Technol. 38, 1–26.

Petty, T.R., 2018. Final List of Critical Minerals 2018. Fed. Regist. 83, 23295–23296.

Pouliot, G., Hofmann, H.J., 1981. Florencite; a first occurrence in Canada. Can. Mineral. 19, 535–540.

Ptáček, P., Kubátová, D., Havlica, J., Brandštetr, J., Šoukal, F., Opravil, T., 2010. The non-isothermal kinetic analysis of the thermal decomposition of kaolinite by thermogravimetric analysis. Powder Technol. 204, 222–227. https://doi.org/10.1016/J.POWTEC.2010.08.004

Rasmussen, B., 1996. Early-diagenetic REE-phosphate minerals (florencite, gorceixite, crandallite, and xenotime) in marine sandstones: A major sink for oceanic phosphorus. Am. J. Sci. 296, 601–632. https://doi.org/10.2475/ajs.296.6.601

Redaoui, D., Sahnoune, F., Heraiz, M., Saheb, N., 2018. Phase formation and crystallization kinetics in cordierite ceramics prepared from kaolinite and magnesia. Ceram. Int. 44, 3649–3657. https://doi.org/10.1016/J.CERAMINT.2017.11.119

Reli, M., Kočí, K., Matějka, V., Kovář, P., Obalová, L., 2012. Effect of Calcination Temperature and Calcination Time on the Kaolinite/TIO2 Composite for Photocatalytic Reduction of Co2/ Vliv Kalcinační Teploty A Doby Kalcinace Na Kompozit Kaolinit/TIO2 Pro Fotokatalytickou Redukci Co2. Geosci. Eng. 58, 10–22.

Repina, S.A., Popova, V.I., Churin, E.I., Belogub, E. V., Khiller, V. V., 2011. Florencite-(Sm)-(Sm,Nd)Al3(PO4)2(OH)6: A new mineral species of the alunite-jarosite group from the subpolar urals. Geol. Ore Depos. 53, 564–574. https://doi.org/10.1134/S1075701511070191

S'Ari, M., Blade, H., Cosgrove, S., Drummond-Brydson, R., Hondow, N., Hughes, L.P.,

Brown, A., 2021. Characterization of Amorphous Solid Dispersions and Identification of Low Levels of Crystallinity by Transmission Electron Microscopy. Mol. Pharm. 18, 1905–1919. https://doi.org/10.1021/ACS.MOLPHARMACEUT.0C00918/SUPPL_FILE/MP0C00918_SI_001.ZIP

Salvador, S., 1995. Pozzolanic properties of flash-calcined kaolinite: A comparative study with soak-calcined products. Cem. Concr. Res. 25, 102–112. https://doi.org/10.1016/0008-8846(94)00118-I

San Cristóbal, A.G., Castelló, R., Martín Luengo, M.A., Vizcayno, C., 2010. Zeolites prepared from calcined and mechanically modified kaolins. A comparative study. Appl. Clay Sci. 49, 239–246. https://doi.org/10.1016/j.clay.2010.05.012

Sangine, E., 2020. Mineral Commodity Summaries 2020, United States Geological Survey.

Schwab, R., Herold, H., Goetz, C., Pinto De Oliveira, N., 1990a. Compounds of the crandallite type : synthesis and properties of pure goyazite, gorceixite and plumbogumnite. Neues Jahrb. für Mineral. Monatshefte 113–126.

Schwab, R., Herold, H., Goetz, C., Pinto De Oliveira, N., 1990b. Compounds of the crandallite type: Synthesis and properties of pure Rare Earth Element-phosphates. Neues Jahrb. für Mineral. Monatshefte 241–254.

Schwab, R.G., Pimpl, T., Schukow, H., Stolle, A., Breitinger, D.K., 2004. Compounds of the crandallite-type: Synthesis, properties and thermodynamic data of pure crandallite and woodhouseite. Neues Jahrb. fur Mineral. Monatshefte 385–409. https://doi.org/10.1127/0028-3649/2004/2004-0385

Sejkora, J., Cejka, J., Srein, V., 2001. Pb dominant members of crandallite group from Cínovec and Moldava deposits, Krušné hory Mts. (Czech Republic). J. Czech Geol. Soc. 46, 53–68.

Seredin, V. V., Dai, S., 2012. Coal deposits as potential alternative sources for lanthanides and yttrium. Int. J. Coal Geol. https://doi.org/10.1016/j.coal.2011.11.001

Sharma, A., Kyotani, T., Tomita, A., 2000. Direct observation of layered structure of coals by a transmission electron microscope. Energy and Fuels 14, 515–516. https://doi.org/10.1021/EF990253H

Sreenivas, T., Moudgil, R., 2021. Developments in Characterization and Mineral

Processing of Coal Fly Ash for Recovery of Rare Earth Elements. Clean Coal Technologies: Beneficiation, Utilization, Transport Phenomena and Prospective. https://doi.org/10.1007/978-3-030-68502-7

Stanley, C.J., 2000. Rare earth element anomalies in crandallite group minerals from the Schugorsk bauxite deposit TeaSe-Tellurium and Selenium Cycling and Supply View project, European Journal of Mineralogy.

Stawski, T.M., Freeman, H.M., Van Driessche, A.E.S., Hövelmann, J., Besselink, R., Wirth, R., Benning, L.G., 2019. Particle-mediated nucleation pathways are imprinted in the internal structure of calcium sulfate single crystals. Cryst. Growth Des. 19, 3714–3721. https://doi.org/10.1021/ACS.CGD.9B00066/SUPPL_FILE/CG9B00066_SI_001.PDF

Sun, S., Wu, Z., Bian, X., Gao, B., Wu, W., Tu, G., 2007. Influence of NaCl-CaCl2 on decomposing REPO4 with CaO. J. Rare Earths 25, 779–782. https://doi.org/10.1016/S1002-0721(08)60024-1

Swain, N., Mishra, S., 2019. A review on the recovery and separation of rare earths and transition metals from secondary resources. J. Clean. Prod. 220, 884–898. https://doi.org/10.1016/j.jclepro.2019.02.094

Taggart, R.K., Hower, J.C., Hsu-Kim, H., 2018. Effects of roasting additives and leaching parameters on the extraction of rare earth elements from coal fly ash. Int. J. Coal Geol. 196, 106–114. https://doi.org/10.1016/j.coal.2018.06.021

Tang, M., Zhou, C., Pan, J., Zhang, N., Liu, C., Cao, S., Hu, T., Ji, W., 2019. Study on extraction of rare earth elements from coal fly ash through alkali fusion – Acid leaching. Miner. Eng. 136, 36–42. https://doi.org/10.1016/j.mineng.2019.01.027

Tantawy, M.A., Ali Alomari, A., 2019. Extraction of Alumina from Nawan Kaolin by Acid Leaching. Orient. J. Chem. 35, 1013–1021. https://doi.org/10.13005/ojc/350313

Taylor, S.R., McLennan, S.M., 1985. The continental crust: its composition and evolution. Blackwell Scientific Pbulications, Oxford.

Vass, C.R., Noble, A., Ziemkiewicz, P.F., 2019. The Occurrence and Concentration of Rare Earth Elements in Acid Mine Drainage and Treatment By-products: Part 1—Initial Survey of the Northern Appalachian Coal Basin. Mining, Metall. Explor. 917–

929. https://doi.org/10.1007/s42461-019-0097-z

Wang, F., Long, G., Bai, M., Wang, J., Zhou, J.L., Zhou, X., 2022. Application of electrolytic manganese residues in cement products through pozzolanic activity motivation and calcination. J. Clean. Prod. 338. https://doi.org/10.1016/J.JCLEPRO.2022.130629

Wang, L., Huang, X., Yu, Y., Zhao, L., Wang, C., Feng, Z., Cui, D., Long, Z., 2017. Towards cleaner production of rare earth elements from bastnaesite in China. J. Clean. Prod. 165, 231–242. https://doi.org/10.1016/J.JCLEPRO.2017.07.107

Wilson, J.A., 1985. Crandallite group minerals in the Helikian Athabasca group in Alberta, Canada. Can. J. Earth Sci. 22, 637–641. https://doi.org/10.1139/e85-065

Wu, W., Bian, X., Sun, S., Tu, G., 2006. Study on roasting decomposition of mixed rare earth concentrate in CaO-NaCl-CaCl2. J. Rare Earths 24, 23–27. https://doi.org/10.1016/S1002-0721(07)60313-5

Wu, W., Bian, X., Wu, Z., Sun, S., Tu, G., 2007. Reaction process of monazite and bastnaesite mixed rare earth minerals calcined by CaO-NaCl-CaCl2. Trans. Nonferrous Met. Soc. China (English Ed. 17, 864–868. https://doi.org/10.1016/S1003-6326(07)60189-7

Wuddivira, M.N., Robinson, D.A., Lebron, I., Bréchet, L., Atwell, M., Caires, S. De, Oatham, M., Jones, S.B., Abdu, H., Verma, A.K., Tuller, M., 2012. Estimation of Soil Clay Content from Hygroscopic Water Content Measurements. Soil Sci. Soc. Am. J. 76, 1529–1535. https://doi.org/10.2136/SSSAJ2012.0034

Xing, P., Zhuang, Y., Tu, G., Guo, J., 2010. High temperature dephosphorization behavior of monazite concentrate with charred coal. Trans. Nonferrous Met. Soc. China 20, 2392–2396. https://doi.org/10.1016/S1003-6326(10)60660-7

Yang, X., Honaker, R.Q., 2020. Leaching Kinetics of Rare Earth Elements from Fire Clay Seam Coal. Minerals 10. https://doi.org/10.3390/min10060491

Yang, X., Werner, J., Honaker, R.Q., 2019. Leaching of rare Earth elements from an Illinois basin coal source. J. Rare Earths 37, 312–321. https://doi.org/10.1016/j.jre.2018.07.003

Yariv, S., 2005. Differential thermal analysis (DTA) of organo-clay complexes. Therm. Anal. Geosci. 328–351. https://doi.org/10.1007/BFB0010274

Yoon, R.H., Gupta, N., Li, B., Luttrell, G., Bratton, R., Reyher, J., Suboleski, S., 2016. Hydrophobic-hydrophilic separation (hhs) process for simultaneous recovery and dewatering of fine particles, in: IMPC 2016 - 28th International Mineral Processing Congress. pp. 706–709.

Yu, X., Lang, X., Wang, Z., 2009. Extraction of rare earths from Baotou Concentrating Mill′ s tailing by MgO roasting and carbochlorination reaction. J. Chinese Rare Earth Soc. 27, 309–312.

Yuan, S., Yang, H., Xue, X.X., Zhou, Y., 2017. Kinetics of roasting decomposition of the rare earth elements by CaO and coal. Metals (Basel). 7. https://doi.org/10.3390/met7060213

Zhang, P., Han, Z., Jia, J., Wei, C., Liu, Q., Wang, X., Zhou, J., Li, F., Miao, S., 2017. Occurrence and Distribution of Gallium, Scandium, and Rare Earth Elements in Coal Gangue Collected from Junggar Basin, China, International Journal of Coal Preparation and Utilization. https://doi.org/10.1080/19392699.2017.1334645

Zhang, W., Groppo, J., Honaker, R., 2015a. Ash beneficiation for REE recovery, in: 2015 World Coal Ash Conference, Nashville, TN.

Zhang, W., Honaker, R., 2020. Characterization and recovery of rare earth elements and other critical metals (Co, Cr, Li, Mn, Sr, and V) from the calcination products of a coal refuse sample. Fuel 267, 117236. https://doi.org/10.1016/j.fuel.2020.117236

Zhang, W., Honaker, R., 2019a. Calcination pretreatment effects on acid leaching characteristics of rare earth elements from middlings and coarse refuse material associated with a bituminous coal source. Fuel 249, 130–145. https://doi.org/10.1016/j.fuel.2019.03.063

Zhang, W., Honaker, R., 2019b. Enhanced leachability of rare earth elements from calcined products of bituminous coals. Miner. Eng. 142, 105935. https://doi.org/10.1016/j.mineng.2019.105935

Zhang, W., Honaker, R., Groppo, J., 2017. Concentration of rare earth minerals from coal by froth flotation. SME Annu. Conf. Expo 2017 Creat. Value a Cyclical Environ. 34, 647–651.

Zhang, W., Noble, A., 2020. Mineralogy characterization and recovery of rare earth elements from the roof and floor materials of the Guxu coalfield. Fuel 270, 117533.

https://doi.org/10.1016/j.fuel.2020.117533

Zhang, W., Noble, A., Yang, X., Honaker, R., 2020. A Comprehensive Review of Rare Earth Elements Recovery from Coal-Related Materials. Minerals 10, 451. https://doi.org/10.3390/min10050451

Zhang, W., Rezaee, M., Bhagavatula, A., Li, Y., Groppo, J., Honaker, R., 2015b. A review of the occurrence and promising recovery methods of rare earth elements from coal and coal by-products. Int. J. Coal Prep. Util. 35, 295–330. https://doi.org/10.1080/19392699.2015.1033097

Zhang, W., Yang, X., Honaker, R.Q., 2018. Association characteristic study and preliminary recovery investigation of rare earth elements from Fire Clay seam coal middlings. Fuel 215, 551–560. https://doi.org/10.1016/j.fuel.2017.11.075

Zheng, J., Zhang, Y., Hu, T., Lv, T., Meng, C., 2018. New Strategy for the Morphology-Controlled Synthesis of V2O5 Microcrystals with Enhanced Capacitance as Battery-type Supercapacitor Electrodes. Cryst. Growth Des. 18, 5365–5376. https://doi.org/10.1021/ACS.CGD.8B00776/SUPPL_FILE/CG8B00776_SI_001.PDF

Zhou, H.M., Qiao, X.C., Yu, J.G., 2013. Influences of quartz and muscovite on the formation of mullite from kaolinite. Appl. Clay Sci. 80–81, 176–181. https://doi.org/10.1016/j.clay.2013.04.004

Zhu, G., Chi, R., Shi, W., Xu, Z., 2003. Chlorination kinetics of fluorine-fixed rare earth concentrate. Miner. Eng. 16, 671–674. https://doi.org/10.1016/S0892-6875(03)00129-8

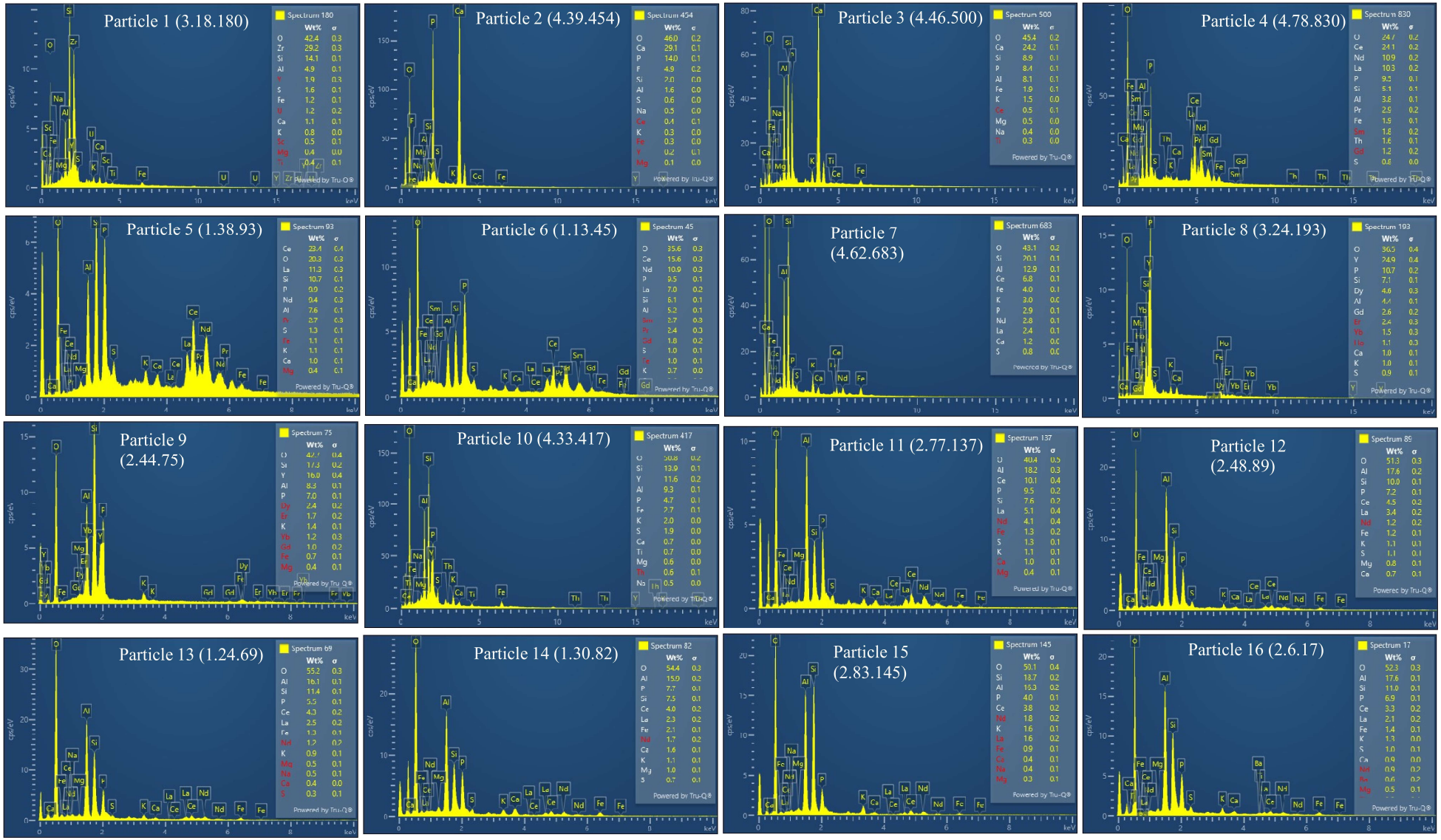
Appendices

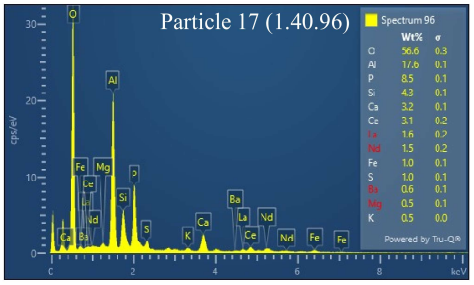
Appendix A Supporting materials for Chapter 2

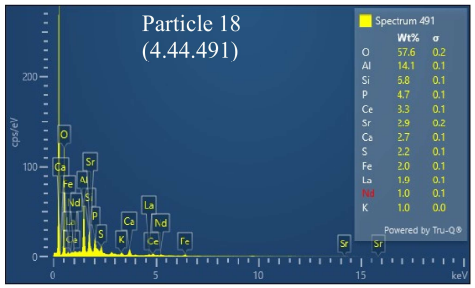
Table A.1 Elemental compositions of the particles containing REEs found from the Western Kentucky No. 13 coal waste through SEM-EDS analysis.

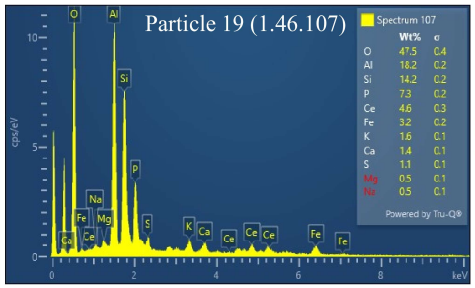
Particle #	Specimen #	Site #	Spectrum #	Mineral	Al (%)	Si (%)	O (%)	Ca (%)	P (%)	Fe (%)	K (%)	S (%)	Ba (%)	Mg (%)	Ti (%)	Na (%)	Sr (%)	F(%)	Zr (%)	Sc (%)	La (%)	Ce(%)	Pr (%)	Nd(%)	Sm (%)	Gd (%)	Y(%)	Dy (%)	Er (%)	Yb (%)	Ho (%)	Th(%)	U (%)	TREE (%	Sum (%)	Al/Si	Al/P	TREE/P
Particle 1	3	18	180	Zircon	4.9	14.1	42.4	1.1	0.0	1.2	0.8	1.6	0.0	0.4	0.4	0.2	0.0	0.0	29.2	0.5	0.0	0.0	0.0	0.0	0.0	0.0	1.9	0.0	0.0	0.0	0.0	0.0	1.2	1.9	100	0.35	NA	NA
Particle 2	4	39	454	Apatite	1.6	2.0	46.0	29.1	14.0	0.3	0.3	0.6	0.0	0.1	0.0	0.5	0.0	4.9	0.0	0.0	0.0	0.4	0.0	0.0	0.0	0.0	0.2	0.0	0.0	0.0	0.0	0.0	0.0	0.6	100	0.80	0.11	0.04
Particle 3	4	46	500	Apatite	8.1	8.9	45.4	24.2	8.4	1.9	1.5	0.0	0.0	0.5	0.3	0.4	0.0	0.0	0.0	0.0	0.0	0.5	0.0	0.0	0.0	0.0	0.0	0.0	0.0	0.0	0.0	0.0	0.0	0.5	100	0.91	0.96	0.06
Particle 4	4	78	830	Monazite	3.8	5.1	24.7	0.4	9.5	1.9	0.5	0.8	0.0	0.5	0.0	0.0	0.0	0.0	0.0	0.0	10.3	24.1	2.9	10.9	1.8	1.2	0.0	0.0	0.0	0.0	0.0	1.6	0.0	51.2	100	0.75	0.40	5.39
Particle 5	1	38	93	Monazite	7.6	10.7	20.3	1.0	9.9	1.1	1.1	1.3	0.0	0.4	0.0	0.0	0.0	0.0	0.0	0.0	11.3	23.4	2.7	9.4	0.0	0.0	0.0	0.0	0.0	0.0	0.0	0.0	0.0	46.8	100	0.71	0.77	4.73
Particle 6	1	13	45	Monazite	5.2	6.1	35.6	0.5	9.5	1.0	0.7	1.0	0.0	0.0	0.0	0.0	0.0	0.0	0.0	0.0	7.0	15.6	2.4	10.9	2.7	1.8	0.0	0.0	0.0	0.0	0.0	0.0	0.0	40.4	100	0.85	0.55	4.25
Particle 7	4	62	683	Monazite	12.9	20.1	43.1	1.2	2.9	4.0	3.0	0.8	0.0	0.0	0.0	0.0	0.0	0.0	0.0	0.0	2.4	6.8	2.8	0.0	0.0	0.0	0.0	0.0	0.0	0.0	0.0	0.0	0.0	12.0	100	0.64	4.45	4.14
Particle 8	3	24	193	Xenotime	4.4	7.1	36.5	1.0	10.7	0.8	1.0	0.9	0.0	0.5	0.0	0.0	0.0	0.0	0.0	0.0	0.0	0.0	0.0	0.0	0.0	2.6	24.9	4.6	2.4	1.5	1.1	0.0	0.0	36.0	100	0.62	0.41	3.36
Particle 9	2	44	75	Xenotime	8.3	17.3	42.7	0.0	7.0	0.7	1.4	0.0	0.0	0.4	0.0	0.0	0.0	0.0	0.0	0.0	0.0	0.0	0.0	0.0	0.0	1.0	16.0	2.4	1.7	1.2	0.0	0.0	0.0	22.3	100	0.48	1.19	3.19
Particle 10	4	33	417	Xenotime	9.3	13.9	50.8	0.7	4.7	2.7	2.0	1.9	0.0	0.6	0.7	0.5	0.0	0.0	0.0	0.0	0.0	0.0	0.0	0.0	0.0	0.0	11.6	0.0	0.0	0.0	0.0	0.6	0.0	11.6	100	0.67	1.98	2.47
Particle 11	2	77	137	Crandallite	18.2	7.6	40.4	1.0	9.5	1.3	1.1	1.3	0.0	0.4	0.0	0.0	0.0	0.0	0.0	0.0	5.1	10.1	0.0	4.1	0.0	0.0	0.0	0.0	0.0	0.0	0.0	0.0	0.0	19.3	100	2.39	1.92	2.03
Particle 12	2	48	89	Crandallite	17.6	10.0	51.3	0.7	7.2	1.2	1.1	1.1	0.0	0.8	0.0	0.0	0.0	0.0	0.0	0.0	3.4	4.5	0.0	1.2	0.0	0.0	0.0	0.0	0.0	0.0	0.0	0.0	0.0	9.1	100	1.76	2.44	1.26
Particle 13	1	24	69	Crandallite	16.1	11.4	55.2	0.4	5.5	1.3	0.9	0.3	0.0	0.5	0.0	0.5	0.0	0.0	0.0	0.0	2.5	4.3	0.0	1.2	0.0	0.0	0.0	0.0	0.0	0.0	0.0	0.0	0.0	8.0	100	1.41	2.93	1.45
Particle 14	1	30	82	Crandallite	15.9	7.5	54.4	1.6	7.7	2.1	1.1	0.7	0.0	1.0	0.0	0.0	0.0	0.0	0.0	0.0	2.3	4.0	0.0	1.7	0.0	0.0	0.0	0.0	0.0	0.0	0.0	0.0	0.0	8.0	100	2.12	2.06	1.04
Particle 15	2	83	145	Crandallite	16.3	18.7	50.1	0.4	4.0	0.9	1.6	0.0	0.0	0.3	0.0	0.4	0.0	0.0	0.0	0.0	1.6	3.8	0.0	1.8	0.0	0.0	0.0	0.0	0.0	0.0	0.0	0.0	0.0	7.2	100	0.87	4.08	1.80
Particle 16	2	6	17	Crandallite	17.8	9.8	52.4	0.8	7.3	1.6	1.2	1.1	0.6	0.5	0.3	0.0	0.0	0.0	0.0	0.0	2.1	3.5	0.0	1.0	0.0	0.0	0.0	0.0	0.0	0.0	0.0	0.0	0.0	6.6	100	1.82	2.44	0.90
Particle 17	1	40	96	Crandallite	17.6	4.3	56.6	3.2	8.5	1.0	0.5	1.0	0.6	0.5	0.0	0.0	0.0	0.0	0.0	0.0	1.6	3.1	0.0	1.5	0.0	0.0	0.0	0.0	0.0	0.0	0.0	0.0	0.0	6.2	100	4.09	2.07	0.73
Particle 18	4	44	491	Crandallite	14.1	6.8	57.6	2.7	4.7	2.0	1.0	2.2	0.0	0.0	0.0	0.0	2.9	0.0	0.0	0.0	1.9	3.3	0.0	1.0	0.0	0.0	0.0	0.0	0.0	0.0	0.0	0.0	0.0	6.2	100	2.07	3.00	1.32
Particle 19	1	46	107	Crandallite	18.2	14.2	47.5	1.4	7.3	3.2	1.6	1.1	0.0	0.5	0.0	0.5	0.0	0.0	0.0	0.0	0.0	4.6	0.0	0.0	0.0	0.0	0.0	0.0	0.0	0.0	0.0	0.0	0.0	4.6	100	1.28	2.49	0.63
Particle 20	4	13	285	Crandallite	18.9	13.0	34.4	1.7	6.1	6.5	2.0	3.3	2.8	0.5	0.0	0.4	5.9	0.0	0.0	0.0	0.0	3.1	1.4	0.0	0.0	0.0	0.0	0.0	0.0	0.0	0.0	0.0	0.0	4.5	100	1.45	3.10	0.74
Particle 21	2	15	33	Crandallite	18.7	16.3	48.8	1.7	4.0	2.4	1.9	0.8	0.0	0.5	0.5	0.5	0.0	0.0	0.0	0.0	1.5	2.5	0.0	0.0	0.0	0.0	0.0	0.0	0.0	0.0	0.0	0.0	0.0	4.0	100	1.15	4.68	1.00
Particle 22	4	60	648	Crandallite	13.6	21.6	51.8	0.3	2.3	1.9	1.5	1.3	0.0	0.5	0.3	0.0	2.0	0.0	0.0	0.0	0.7	1.5	0.0	0.6	0.0	0.0	0.0	0.0	0.0	0.0	0.0	0.0	0.0	2.8	100	0.63	5.91	1.22
Particle 23	4	7	261	Crandallite	18.5	19.5	37.1	1.7	2.9	5.0	2.6	1.4	2.5	0.9	1.0	0.4	3.9	0.0	0.0	0.0	0.7	1.5	0.0	0.5	0.0	0.0	0.0	0.0	0.0	0.0	0.0	0.0	0.0	2.7	100	0.95	6.38	0.93
Particle 24	4	49	526	Crandallite	14.6	18.4	50.5	0.7	2.4	3.0	2.4	1.0	0.4	0.8	0.2	0.4	2.6	0.0	0.0	0.0	1.0	1.3	0.0	0.3	0.0	0.0	0.0	0.0	0.0	0.0	0.0	0.0	0.0	2.6	100	0.79	6.08	1.08
Particle 25	4	9	265	Crandallite	16.9	10.5	50.4	1.0	6.6	1.7	1.6	0.8	1.6	0.4	0.0	0.3	5.7	0.0	0.0	0.0	0.0	2.4	0.0	0.0	0.0	0.0	0.0	0.0	0.0	0.0	0.0	0.0	0.0	2.4	100	1.61	2.56	0.36
Particle 26	1	6	15	Crandallite	16.5	8.0	57.4	3.7	7.9	1.4	0.9	1.4	0.0	0.3	0.0	0.3	0.0	0.0	0.0	0.0	0.0	1.6	0.0	0.7	0.0	0.0	0.0	0.0	0.0	0.0	0.0	0.0	0.0	2.3	100	2.06	2.09	0.29
Particle 27	2	2	1	Crandallite	17.9	16.1	51.2	0.6	4.1	2.5	1.8	2.1	0.0	0.6	0.6	0.3	0.0	0.0	0.0	0.0	0.0	2.1	0.0	0.0	0.0	0.0	0.0	0.0	0.0	0.0	0.0	0.0	0.0	2.1	100	1.11	4.37	0.51
Particle 28	1	16	49	Crandallite	16.2	13.8	54.2	0.8	6.4	1.8	1.4	1.3	1.6	0.5	0.0	0.0	0.0	0.0	0.0	0.0	0.0	1.9	0.0	0.0	0.0	0.0	0.0	0.0	0.0	0.0	0.0	0.0	0.0	1.9	100	1.17	2.53	0.30
Particle 29	1	7	16	Crandallite	16.2	6.4	57.1	1.8	6.0	4.0	0.7	4.6	1.5	0.0	0.0	0.0	0.0	0.0	0.0	0.0	0.0	0.9	0.0	0.9	0.0	0.0	0.0	0.0	0.0	0.0	0.0	0.0	0.0	1.8	100	2.53	2.70	0.30
Particle 30	4	5	246	Crandallite	13.1	12.5	52.3	1.6	4.1	6.3	1.0	0.0	0.0	3.7	0.1	0.0	3.3	0.0	0.0	0.0	0.5	1.3	0.0	0.0	0.0	0.0	0.0	0.0	0.0	0.0	0.0	0.0	0.0	1.8	100	1.05	3.20	0.44
Particle 31	3	9	166	Crandallite	14.7	11.6	53.4	1.0	5.7	2.2	1.0	1.6	1.5	0.4	0.0	0.4	11.6	0.0	0.0	0.0	0.0	1.8	0.0	0.0	0.0	0.0	0.0	0.0	0.0	0.0	0.0	0.0	0.0	1.8	107	1.27	2.58	0.32
Particle 32	1	18	55	Crandallite	10.4	17.5	55.3	1.1	2.0	7.0	1.9	2.2	0.0	1.0	0.0	0.0	0.0	0.0	0.0	0.0	0.6	0.8	0.0	0.4	0.0	0.0	0.0	0.0	0.0	0.0	0.0	0.0	0.0	1.8	100	0.59	5.20	0.90
Particle 33	4	74	805	Crandallite	18.4	21.3	46.9	0.7	1.9	2.4	2.8	1.0	1.0	0.7	0.3	0.9	0.0	0.0	0.0	0.0	0.5	0.9	0.0	0.3	0.0	0.0	0.0	0.0	0.0	0.0	0.0	0.0	0.0	1.7	100	0.86	9.68	0.89
Particle 34	4	29	396	Crandallite	13.4	10.8	50.7	2.3	4.9	2.9	1.7	3.3	0.9	0.7	0.3	0.9	5.6	0.0	0.0	0.0	0.0	0.9	0.0	0.6	0.0	0.0	0.0	0.0	0.0	0.0	0.0	0.0	0.0	1.5	100	1.24	2.73	0.31
Particle 35	4	37	445	Crandallite	16.9	7.9	44.8	2.4	7.2	3.2	1.0	3.6	2.1	0.4	0.0	0.0	8.9	0.0	0.0	0.0	0.0	0.9	0.0	0.6	0.0	0.0	0.0	0.0	0.0	0.0	0.0	0.0	0.0	1.5	100	2.14	2.35	0.21
Particle 36	4	49	530	Crandallite	13.3	25.3	50.6	0.6	1.4	2.5	2.4	1.6	0.0	0.7	0.3	0.0	0.0	0.0	0.0	0.0	0.3	0.6	0.0	0.3	0.0	0.0	0.0	0.0	0.0	0.0	0.0	0.0	0.0	1.2	100	0.53	9.50	0.86
Particle 37	4	10	273	Crandallite	20.4	22.7	47.0	0.6	1.6	2.1	1.9	1.1	0.0	0.6	0.5	0.4	0.0	0.0	0.0	0.0	0.0	0.7	0.4	0.0	0.0	0.0	0.0	0.0	0.0	0.0	0.0	0.0	0.0	1.1	100	0.90	12.75	0.69
Particle 38	4	42	477	Crandallite	17.4	22.3	48.3	0.0	1.9	2.2	5.8	0.0	0.0	0.8	0.0	0.2	0.0	0.0	0.0	0.0	0.0	0.8	0.0	0.3	0.0	0.0	0.0	0.0	0.0	0.0	0.0	0.0	0.0	1.1	100	0.78	9.16	0.58
Particle 39	4	70	760	Crandallite	16.5	18.5	53.8	0.4	2.4	1.7	1.1	0.8	0.8	0.4	0.0	0.3	2.4	0.0	0.0	0.0	0.0	1.0	0.0	0.0	0.0	0.0	0.0	0.0	0.0	0.0	0.0	0.0	0.0	1.0	100	0.89	6.88	0.42
Particle 40	3	32	213	Crandallite	15.8	15.6	50.3	0.7	4.8	1.5	1.8	1.3	0.9	0.6	0.0	0.0	5.6	0.0	0.0	0.0	0.0	1.0	0.0	0.0	0.0	0.0	0.0	0.0	0.0	0.0	0.0	0.0	0.0	1.0	100	1.01	3.29	0.21
Particle 41	1	59	187	Crandallite	16.0	13.7	56.4	0.7	4.3	2.3	2.1	2.6	0.0	0.4	0.0	0.5	0.0	0.0	0.0	0.0	0.0	0.9	0.0	0.0	0.0	0.0	0.0	0.0	0.0	0.0	0.0	0.0	0.0	0.9	100	1.17	3.72	0.21
Particle 42	4	58	629	Crandallite	13.5	21.3	55.4	0.4	2.7	1.2	1.4	0.2	0.0	0.3	0.0	0.0	2.8	0.0	0.0	0.0	0.0	0.6	0.0	0.2	0.0	0.0	0.0	0.0	0.0	0.0	0.0	0.0	0.0	0.8	100	0.63	5.00	0.30
Particle 43	4	76	815	Crandallite	15.5	16.0	41.0	2.3	6.0	3.4	1.3	2.2	3.7	0.5	0.2	1.4	5.8	0.0	0.0	0.0	0.0	0.5	0.0	0.3	0.0	0.0	0.0	0.0	0.0	0.0	0.0	0.0	0.0	0.8	100	0.97	2.58	0.13
Particle 44	4	46	503	Crandallite	16.3	13.8	45.5	2.6	4.7	3.8	2.1	2.0	1.6	0.5	0.7	0.0	5.7	0.0	0.0	0.0	0.0	0.6	0.0	0.0	0.0	0.0	0.0	0.0	0.0	0.0	0.0	0.0	0.0	0.6	100	1.18	3.47	0.13
Particle 45	1	34	88	Crandallite	17.1	6.5	50.8	0.8	5.5	1.5	1.1	4.8	0.9	0.3	0.0	0.2	10.0	0.0	0.0	0.0	0.0	0.5	0.0	0.0	0.0	0.0	0.0	0.0	0.0	0.0	0.0	0.0	0.0	0.5	100	2.63	3.11	0.09
Particle 46	1	31	83	Crandallite	12.0	11.1	58.6	4.6	1.9	1.3	0.9	5.1	0.4	0.4	1.9	1.5	0.0	0.0	0.0	0.0	0.0	0.3	0.0	0.0	0.0	0.0	0.0	0.0	0.0	0.0	0.0	0.0	0.0	0.3	100	1.08	6.32	0.16
Particle 47	4	36	438	Crandallite	16.5	6.3	53.1	0.7	5.0	1.0	0.9	4.6	0.8	0.0	0.0	0.0	10.6	0.0	0.0	0.0	0.0	0.3	0.0	0.0	0.0	0.0	0.0	0.0	0.0	0.0	0.0	0.0	0.0	0.3	100	2.62	3.30	0.06
Particle 48	4	17	307	Crandallite	19.4	21.5	43.7	0.5	1.6	2.3	2.4	2.2	0.5	0.7	0.3	0.4	4.1	0.0	0.0	0.0	0.0	0.2	0.0	0.0	0.0	0.0	0.0	0.0	0.0	0.0	0.0	0.0	0.0	0.2	100	0.90	12.13	0.13
Particle 49	4	18	316	Crandallite	18.7	20.0	52.5	0.3	1.1	1.4	2.9	1.6	0.4	0.4	0.2	0.3	0.0	0.0	0.0	0.0	0.0	0.1	0.0	0.0	0.0	0.0	0.0	0.0	0.0	0.0	0.0	0.0	0.0	0.1	100	0.94	17.00	0.09

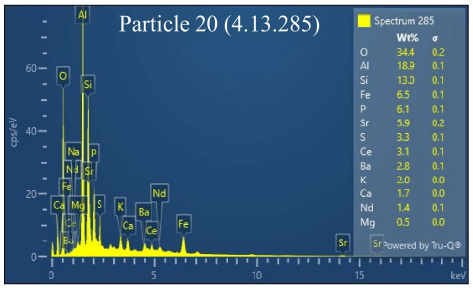
Figure A.1 EDS spectra of the particles containing REEs found from the Western Kentucky No. 13 (WK No. 13) coal waste. (The spectra are labelled as Particle # (Specimen #. Site #. Spectrum #))

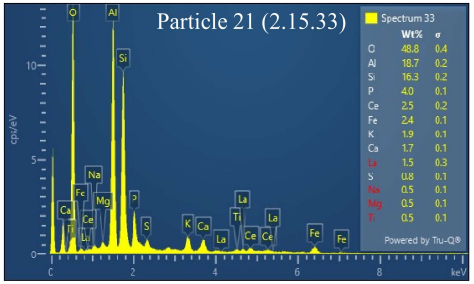


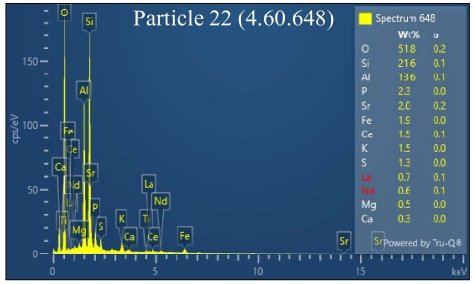

Particle 17 (1.40.96)
Spectrum 96
Wt% σ
O 56.6 0.3
Al 17.6 0.1
P 8.5 0.1
Si 4.3 0.1
Ca 3.2 0.1
Ce 3.1 0.2
La 1.6 0.2
Nd 1.5 0.2
Fe 1.0 0.1
S 1.0 0.1
Ba 0.6 0.1
Mg 0.5 0.1
K 0.5 0.0
Powered by Tru-Q®
cps/eV
keV

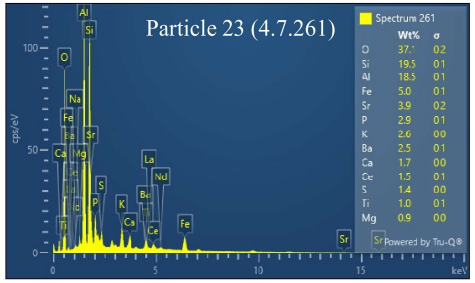

Particle 18
(4.44.491)
Spectrum 491
Wt% σ
O 57.6 0.2
Al 14.1 0.1
Si 5.8 0.1
P 4.7 0.1
Ce 3.3 0.1
Sr 2.9 0.2
Ca 2.7 0.1
S 2.2 0.1
Fe 2.0 0.1
La 1.9 0.1
Nd 1.0 0.1
K 1.0 0.0
Powered by Tru-Q®
cps/eV
keV

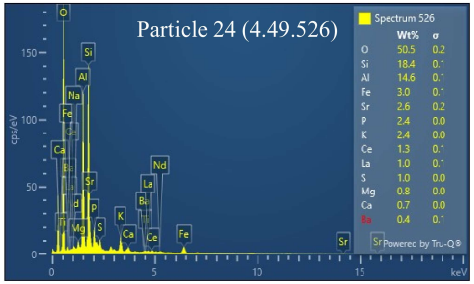

Particle 19 (1.46.107)
Spectrum 107
Wt% σ
O 47.5 0.4
Al 18.2 0.2
Si 14.2 0.2
P 7.3 0.2
Ce 4.6 0.3
Fe 3.2 0.2
K 1.6 0.1
Ca 1.4 0.1
S 1.1 0.1
Mg 0.5 0.1
Na 0.5 0.1
Powered by Tru-Q®
cps/eV
keV

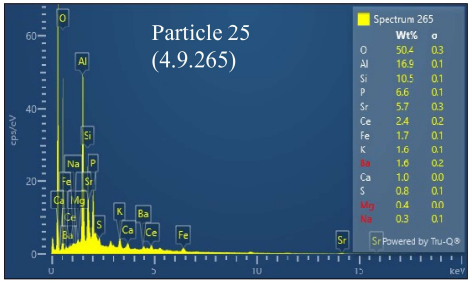

Particle 20 (4.13.285)
Spectrum 285
Wt% σ
O 34.4 0.2
Al 18.9 0.1
Si 13.0 0.1
Fe 6.5 0.1
P 6.1 0.1
Sr 5.9 0.2
S 3.3 0.1
Ce 3.1 0.1
Ba 2.8 0.1
K 2.0 0.0
Ca 1.7 0.0
Nd 1.4 0.1
Mg 0.5 0.0
Powered by Tru-Q®
cps/eV
keV

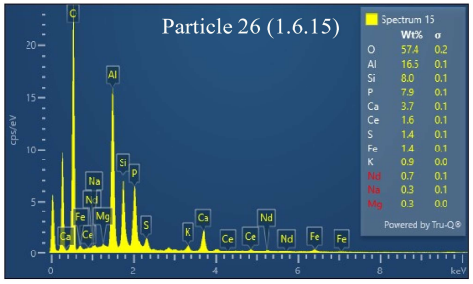

Particle 21 (2.15.33)
Spectrum 33
Wt% σ
O 48.8 0.4
Al 18.7 0.2
Si 16.3 0.2
P 4.0 0.1
Ce 2.5 0.2
Fe 2.4 0.1
K 1.9 0.1
Ca 1.7 0.1
La 1.5 0.3
S 0.8 0.1
Na 0.5 0.1
Mg 0.5 0.1
Ti 0.5 0.1
Powered by Tru-Q®
cps/eV
keV

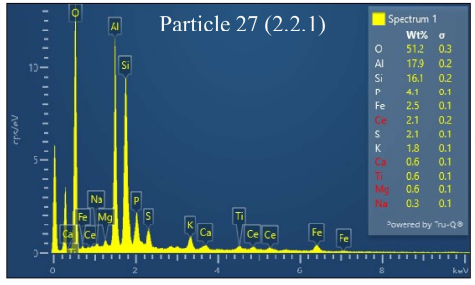

Particle 22 (4.60.648)
Spectrum 648
Wt% σ
O 51.8 0.2
Si 21.6 0.1
Al 13.6 0.1
P 2.3 0.0
Sr 2.0 0.2
Fe 1.5 0.0
Ce 1.5 0.1
K 1.5 0.0
S 1.3 0.0
La 0.7 0.1
Na 0.6 0.1
Mg 0.5 0.0
Ca 0.3 0.0
Powered by Tru-Q®
cps/eV
keV

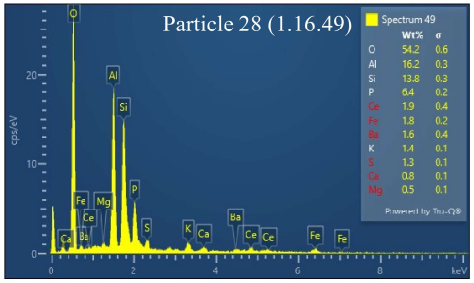

Particle 23 (4.7.261)
Spectrum 261
Wt% σ
O 37.1 0.2
Si 19.5 0.1
Al 18.5 0.1
Fe 5.0 0.1
Sr 3.9 0.2
P 2.9 0.1
K 2.6 0.0
Ba 2.5 0.1
Ca 1.7 0.0
Ce 1.5 0.1
S 1.4 0.0
Ti 1.0 0.1
Mg 0.9 0.0
Powered by Tru-Q®
cps/eV
keV

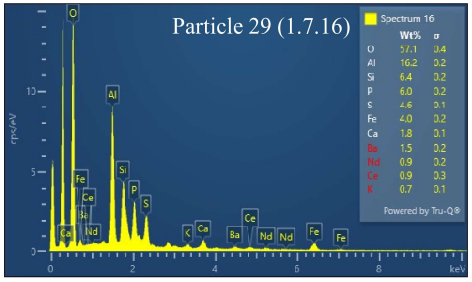

Particle 24 (4.49.526)
Spectrum 526
Wt% σ
O 50.5 0.2
Si 18.4 0.1
Al 14.6 0.1
Fe 3.0 0.1
Sr 2.6 0.2
P 2.4 0.0
K 2.4 0.0
Ce 1.3 0.1
La 1.0 0.1
S 1.0 0.0
Mg 0.8 0.0
Ca 0.7 0.0
Ba 0.4 0.1
Powered by Tru-Q®
cps/eV
keV

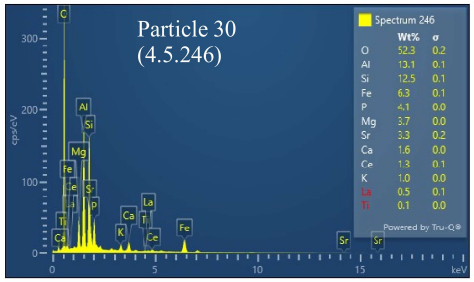

Particle 25
(4.9.265)
Spectrum 265
Wt% σ
O 50.4 0.3
Al 16.9 0.1
Si 10.5 0.1
P 6.6 0.1
Sr 5.7 0.3
Ce 2.4 0.2
Fe 1.7 0.1
K 1.6 0.1
Ba 1.6 0.2
Ca 1.0 0.0
S 0.8 0.1
Mg 0.4 0.0
Na 0.3 0.1
Powered by Tru-Q®
cps/eV
keV

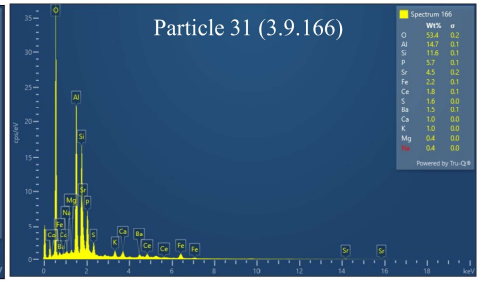

Particle 26 (1.6.15)
Spectrum 15
Wt% σ
O 57.4 0.2
Al 16.3 0.1
Si 8.0 0.1
P 7.9 0.1
Ca 3.7 0.1
Ce 1.6 0.1
S 1.4 0.1
Fe 1.4 0.1
K 0.9 0.0
Nd 0.7 0.1
Na 0.3 0.1
Mg 0.3 0.0
Powered by Tru-Q®
cps/eV
keV

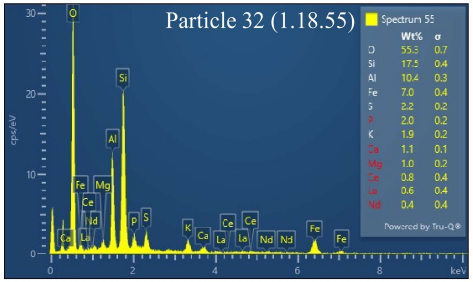

Particle 27 (2.2.1)
Spectrum 1
Wt% σ
O 51.2 0.3
Al 17.9 0.2
Si 16.1 0.2
P 4.1 0.1
Fe 2.5 0.1
Ce 2.1 0.2
S 2.1 0.1
K 1.8 0.1
Ca 0.6 0.1
Ti 0.6 0.1
Mg 0.6 0.1
Na 0.3 0.1
Powered by Tru-Q®
cps/eV
keV

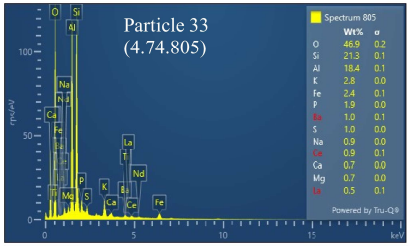

Particle 28 (1.16.49)
Spectrum 49
Wt% σ
O 54.2 0.6
Al 16.2 0.3
Si 13.8 0.3
P 6.4 0.2
Ce 1.9 0.4
Fe 1.8 0.2
Ba 1.6 0.4
K 1.4 0.1
S 1.3 0.1
Ca 0.8 0.1
Mg 0.5 0.1
Powered by Tru-Q®
cps/eV
keV

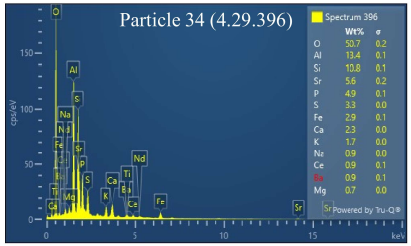

Particle 29 (1.7.16)
Spectrum 16
Wt% σ
O 57.1 0.4
Al 16.2 0.2
Si 6.4 0.2
P 6.0 0.2
S 4.6 0.1
Fe 4.0 0.2
Ca 1.8 0.1
Ba 1.5 0.2
Nd 0.9 0.2
Ce 0.9 0.3
K 0.7 0.1
Powered by Tru-Q®
cps/eV
keV

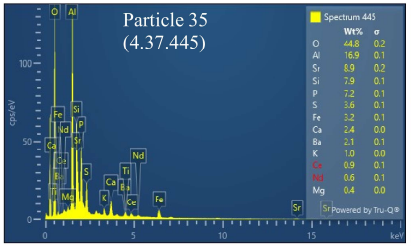

Particle 30
(4.5.246)
Spectrum 246
Wt% σ
O 52.3 0.2
Al 13.1 0.1
Si 12.5 0.1
Fe 6.3 0.1
P 4.1 0.0
Mg 3.7 0.0
Sr 3.3 0.2
Ca 1.6 0.0
Ce 1.3 0.1
K 1.0 0.0
La 0.5 0.1
Ti 0.1 0.0
Powered by Tru-Q®
cps/eV
keV

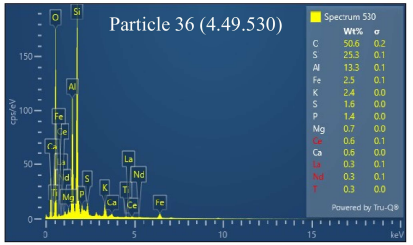

Particle 31 (3.9.166)
Spectrum 166
Wt% σ
O 53.4 0.2
Al 14.7 0.1
Si 11.6 0.1
P 5.7 0.1
Sr 4.5 0.2
Fe 2.2 0.1
Ce 1.8 0.1
S 1.6 0.0
Ba 1.5 0.1
Ca 1.0 0.0
K 1.0 0.0
Mg 0.4 0.0
Nd 0.4 0.0
Powered by Tru-Q®
cps/eV
keV

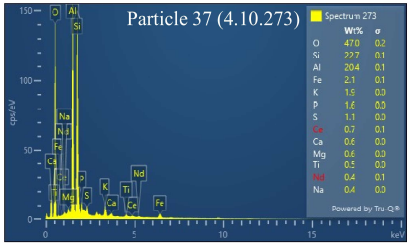

Particle 32 (1.18.55)
Spectrum 55
Wt% σ
O 55.3 0.7
Si 17.5 0.4
Al 10.4 0.3
Fe 7.0 0.4
S 2.2 0.2
Ca 2.0 0.2
K 1.9 0.2
La 1.1 0.1
Mg 1.0 0.2
Ce 0.8 0.4
Ba 0.6 0.4
Nd 0.4 0.4
Powered by Tru-Q®
cps/eV
keV

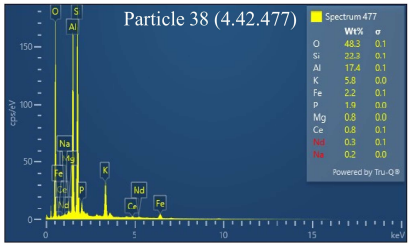

Particle 33
(4.74.805)

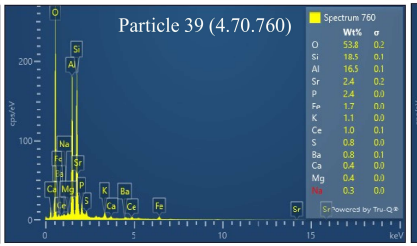

Particle 34 (4.29.396)

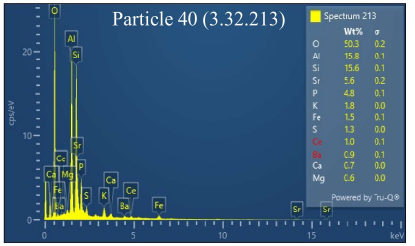

Particle 35
(4.37.445)

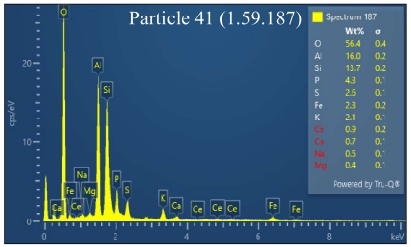

Particle 36 (4.49.530)

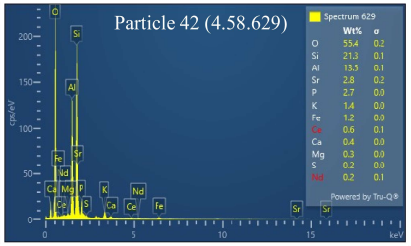

Particle 37 (4.10.273)

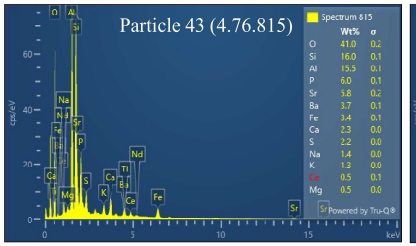

Particle 38 (4.42.477)

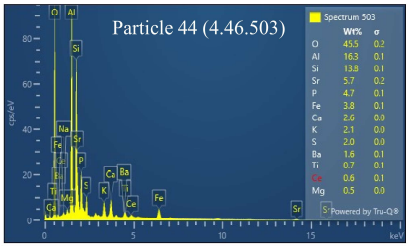

Particle 39 (4.70.760)

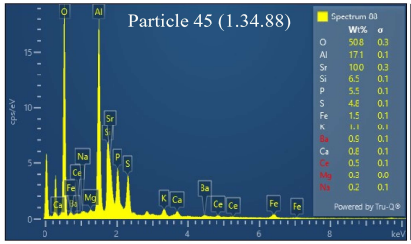

Particle 40 (3.32.213)

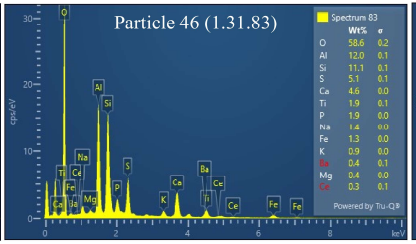

Particle 41 (1.59.187)

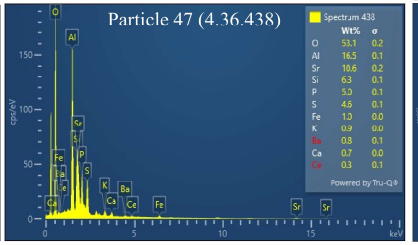

Particle 42 (4.58.629)

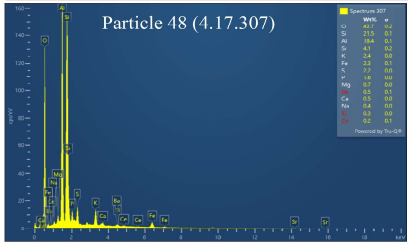

Particle 43 (4.76.815)


Particle 44 (4.46.503)


Particle 45 (1.34.88)


Particle 46 (1.31.83)


Particle 47 (4.36.438)


Particle 48 (4.17.307)

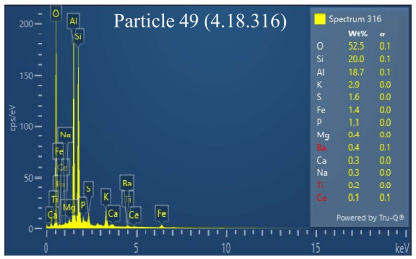
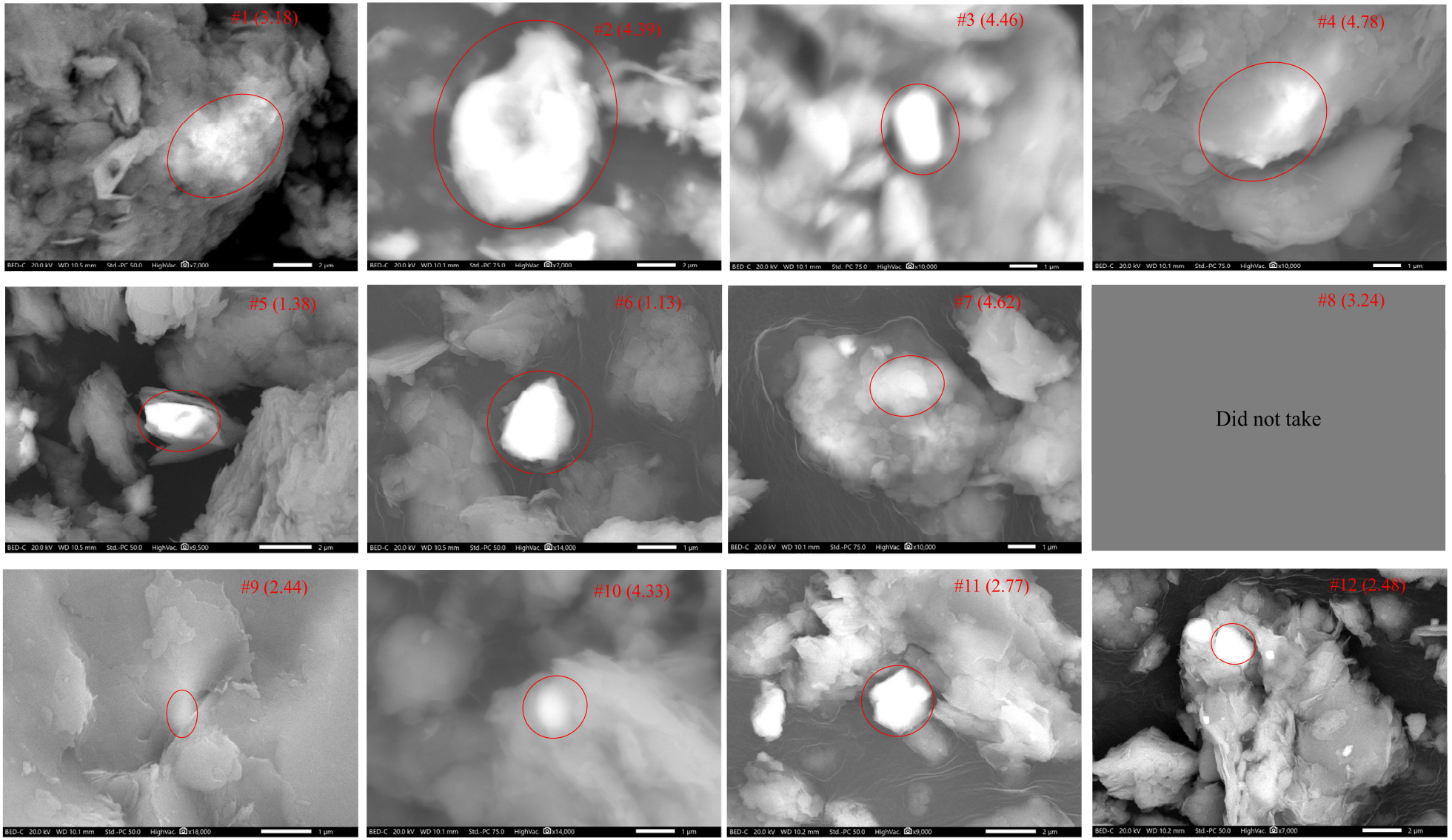
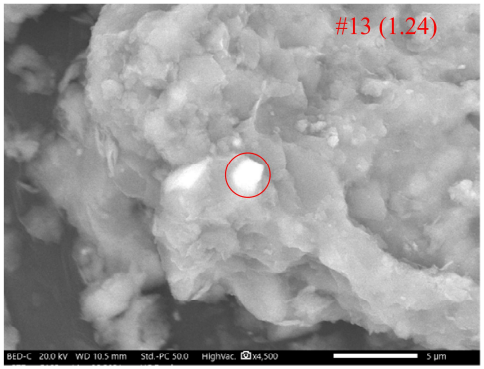
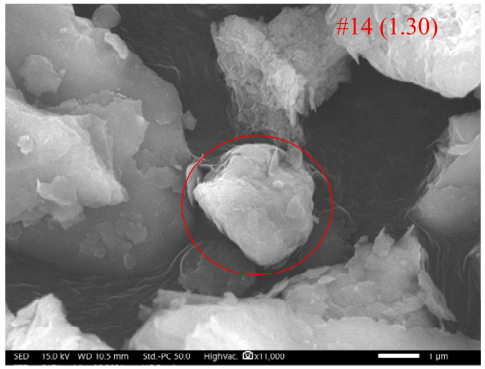
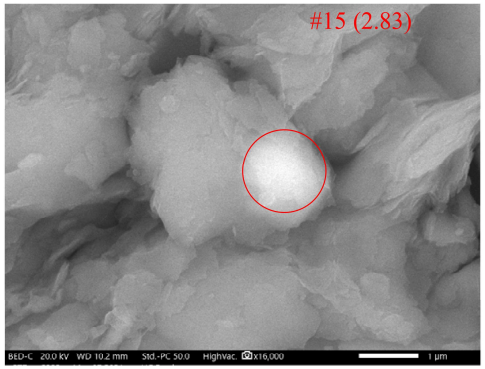

Particle 49 (4.18.316)

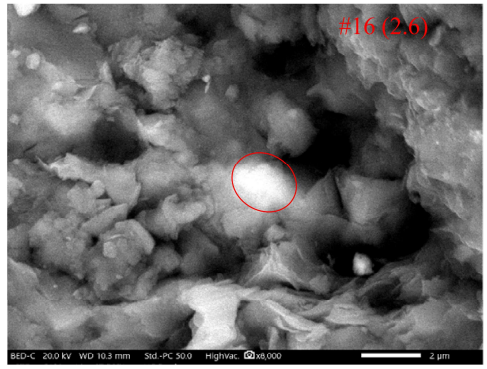
Figure A.2 SEM images of the particles containing REEs found from the Western Kentucky No. 13 (WK No. 13) coal waste. (The images are labelled as # Particle (Specimen #. Site #))



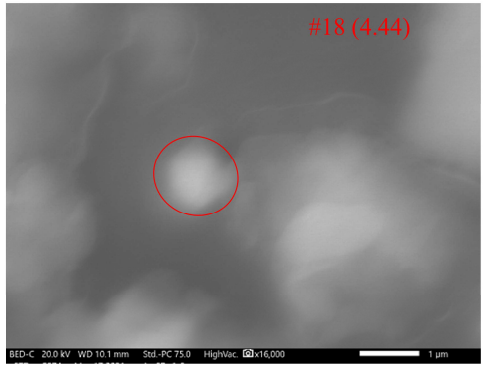

#13 (1.24)


#14 (1.30)


#15 (2.83)

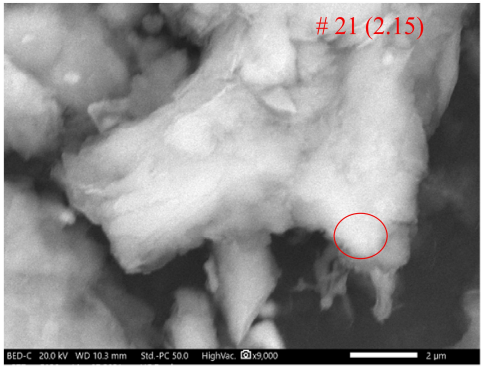

#16 (2.6)


#17 (1.40)


#18 (4.44)

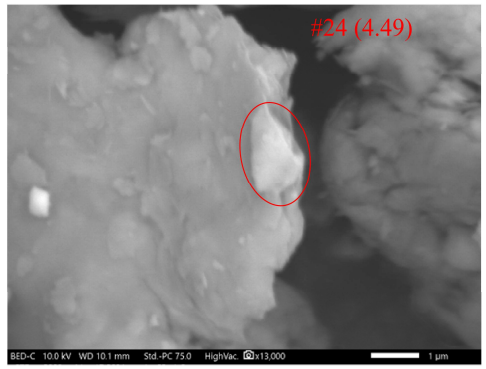

#19 (1.46)

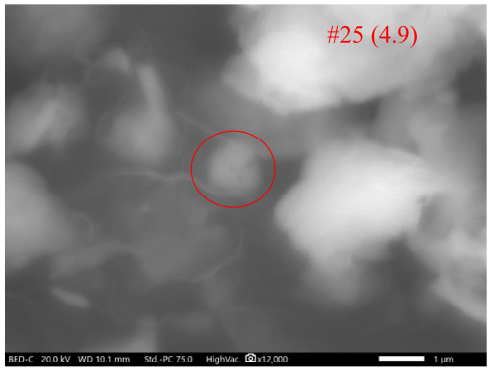

#20 (4.13)

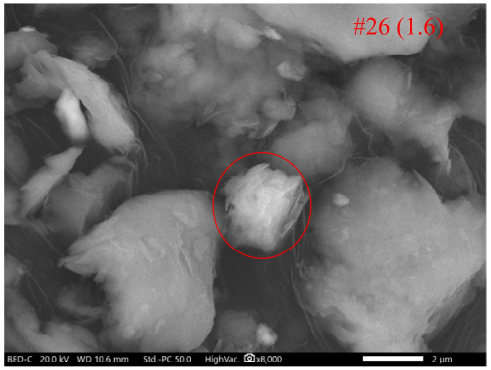

21 (2.15)

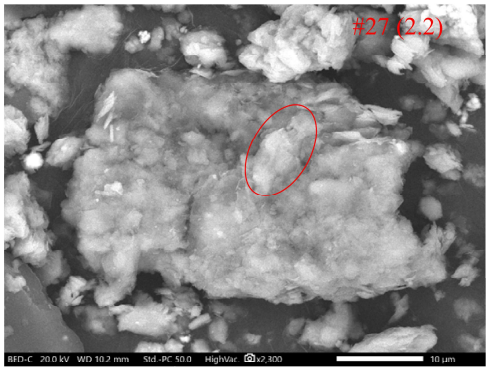

#22 (4.60)

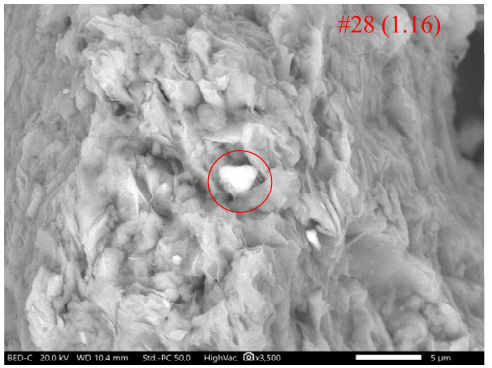

#23 (4.7)


#24 (4.49)


#25 (4.9)

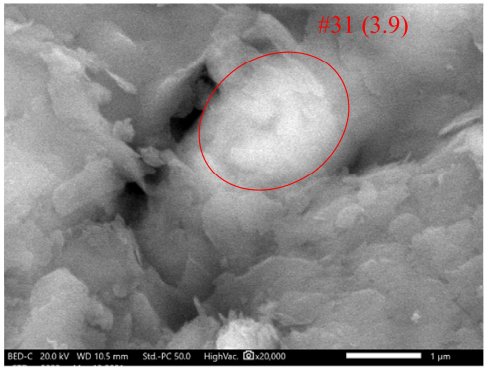

#26 (1.6)

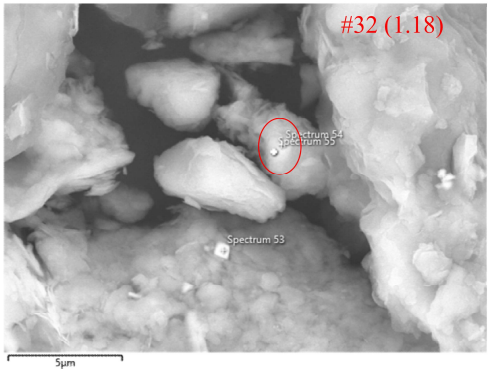

#27 (2.2)

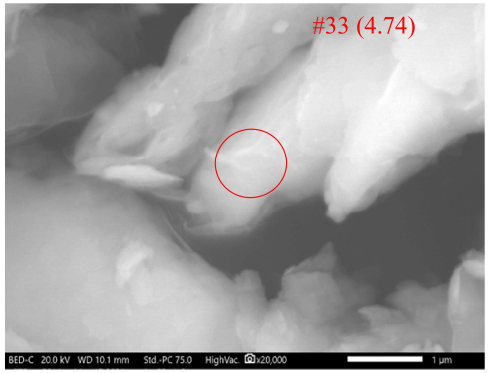

#28 (1.16)

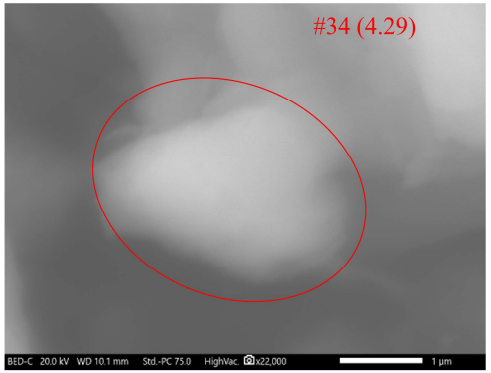

#29 (1.7)

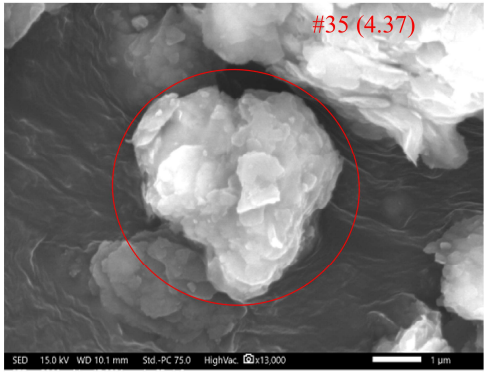

#30 (4.5)

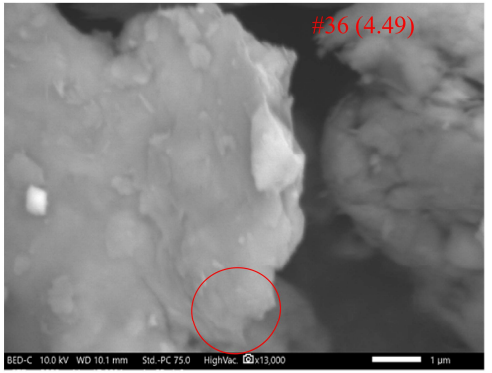

#31 (3.9)

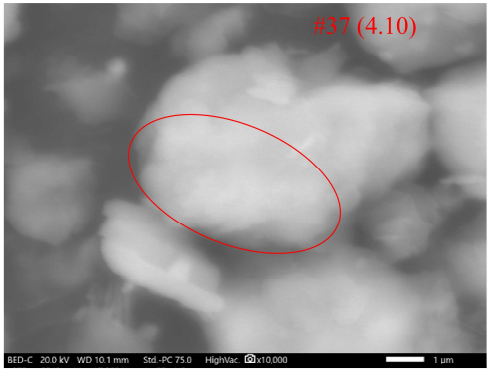

#32 (1.18)
Spectrum 54
Spectrum 55
Spectrum 53
5µm

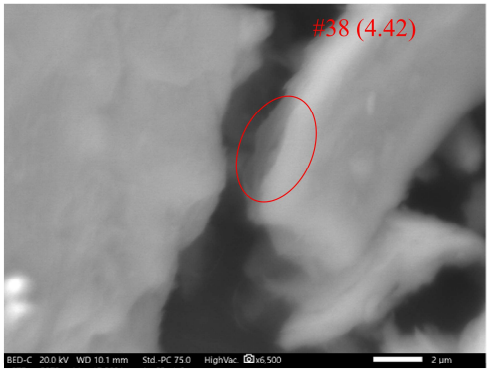

#33 (4.74)

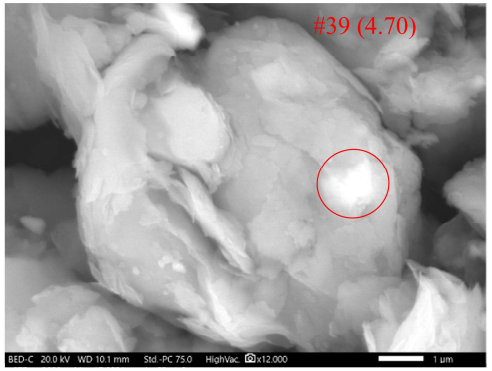

#34 (4.29)

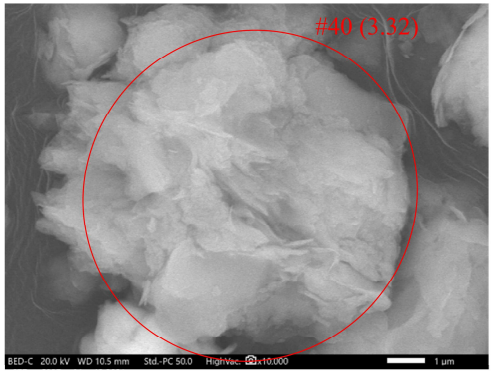

#35 (4.37)

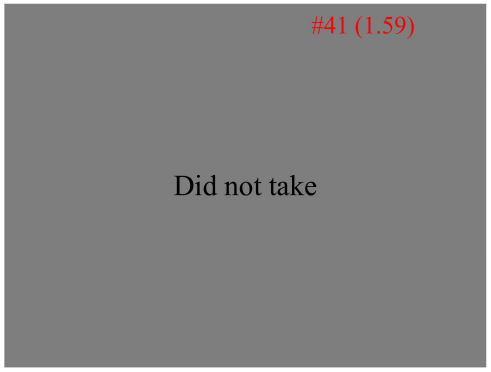

#36 (4.49)


#37 (4.10)

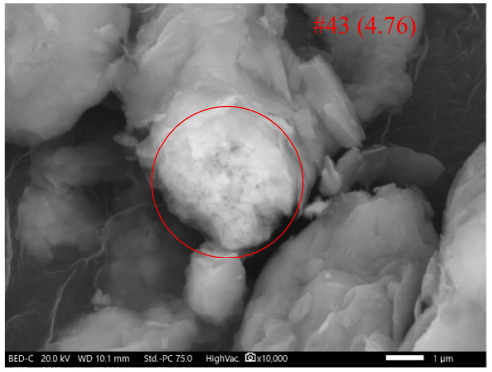

#38 (4.42)

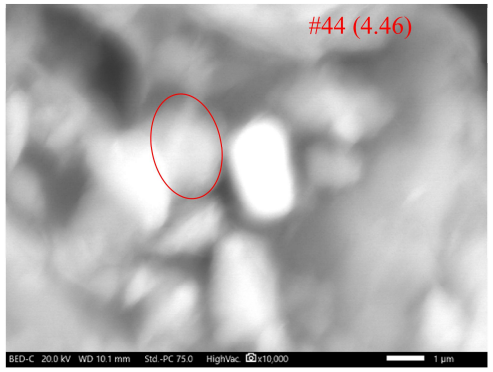

#39 (4.70)

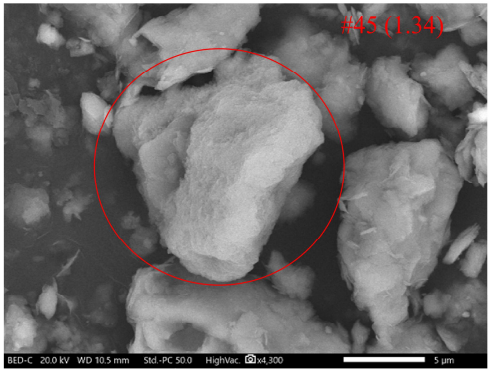

#40 (3.32)

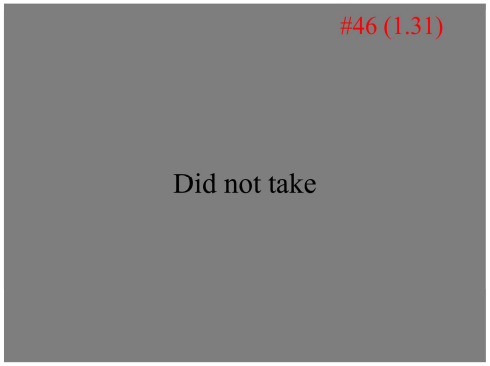

#41 (1.59)
Did not take

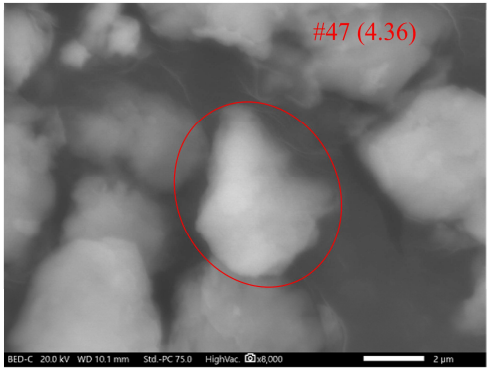

#42 (4.58)


#43 (4.76)


#44 (4.46)


#45 (1.34)


#46 (1.31)
Did not take


#47 (4.36)


#48 (4.17)

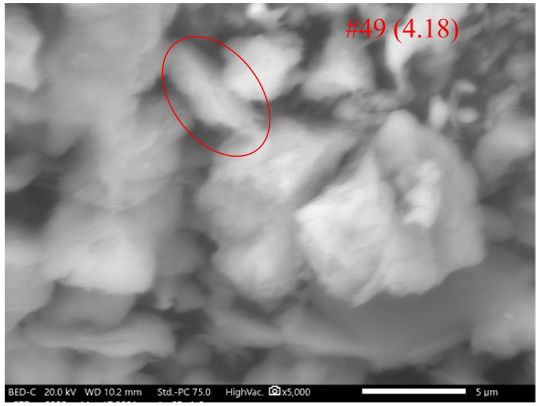
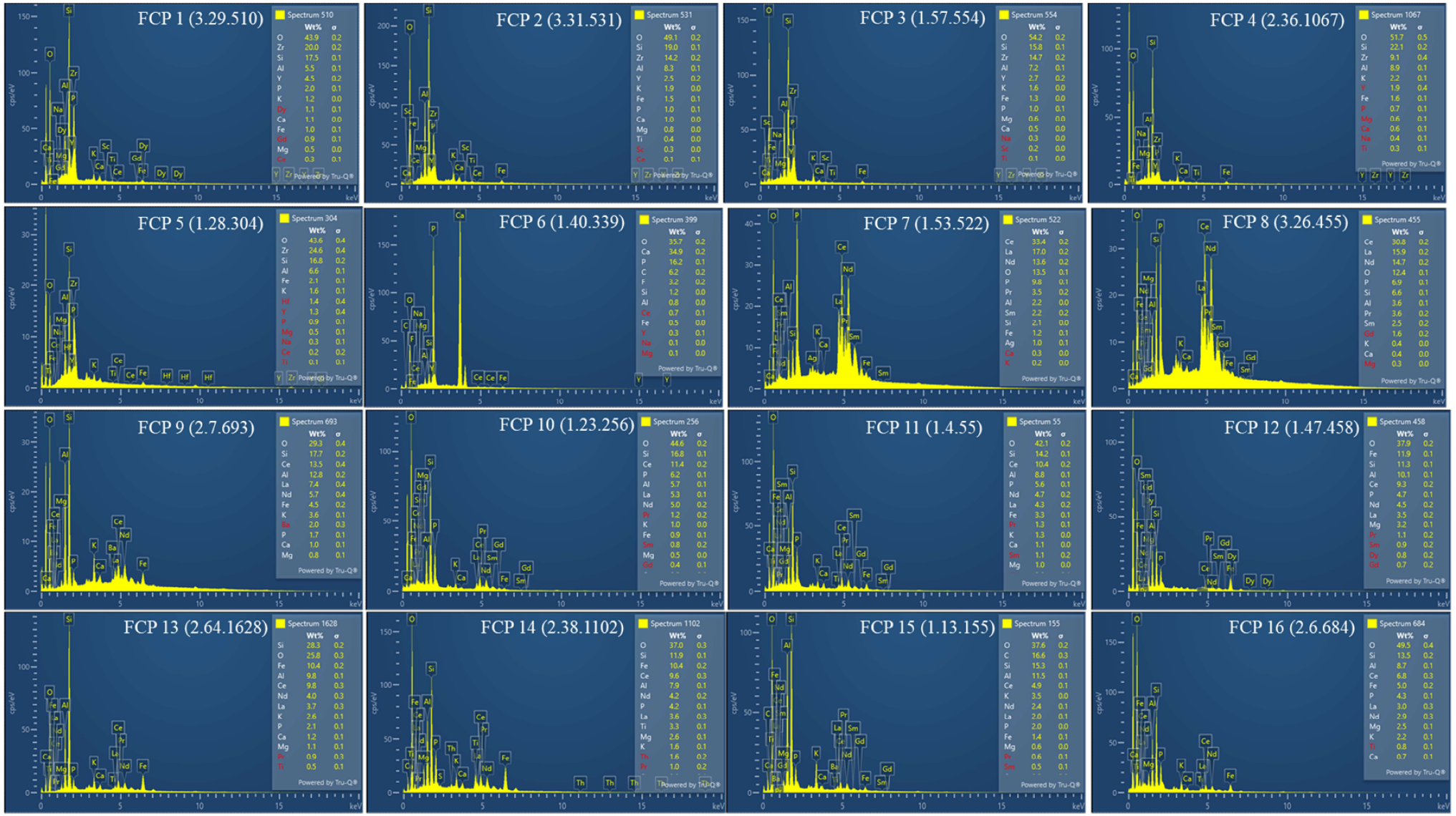
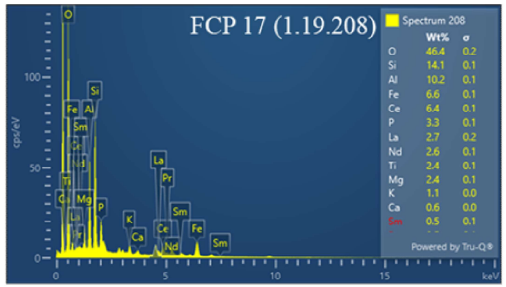

#49 (4.18)
BED-C 20.0 kV WD 10.2 mm Std.-PC 75.0 HighVac. x5,000 5 µm

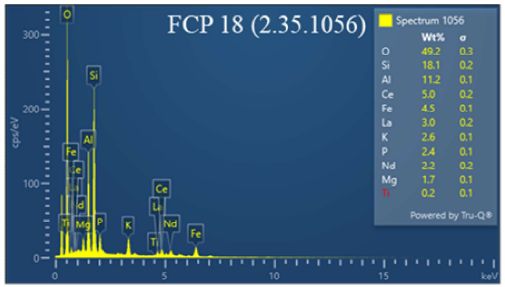
Table A.2 Elemental compositions of the particles containing REEs found from the Fire Clay coal waste through SEM-EDS analysis.

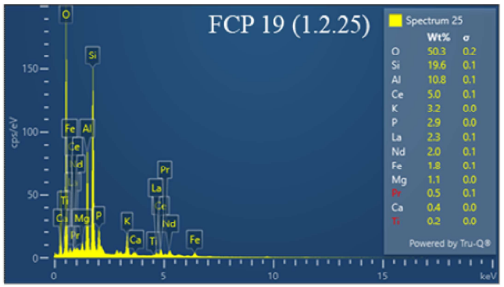
Particle #	Specimen #	Site #	Spectrum #	Mineral	Al (%)	Si (%)	O (%)	Ca (%)	P (%)	Fe (%)	K (%)	S (%)	Ba (%)	Mg (%)	Ti (%)	Na (%)	Sr (%)	F(%)	Zr (%)	Sc (%)	La (%)	Ce(%)	Pr (%)	Nd(%)	Sm (%)	Gd (%)	Y(%)	Dy (%)	Er (%)	Yb (%)	Ho (%)	Th(%)	U (%)	TREE (%)	Sum (%)	Al/Si	Al/P	TREE/P
FCP 1	3	29	510	Zircon	5.5	17.5	43.9	1.1	2.0	1.0	1.2	0.0	0.0	0.5	0.1	0.2	0.0	0.0	20.0	0.2	0.0	0.3	0.0	0.0	0.0	0.9	4.5	1.1	0.0	0.0	0.0	0.0	0.0	7.0	100	0.31	2.75	3.50
FCP 2	3	31	531	Zircon	8.3	19.0	49.1	1.0	1.0	1.5	1.9	0.0	0.0	0.8	0.4	0.0	0.0	0.0	14.2	0.3	0.0	0.1	0.0	0.0	0.0	0.0	2.5	0.0	0.0	0.0	0.0	0.0	0.0	2.9	100	0.44	8.30	2.90
FCP 3	1	57	554	Zircon	7.2	15.8	54.2	0.5	1.0	1.3	1.6	0.0	0.0	0.6	0.1	0.3	0.0	0.0	14.7	0.2	0.0	0.0	0.0	0.0	0.0	0.0	2.7	0.0	0.0	0.0	0.0	0.0	0.0	2.9	100	0.46	7.20	2.90
FCP 4	2	36	1067	Zircon	8.9	22.1	51.7	0.6	0.7	1.6	2.2	0.0	0.0	0.6	0.3	0.4	0.0	0.0	9.1	0.0	0.0	0.0	0.0	0.0	0.0	0.0	1.9	0.0	0.0	0.0	0.0	0.0	0.0	1.9	100	0.40	12.71	2.71
FCP 5	1	28	304	Zircon	6.8	16.6	44.8	0.0	0.9	2.1	1.7	0.0	0.0	0.5	0.0	0.3	0.0	0.0	24.8	0.0	0.0	0.0	0.0	0.0	0.0	0.0	1.5	0.0	0.0	0.0	0.0	0.0	0.0	1.5	100	0.41	7.56	1.67
FCP 6	1	40	399	Apatite	0.8	1.3	37.9	37.4	17.5	0.5	0.0	0.0	0.0	0.1	0.0	0.1	0.0	3.5	0.0	0.0	0.0	0.7	0.0	0.0	0.0	0.0	0.0	0.0	0.0	0.0	0.0	0.0	0.0	0.7	100	0.62	0.05	0.04
FCP 7	1	53	522	Monazite	2.3	2.2	13.3	0.3	10.0	1.2	0.2	0.0	0.0	0.0	0.0	0.0	0.0	0.0	0.0	0.0	17.2	33.8	3.5	13.8	2.2	0.0	0.0	0.0	0.0	0.0	0.0	0.0	0.0	70.5	100	1.05	0.23	7.05
FCP 8	3	26	455	Monazite	3.6	6.6	12.4	0.4	6.9	0.2	0.4	0.0	0.0	0.3	0.0	0.0	0.0	0.0	0.0	0.0	15.9	30.8	3.6	14.7	2.5	1.6	0.0	0.0	0.0	0.0	0.0	0.0	0.0	69.1	100	0.55	0.52	10.01
FCP 9	2	7	693	Monazite	12.8	17.7	29.3	1.0	1.7	4.5	3.6	0.0	2.0	0.8	0.0	0.0	0.0	0.0	0.0	0.0	7.4	13.5	0.0	5.7	0.0	0.0	0.0	0.0	0.0	0.0	0.0	0.0	0.0	26.6	100	0.72	7.53	15.65
FCP 10	1	23	256	Monazite	5.7	16.8	44.6	0.3	6.2	0.9	1.0	0.0	0.0	0.5	0.0	0.0	0.0	0.0	0.0	0.0	5.3	11.4	1.2	5.0	0.8	0.4	0.0	0.0	0.0	0.0	0.0	0.0	0.0	24.1	100	0.34	0.92	3.89
FCP 11	1	4	55	Monazite	8.8	14.2	42.1	1.1	5.6	3.3	1.3	0.0	0.0	1.0	0.2	0.0	0.0	0.0	0.0	0.0	4.3	10.4	1.3	4.7	1.1	0.8	0.0	0.0	0.0	0.0	0.0	0.0	0.0	22.6	100	0.62	1.57	4.04
FCP 12	1	47	458	Monazite	10.1	11.3	37.9	0.0	4.7	11.9	0.0	0.0	0.0	3.2	0.0	0.0	0.0	0.0	0.0	0.0	3.5	9.3	1.1	4.5	0.9	0.7	0.0	0.8	0.0	0.0	0.0	0.0	0.0	20.8	100	0.89	2.15	4.43
FCP 13	2	64	1628	Monazite	9.8	28.3	25.8	1.2	2.1	10.4	2.6	0.0	0.0	1.1	0.5	0.0	0.0	0.0	0.0	0.0	3.7	9.8	0.9	4.0	0.0	0.0	0.0	0.0	0.0	0.0	0.0	0.0	0.0	18.4	100	0.35	4.67	8.76
FCP 14	2	38	1102	Monazite	7.9	11.9	37.0	0.9	4.2	10.4	1.6	0.2	0.0	2.6	3.3	0.0	0.0	0.0	0.0	0.0	3.6	9.6	1.0	4.2	0.0	0.0	0.0	0.0	0.0	0.0	0.0	1.6	0.0	18.4	100	0.66	1.88	4.38
FCP 15	1	13	155	Monazite	15.0	20.4	40.5	0.6	2.7	1.8	4.5	0.0	0.0	0.8	0.0	0.2	0.0	0.0	0.0	0.0	2.5	6.3	0.7	2.9	0.6	0.5	0.0	0.0	0.0	0.0	0.0	0.0	0.0	13.5	100	0.74	5.56	5.00
FCP 16	2	6	684	Monazite	8.7	13.5	49.5	0.7	4.3	5.0	2.2	0.0	0.0	2.5	0.8	0.0	0.0	0.0	0.0	0.0	3.0	6.8	0.0	2.9	0.0	0.0	0.0	0.0	0.0	0.0	0.0	0.0	0.0	12.7	100	0.64	2.02	2.95
FCP 17	1	19	208	Monazite	10.2	14.1	46.4	0.6	3.3	6.6	1.1	0.0	0.0	2.4	2.4	0.0	0.0	0.0	0.0	0.0	2.7	6.4	0.5	2.6	0.5	0.0	0.0	0.0	0.0	0.0	0.0	0.0	0.0	12.7	100	0.72	3.09	3.85
FCP 18	2	35	1056	Monazite	11.2	18.1	49.2	0.0	2.4	4.5	2.6	0.0	0.0	1.7	0.2	0.0	0.0	0.0	0.0	0.0	3.0	5.0	0.0	2.2	0.0	0.0	0.0	0.0	0.0	0.0	0.0	0.0	0.0	10.2	100	0.62	4.67	4.25
FCP 19	1	2	25	Monazite	10.8	19.6	50.3	0.4	2.9	1.8	3.2	0.0	0.0	1.1	0.2	0.0	0.0	0.0	0.0	0.0	2.3	5.0	0.5	2.0	0.0	0.0	0.0	0.0	0.0	0.0	0.0	0.0	0.0	9.8	100	0.55	3.72	3.38
FCP 20	3	6	84	Monazite	19.2	26.6	32.5	0.5	1.2	5.1	4.0	0.0	0.0	1.3	0.2	0.0	0.0	0.0	0.0	0.0	1.8	4.3	0.5	1.8	0.5	0.4	0.0	0.0	0.0	0.0	0.0	0.0	0.0	9.3	100	0.72	16.00	7.75
FCP 21	2	33	1039	Monazite	12.5	18.9	48.4	0.4	2.5	2.4	4.5	0.0	0.0	1.1	0.2	0.0	0.0	0.0	0.0	0.0	2.3	4.6	0.0	2.1	0.0	0.0	0.0	0.0	0.0	0.0	0.0	0.0	0.0	9.0	100	0.66	5.00	3.60
FCP 22	1	21	234	Monazite	9.8	15.1	48.3	0.5	2.0	9.0	2.2	0.0	0.0	2.5	3.5	0.0	0.0	0.0	0.0	0.0	1.7	3.7	0.0	1.7	0.0	0.0	0.0	0.0	0.0	0.0	0.0	0.0	0.0	7.1	100	0.65	4.90	3.55
FCP 23	1	30	319	Monazite	10.8	17.5	50.6	0.4	1.5	7.4	2.4	0.0	0.0	2.7	0.5	0.0	0.0	0.0	0.0	0.0	1.4	3.4	0.0	1.3	0.0	0.0	0.0	0.0	0.0	0.0	0.0	0.0	0.0	6.1	100	0.62	7.20	4.07
FCP 24	3	37	621	Monazite	13.9	22.6	48.2	0.0	1.7	3.3	3.2	0.0	0.0	1.3	0.5	0.4	0.0	0.0	0.0	0.0	0.0	0.0	0.0	0.0	0.0	0.6	3.8	0.0	0.6	0.0	0.0	0.0	0.0	5.0	100	0.62	8.18	2.94
FCP 25	1	50	484	Xenotime	3.1	7.1	31.7	0.4	11.0	0.3	0.6	0.0	0.0	0.0	0.1	0.0	0.0	0.0	5.6	0.0	0.0	0.0	0.0	0.0	0.5	2.7	25.0	5.5	3.0	2.4	1.0	0.0	0.0	40.1	100	0.44	0.28	3.65
FCP 26	1	49	475	Xenotime	3.4	4.9	44.5	0.0	10.3	0.4	0.0	0.0	0.0	0.0	0.1	0.0	0.0	0.0	0.0	0.0	0.0	0.0	0.0	0.0	1.2	4.1	24.2	4.3	2.1	0.0	0.0	0.0	0.0	35.9	100	0.69	0.33	3.49
FCP 27	1	27	292	Crandallite	18.4	7.8	43.2	0.9	9.6	0.7	1.0	0.0	0.0	0.0	0.0	0.0	0.0	0.0	0.0	0.0	4.4	9.2	1.1	3.8	0.0	0.0	0.0	0.0	0.0	0.0	0.0	0.0	0.0	18.5	100	2.36	1.92	1.93
FCP 28	3	13	179	Crandallite	19.8	15.4	29.2	0.5	7.3	1.2	2.4	0.0	0.9	0.0	0.3	0.0	3.9	0.0	0.0	0.0	4.5	8.7	0.8	4.0	0.6	0.0	0.0	0.0	0.0	0.0	0.0	0.7	0.0	18.6	100	1.29	2.71	2.55
FCP 29	1	32	339	Crandallite	16.0	9.2	49.0	0.2	7.2	1.1	1.1	0.0	0.0	0.5	0.2	0.0	0.0	0.0	0.0	0.0	3.1	7.1	0.9	3.7	0.6	0.0	0.0	0.0	0.0	0.0	0.0	0.0	0.0	15.4	100	1.74	2.22	2.14
FCP 30	2	50	1311	Crandallite	18.4	11.4	48.2	0.2	6.3	1.0	2.1	0.0	0.0	0.4	0.4	0.0	0.0	0.0	0.0	0.0	3.4	5.9	0.0	2.2	0.0	0.0	0.0	0.0	0.0	0.0	0.0	0.0	0.0	11.5	100	1.61	2.92	1.83
FCP 31	1	42	414	Crandallite	16.1	12.8	44.0	0.3	7.2	1.1	1.6	0.0	0.7	0.4	0.1	1.1	3.1	0.0	0.0	0.0	3.2	5.6	0.0	2.2	0.0	0.0	0.0	0.0	0.0	0.0	0.0	0.6	0.0	11.0	100	1.26	2.24	1.53
FCP 32	3	23	409	Crandallite	15.4	7.8	53.6	0.2	7.6	1.2	1.0	0.0	0.0	0.4	0.0	0.0	3.6	0.0	0.0	0.0	2.8	4.5	0.4	1.4	0.0	0.0	0.0	0.0	0.0	0.0	0.0	0.0	0.0	9.1	100	1.97	2.03	1.20
FCP 33	2	18	835	Crandallite	15.5	11.9	52.9	0.4	7.6	1.3	1.1	0.0	0.0	0.5	0.4	0.0	0.0	0.0	0.0	0.0	2.2	4.3	0.0	2.0	0.0	0.0	0.0	0.0	0.0	0.0	0.0	0.0	0.0	8.5	100	1.30	2.04	1.12
FCP 34	3	18	299	Crandallite	17.6	7.7	47.8	1.2	8.6	1.6	0.6	0.0	2.1	0.0	0.1	0.0	5.0	0.0	0.0	0.0	3.3	2.6	0.4	1.3	0.0	0.0	0.0	0.0	0.0	0.0	0.0	0.0	0.0	7.6	100	2.29	2.05	0.88
FCP 35	1	59	570	Crandallite	15.3	8.3	52.7	0.6	7.6	0.9	1.2	0.0	0.9	0.4	0.1	0.0	4.0	0.0	0.0	0.0	1.8	4.0	0.4	1.7	0.0	0.0	0.0	0.0	0.0	0.0	0.0	0.0	0.0	7.9	100	1.84	2.01	1.04
FCP 36	3	11	159	Crandallite	16.7	7.5	53.7	0.3	6.7	0.6	1.2	1.9	0.0	0.0	0.2	0.0	3.8	0.0	0.0	0.0	2.2	4.0	0.0	1.1	0.0	0.0	0.0	0.0	0.0	0.0	0.0	0.0	0.0	7.3	100	2.23	2.49	1.09
FCP 37	1	33	345	Crandallite	16.2	13.8	54.4	0.4	4.5	1.4	0.7	0.0	0.4	0.0	0.1	0.0	1.9	0.0	0.0	0.0	1.9	3.2	0.0	1.2	0.0	0.0	0.0	0.0	0.0	0.0	0.0	0.0	0.0	6.3	100	1.17	3.60	1.40
FCP 38	2	15	793	Crandallite	16.1	13.1	54.6	1.2	4.8	0.9	2.4	0.0	0.0	0.4	0.0	0.7	0.0	0.0	0.0	0.0	1.6	2.9	0.0	1.3	0.0	0.0	0.0	0.0	0.0	0.0	0.0	0.0	0.0	5.8	100	1.23	3.35	1.21
FCP 39	2	19	871	Crandallite	14.9	14.9	53.9	0.4	3.8	1.2	2.2	0.2	0.0	0.7	0.3	0.5	2.4	0.0	0.0	0.0	1.4	2.6	0.0	0.8	0.0	0.0	0.0	0.0	0.0	0.0	0.0	0.0	0.0	4.8	100	1.00	3.92	1.26
FCP 40	2	24	915	Crandallite	15.0	10.5	54.5	0.6	5.3	2.1	1.6	0.2	0.6	0.8	0.0	0.0	4.5	0.0	0.0	0.0	1.4	1.9	0.0	0.9	0.0	0.0	0.0	0.0	0.0	0.0	0.0	0.0	0.0	4.2	100	1.43	2.83	0.79
FCP 41	2	56	1446	Crandallite	17.1	14.6	48.8	0.8	5.8	1.5	2.5	0.0	0.9	0.6	0.0	0.0	4.0	0.0	0.0	0.0	0.0	0.6	1.6	0.0	1.3	0.0	0.0	0.0	0.0	0.0	0.0	0.0	0.0	3.5	100	1.17	2.95	0.60
FCP 42	2	40	1150	Crandallite	15.3	6.0	57.7	0.9	8.5	0.8	0.6	0.0	1.5	0.4	0.0	0.0	5.3	0.0	0.0	0.0	0.0	1.9	0.0	1.2	0.0	0.0	0.0	0.0	0.0	0.0	0.0	0.0	0.0	3.1	100	2.55	1.80	0.36
FCP 43	2	56	1439	Crandallite	17.1	17.6	50.5	0.7	4.5	1.6	3.3	0.0	0.0	0.9	0.2	0.0	0.0	0.0	0.0	0.0	0.7	1.8	0.0	1.1	0.0	0.0	0.0	0.0	0.0	0.0	0.0	0.0	0.0	3.6	100	0.97	3.80	0.80
FCP 44	2	48	1282	Crandallite	16.1	21.8	38.6	0.0	3.6	7.3	4.6	0.0	0.0	0.8	0.7	0.5	0.0	0.0	0.0	0.0	0.0	0.0	0.0	0.0	0.0	0.0	6.1	0.0	0.0	0.0	0.0	0.0	0.0	6.1	100	0.74	4.47	1.69
FCP 45	3	24	426	Crandallite	18.2	22.0	49.4	0.0	0.8	1.4	5.5	0.0	0.0	0.8	0.1	0.8	0.0	0.0	0.0	0.0	0.0	1.0	0.0	0.0	0.0	0.0	0.0	0.0	0.0	0.0	0.0	0.0	0.0	1.0	100	0.83	22.75	1.25
FCP 46	1	36	380	Crandallite	18.1	19.5	53.2	0.5	1.9	1.2	3.6	0.0	0.0	0.6	0.2	0.6	0.0	0.0	0.0	0.0	0.0	0.6	0.0	0.0	0.0	0.0	0.0	0.0	0.0	0.0	0.0	0.0	0.0	0.6	100	0.93	9.53	0.32
FCP 47	2	42	1158	Crandallite	17.9	18.1	51.2	0.8	2.7	2.7	3.1	0.8	0.0	0.8	0.4	0.5	0.0	0.0	0.0	0.0	0.0	1.2	0.0	0.0	0.0	0.0	0.0	0.0	0.0	0.0	0.0	0.0	0.0	1.2	100	0.99	6.63	0.44
FCP 48	2	8	707	Crandallite	15.5	19.5	52.1	0.3	2.3	3.5	4.0	0.0	0.0	1.0	0.0	0.3	0.0	0.0	0.0	0.0	0.0	1.4	0.0	0.0	0.0	0.0	0.0	0.0	0.0	0.0	0.0	0.0	0.0	1.4	100	0.79	6.74	0.61
FCP 49	2	20	866	Crandallite	17.4	23.7	41.4	0.6	2.2	3.5	7.2	0.0	0.0	0.8	0.8	0.0	0.0	0.0	0.0	0.0	0.0	1.5	0.0	0.9	0.0	0.0	0.0	0.0	0.0	0.0	0.0	0.0	0.0	2.4	100	0.73	7.91	1.09
FCP 50	1	11	126	Crandallite	14.8	17.2	47.7	0.4	2.8	7.3	2.4	0.0	0.0	2.7	0.3	0.0	0.0	0.0	0.0	0.0	1.2	2.4	0.0	0.8	0.0	0.0	0.0	0.0	0.0	0.0	0.0	0.0	0.0	4.4	100	0.86	5.29	1.57

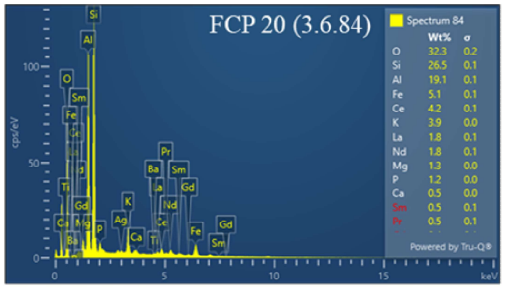
Figure A.3 EDS spectra of the particles containing REEs found from the Fire Clay coal waste. (The spectra are labelled as # Particle (Specimen #. Site #. Spectrum #))

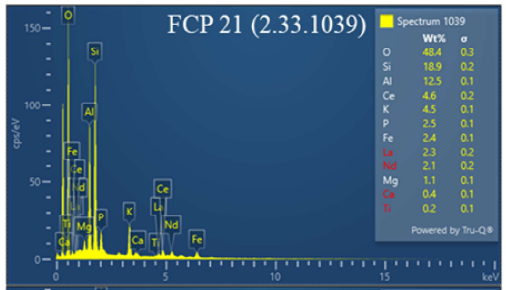


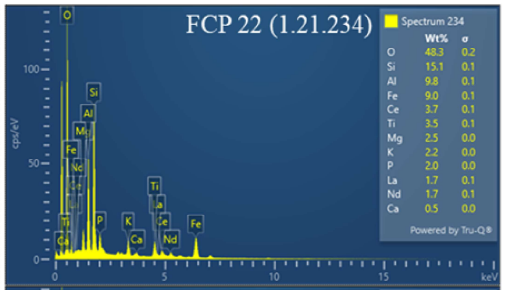

FCP 17 (1.19.208)
Spectrum 208
Wt% σ
O 46.4 0.2
Si 14.1 0.1
Al 10.2 0.1
Fe 6.6 0.1
Ce 6.4 0.1
P 3.3 0.1
La 2.7 0.2
Nd 2.6 0.1
Ti 2.4 0.1
Mg 2.4 0.1
K 1.1 0.0
Ca 0.6 0.0
Sm 0.5 0.1
Powered by Tru-Q®
cps/eV
keV

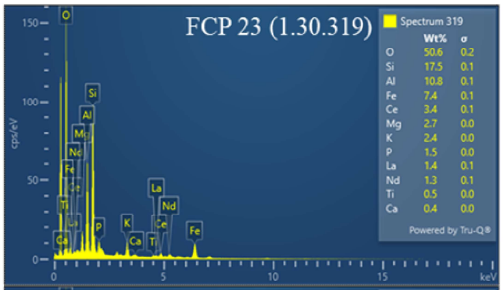

FCP 18 (2.35.1056)
Spectrum 1056
Wt% σ
O 49.2 0.3
Si 18.1 0.2
Al 11.2 0.1
Ce 5.0 0.2
Fe 4.5 0.1
La 3.0 0.2
K 2.6 0.1
P 2.4 0.1
Nd 2.2 0.2
Mg 1.7 0.1
Ti 0.2 0.1
Powered by Tru-Q®
cps/eV
keV

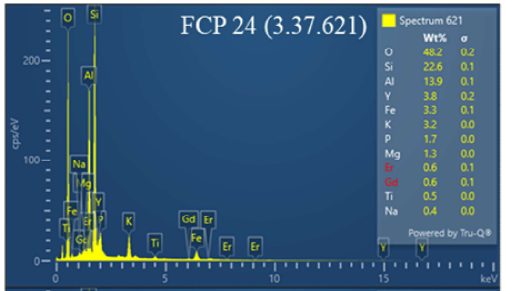

FCP 19 (1.2.25)
Spectrum 25
Wt% σ
O 50.3 0.2
Si 19.6 0.1
Al 10.8 0.1
Ce 5.0 0.1
K 3.2 0.0
P 2.9 0.0
La 2.3 0.1
Nd 2.0 0.1
Fe 1.8 0.1
Mg 1.1 0.0
Pr 0.5 0.1
Ca 0.4 0.0
Ti 0.2 0.0
Powered by Tru-Q®
cps/eV
keV

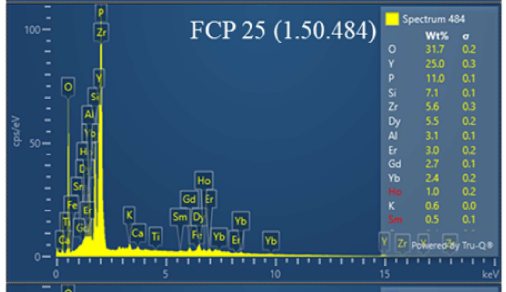

FCP 20 (3.6.84)
Spectrum 84
Wt% σ
O 32.3 0.2
Si 26.5 0.1
Al 19.1 0.1
Fe 5.1 0.1
Ce 4.2 0.1
K 3.9 0.0
La 1.8 0.1
Nd 1.8 0.1
Mg 1.3 0.0
P 1.2 0.0
Ca 0.5 0.0
Sm 0.5 0.1
Pr 0.5 0.1
Powered by Tru-Q®
cps/eV
keV

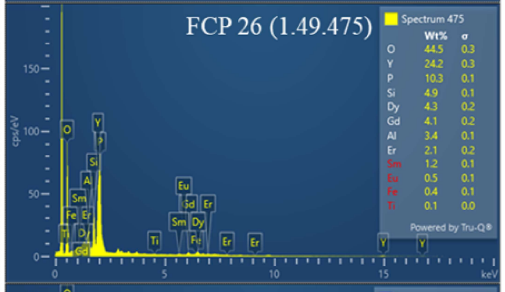

FCP 21 (2.33.1039)
Spectrum 1039
Wt% σ
O 48.4 0.3
Si 18.9 0.2
Al 12.5 0.1
Ce 4.6 0.2
K 4.5 0.1
P 2.5 0.1
Fe 2.4 0.1
La 2.3 0.2
Nd 2.1 0.2
Mg 1.1 0.1
Ca 0.4 0.1
Ti 0.2 0.1
Powered by Tru-Q®
cps/eV
keV

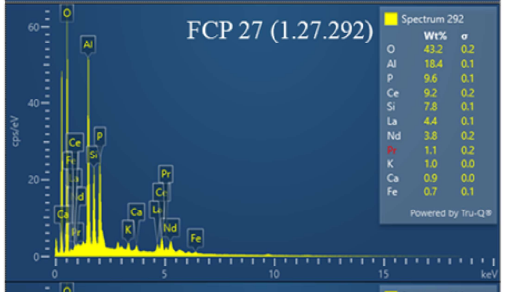

FCP 22 (1.21.234)
Spectrum 234
Wt% σ
O 48.3 0.2
Si 15.1 0.1
Al 9.8 0.1
Fe 9.0 0.1
Ce 3.7 0.1
Ti 3.5 0.1
Mg 2.5 0.0
K 2.2 0.0
P 2.0 0.0
La 1.7 0.1
Nd 1.7 0.1
Ca 0.5 0.0
Powered by Tru-Q®
cps/eV
keV

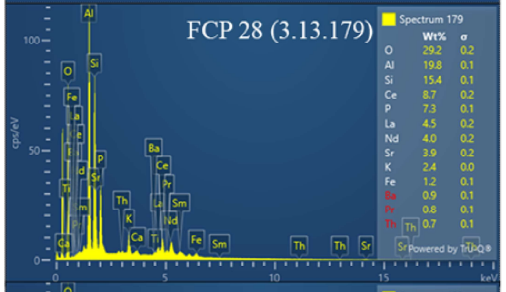

FCP 23 (1.30.319)
Spectrum 319
Wt% σ
O 50.6 0.2
Si 17.5 0.1
Al 10.8 0.1
Fe 7.4 0.1
Ce 3.4 0.1
Mg 2.7 0.0
K 2.4 0.0
P 1.5 0.0
La 1.4 0.1
Nd 1.3 0.1
Ti 0.5 0.0
Ca 0.4 0.0
Powered by Tru-Q®
cps/eV
keV

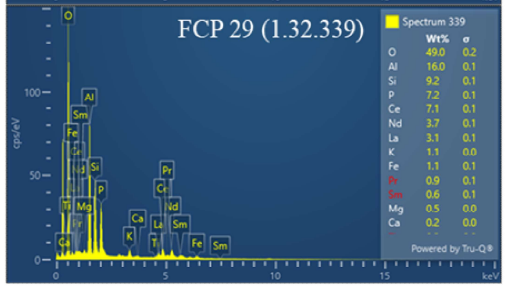

FCP 24 (3.37.621)
Spectrum 621
Wt% σ
O 48.2 0.2
Si 22.6 0.1
Al 13.9 0.1
Y 3.8 0.2
Fe 3.3 0.1
K 3.2 0.0
P 1.7 0.0
Mg 1.3 0.0
Er 0.6 0.1
Gd 0.6 0.1
Ti 0.5 0.0
Na 0.4 0.0
Powered by Tru-Q®
cps/eV
keV

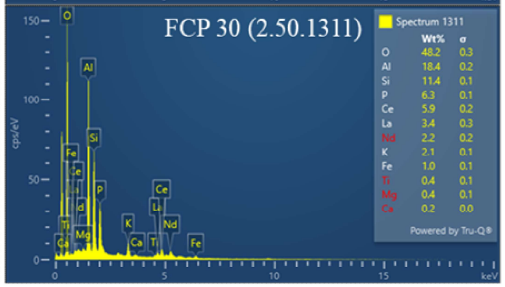

FCP 25 (1.50.484)
Spectrum 484
Wt% σ
O 31.7 0.2
Y 25.0 0.3
P 11.0 0.1
Si 7.1 0.1
Zr 5.6 0.3
Dy 5.5 0.2
Al 3.1 0.1
Er 3.0 0.2
Gd 2.7 0.1
Yb 2.4 0.2
Ho 1.0 0.2
K 0.6 0.0
Sm 0.5 0.1
Powered by Tru-Q®
cps/eV
keV

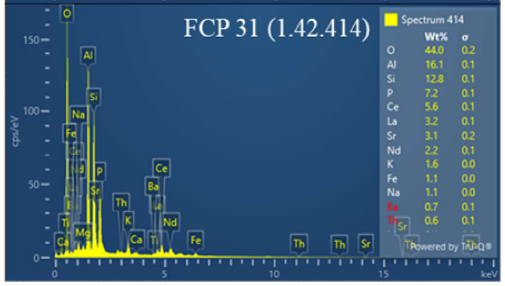

FCP 26 (1.49.475)
Spectrum 475
Wt% σ
O 44.5 0.3
Y 24.2 0.3
P 10.3 0.1
Si 4.9 0.1
Dy 4.3 0.2
Gd 4.1 0.2
Al 3.4 0.1
Er 2.1 0.2
Sm 1.2 0.1
Eu 0.5 0.1
Fe 0.4 0.1
Ti 0.1 0.0
Powered by Tru-Q®
cps/eV
keV

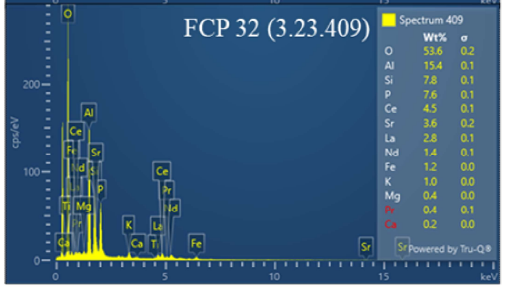

FCP 27 (1.27.292)
Spectrum 292
Wt% σ
O 43.2 0.2
Al 18.4 0.1
P 9.6 0.1
Ce 9.2 0.2
Si 7.8 0.1
La 4.4 0.1
Nd 3.8 0.2
Pr 1.1 0.2
K 1.0 0.0
Ca 0.9 0.0
Fe 0.7 0.1
Powered by Tru-Q®
cps/eV
keV

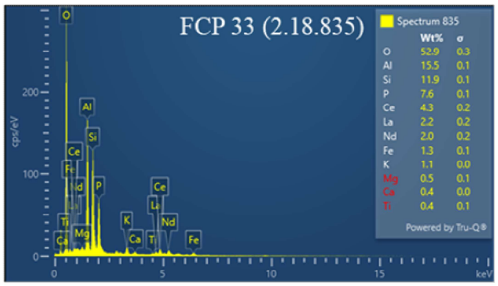

FCP 28 (3.13.179)
Spectrum 179
Wt% σ
O 29.2 0.2
Al 19.8 0.1
Si 15.4 0.1
Ce 8.7 0.2
P 7.3 0.1
La 4.5 0.2
Nd 4.0 0.2
Sr 3.9 0.2
K 2.4 0.0
Fe 1.2 0.1
Ba 0.9 0.1
Pr 0.8 0.1
Th 0.7 0.1
Powered by Tru-Q®
cps/eV
keV

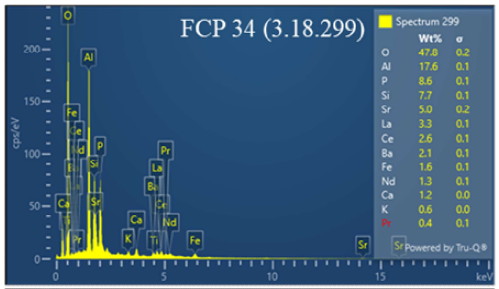

FCP 29 (1.32.339)
Spectrum 339
Wt% σ
O 49.0 0.2
Al 16.0 0.1
Si 9.2 0.1
P 7.2 0.1
Ce 7.1 0.1
Nd 3.7 0.1
La 3.1 0.1
K 1.1 0.0
Fe 1.1 0.1
Pr 0.9 0.1
Sm 0.6 0.1
Mg 0.5 0.0
Ca 0.2 0.0
Powered by Tru-Q®
cps/eV
keV

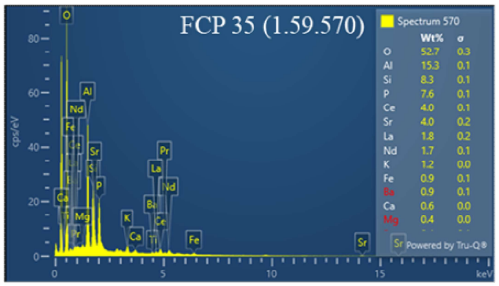

FCP 30 (2.50.1311)
Spectrum 1311
Wt% σ
O 48.2 0.3
Al 18.4 0.2
Si 11.4 0.1
P 6.3 0.1
Ce 5.9 0.2
La 3.4 0.3
Nd 2.2 0.2
K 2.1 0.1
Fe 1.0 0.1
Ti 0.4 0.1
Mg 0.4 0.1
Ca 0.2 0.0
Powered by Tru-Q®
cps/eV
keV

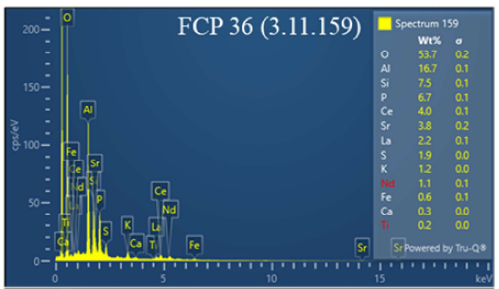

FCP 31 (1.42.414)
Spectrum 414
Wt% σ
O 44.0 0.2
Al 16.1 0.1
Si 12.8 0.1
P 7.2 0.1
Ce 5.6 0.1
La 3.2 0.1
Sr 3.1 0.2
Nd 2.2 0.1
K 1.6 0.0
Fe 1.1 0.0
Na 1.1 0.0
Ba 0.7 0.1
Ti 0.6 0.1
Powered by Tru-Q®
cps/eV
keV

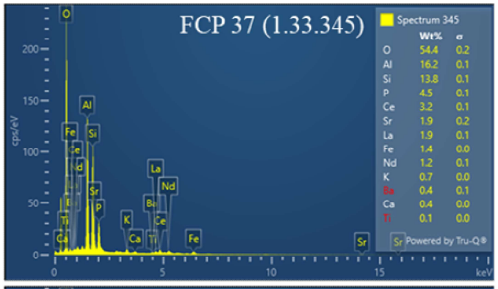

FCP 32 (3.23.409)
Spectrum 409
Wt% σ
O 53.6 0.2
Al 15.4 0.1
Si 7.8 0.1
P 7.6 0.1
Ce 4.5 0.1
Sr 3.6 0.2
La 2.8 0.1
Nd 1.4 0.1
Fe 1.2 0.0
K 1.0 0.0
Mg 0.4 0.0
Pr 0.4 0.1
Ca 0.2 0.0
Powered by Tru-Q®
cps/eV
keV

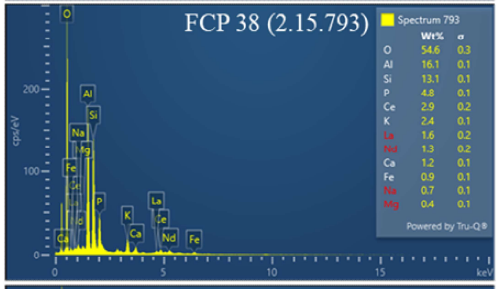

FCP 33 (2.18.835)
Spectrum 835
Wt% σ
O 52.9 0.3
Al 15.5 0.1
Si 11.9 0.1
P 7.6 0.1
Ce 4.3 0.2
La 2.2 0.2
Nd 2.0 0.2
Fe 1.3 0.1
K 1.1 0.0
Mg 0.5 0.1
Ca 0.4 0.0
Ti 0.4 0.1
Powered by Tru-Q®
cps/eV
keV

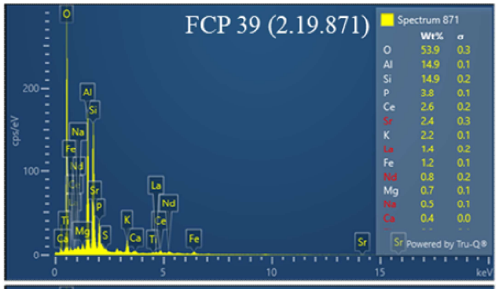

FCP 34 (3.18.299)
Spectrum 299
Wt% σ
O 47.8 0.2
Al 17.6 0.1
P 8.6 0.1
Si 7.7 0.1
Sr 5.0 0.2
La 3.3 0.1
Ce 2.6 0.1
Ba 2.1 0.1
Fe 1.6 0.1
Nd 1.3 0.1
Ca 1.2 0.0
K 0.6 0.0
Pr 0.4 0.1
Powered by Tru-Q®
cps/eV
keV

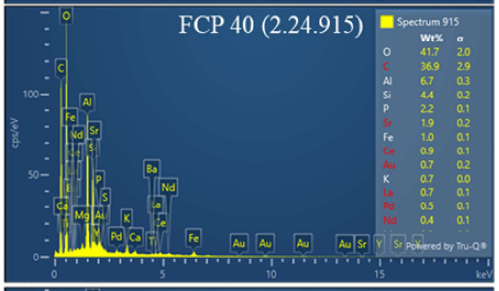

FCP 35 (1.59.570)
Spectrum 570
Wt% σ
O 52.7 0.3
Al 15.3 0.1
Si 8.3 0.1
P 7.6 0.1
Ce 4.0 0.1
Sr 4.0 0.2
La 1.8 0.2
Nd 1.7 0.1
K 1.2 0.0
Fe 0.9 0.1
Ba 0.9 0.1
Ca 0.6 0.0
Mg 0.4 0.0
Powered by Tru-Q®
cps/eV
keV

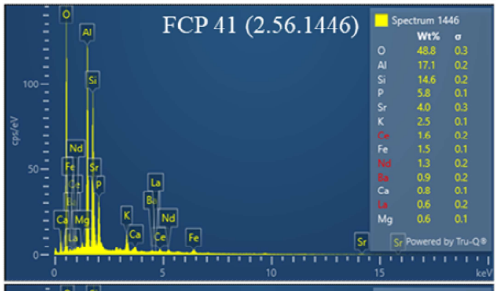

FCP 36 (3.11.159)
Spectrum 159
Wt% σ
O 53.7 0.2
Al 16.7 0.1
Si 7.5 0.1
P 6.7 0.1
Ce 4.0 0.1
Sr 3.8 0.2
La 2.2 0.1
S 1.9 0.0
K 1.2 0.0
Nd 1.1 0.1
Fe 0.6 0.1
Ca 0.3 0.0
Ti 0.2 0.0
Powered by Tru-Q®
cps/eV
keV

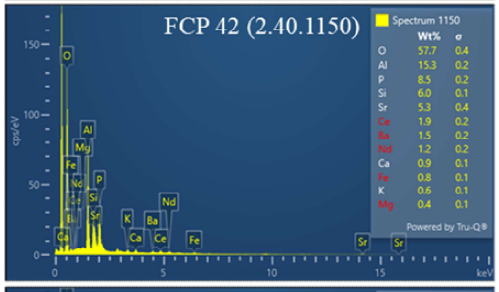

FCP 37 (1.33.345)
Spectrum 345
Wt% σ
O 54.4 0.2
Al 16.2 0.1
Si 13.8 0.1
P 4.5 0.1
Ce 3.2 0.1
Sr 1.9 0.2
La 1.9 0.1
Fe 1.4 0.0
Nd 1.2 0.1
K 0.7 0.0
Ba 0.4 0.1
Ca 0.4 0.0
Ti 0.1 0.0
Powered by Tru-Q®
cps/eV
keV

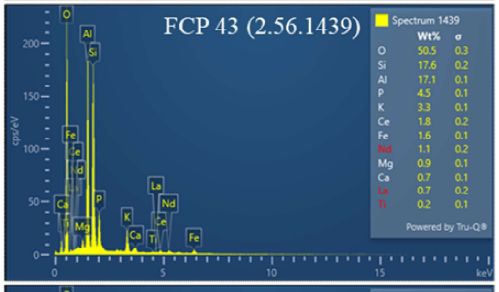

FCP 38 (2.15.793)
Spectrum 793
Wt% σ
O 54.6 0.3
Al 16.1 0.1
Si 13.1 0.1
P 4.8 0.1
Ce 2.9 0.2
K 2.4 0.1
La 1.6 0.2
Nd 1.3 0.2
Ca 1.2 0.1
Fe 0.9 0.1
Na 0.7 0.1
Mg 0.4 0.1
Powered by Tru-Q®
cps/eV
keV

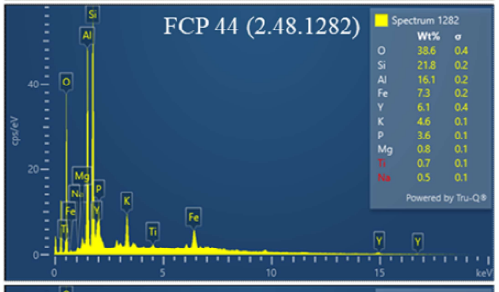

FCP 39 (2.19.871)
Spectrum 871
Wt% σ
O 53.9 0.3
Al 14.9 0.1
Si 14.9 0.2
P 3.8 0.1
Ce 2.6 0.2
Sr 2.4 0.3
K 2.2 0.1
La 1.4 0.2
Fe 1.2 0.1
Nd 0.8 0.2
Mg 0.7 0.1
Na 0.5 0.1
Ca 0.4 0.0
Powered by Tru-Q®
cps/eV
keV

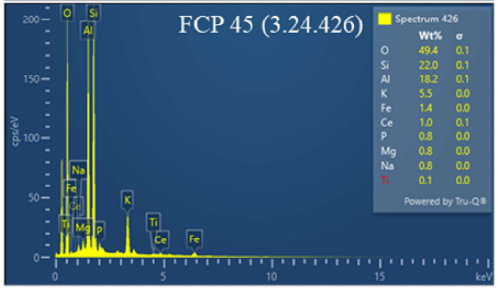

FCP 40 (2.24.915)
Spectrum 915
Wt% σ
O 41.7 2.0
C 36.9 2.9
Al 6.7 0.3
Si 4.4 0.2
P 2.2 0.1
Sr 1.9 0.2
Fe 1.0 0.1
Ce 0.9 0.1
Au 0.7 0.2
K 0.7 0.0
La 0.7 0.1
Pd 0.5 0.1
Nd 0.4 0.1
Powered by Tru-Q®
cps/eV
keV

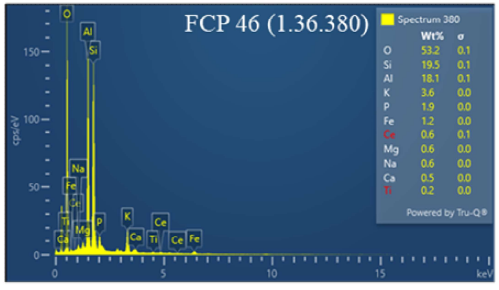

FCP 41 (2.56.1446)
Spectrum 1446
Wt% σ
O 48.8 0.3
Al 17.1 0.2
Si 14.6 0.2
P 5.8 0.1
Sr 4.0 0.3
K 2.5 0.1
Ce 1.6 0.2
Fe 1.5 0.1
Nd 1.3 0.2
Ba 0.9 0.2
Ca 0.8 0.1
La 0.6 0.2
Mg 0.6 0.1
Powered by Tru-Q®
cps/eV
keV

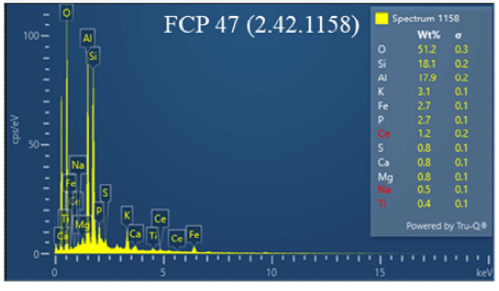

FCP 42 (2.40.1150)
Spectrum 1150
Wt% σ
O 57.7 0.4
Al 15.3 0.2
P 8.5 0.2
Si 6.0 0.1
Sr 5.3 0.4
Ce 1.9 0.2
Ba 1.5 0.2
Nd 1.2 0.2
Ca 0.9 0.1
Fe 0.8 0.1
K 0.6 0.1
Mg 0.4 0.1
Powered by Tru-Q®
cps/eV
keV

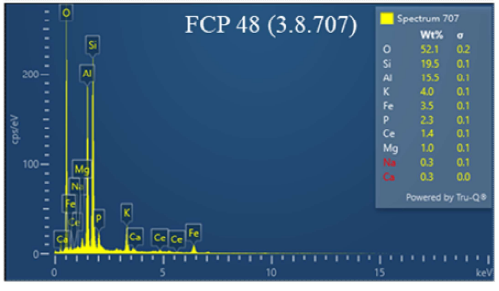

FCP 43 (2.56.1439)
Spectrum 1439
Wt% σ
O 50.5 0.3
Si 17.6 0.2
Al 17.1 0.1
P 4.5 0.1
K 3.3 0.1
Ce 1.8 0.2
Fe 1.6 0.1
Nd 1.1 0.2
Mg 0.9 0.1
Ca 0.7 0.1
La 0.7 0.2
Ti 0.2 0.1
Powered by Tru-Q®
cps/eV
keV

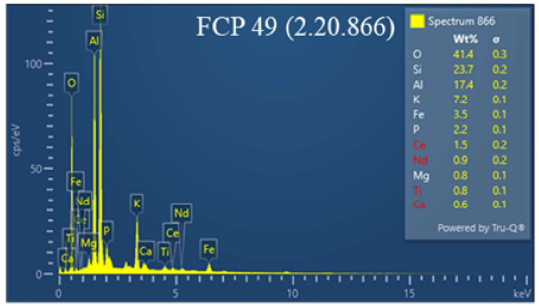

FCP 44 (2.48.1282)
Spectrum 1282
Wt% σ
O 38.6 0.4
Si 21.8 0.2
Al 16.1 0.2
Fe 7.3 0.2
Y 6.1 0.4
K 4.6 0.1
P 3.6 0.1
Mg 0.8 0.1
Ti 0.7 0.1
Na 0.5 0.1
Powered by Tru-Q®
cps/eV
keV


FCP 45 (3.24.426)
Spectrum 426
Wt% σ
O 49.4 0.1
Si 22.0 0.1
Al 18.2 0.1
K 5.5 0.0
Fe 1.4 0.0
Ce 1.0 0.1
P 0.8 0.0
Mg 0.8 0.0
Na 0.8 0.0
Ti 0.1 0.0
Powered by Tru-Q®
cps/eV
keV


FCP 46 (1.36.380)
Spectrum 380
Wt% σ
O 53.2 0.1
Si 19.5 0.1
Al 18.1 0.1
K 3.6 0.0
P 1.9 0.0
Fe 1.2 0.0
Ce 0.6 0.1
Mg 0.6 0.0
Na 0.6 0.0
Ca 0.5 0.0
Ti 0.2 0.0
Powered by Tru-Q®
cps/eV
keV


FCP 47 (2.42.1158)
Spectrum 1158
Wt% σ
O 51.2 0.3
Si 18.1 0.2
Al 17.9 0.2
K 3.1 0.1
Fe 2.7 0.1
P 2.7 0.1
Ce 1.2 0.2
S 0.8 0.1
Ca 0.8 0.1
Mg 0.8 0.1
Na 0.5 0.1
Ti 0.4 0.1
Powered by Tru-Q®
cps/eV
keV


FCP 48 (3.8.707)
Spectrum 707
Wt% σ
O 52.1 0.2
Si 19.5 0.1
Al 15.5 0.1
K 4.0 0.1
Fe 3.5 0.1
P 2.3 0.1
Ce 1.4 0.1
Mg 1.0 0.1
Na 0.3 0.1
Ca 0.3 0.0
Powered by Tru-Q®
cps/eV
keV


FCP 49 (2.20.866)
Spectrum 866
Wt% σ
O 41.4 0.3
Si 23.7 0.2
Al 17.4 0.2
K 7.2 0.1
Fe 3.5 0.1
P 2.2 0.1
Ce 1.5 0.2
Nd 0.9 0.2
Mg 0.8 0.1
Ti 0.8 0.1
Ca 0.6 0.1
Powered by Tru-Q®
cps/eV
keV

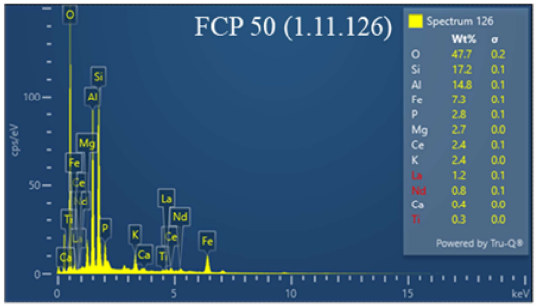
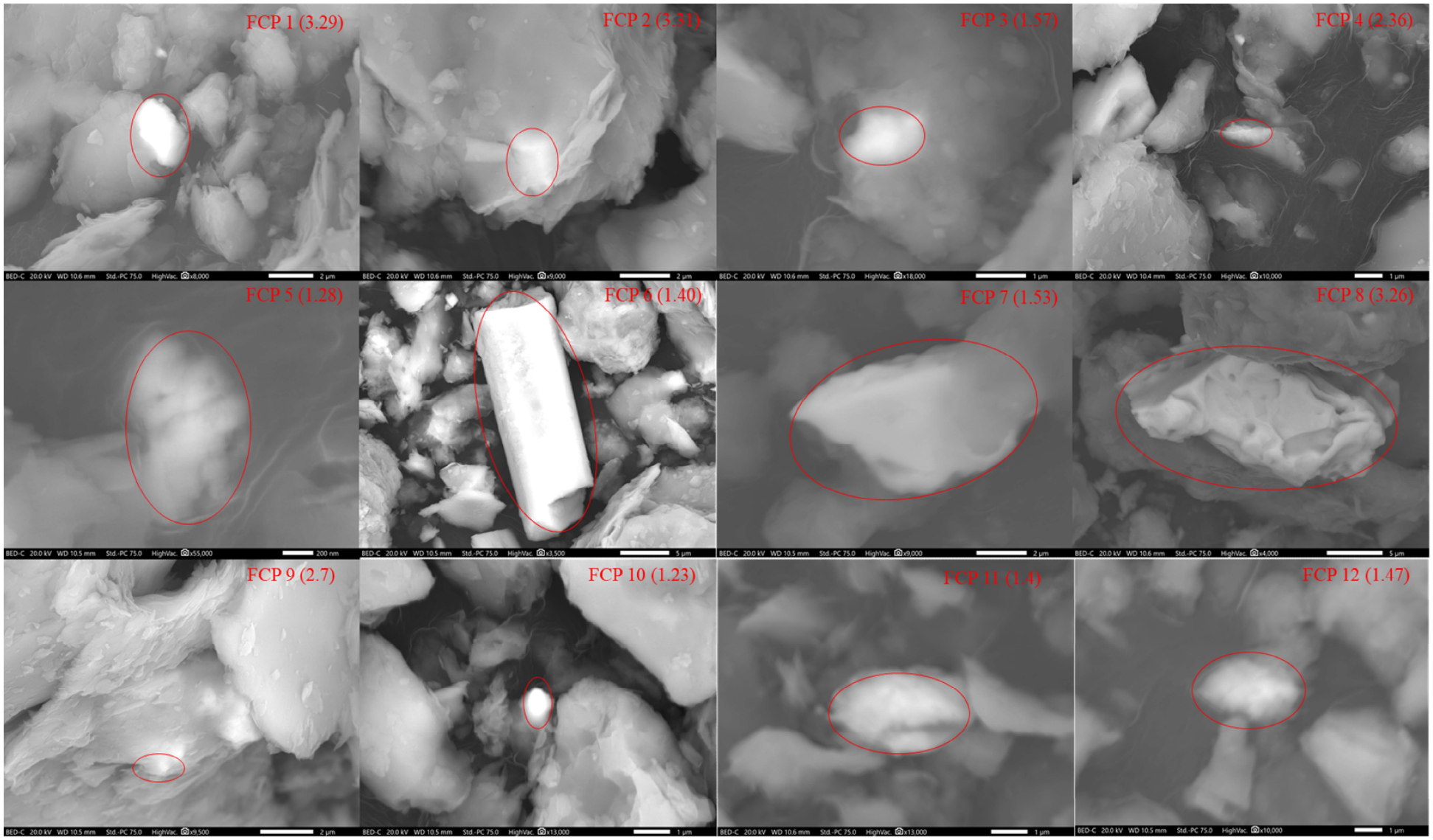
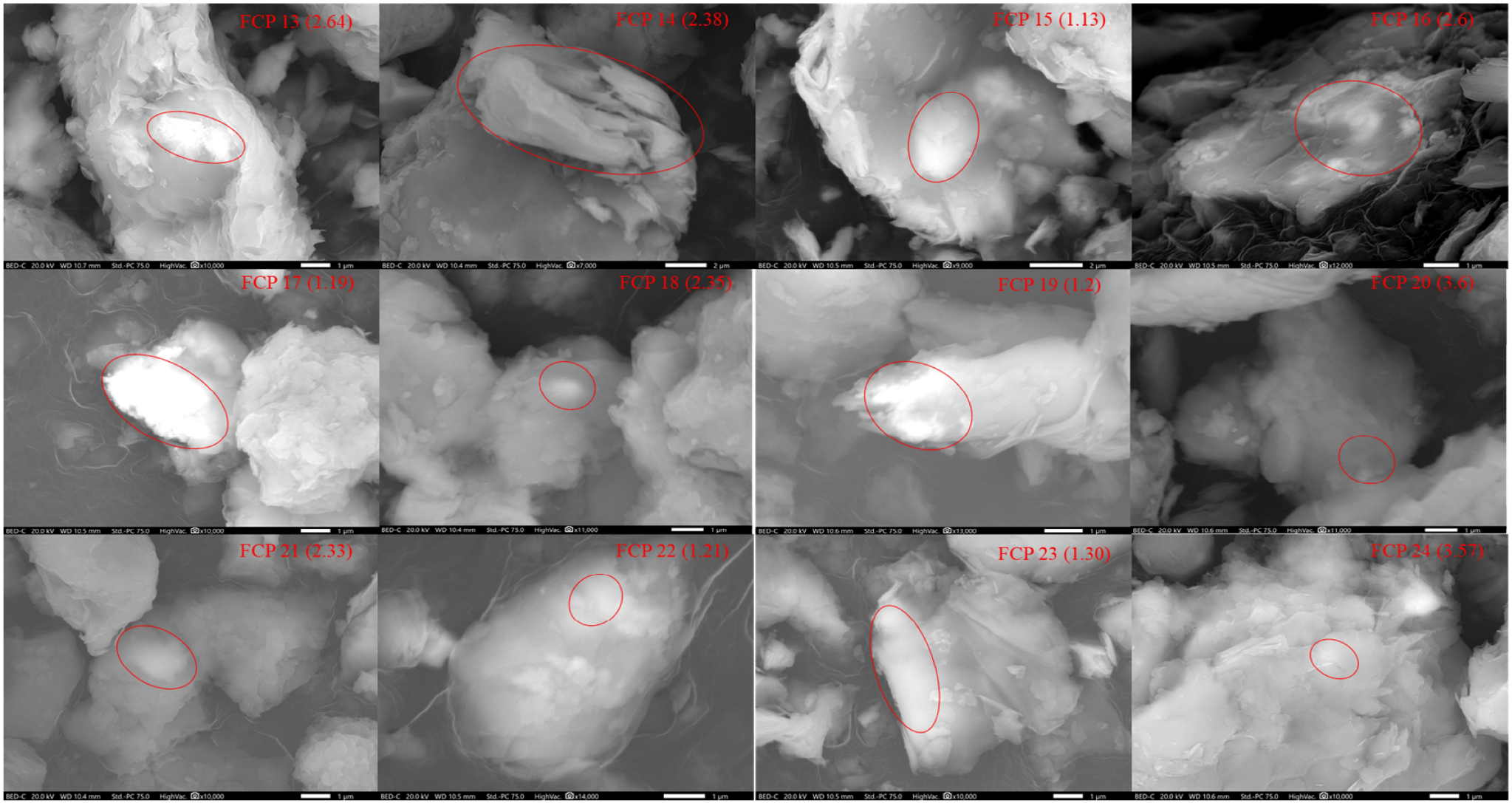
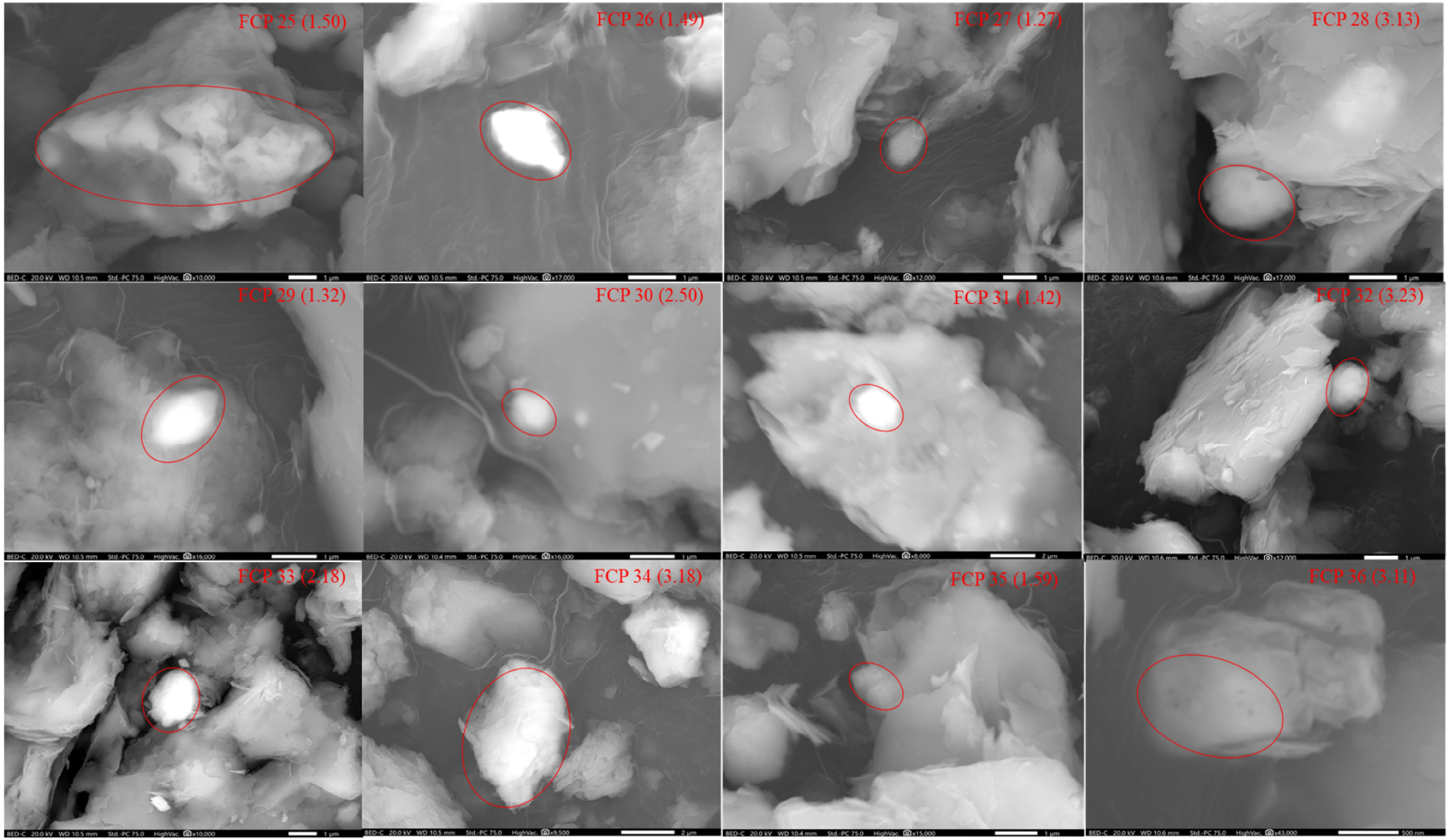
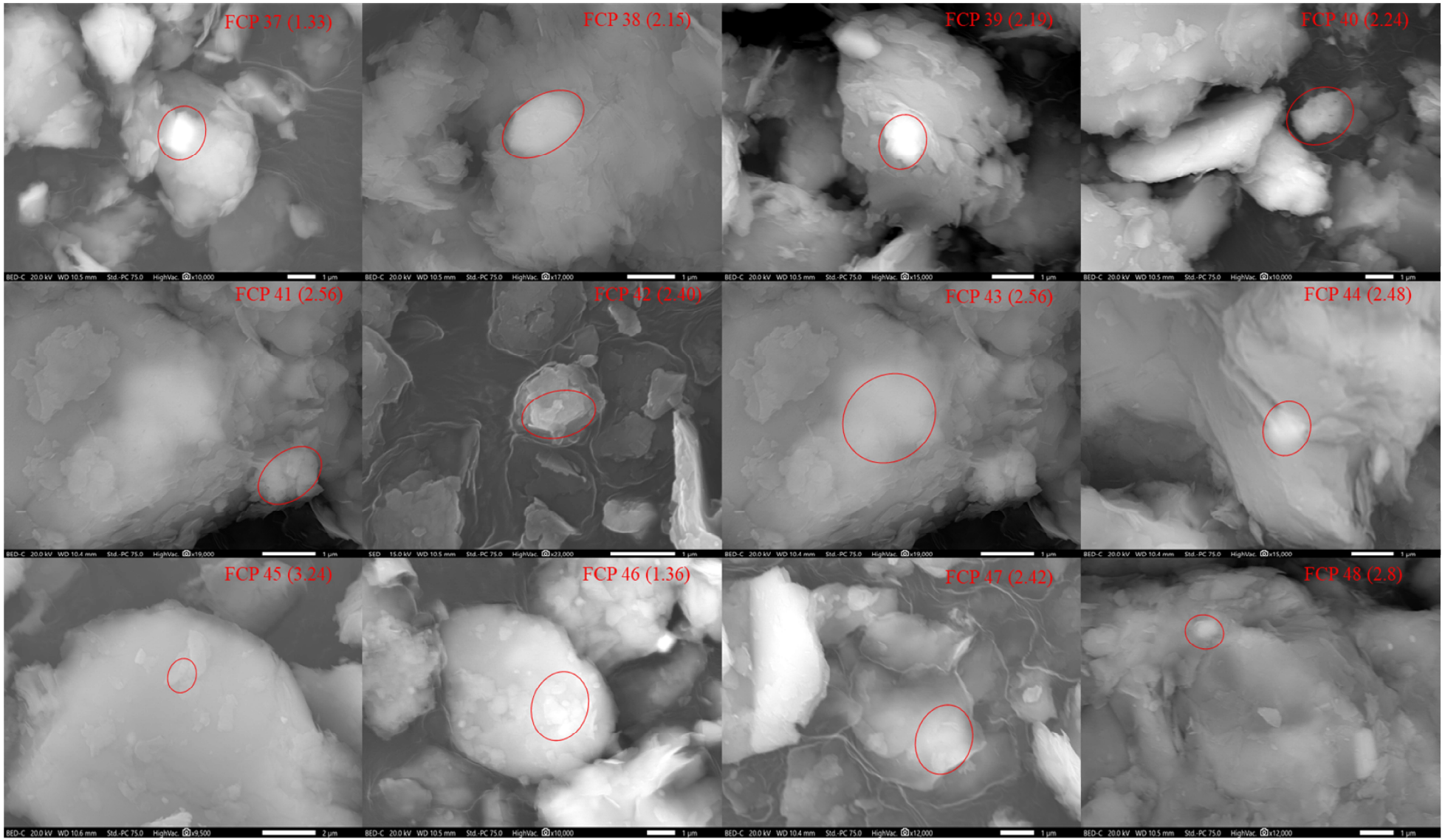

FCP 50 (1.11.126)
Spectrum 126
Wt% σ
O 47.7 0.2
Si 17.2 0.1
Al 14.8 0.1
Fe 7.3 0.1
P 2.8 0.1
Mg 2.7 0.0
Ce 2.4 0.1
K 2.4 0.0
La 1.2 0.1
Nd 0.8 0.1
Ca 0.4 0.0
Ti 0.3 0.0
Powered by Tru-Q®
cps/eV
keV

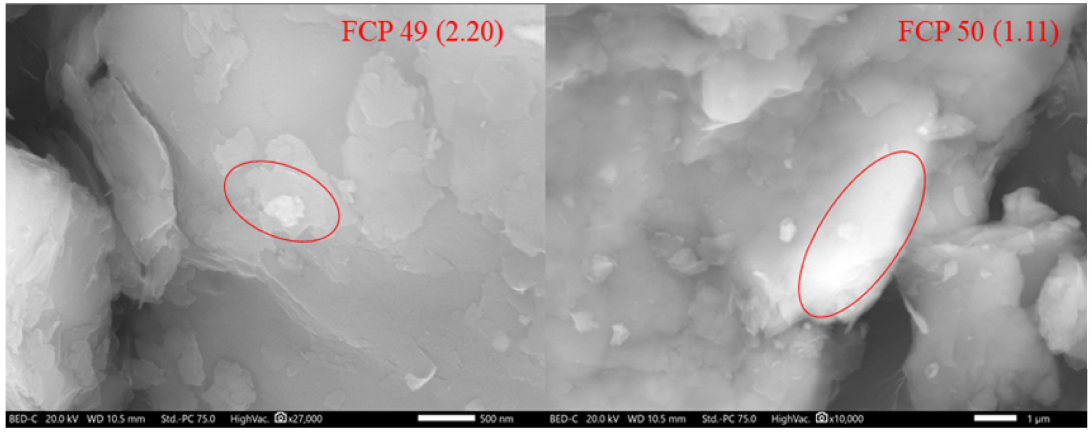
Figure A.4 SEM images of the particles containing REEs found from the Fire Clay coal waste. (The images are labelled as # Particle (Specimen #. Site #))




FCP 13 (2.64)
FCP 14 (2.38)
FCP 15 (1.13)
FCP 16 (2.6)
FCP 17 (1.19)
FCP 18 (2.35)
FCP 19 (1.2)
FCP 20 (3.6)
FCP 21 (2.33)
FCP 22 (1.21)
FCP 23 (1.30)
FCP 24 (3.57)


FCP 25 (1.50)
FCP 26 (1.49)
FCP 27 (1.27)
FCP 28 (3.13)
FCP 29 (1.32)
FCP 30 (2.50)
FCP 31 (1.42)
FCP 32 (3.23)
FCP 33 (2.18)
FCP 34 (3.18)
FCP 35 (1.59)
FCP 36 (3.11)


FCP 37 (1.33)
FCP 38 (2.15)
FCP 39 (2.19)
FCP 40 (2.24)
FCP 41 (2.56)
FCP 42 (2.40)
FCP 43 (2.56)
FCP 44 (2.48)
FCP 45 (3.24)
FCP 46 (1.36)
FCP 47 (2.42)
FCP 48 (2.8)

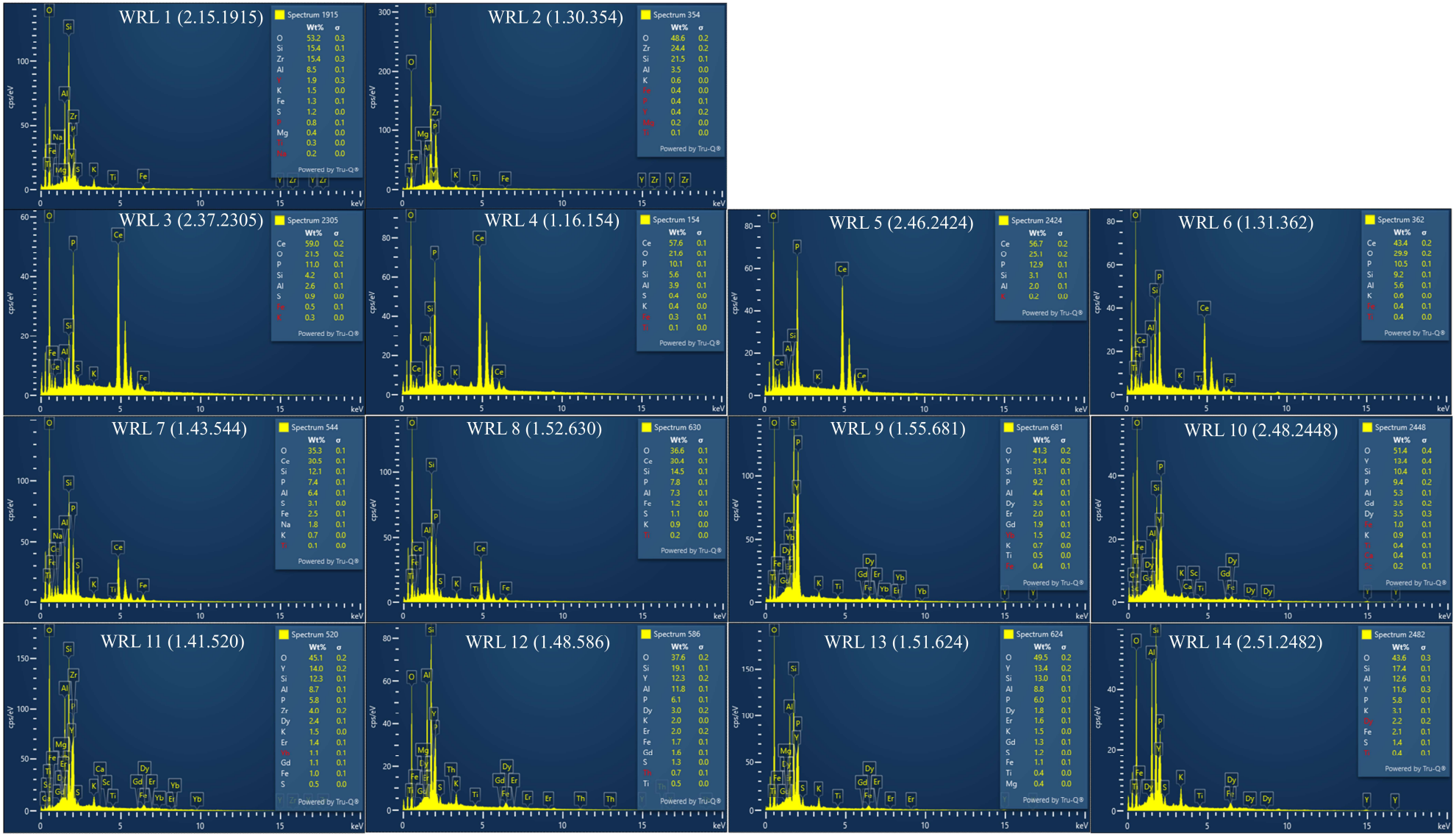

FCP 49 (2.20)
FCP 50 (1.11)
BED-C 20.0 kV WD 10.5 mm Std.-PC 75.0 HighVac. x27,000 500 nm
BED-C 20.0 kV WD 10.5 mm Std.-PC 75.0 HighVac. x10,000 1 µm

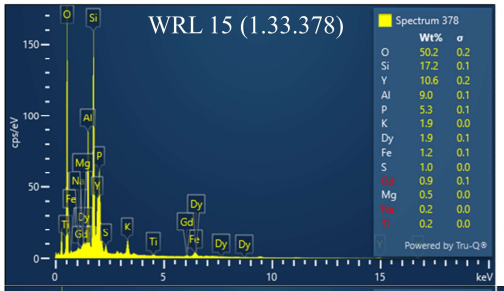
Appendix B Supporting materials for Chapter 3

Table B.1Elemental compositions of the particles containing REEs found from the raw Western Kentucky No. 13 (WK No. 13) coal waste leaching residue through SEM-EDS analysis.

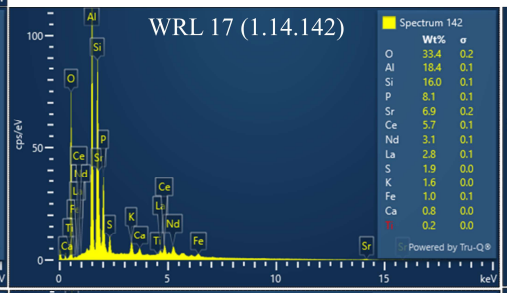
Particle #	Specimen #	ie (Area	Spectrum #	Mineral	Al (%)	Si (%)	O (%)	Ca (%)	P (%)	Fe (%)	K (%)	S (%)	Ba (%)	Mg (%)	Ti (%)	Na (%)	Sr (%)	F(%)	Zr (%)	Sc (%)	La (%)	Ce(%)	Pr (%)	Nd(%)	Sm (%)	Gd (%)	Y(%)	Dy (%)	Er (%)	Yb (%)	Ho (%)	Th(%)	U (%)	TREE (%	Sum (%)	Al/Si	Al/P	TREE/P
WRL 1	2	15	1915	Zircon	8.5	15.4	53.2	0.0	0.8	1.3	1.5	1.2	0.0	0.4	0.3	0.2	0.0	0.0	15.4	0.0	0.0	0.0	0.0	0.0	0.0	0.0	1.9	0.0	0.0	0.0	0.0	0.0	0.0	1.9	100	0.6	10.6	2.4
WRL 2	1	30	354	Zircon	3.5	21.5	48.6	0.0	0.4	0.4	0.6	0.0	0.0	0.2	0.1	0.0	0.0	0.0	24.4	0.0	0.0	0.0	0.0	0.0	0.0	0.0	0.4	0.0	0.0	0.0	0.0	0.0	0.0	0.4	100	0.2	8.8	1.0
WRL 3	2	37	2305	Monazite	2.6	4.2	21.5	0.0	11.0	0.5	0.3	0.9	0.0	0.0	0.0	0.0	0.0	0.0	0.0	0.0	0.0	59.0	0.0	0.0	0.0	0.0	0.0	0.0	0.0	0.0	0.0	0.0	0.0	59.0	100	0.6	0.2	5.4
WRL 4	1	16	154	Monazite	3.9	5.6	21.6	0.0	10.1	0.3	0.4	0.4	0.0	0.0	0.1	0.0	0.0	0.0	0.0	0.0	0.0	57.6	0.0	0.0	0.0	0.0	0.0	0.0	0.0	0.0	0.0	0.0	0.0	57.6	100	0.7	0.4	5.7
WRL 5	2	46	2424	Monazite	2.0	3.1	25.1	0.0	12.9	0.0	0.2	0.0	0.0	0.0	0.0	0.0	0.0	0.0	0.0	0.0	0.0	56.7	0.0	0.0	0.0	0.0	0.0	0.0	0.0	0.0	0.0	0.0	0.0	56.7	100	0.6	0.2	4.4
WRL 6	1	31	362	Monazite	5.6	9.2	29.9	0.0	10.5	0.4	0.6	0.0	0.0	0.0	0.4	0.0	0.0	0.0	0.0	0.0	0.0	43.4	0.0	0.0	0.0	0.0	0.0	0.0	0.0	0.0	0.0	0.0	0.0	43.4	100	0.6	0.5	4.1
WRL 7	1	43	544	Monazite	6.4	12.1	35.3	0.0	7.4	2.5	0.7	3.1	0.0	0.0	0.1	1.8	0.0	0.0	0.0	0.0	0.0	30.5	0.0	0.0	0.0	0.0	0.0	0.0	0.0	0.0	0.0	0.0	0.0	30.5	100	0.5	0.9	4.1
WRL 8	1	52	630	Monazite	7.3	14.5	36.6	0.0	7.8	1.2	0.9	1.1	0.0	0.0	0.2	0.0	0.0	0.0	0.0	0.0	0.0	30.4	0.0	0.0	0.0	0.0	0.0	0.0	0.0	0.0	0.0	0.0	0.0	30.4	100	0.5	0.9	3.9
WRL 9	1	55	681	Xenotime	4.4	13.1	41.3	0.0	9.2	0.4	0.7	0.0	0.0	0.0	0.5	0.0	0.0	0.0	0.0	0.0	0.0	0.0	0.0	0.0	0.0	1.9	21.4	3.5	2.0	1.5	0.0	0.0	0.0	30.3	100	0.3	0.5	3.3
WRL 10	2	48	2448	Xenotime	5.3	10.4	51.4	0.4	9.4	1.0	0.9	0.0	0.0	0.0	0.4	0.0	0.0	0.0	0.0	0.2	0.0	0.0	0.0	0.0	0.0	3.5	13.4	3.5	0.0	0.0	0.0	0.0	0.0	20.6	100	0.5	0.6	2.2
WRL 11	1	41	520	Xenotime	9.4	13.5	46.1	0.2	6.8	1.1	1.6	0.5	0.0	0.5	0.4	0.0	0.0	0.0	0.0	0.1	0.0	0.0	0.0	0.0	0.0	1.2	13.5	2.5	1.5	1.2	0.0	0.0	0.0	20.0	100	0.7	1.4	2.9
WRL 12	1	48	586	Xenotime	11.8	19.1	37.6	0.0	6.1	1.7	2.0	1.3	0.0	0.5	0.5	0.0	0.0	0.0	0.0	0.0	0.0	0.0	0.0	0.0	0.0	1.6	12.3	3.0	2.0	0.0	0.0	0.7	0.0	18.9	100	0.6	1.9	3.1
WRL 13	1	51	624	Xenotime	8.8	13.0	49.5	0.0	6.0	1.1	1.5	1.2	0.0	0.4	0.4	0.0	0.0	0.0	0.0	0.0	0.0	0.0	0.0	0.0	0.0	1.3	13.4	1.8	1.6	0.0	0.0	0.0	0.0	18.1	100	0.7	1.5	3.0
WRL 14	2	51	2482	Xenotime	12.6	17.4	43.6	0.0	5.8	2.1	3.1	1.4	0.0	0.0	0.4	0.0	0.0	0.0	0.0	0.0	0.0	0.0	0.0	0.0	0.0	0.0	11.6	2.2	0.0	0.0	0.0	0.0	0.0	13.8	100	0.7	2.2	2.4
WRL 15	1	33	378	Xenotime	9.0	17.2	50.2	0.0	5.3	1.2	1.9	1.0	0.0	0.5	0.2	0.0	0.0	0.0	0.0	0.0	0.0	0.0	0.0	0.0	0.0	0.9	10.6	1.9	0.0	0.0	0.0	0.0	0.0	13.4	100	0.5	1.7	2.5
WRL 16	1	35	424	Crandallite	16.9	6.3	44.4	0.6	10.3	0.8	0.6	1.5	0.4	0.0	0.0	0.0	5.5	0.0	0.0	0.0	2.8	5.5	0.7	3.4	0.5	0.0	0.0	0.0	0.0	0.0	0.0	0.0	0.0	12.9	100	2.7	1.6	1.3
WRL 17	1	14	142	Crandallite	18.4	16.0	33.4	0.8	8.1	1.0	1.6	1.9	0.0	0.0	0.2	0.0	6.9	0.0	0.0	0.0	2.8	5.7	0.0	3.1	0.0	0.0	0.0	0.0	0.0	0.0	0.0	0.0	0.0	11.6	100	1.2	2.3	1.4
WRL 18	2	42	2372	Crandallite	13.5	19.7	46.3	0.2	5.8	0.6	1.4	0.4	0.0	0.3	0.0	1.0	1.8	0.0	0.0	0.0	2.1	4.4	0.5	2.0	0.0	0.0	0.0	0.0	0.0	0.0	0.0	0.0	0.0	9.0	100	0.7	2.3	1.6
WRL 19	1	57	702	Crandallite	11.3	16.9	54.2	0.2	5.6	0.4	0.6	0.6	0.0	0.0	0.2	0.0	1.8	0.0	0.0	0.0	2.4	4.2	0.0	1.6	0.0	0.0	0.0	0.0	0.0	0.0	0.0	0.0	0.0	8.2	100	0.7	2.0	1.5
WRL 20	1	39	504	Crandallite	17.4	22.3	40.9	0.3	3.6	1.7	2.8	0.7	0.0	0.6	0.3	0.0	2.4	0.0	0.0	0.0	1.8	3.7	0.0	1.4	0.0	0.0	0.0	0.0	0.0	0.0	0.0	0.0	0.0	6.9	100	0.8	4.8	1.9
WRL 21	2	18	1959	Crandallite	9.8	20.4	54.1	0.2	4.3	0.5	0.7	0.7	0.0	0.0	0.0	1.2	1.7	0.0	0.0	0.0	1.8	3.2	0.4	1.1	0.0	0.0	0.0	0.0	0.0	0.0	0.0	0.0	0.0	6.5	100	0.5	2.3	1.5
WRL 22	2	33	2265	Crandallite	15.7	13.5	48.6	0.4	5.4	1.0	1.5	2.0	0.0	0.4	0.2	0.0	4.9	0.0	0.0	0.0	1.2	2.8	0.4	1.6	0.4	0.0	0.0	0.0	0.0	0.0	0.0	0.0	0.0	6.4	100	1.2	2.9	1.2
WRL 23	1	23	246	Crandallite	16.8	18.8	43.6	0.6	4.6	1.4	3.0	0.7	0.0	0.6	0.5	0.0	3.2	0.0	0.0	0.0	1.5	3.0	0.4	1.2	0.0	0.0	0.0	0.0	0.0	0.0	0.0	0.0	0.0	6.1	100	0.9	3.7	1.3
WRL 24	1	18	193	Crandallite	16.8	13.2	43.6	0.8	6.0	1.5	1.8	4.7	0.0	0.3	0.8	0.6	4.3	0.0	0.0	0.0	1.2	3.1	0.3	1.0	0.0	0.0	0.0	0.0	0.0	0.0	0.0	0.0	0.0	5.6	100	1.3	2.8	0.9
WRL 25	2	2	1652	Crandallite	19.8	8.1	37.0	2.2	8.9	3.7	1.0	3.6	1.0	0.0	0.3	0.0	9.6	0.0	0.0	0.0	1.3	2.5	0.0	0.9	0.0	0.0	0.0	0.0	0.0	0.0	0.0	0.0	0.0	4.7	100	2.4	2.2	0.5
WRL 26	2	9	1793	Crandallite	13.8	18.8	47.5	0.9	4.8	1.9	1.4	1.7	0.8	0.4	0.4	0.0	3.9	0.0	0.0	0.0	1.0	2.1	0.0	0.8	0.0	0.0	0.0	0.0	0.0	0.0	0.0	0.0	0.0	3.9	100	0.7	2.9	0.8
WRL 27	1	37	453	Crandallite	14.1	12.9	54.6	0.2	4.4	1.2	1.6	3.1	0.0	0.3	0.2	0.6	3.7	0.0	0.0	0.0	0.7	1.8	0.0	0.7	0.0	0.0	0.0	0.0	0.0	0.0	0.0	0.0	0.0	3.2	100	1.1	3.2	0.7
WRL 28	2	40	2347	Crandallite	16.6	8.3	51.2	1.1	7.0	2.0	0.9	1.9	1.4	0.3	0.0	0.0	6.0	0.0	0.0	0.0	0.0	2.3	0.0	0.9	0.0	0.0	0.0	0.0	0.0	0.0	0.0	0.0	0.0	3.2	100	2.0	2.4	0.5
WRL 29	2	3	1660	Crandallite	14.4	18.4	50.2	1.1	3.5	1.8	2.0	2.1	0.9	0.0	0.2	0.0	3.2	0.0	0.0	0.0	0.6	1.1	0.0	0.5	0.0	0.0	0.0	0.0	0.0	0.0	0.0	0.0	0.0	2.2	100	0.8	4.1	0.6
WRL 30	2	36	2298	Crandallite	15.4	18.4	52.5	0.3	2.6	1.3	2.6	0.9	0.0	0.7	0.4	0.0	2.8	0.0	0.0	0.0	0.8	1.2	0.0	0.0	0.0	0.0	0.0	0.0	0.0	0.0	0.0	0.0	0.0	2.0	100	0.8	5.9	0.8
WRL 31	2	34	2267	Crandallite	19.1	18.2	50.2	0.2	3.1	1.0	1.3	1.8	0.0	0.0	0.2	0.0	3.5	0.0	0.0	0.0	0.0	1.0	0.0	0.5	0.0	0.0	0.0	0.0	0.0	0.0	0.0	0.0	0.0	1.5	100	1.0	6.2	0.5
WRL 32	2	4	1666	Crandallite	15.2	20.7	49.8	0.4	2.7	2.5	3.2	0.6	0.0	0.9	0.0	0.0	2.9	0.0	0.0	0.0	0.0	1.0	0.0	0.0	0.0	0.0	0.0	0.0	0.0	0.0	0.0	0.0	0.0	1.0	100	0.7	5.6	0.4
WRL 33	2	50	2467	Crandallite	16.6	5.6	51.7	1.8	8.0	1.7	0.5	2.8	1.9	0.0	0.0	0.0	8.4	0.0	0.0	0.0	0.0	0.6	0.0	0.4	0.0	0.0	0.0	0.0	0.0	0.0	0.0	0.0	0.0	1.0	100	3.0	2.1	0.1
WRL 34	1	2	16	Crandallite	16.0	15.0	47.0	1.0	5.7	2.3	1.9	1.9	1.3	0.4	0.3	0.0	6.4	0.0	0.0	0.0	0.0	0.4	0.0	0.4	0.0	0.0	0.0	0.0	0.0	0.0	0.0	0.0	0.0	0.8	100	1.1	2.8	0.1
WRL 35	2	10	1809	Crandallite	16.3	19.7	53.0	0.5	2.3	1.4	2.5	0.6	0.0	0.6	0.1	0.0	2.1	0.0	0.0	0.0	0.0	0.8	0.0	0.0	0.0	0.0	0.0	0.0	0.0	0.0	0.0	0.0	0.0	0.8	100	0.8	7.1	0.3
WRL 36	2	12	1844	Crandallite	14.6	13.9	55.9	0.9	4.3	1.1	1.6	2.3	0.0	0.4	0.0	0.4	3.7	0.0	0.0	0.0	0.0	0.7	0.0	0.0	0.0	0.0	0.0	0.0	0.0	0.0	0.0	0.0	0.0	0.7	100	1.1	3.4	0.2
WRL 37	2	25	2095	Crandallite	15.7	7.7	50.2	1.4	7.5	1.9	1.0	3.8	0.0	0.2	0.8	0.0	9.1	0.0	0.0	0.0	0.7	0.0	0.0	0.0	0.0	0.0	0.0	0.0	0.0	0.0	0.0	0.0	0.0	0.7	100	2.0	2.1	0.1
WRL 38	2	21	2034	Crandallite	20.1	14.0	39.9	2.8	8.5	2.1	1.7	1.6	1.6	0.0	0.0	0.0	7.2	0.0	0.0	0.0	0.0	0.6	0.0	0.0	0.0	0.0	0.0	0.0	0.0	0.0	0.0	0.0	0.0	0.6	100	1.4	2.4	0.1
WRL 39	2	28	2156	Crandallite	17.3	21.0	44.5	0.5	3.3	2.2	2.6	2.2	0.0	0.7	0.4	0.0	4.7	0.0	0.0	0.0	0.0	0.6	0.0	0.0	0.0	0.0	0.0	0.0	0.0	0.0	0.0	0.0	0.0	0.6	100	0.8	5.2	0.2
WRL 40	1	65	791	Crandallite	13.7	10.9	52.9	0.5	4.3	2.9	1.1	4.8	0.8	0.2	0.3	0.3	6.8	0.0	0.0	0.0	0.0	0.5	0.0	0.0	0.0	0.0	0.0	0.0	0.0	0.0	0.0	0.0	0.0	0.5	100	1.3	3.2	0.1
WRL 41	1	42	539	Crandallite	14.3	11.8	55.1	0.7	4.0	2.2	1.3	2.7	0.9	0.4	0.4	0.0	5.6	0.0	0.0	0.0	0.0	0.5	0.0	0.0	0.0	0.0	0.0	0.0	0.0	0.0	0.0	0.0	0.0	0.5	100	1.2	3.6	0.1
WRL 42	2	8	1776	Crandallite	16.0	15.3	49.3	0.5	3.8	2.7	1.9	2.2	0.9	0.4	1.0	0.3	5.1	0.0	0.0	0.0	0.0	0.5	0.0	0.0	0.0	0.0	0.0	0.0	0.0	0.0	0.0	0.0	0.0	0.5	100	1.0	4.2	0.1
WRL 43	2	43	2380	Crandallite	14.1	14.5	55.8	0.6	4.4	1.1	1.9	1.1	0.9	0.4	0.2	0.3	4.3	0.0	0.0	0.0	0.0	0.5	0.0	0.0	0.0	0.0	0.0	0.0	0.0	0.0	0.0	0.0	0.0	0.5	100	1.0	3.2	0.1
WRL 44	1	4	39	Crandallite	15.9	14.8	45.9	0.4	3.3	4.9	2.1	4.9	0.7	0.5	0.2	0.0	5.9	0.0	0.0	0.0	0.0	0.4	0.0	0.0	0.0	0.0	0.0	0.0	0.0	0.0	0.0	0.0	0.0	0.4	100	1.1	4.8	0.1
WRL 45	1	22	233	Crandallite	12.9	22.1	52.4	0.3	2.0	1.6	3.2	1.2	0.0	1.0	0.2	0.3	2.5	0.0	0.0	0.0	0.0	0.4	0.0	0.0	0.0	0.0	0.0	0.0	0.0	0.0	0.0	0.0	0.0	0.4	100	0.6	6.5	0.2
WRL 46	1	25	265	Crandallite	16.2	20.3	49.8	0.4	2.7	1.2	3.3	0.6	0.0	0.5	1.4	0.0	3.1	0.0	0.0	0.0	0.0	0.4	0.0	0.0	0.0	0.0	0.0	0.0	0.0	0.0	0.0	0.0	0.0	0.4	100	0.8	6.0	0.1
WRL 47	1	50	609	Crandallite	16.5	5.6	49.1	0.5	4.6	2.7	2.0	8.4	1.0	0.0	0.0	0.5	8.7	0.0	0.0	0.0	0.0	0.4	0.0	0.0	0.0	0.0	0.0	0.0	0.0	0.0	0.0	0.0	0.0	0.4	100	2.9	3.6	0.1
WRL 48	1	7	72	Crandallite	16.7	14.8	41.1	1.4	5.8	3.2	2.1	4.5	1.9	0.3	0.2	0.3	7.4	0.0	0.0	0.0	0.0	0.3	0.0	0.0	0.0	0.0	0.0	0.0	0.0	0.0	0.0	0.0	0.0	0.3	100	1.1	2.9	0.1
WRL 49	1	9	95	Crandallite	15.9	17.2	42.6	1.2	4.8	2.7	2.4	4.0	1.7	0.5	0.4	0.3	6.1	0.0	0.0	0.0	0.0	0.3	0.0	0.0	0.0	0.0	0.0	0.0	0.0	0.0	0.0	0.0	0.0	0.3	100	0.9	3.3	0.1

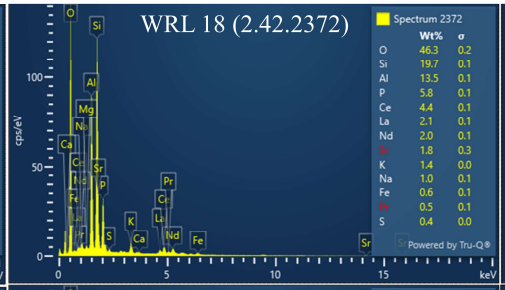
Figure B.1 EDS spectra of the particles containing REEs found from the raw Western Kentucky No. 13 (WK No. 13) coal waste leaching residue. (The spectra are labelled as WRL # (Specimen #. Site #. Spectrum #))

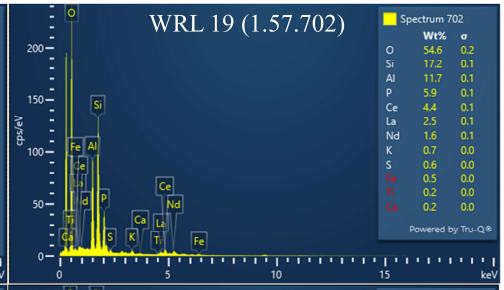


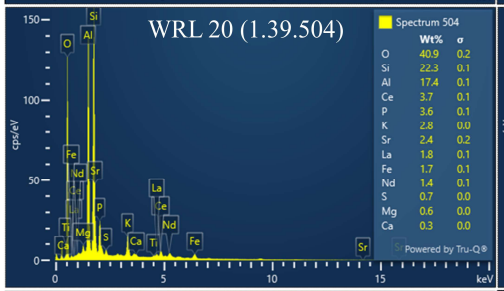

WRL 15 (1.33.378)
Spectrum 378
Wt% σ
O 50.2 0.2
Si 17.2 0.1
Y 10.6 0.2
Al 9.0 0.1
P 5.3 0.1
K 1.9 0.0
Dy 1.9 0.1
Fe 1.2 0.1
S 1.0 0.0
Nd 0.9 0.1
Mg 0.5 0.0
Na 0.2 0.0
Yt 0.2 0.0
Powered by Tru-Q®
cps/eV
keV

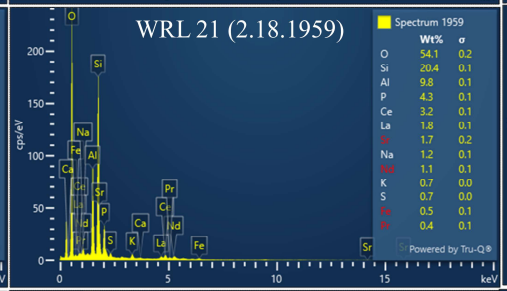

WRL 16 (1.35.424)
Spectrum 424
Wt% σ
O 44.4 0.2
Al 16.9 0.1
P 10.3 0.1
Si 6.3 0.1
Ce 5.5 0.1
Sr 5.5 0.2
Nd 3.4 0.1
La 2.8 0.1
S 1.5 0.0
Fe 0.8 0.1
Pr 0.7 0.1
Ca 0.6 0.0
K 0.6 0.0
Powered by Tru-Q®
cps/eV
keV

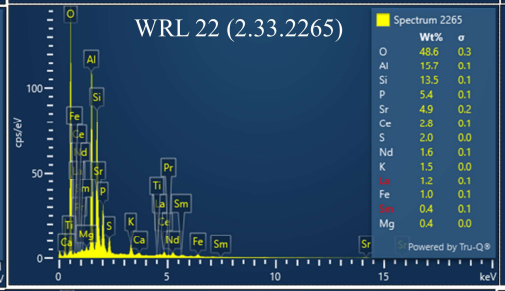

WRL 17 (1.14.142)
Spectrum 142
Wt% σ
O 33.4 0.2
Al 18.4 0.1
Si 16.0 0.1
P 8.1 0.1
Sr 6.9 0.2
Ce 5.7 0.1
Nd 3.1 0.1
La 2.8 0.1
S 1.9 0.0
K 1.6 0.0
Fe 1.0 0.1
Ca 0.8 0.0
Yt 0.2 0.0
Powered by Tru-Q®
cps/eV
keV

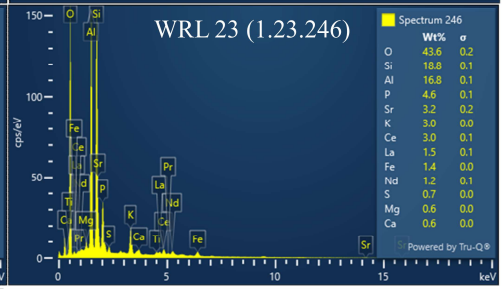

WRL 18 (2.42.2372)
Spectrum 2372
Wt% σ
O 46.3 0.2
Si 19.7 0.1
Al 13.5 0.1
P 5.8 0.1
Ce 4.4 0.1
La 2.1 0.1
Nd 2.0 0.1
Pr 1.8 0.3
K 1.4 0.0
Na 1.0 0.1
Fe 0.6 0.1
Ba 0.5 0.1
S 0.4 0.0
Powered by Tru-Q®
cps/eV
keV

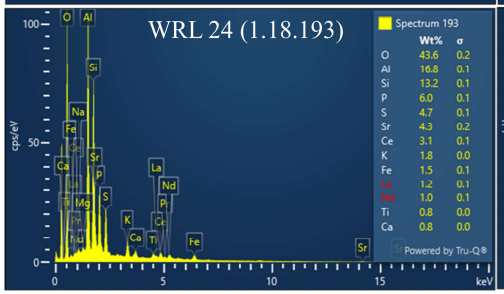

WRL 19 (1.57.702)
Spectrum 702
Wt% σ
O 54.6 0.2
Si 17.2 0.1
Al 11.7 0.1
P 5.9 0.1
Ce 4.4 0.1
La 2.5 0.1
Nd 1.6 0.1
K 0.7 0.0
S 0.6 0.0
Ba 0.5 0.0
Pr 0.2 0.0
Ca 0.2 0.0
Powered by Tru-Q®
cps/eV
keV

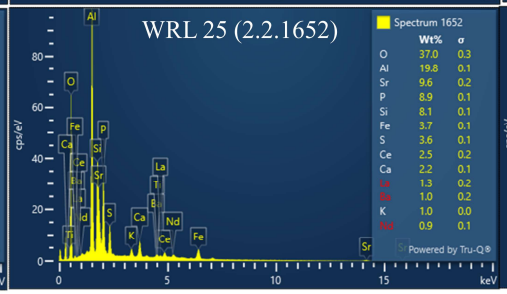

WRL 20 (1.39.504)
Spectrum 504
Wt% σ
O 40.9 0.2
Si 22.3 0.1
Al 17.4 0.1
Ce 3.7 0.1
P 3.6 0.1
K 2.8 0.0
Sr 2.4 0.2
La 1.8 0.1
Fe 1.7 0.1
Nd 1.4 0.1
S 0.7 0.0
Mg 0.6 0.0
Ca 0.3 0.0
Powered by Tru-Q®
cps/eV
keV

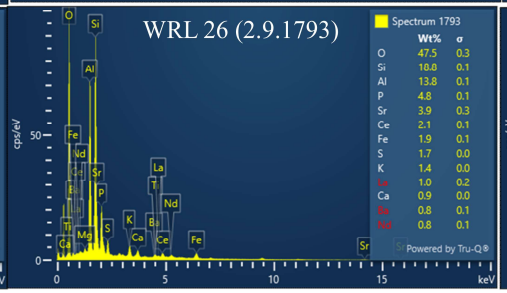

WRL 21 (2.18.1959)
Spectrum 1959
Wt% σ
O 54.1 0.2
Si 20.4 0.1
Al 9.8 0.1
P 4.3 0.1
Ce 3.2 0.1
La 1.8 0.1
Sr 1.7 0.2
Na 1.2 0.1
Nd 1.1 0.1
K 0.7 0.0
S 0.7 0.0
Fe 0.5 0.1
Pr 0.4 0.1
Powered by Tru-Q®
cps/eV
keV

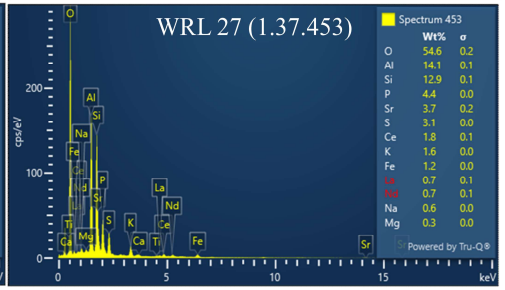

WRL 22 (2.33.2265)
Spectrum 2265
Wt% σ
O 48.6 0.3
Al 15.7 0.1
Si 13.5 0.1
P 5.4 0.1
Sr 4.9 0.2
Ce 2.8 0.1
S 2.0 0.0
Nd 1.6 0.1
K 1.5 0.0
Na 1.2 0.1
Fe 1.0 0.1
Sm 0.4 0.1
Mg 0.4 0.0
Powered by Tru-Q®
cps/eV
keV

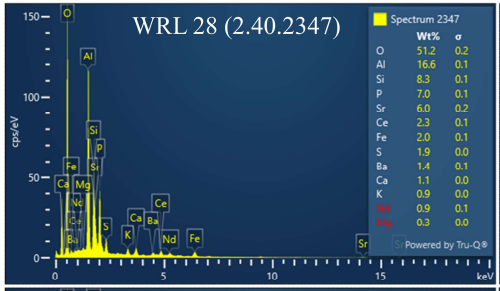

WRL 23 (1.23.246)
Spectrum 246
Wt% σ
O 43.6 0.2
Si 18.8 0.1
Al 16.8 0.1
P 4.6 0.1
Sr 3.2 0.2
K 3.0 0.0
Ce 3.0 0.1
La 1.5 0.1
Fe 1.4 0.0
Nd 1.2 0.1
S 0.7 0.0
Mg 0.6 0.0
Ca 0.6 0.0
Powered by Tru-Q®
cps/eV
keV

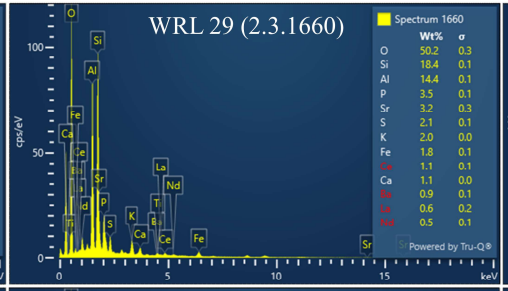

WRL 24 (1.18.193)
Spectrum 193
Wt% σ
O 43.6 0.2
Al 16.8 0.1
Si 13.2 0.1
P 6.0 0.1
S 4.7 0.1
Sr 4.3 0.2
Ce 3.1 0.1
K 1.8 0.0
Fe 1.5 0.1
La 1.2 0.1
Nd 1.0 0.1
Ti 0.8 0.0
Ca 0.8 0.0
Powered by Tru-Q®
cps/eV
keV

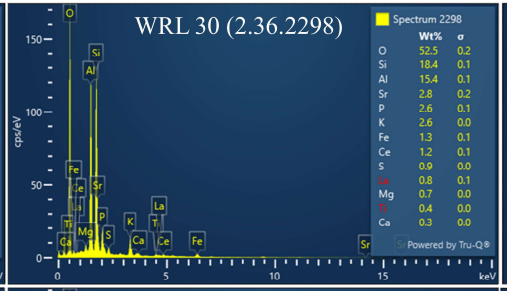

WRL 25 (2.2.1652)
Spectrum 1652
Wt% σ
O 37.0 0.3
Al 19.8 0.1
Sr 9.6 0.2
P 8.9 0.1
Si 8.1 0.1
Fe 3.7 0.1
S 3.6 0.1
Ce 2.5 0.2
Ca 2.2 0.1
La 1.3 0.2
Ba 1.0 0.2
K 1.0 0.0
Nd 0.9 0.1
Powered by Tru-Q®
cps/eV
keV

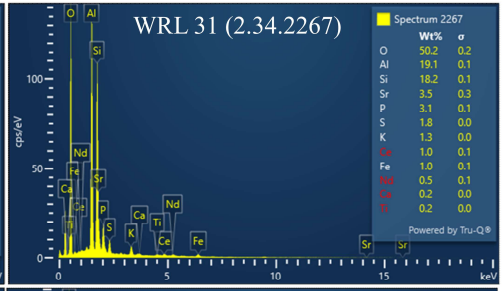

WRL 26 (2.9.1793)
Spectrum 1793
Wt% σ
O 47.5 0.3
Si 18.8 0.1
Al 13.8 0.1
P 4.8 0.1
Sr 3.9 0.3
Ce 2.1 0.1
Fe 1.9 0.1
S 1.7 0.0
K 1.4 0.0
La 1.0 0.2
Ca 0.9 0.0
Ba 0.8 0.1
Nd 0.8 0.1
Powered by Tru-Q®
cps/eV
keV

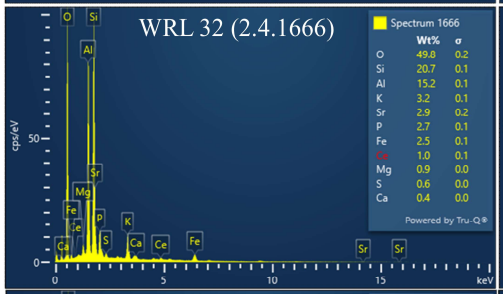

WRL 27 (1.37.453)
Spectrum 453
Wt% σ
O 54.6 0.2
Al 14.1 0.1
Si 12.9 0.1
P 4.4 0.0
Sr 3.7 0.2
S 3.1 0.0
Ce 1.8 0.1
K 1.6 0.0
Fe 1.2 0.0
La 0.7 0.1
Nd 0.7 0.1
Na 0.6 0.0
Mg 0.3 0.0
Powered by Tru-Q®
cps/eV
keV

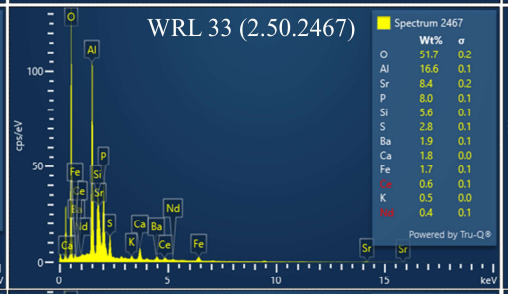

WRL 28 (2.40.2347)
Spectrum 2347
Wt% σ
O 51.2 0.2
Al 16.6 0.1
Si 8.3 0.1
P 7.0 0.1
Sr 6.0 0.2
Ce 2.3 0.1
Fe 2.0 0.1
S 1.9 0.0
Ba 1.4 0.1
Ca 1.1 0.0
K 0.9 0.0
Nd 0.9 0.1
Mg 0.3 0.0
Powered by Tru-Q®
cps/eV
keV

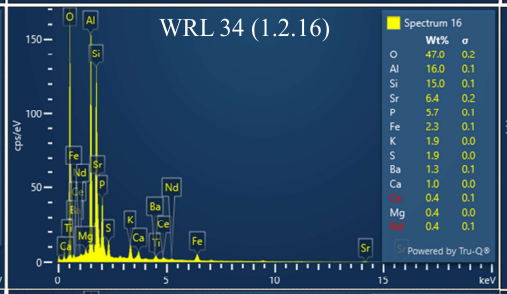

WRL 29 (2.3.1660)
Spectrum 1660
Wt% σ
O 50.2 0.3
Si 18.4 0.1
Al 14.4 0.1
P 3.5 0.1
Sr 3.2 0.3
S 2.1 0.1
K 2.0 0.0
Fe 1.8 0.1
Ce 1.1 0.1
Ca 1.1 0.0
Ba 0.9 0.1
La 0.6 0.2
Nd 0.5 0.1
Powered by Tru-Q®
cps/eV
keV

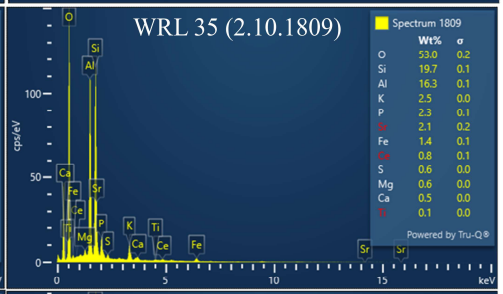

WRL 30 (2.36.2298)
Spectrum 2298
Wt% σ
O 52.5 0.2
Si 18.4 0.1
Al 15.4 0.1
Sr 2.8 0.2
P 2.6 0.1
K 2.6 0.0
Fe 1.3 0.1
Ce 1.2 0.1
S 0.9 0.0
Nd 0.8 0.1
Mg 0.7 0.0
Ti 0.4 0.0
Ca 0.3 0.0
Powered by Tru-Q®
cps/eV
keV

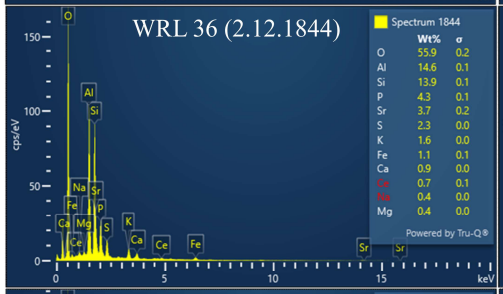

WRL 31 (2.34.2267)
Spectrum 2267
Wt% σ
O 50.2 0.2
Al 19.1 0.1
Si 18.2 0.1
Sr 3.5 0.3
P 3.1 0.1
S 1.8 0.0
K 1.3 0.0
Ce 1.0 0.1
Fe 1.0 0.1
Nd 0.5 0.1
Ca 0.2 0.0
Ti 0.2 0.0
Powered by Tru-Q®
cps/eV
keV

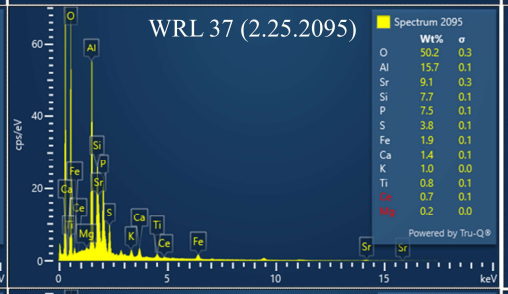

WRL 32 (2.4.1666)
Spectrum 1666
Wt% σ
O 49.8 0.2
Si 20.7 0.1
Al 15.2 0.1
K 3.2 0.1
Sr 2.9 0.2
P 2.7 0.1
Fe 2.5 0.1
Ce 1.0 0.1
Mg 0.9 0.0
S 0.6 0.0
Ca 0.4 0.0
Powered by Tru-Q®
cps/eV
keV

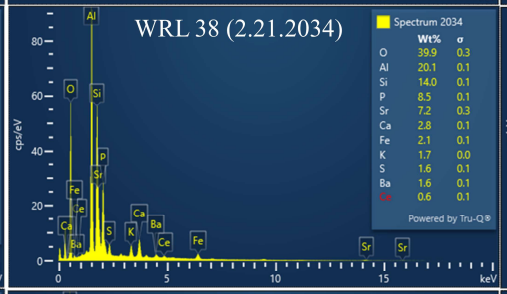

WRL 33 (2.50.2467)
Spectrum 2467
Wt% σ
O 51.7 0.2
Al 16.6 0.1
Sr 8.4 0.2
P 8.0 0.1
Si 5.6 0.1
S 2.8 0.1
Ba 1.9 0.1
Ca 1.8 0.0
Fe 1.7 0.1
Ce 0.6 0.1
K 0.5 0.0
Nd 0.4 0.1
Powered by Tru-Q®
cps/eV
keV

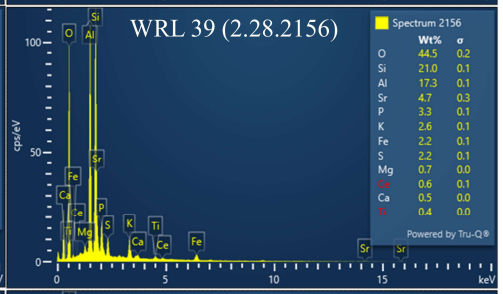

WRL 34 (1.2.16)
Spectrum 16
Wt% σ
O 47.0 0.2
Al 16.0 0.1
Si 15.0 0.1
Sr 6.4 0.2
P 5.7 0.1
Fe 2.3 0.1
K 1.9 0.0
S 1.9 0.0
Ba 1.3 0.1
Ca 1.0 0.0
Ce 0.4 0.1
Mg 0.4 0.0
Nd 0.4 0.1
Powered by Tru-Q®
cps/eV
keV

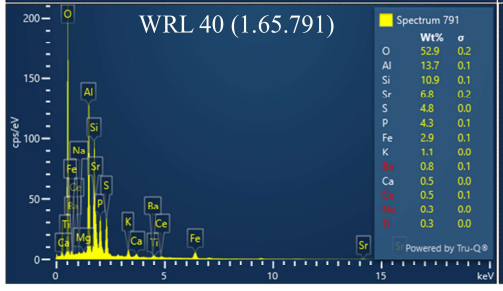

WRL 35 (2.10.1809)
Spectrum 1809
Wt% σ
O 53.0 0.2
Si 19.7 0.1
Al 16.3 0.1
K 2.5 0.0
P 2.3 0.1
Sr 2.1 0.2
Fe 1.4 0.1
Ce 0.8 0.1
S 0.6 0.0
Mg 0.6 0.0
Ca 0.5 0.0
Ti 0.1 0.0
Powered by Tru-Q®
cps/eV
keV


WRL 36 (2.12.1844)
Spectrum 1844
Wt% σ
O 55.9 0.2
Al 14.6 0.1
Si 13.9 0.1
P 4.3 0.1
Sr 3.7 0.2
S 2.3 0.0
K 1.6 0.0
Fe 1.1 0.1
Ca 0.9 0.0
Ce 0.7 0.1
Na 0.4 0.0
Mg 0.4 0.0
Powered by Tru-Q®
cps/eV
keV

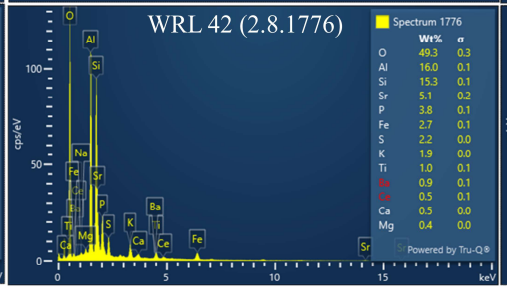

WRL 37 (2.25.2095)
Spectrum 2095
Wt% σ
O 50.2 0.3
Al 15.7 0.1
Sr 9.1 0.3
Si 7.7 0.1
P 7.5 0.1
S 3.8 0.1
Fe 1.9 0.1
Ca 1.4 0.1
K 1.0 0.0
Ti 0.8 0.1
Ce 0.7 0.1
Mg 0.2 0.0
Powered by Tru-Q®
cps/eV
keV

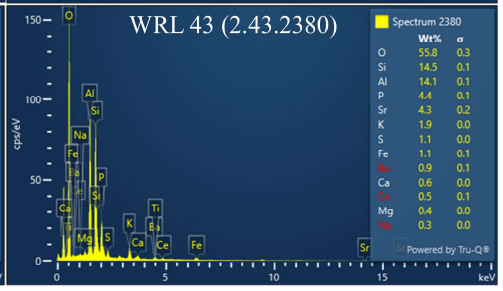

WRL 38 (2.21.2034)
Spectrum 2034
Wt% σ
O 39.9 0.3
Al 20.1 0.1
Si 14.0 0.1
P 8.5 0.1
Sr 7.2 0.3
Ca 2.8 0.1
Fe 2.1 0.1
K 1.7 0.0
S 1.6 0.1
Ba 1.6 0.1
Ce 0.6 0.1
Powered by Tru-Q®
cps/eV
keV

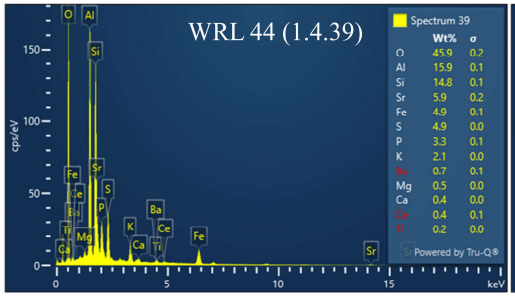

WRL 39 (2.28.2156)
Spectrum 2156
Wt% σ
O 44.5 0.2
Si 21.0 0.1
Al 17.3 0.1
Sr 4.7 0.3
P 3.3 0.1
K 2.6 0.1
Fe 2.2 0.1
S 2.2 0.1
Mg 0.7 0.0
Ce 0.6 0.1
Ca 0.5 0.0
Ti 0.4 0.0
Powered by Tru-Q®
cps/eV
keV

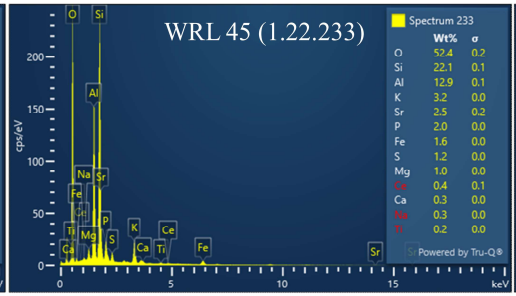

WRL 40 (1.65.791)
Spectrum 791
Wt% σ
O 52.9 0.2
Al 13.7 0.1
Si 10.9 0.1
Sr 6.8 0.2
S 4.8 0.0
P 4.3 0.1
Fe 2.9 0.1
K 1.1 0.0
Ba 0.8 0.1
Ca 0.5 0.0
Ce 0.5 0.1
Na 0.3 0.0
Ti 0.3 0.0
Powered by Tru-Q®
cps/eV
keV

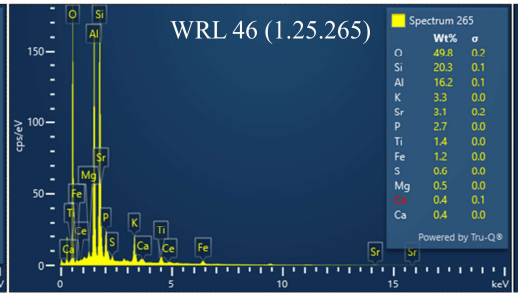

WRL 41 (1.42.539)
Spectrum 539
Wt% σ
O 55.1 0.2
Al 14.1 0.1
Si 11.4 0.1
Sr 5.1 0.2
P 3.7 0.1
S 2.7 0.0
Fe 2.1 0.0
Zr 1.7 0.1
K 1.3 0.0
Ba 0.9 0.1
Ca 0.7 0.0
Ce 0.5 0.1
Ti 0.4 0.0
Powered by Tru-Q®
cps/eV
keV

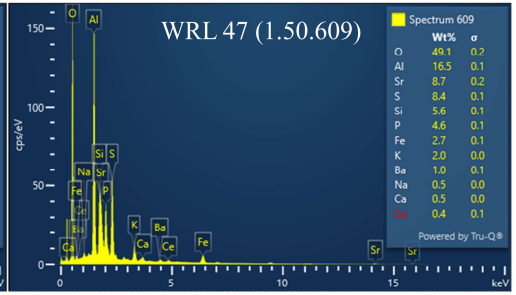

WRL 42 (2.8.1776)
Spectrum 1776
Wt% σ
O 49.3 0.3
Al 16.0 0.1
Si 15.3 0.1
Sr 5.1 0.2
P 3.8 0.1
Fe 2.7 0.1
S 2.2 0.0
K 1.9 0.0
Ti 1.0 0.1
Na 0.9 0.1
Ce 0.5 0.1
Ca 0.5 0.0
Mg 0.4 0.0
Powered by Tru-Q®
cps/eV
keV

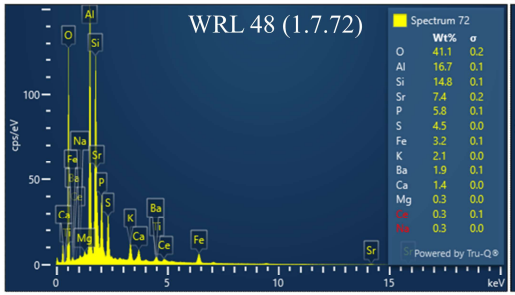

WRL 43 (2.43.2380)
Spectrum 2380
Wt% σ
O 55.8 0.3
Si 14.5 0.1
Al 14.1 0.1
P 4.4 0.1
Sr 4.3 0.2
K 1.9 0.0
S 1.1 0.0
Fe 1.1 0.1
Ba 0.9 0.1
Ca 0.6 0.0
Ce 0.5 0.1
Mg 0.4 0.0
Na 0.3 0.0
Powered by Tru-Q®
cps/eV
keV


WRL 44 (1.4.39)
Spectrum 39
Wt% σ
O 45.9 0.2
Al 15.9 0.1
Si 14.8 0.1
Sr 5.9 0.2
Fe 4.9 0.1
S 4.9 0.0
P 3.3 0.1
K 2.1 0.0
Ba 0.7 0.1
Mg 0.5 0.0
Ca 0.4 0.0
Ce 0.4 0.1
Ti 0.2 0.0
Powered by Tru-Q®
cps/eV
keV


WRL 45 (1.22.233)
Spectrum 233
Wt% σ
O 52.4 0.2
Si 22.1 0.1
Al 12.9 0.1
K 3.2 0.0
Sr 2.5 0.2
P 2.0 0.0
Fe 1.6 0.0
S 1.2 0.0
Mg 1.0 0.0
Ce 0.4 0.1
Ca 0.3 0.0
Na 0.3 0.0
Ti 0.2 0.0
Powered by Tru-Q®
cps/eV
keV


WRL 46 (1.25.265)
Spectrum 265
Wt% σ
O 49.8 0.2
Si 20.3 0.1
Al 16.2 0.1
K 3.3 0.0
Sr 3.1 0.2
P 2.7 0.0
Ti 1.4 0.0
Fe 1.2 0.0
S 0.6 0.0
Mg 0.5 0.0
Ce 0.4 0.1
Ca 0.4 0.0
Powered by Tru-Q®
cps/eV
keV


WRL 47 (1.50.609)
Spectrum 609
Wt% σ
O 49.1 0.2
Al 16.5 0.1
Sr 8.7 0.2
S 8.4 0.1
Si 5.6 0.1
P 4.6 0.1
Fe 2.7 0.1
K 2.0 0.0
Ba 1.0 0.1
Na 0.5 0.0
Ca 0.5 0.0
Ce 0.4 0.1
Powered by Tru-Q®
cps/eV
keV


WRL 48 (1.7.72)
Spectrum 72
Wt% σ
O 41.1 0.2
Al 16.7 0.1
Si 14.8 0.1
Sr 7.4 0.2
P 5.8 0.1
S 4.5 0.0
Fe 3.2 0.1
K 2.1 0.0
Ba 1.9 0.1
Ca 1.4 0.0
Mg 0.3 0.0
Ce 0.3 0.1
Na 0.3 0.0
Powered by Tru-Q®
cps/eV
keV

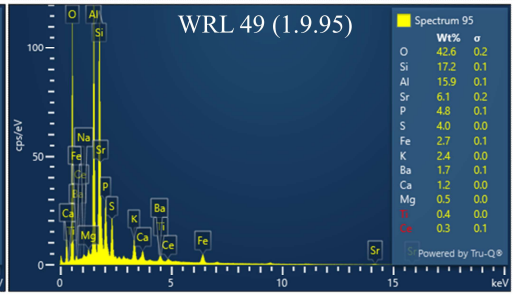
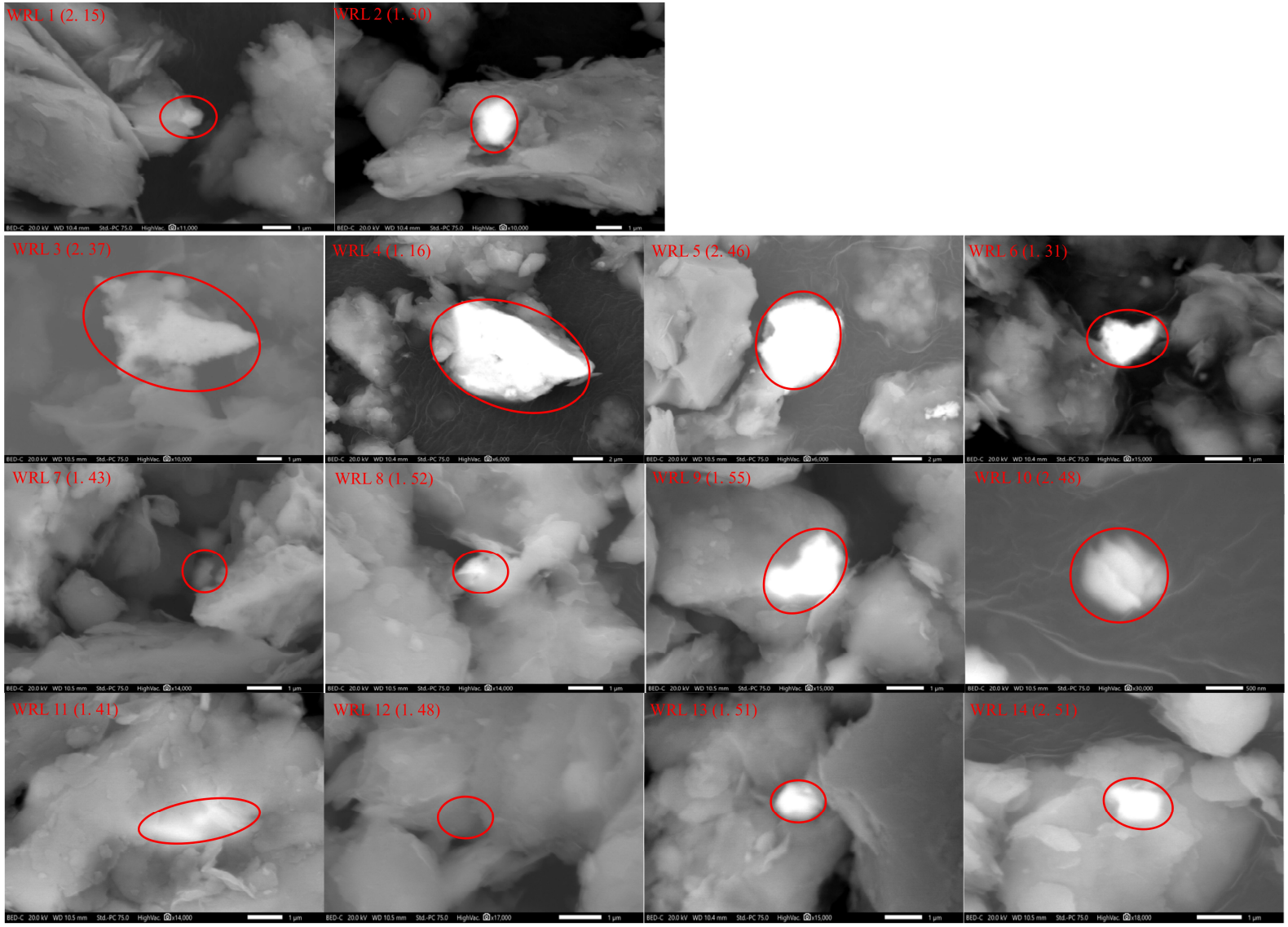
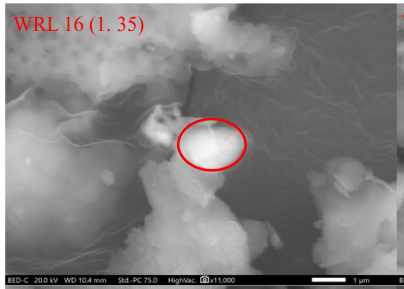

WRL 49 (1.9.95)
Spectrum 95
Wt% σ
O 42.6 0.2
Si 17.2 0.1
Al 15.9 0.1
Sr 6.1 0.2
P 4.8 0.1
S 4.0 0.0
Fe 2.7 0.1
K 2.4 0.0
Ba 1.7 0.1
Ca 1.2 0.0
Mg 0.5 0.0
Ti 0.4 0.0
Co 0.3 0.1
Powered by Tru-Q®
cps/eV
keV

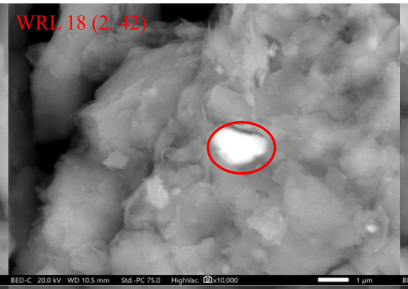
Figure B.2 SEM images of the particles containing REEs found from the raw Western Kentucky No. 13 (WK No. 13) coal waste leaching residue. (The images are labelled as WRL # (Specimen #. Site #))

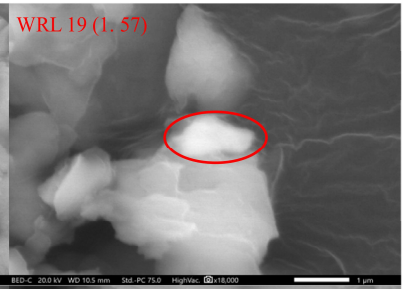



WRL 15 (1. 33)


WRL 16 (1. 35)


WRL 17 (1. 14)


WRL 18 (2. 42)


WRL 19 (1. 57)


WRL 20 (1. 39)


WRL 21 (2. 18)


WRL 22 (2. 33)


WRL 23 (1. 23)


WRL 24 (1. 18)

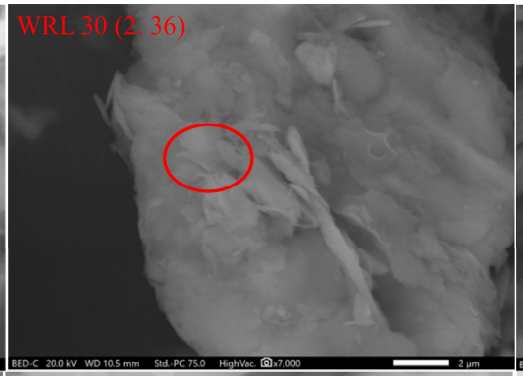

WRL 25 (2. 2)


WRL 26 (2. 9)


WRL 27 (1. 37)


WRL 28 (2. 40)


WRL 29 (2. 3)


WRL 30 (2. 36)

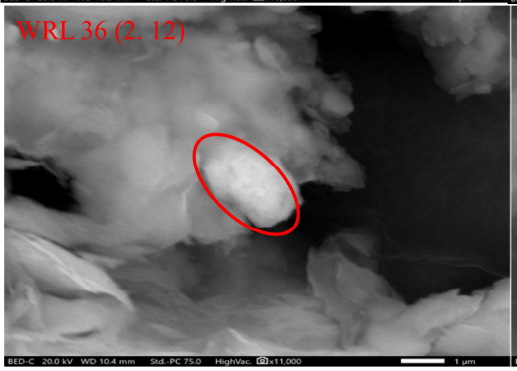

WRL 31 (2. 34)

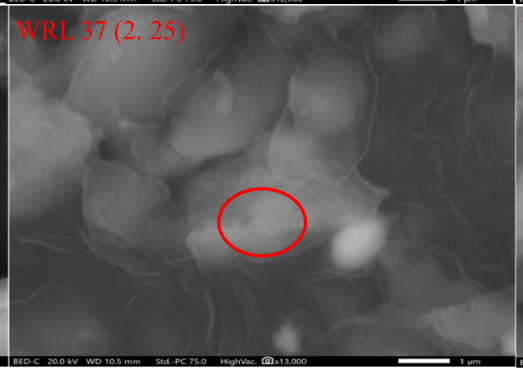

WRL 32 (2. 4)


WRL 33 (2. 50)


WRL 34 (1. 2)


WRL 35 (2. 10)

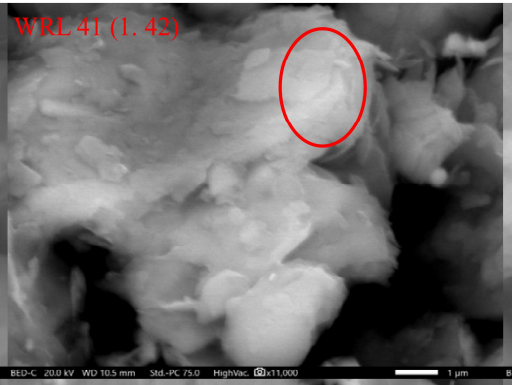

WRL 36 (2. 12)


WRL 37 (2. 25)


WRL 38 (2. 21)


WRL 39 (2. 28)


WRL 40 (1. 65)


WRL 41 (1. 42)


WRL 42 (2. 8)

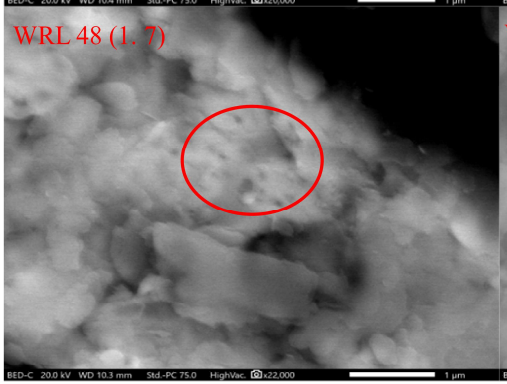

WRL 43 (2. 43)


WRL 44 (1. 4)


WRL 45 (1. 22)


WRL 46 (1. 25)


WRL 47 (1. 50)

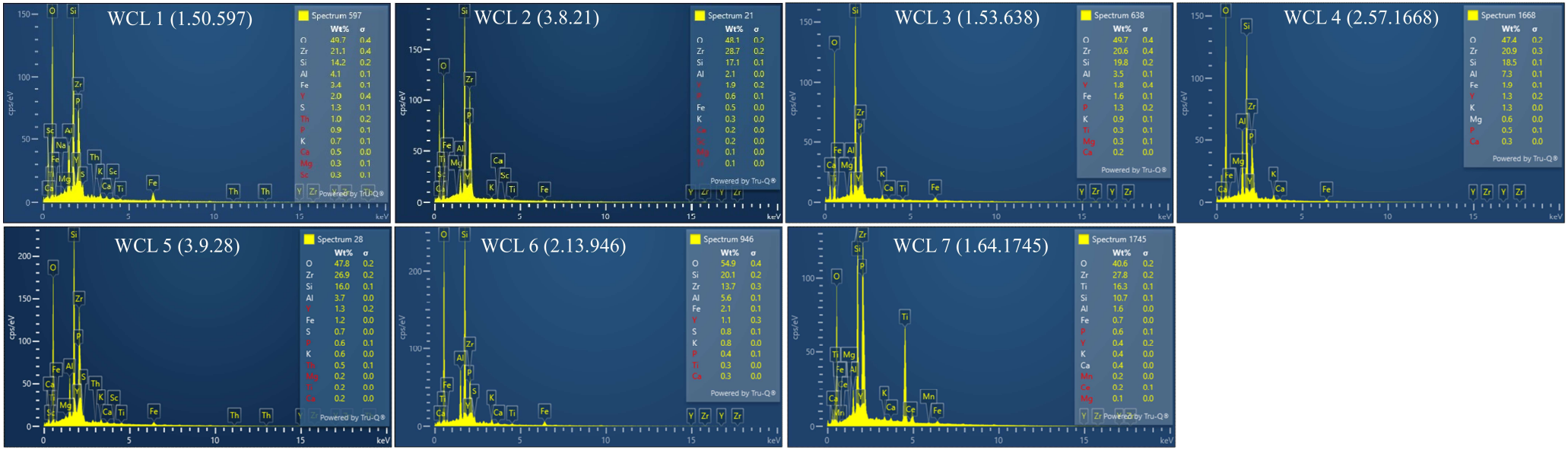

WRL 48 (1. 7)

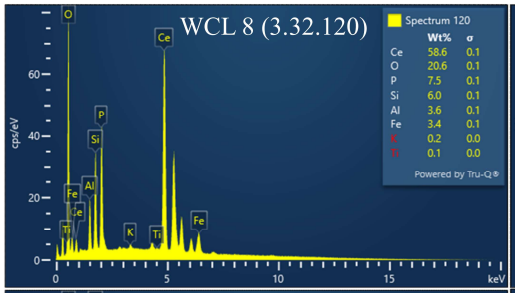

WRL 49 (1. 9)

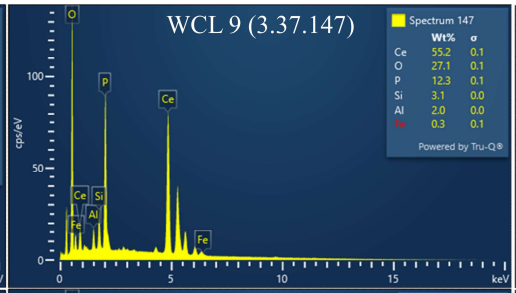
Table B.2 Elemental compositions of the particles containing REEs found from the calcined Western Kentucky No. 13 (WK No. 13) coal waste leaching residue through SEM-EDS analysis.

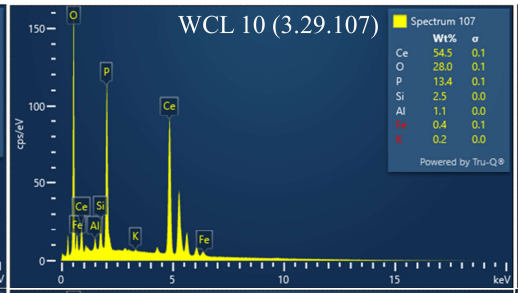
Particle #	Specimen #	Site #	Spectrum #	Mineral	Al (%)	Si (%)	O (%)	Ca (%)	P (%)	Fe (%)	K (%)	S (%)	Ba (%)	Mg (%)	Ti (%)	Na (%)	Sr (%)	F(%)	Zr (%)	Sc (%)	La (%)	Ce(%)	Pr (%)	Nd(%)	Sm (%)	Gd (%)	Y(%)	Dy (%)	Er (%)	Yb (%)	Ho (%)	Th(%)	U (%)	TREE (%	Sum (%)	Al/Si	Al/P	TREE/P
WCL 1	1	50	597	Zircon	4.1	14.2	49.7	0.5	0.9	3.4	0.7	1.3	0.0	0.3	0.3	0.3	0.0	0.0	21.1	0.3	0.0	0.0	0.0	0.0	0.0	0.0	2.0	0.0	0.0	0.0	0.0	1.0	0.0	2.3	100	0.29	4.56	2.56
WCL 2	3	8	21	Zircon	2.1	17.1	48.1	0.2	0.6	0.5	0.3	0.0	0.0	0.1	0.1	0.0	0.0	0.0	28.7	0.2	0.0	0.0	0.0	0.0	0.0	0.0	1.9	0.0	0.0	0.0	0.0	0.0	0.0	2.1	100	0.12	3.50	3.50
WCL 3	1	53	638	Zircon	3.5	19.8	49.7	0.2	1.3	1.6	0.9	0.0	0.0	0.3	0.3	0.0	0.0	0.0	20.6	0.0	0.0	0.0	0.0	0.0	0.0	0.0	1.8	0.0	0.0	0.0	0.0	0.0	0.0	1.8	100	0.18	2.69	1.38
WCL 4	2	57	1668	Zircon	7.3	18.5	47.4	0.3	0.5	1.9	1.3	0.0	0.0	0.6	0.0	0.0	0.0	0.0	20.9	0.0	0.0	0.0	0.0	0.0	0.0	0.0	1.3	0.0	0.0	0.0	0.0	0.0	0.0	1.3	100	0.39	14.60	2.60
WCL 5	3	9	28	Zircon	3.7	16.0	47.8	0.2	0.6	1.2	0.6	0.7	0.0	0.2	0.2	0.0	0.0	0.0	26.9	0.0	0.0	0.0	0.0	0.0	0.0	0.0	1.3	0.0	0.0	0.0	0.0	0.5	0.0	1.3	100	0.23	6.17	2.17
WCL 6	2	13	946	Zircon	5.6	20.1	54.9	0.3	0.4	2.1	0.8	0.8	0.0	0.0	0.3	0.0	0.0	0.0	13.7	0.0	0.0	0.0	0.0	0.0	0.0	0.0	1.1	0.0	0.0	0.0	0.0	0.0	0.0	1.1	100	0.28	14.00	2.75
WCL 7	1	64	1745	Zircon	1.6	10.7	40.6	0.4	0.6	0.7	0.4	0.0	0.0	0.1	16.3	0.0	0.0	0.0	27.8	0.0	0.0	0.2	0.0	0.0	0.0	0.0	0.4	0.0	0.0	0.0	0.0	0.0	0.0	0.6	100	0.15	2.67	1.00
WCL 8	3	32	120	Monazite	3.6	6.0	20.6	0.0	7.5	3.4	0.2	0.0	0.0	0.0	0.1	0.0	0.0	0.0	0.0	0.0	0.0	58.6	0.0	0.0	0.0	0.0	0.0	0.0	0.0	0.0	0.0	0.0	0.0	58.6	100	0.60	0.48	7.81
WCL 9	3	37	147	Monazite	2.0	3.1	27.1	0.0	12.3	0.3	0.0	0.0	0.0	0.0	0.0	0.0	0.0	0.0	0.0	0.0	0.0	55.2	0.0	0.0	0.0	0.0	0.0	0.0	0.0	0.0	0.0	0.0	0.0	55.2	100	0.65	0.16	4.49
WCL 10	3	29	107	Monazite	1.1	2.5	28.0	0.0	13.4	0.4	0.2	0.0	0.0	0.0	0.0	0.0	0.0	0.0	0.0	0.0	0.0	54.5	0.0	0.0	0.0	0.0	0.0	0.0	0.0	0.0	0.0	0.0	0.0	54.5	100	0.44	0.08	4.07
WCL 11	3	22	79	Monazite	3.9	11.5	20.2	0.0	9.8	1.0	0.4	0.0	0.0	0.0	0.1	0.0	0.0	0.0	0.0	0.0	0.0	53.1	0.0	0.0	0.0	0.0	0.0	0.0	0.0	0.0	0.0	0.0	0.0	53.1	100	0.34	0.40	5.42
WCL 12	1	4	99	Monazite	3.6	11.4	21.3	0.0	10.3	1.3	0.6	0.0	0.0	0.0	0.1	0.0	0.0	0.0	0.0	0.0	0.0	51.5	0.0	0.0	0.0	0.0	0.0	0.0	0.0	0.0	0.0	0.0	0.0	51.5	100	0.32	0.35	5.00
WCL 13	3	2	5	Monazite	2.8	4.0	29.9	0.0	12.6	0.5	0.0	0.0	0.0	0.0	0.2	0.0	0.0	0.0	0.0	0.0	0.0	49.3	0.0	0.0	0.0	0.8	0.0	0.0	0.0	0.0	0.0	0.0	0.0	50.1	100	0.70	0.22	3.98
WCL 14	3	3	7	Monazite	1.5	2.4	33.9	0.0	13.2	1.1	0.0	0.0	0.0	0.0	0.0	0.0	0.0	0.0	0.0	0.0	0.0	47.9	0.0	0.0	0.0	0.0	0.0	0.0	0.0	0.0	0.0	0.0	0.0	47.9	100	0.63	0.11	3.63
WCL 15	1	36	430	Monazite	4.4	9.5	27.5	0.0	9.8	0.7	0.4	0.0	0.0	0.0	0.0	0.0	0.0	0.0	0.0	0.0	0.0	47.5	0.0	0.0	0.0	0.0	0.0	0.0	0.0	0.0	0.0	0.0	0.0	47.5	100	0.46	0.45	4.85
WCL 16	3	30	111	Monazite	1.9	4.8	33.3	0.0	12.4	0.5	0.2	0.0	0.0	0.0	0.0	0.0	0.0	0.0	0.0	0.0	0.0	46.9	0.0	0.0	0.0	0.0	0.0	0.0	0.0	0.0	0.0	0.0	0.0	46.9	100	0.40	0.15	3.78
WCL 17	2	46	1523	Monazite	5.9	9.4	26.4	0.0	9.9	1.4	0.0	0.0	0.0	0.0	0.2	0.0	0.0	0.0	0.0	0.0	0.0	46.8	0.0	0.0	0.0	0.0	0.0	0.0	0.0	0.0	0.0	0.0	0.0	46.8	100	0.63	0.60	4.73
WCL 18	1	46	543	Monazite	3.9	5.4	31.6	0.0	11.5	0.8	0.3	0.0	0.0	0.0	0.0	0.0	0.0	0.0	0.0	0.0	0.0	46.6	0.0	0.0	0.0	0.0	0.0	0.0	0.0	0.0	0.0	0.0	0.0	46.6	100	0.72	0.34	4.05
WCL 19	2	37	1383	Monazite	3.0	9.5	31.0	0.0	10.4	0.6	0.3	0.0	0.0	0.0	0.0	0.0	0.0	0.0	0.0	0.0	0.0	45.2	0.0	0.0	0.0	0.0	0.0	0.0	0.0	0.0	0.0	0.0	0.0	45.2	100	0.32	0.29	4.35
WCL 20	3	17	66	Monazite	3.0	8.2	32.4	0.4	10.1	0.6	0.4	0.3	0.0	0.0	0.0	0.0	0.0	0.0	0.0	0.0	0.0	44.5	0.0	0.0	0.0	0.0	0.0	0.0	0.0	0.0	0.0	0.0	0.0	44.5	100	0.37	0.30	4.41
WCL 21	3	23	83	Monazite	2.8	7.4	33.0	0.0	11.2	0.7	0.3	0.0	0.0	0.0	0.1	0.0	0.0	0.0	0.0	0.0	0.0	44.5	0.0	0.0	0.0	0.0	0.0	0.0	0.0	0.0	0.0	0.0	0.0	44.5	100	0.38	0.25	3.97
WCL 22	2	51	1596	Monazite	6.7	15.8	23.9	0.0	8.0	2.2	0.8	0.0	0.0	0.0	0.2	0.0	0.0	0.0	0.0	0.0	0.0	42.2	0.0	0.0	0.0	0.0	0.0	0.0	0.0	0.0	0.0	0.0	0.0	42.2	100	0.42	0.84	5.28
WCL 23	1	54	646	Monazite	2.7	5.6	34.2	0.0	10.4	6.8	0.4	0.0	0.0	0.0	0.0	0.0	0.0	0.0	0.0	0.0	0.0	39.9	0.0	0.0	0.0	0.0	0.0	0.0	0.0	0.0	0.0	0.0	0.0	39.9	100	0.48	0.26	3.84
WCL 24	1	8	106	Monazite	5.2	11.8	31.9	0.0	8.0	1.0	0.5	0.0	0.0	0.0	1.8	0.0	0.0	0.0	0.0	0.0	0.0	39.7	0.0	0.0	0.0	0.0	0.0	0.0	0.0	0.0	0.0	0.0	0.0	39.7	100	0.44	0.65	4.96
WCL 25	2	7	831	Monazite	5.3	10.8	30.5	0.0	8.2	6.2	0.6	0.0	0.0	0.0	0.0	0.0	0.0	0.0	0.0	0.0	0.0	38.4	0.0	0.0	0.0	0.0	0.0	0.0	0.0	0.0	0.0	0.0	0.0	38.4	100	0.49	0.65	4.68
WCL 26	2	10	120	Monazite	5.2	9.0	37.8	0.0	9.6	1.1	0.0	0.0	0.0	0.0	0.1	0.0	0.0	0.0	0.0	0.0	0.0	37.3	0.0	0.0	0.0	0.0	0.0	0.0	0.0	0.0	0.0	0.0	0.0	37.3	100	0.58	0.54	3.89
WCL 27	1	43	501	Monazite	5.6	11.2	35.3	0.0	9.5	0.9	0.7	0.0	0.0	0.0	0.3	0.0	0.0	0.0	0.0	0.0	0.0	36.5	0.0	0.0	0.0	0.0	0.0	0.0	0.0	0.0	0.0	0.0	0.0	36.5	100	0.50	0.59	3.84
WCL 28	1	10	95	Monazite	5.6	16.0	35.1	0.0	7.4	1.6	0.7	0.0	0.0	0.0	0.0	0.0	0.0	0.0	0.0	0.0	0.0	33.2	0.0	0.0	0.0	0.0	0.4	0.0	0.0	0.0	0.0	0.0	0.0	33.6	100	0.35	0.76	4.54
WCL 29	1	57	717	Monazite	5.9	13.6	37.1	0.0	8.0	2.4	0.7	0.0	0.0	0.0	0.0	0.0	0.0	0.0	0.0	0.0	0.0	32.2	0.0	0.0	0.0	0.0	0.0	0.0	0.0	0.0	0.0	0.0	0.0	32.2	100	0.43	0.74	4.03
WCL 30	1	22	296	Monazite	3.5	11.9	43.1	0.0	7.6	3.1	0.0	0.0	0.0	0.0	0.0	0.0	0.0	0.0	0.0	0.0	0.0	30.8	0.0	0.0	0.0	0.0	0.0	0.0	0.0	0.0	0.0	0.0	0.0	30.8	100	0.29	0.46	4.05
WCL 31	1	12	69	Monazite	7.2	17.6	37.7	0.0	5.5	2.3	0.8	0.0	0.0	0.0	0.3	0.0	0.0	0.0	0.0	0.0	0.0	28.6	0.0	0.0	0.0	0.0	0.0	0.0	0.0	0.0	0.0	0.0	0.0	28.6	100	0.41	1.31	5.20
WCL 32	2	23	1181	Monazite	7.4	17.8	38.1	0.0	6.2	2.2	1.2	0.0	0.0	0.0	0.0	0.0	0.0	0.0	0.0	0.0	0.0	27.1	0.0	0.0	0.0	0.0	0.0	0.0	0.0	0.0	0.0	0.0	0.0	27.1	100	0.42	1.19	4.37
WCL 33	1	44	511	Monazite	9.2	19.9	40.1	0.0	5.2	1.9	1.1	0.0	0.0	0.3	0.0	0.0	0.0	0.0	0.0	0.0	5.5	11.2	1.1	4.5	0.0	0.0	0.0	0.0	0.0	0.0	0.0	0.0	0.0	22.3	100	0.46	1.77	4.29
WCL 34	2	48	1547	Monazite	8.5	16.6	43.5	0.0	5.8	1.8	1.4	0.0	0.0	0.0	0.2	0.0	0.0	0.0	0.0	0.0	0.0	22.2	0.0	0.0	0.0	0.0	0.0	0.0	0.0	0.0	0.0	0.0	0.0	22.2	100	0.51	1.47	3.83
WCL 35	1	41	482	Monazite	8.3	18.8	40.3	0.0	5.0	5.2	1.2	0.0	0.0	0.5	0.0	0.0	0.0	0.0	0.0	0.0	0.0	20.8	0.0	0.0	0.0	0.0	0.0	0.0	0.0	0.0	0.0	0.0	0.0	20.8	100	0.44	1.66	4.16
WCL 36	2	38	1392	Monazite	6.2	25.2	46.6	0.0	3.3	1.4	1.4	0.0	0.0	0.4	0.0	0.0	0.0	0.0	0.0	0.0	3.2	7.3	1.0	3.2	0.6	0.4	0.0	0.0	0.0	0.0	0.0	0.0	0.0	15.7	100	0.25	1.88	4.76
WCL 37	2	20	1108	Monazite	6.1	26.9	49.9	0.0	3.0	1.2	1.0	0.0	0.0	0.0	0.5	0.0	0.0	0.0	0.0	0.0	0.0	11.5	0.0	0.0	0.0	0.0	0.0	0.0	0.0	0.0	0.0	0.0	0.0	11.5	100	0.23	2.03	3.83
WCL 38	2	53	1614	Monazite	9.4	22.7	48.9	0.0	2.8	2.1	1.4	0.0	0.0	0.4	1.0	0.0	0.0	0.0	0.0	0.0	0.0	11.3	0.0	0.0	0.0	0.0	0.0	0.0	0.0	0.0	0.0	0.0	0.0	11.3	100	0.41	3.36	4.04
WCL 39	1	64	1748	Monazite	12.2	18.8	45.5	0.0	2.6	1.9	5.1	0.0	0.0	1.2	0.4	0.0	0.0	0.0	2.3	0.0	0.0	10.1	0.0	0.0	0.0	0.0	0.0	0.0	0.0	0.0	0.0	0.0	0.0	10.1	100	0.65	4.69	3.88
WCL 40	2	57	1669	Monazite	8.6	19.7	45.1	0.1	1.6	2.1	1.6	0.0	0.0	0.7	0.3	0.0	0.0	0.0	11.4	0.0	0.0	8.9	0.0	0.0	0.0	0.0	0.0	0.0	0.0	0.0	0.0	0.0	0.0	8.9	100	0.44	5.38	5.56
WCL 41	2	24	1200	Monazite	11.2	20.4	47.0	0.0	1.1	10.9	2.2	0.0	0.0	0.8	0.2	0.0	0.0	0.0	0.0	0.0	0.0	6.2	0.0	0.0	0.0	0.0	0.0	0.0	0.0	0.0	0.0	0.0	0.0	6.2	100	0.55	10.18	5.64
WCL 42	2	61	1699	Monazite	9.8	19.6	47.6	0.0	0.7	16.9	1.5	0.0	0.0	0.0	0.6	0.0	0.0	0.0	0.0	0.0	0.0	3.3	0.0	0.0	0.0	0.0	0.0	0.0	0.0	0.0	0.0	0.0	0.0	3.3	100	0.50	14.00	4.71
WCL 43	2	62	1710	Monazite	9.6	21.0	50.1	0.0	0.2	15.6	1.4	0.0	0.0	0.0	0.6	0.0	0.0	0.0	0.0	0.0	0.0	1.5	0.0	0.0	0.0	0.0	0.0	0.0	0.0	0.0	0.0	0.0	0.0	1.5	100	0.46	48.00	7.50
WCL 44	1	20	276	Monazite	16.3	27.3	53.7	0.0	0.1	1.3	1.1	0.0	0.0	0.0	0.0	0.0	0.0	0.0	0.0	0.0	0.0	0.2	0.0	0.0	0.0	0.0	0.0	0.0	0.0	0.0	0.0	0.0	0.0	0.2	100	0.60	163.00	2.00
WCL 45	3	36	138	Xenotime	2.5	9.9	33.0	0.6	12.5	0.7	0.6	0.0	0.0	0.0	0.3	0.0	0.0	0.0	0.0	0.2	0.0	0.0	0.0	0.0	0.0	3.1	27.1	5.1	2.5	1.8	0.0	0.0	0.0	39.8	100	0.25	0.20	3.18
WCL 46	1	66	1766	Xenotime	8.2	22.4	50.2	0.2	3.7	1.4	2.1	0.1	0.0	0.5	0.3	0.0	0.0	0.0	0.0	0.0	0.0	0.0	0.0	0.0	0.0	0.0	9.9	0.0	0.9	0.0	0.0	0.0	0.0	10.8	100	0.37	2.22	2.92
WCL 47	2	26	1231	Xenotime	11.0	22.2	52.6	0.0	2.7	2.7	2.0	0.0	0.0	0.5	0.4	0.0	0.0	0.0	0.0	0.0	0.0	0.0	0.0	0.0	0.0	0.0	6.0	0.0	0.0	0.0	0.0	0.0	0.0	6.0	100	0.50	4.07	2.22

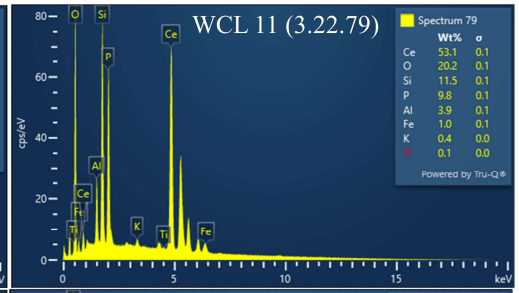
Figure B.3 EDS spectra of the particles containing REEs found from the calcined Western Kentucky No. 13 (WK No. 13) coal waste leaching residue. (The spectra are labelled as WCL # (Specimen #. Site #. Spectrum #))

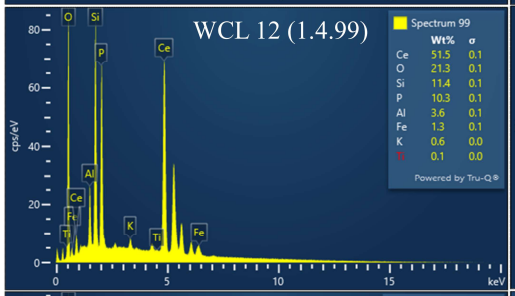


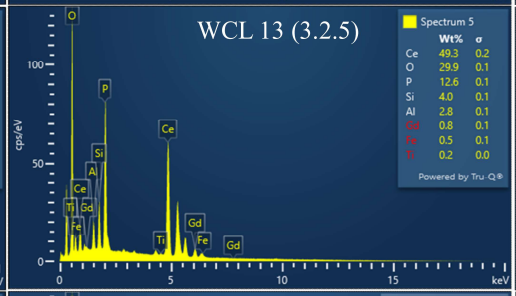

WCL 8 (3.32.120)
Spectrum 120
Wt% σ
Ce 58.6 0.1
O 20.6 0.1
P 7.5 0.1
Si 6.0 0.1
Al 3.6 0.1
Fe 3.4 0.1
K 0.2 0.0
Ti 0.1 0.0
Powered by Tru-Q®
cps/eV
keV

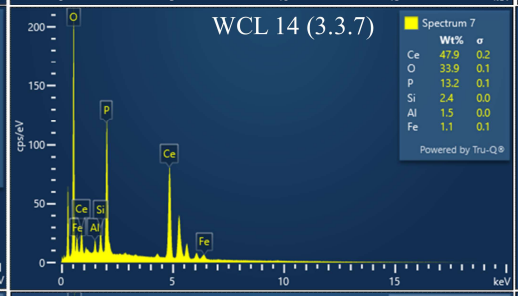

WCL 9 (3.37.147)
Spectrum 147
Wt% σ
Ce 55.2 0.1
O 27.1 0.1
P 12.3 0.1
Si 3.1 0.0
Al 2.0 0.0
Fe 0.3 0.1
Powered by Tru-Q®
cps/eV
keV

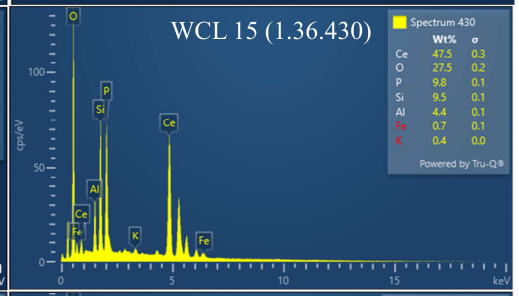

WCL 10 (3.29.107)
Spectrum 107
Wt% σ
Ce 54.5 0.1
O 28.0 0.1
P 13.4 0.1
Si 2.5 0.0
Al 1.1 0.0
Fe 0.4 0.1
K 0.2 0.0
Powered by Tru-Q®
cps/eV
keV

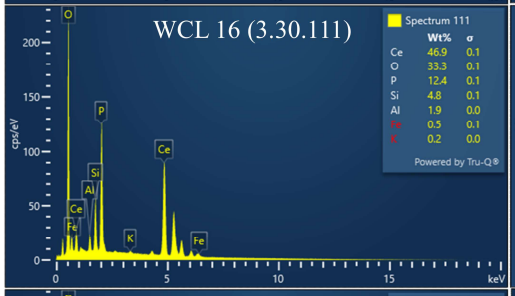

WCL 11 (3.22.79)
Spectrum 79
Wt% σ
Ce 53.1 0.1
O 20.2 0.1
Si 11.5 0.1
P 9.8 0.1
Al 3.9 0.1
Fe 1.0 0.1
K 0.4 0.0
Ti 0.1 0.0
Powered by Tru-Q®
cps/eV
keV

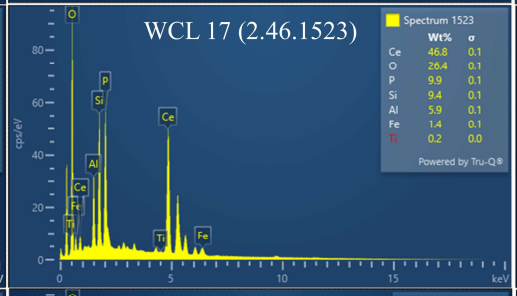

WCL 12 (1.4.99)
Spectrum 99
Wt% σ
Ce 51.5 0.1
O 21.3 0.1
Si 11.4 0.1
P 10.3 0.1
Al 3.6 0.1
Fe 1.3 0.1
K 0.6 0.0
Ti 0.1 0.0
Powered by Tru-Q®
cps/eV
keV

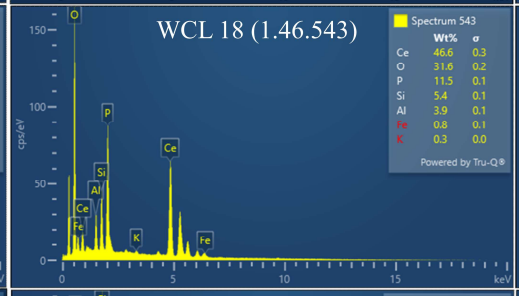

WCL 13 (3.2.5)
Spectrum 5
Wt% σ
Ce 49.3 0.2
O 29.9 0.1
P 12.6 0.1
Si 4.0 0.1
Al 2.8 0.1
Gd 0.8 0.1
Fe 0.5 0.1
Ti 0.2 0.0
Powered by Tru-Q®
cps/eV
keV

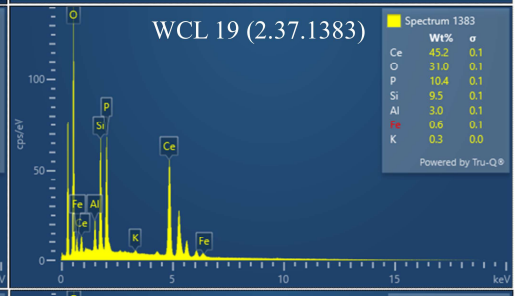

WCL 14 (3.3.7)
Spectrum 7
Wt% σ
Ce 47.9 0.2
O 33.9 0.1
P 13.2 0.1
Si 2.4 0.0
Al 1.5 0.0
Fe 1.1 0.1
Powered by Tru-Q®
cps/eV
keV

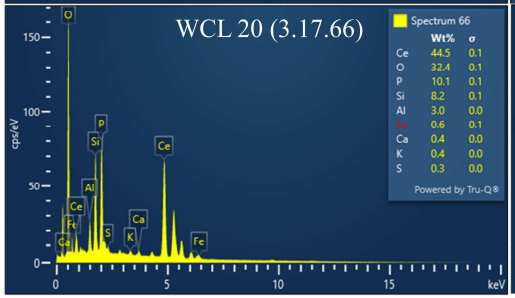

WCL 15 (1.36.430)
Spectrum 430
Wt% σ
Ce 47.5 0.3
O 27.5 0.2
P 9.8 0.1
Si 9.5 0.1
Al 4.4 0.1
Fe 0.7 0.1
K 0.4 0.0
Powered by Tru-Q®
cps/eV
keV

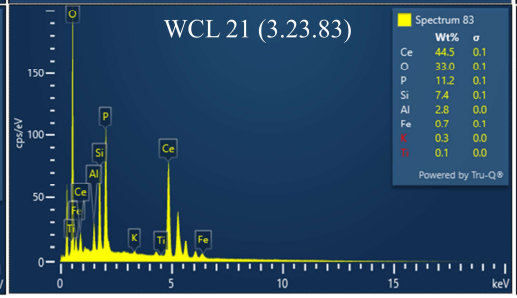

WCL 16 (3.30.111)
Spectrum 111
Wt% σ
Ce 46.9 0.1
O 33.3 0.1
P 12.4 0.1
Si 4.8 0.1
Al 1.9 0.0
Fe 0.5 0.1
K 0.2 0.0
Powered by Tru-Q®
cps/eV
keV

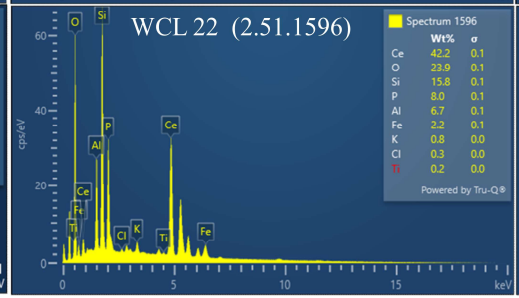

WCL 17 (2.46.1523)
Spectrum 1523
Wt% σ
Ce 46.8 0.1
O 26.4 0.1
P 9.9 0.1
Si 9.4 0.1
Al 5.9 0.1
Fe 1.4 0.1
Ti 0.2 0.0
Powered by Tru-Q®
cps/eV
keV

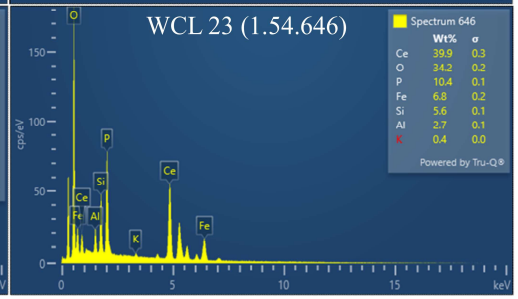

WCL 18 (1.46.543)
Spectrum 543
Wt% σ
Ce 46.6 0.3
O 31.6 0.2
P 11.5 0.1
Si 5.4 0.1
Al 3.9 0.1
Fe 0.8 0.1
K 0.3 0.0
Powered by Tru-Q®
cps/eV
keV

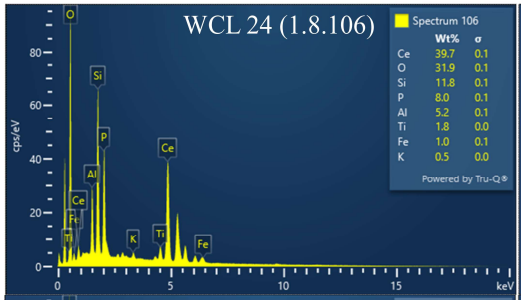

WCL 19 (2.37.1383)
Spectrum 1383
Wt% σ
Ce 45.2 0.1
O 31.0 0.1
P 10.4 0.1
Si 9.5 0.1
Al 3.0 0.1
Fe 0.6 0.1
K 0.3 0.0
Powered by Tru-Q®
cps/eV
keV

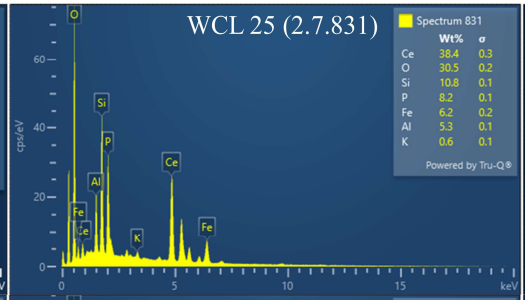

WCL 20 (3.17.66)
Spectrum 66
Wt% σ
Ce 44.5 0.1
O 32.4 0.1
P 10.1 0.1
Si 8.2 0.1
Al 3.0 0.0
Fe 0.6 0.1
Ca 0.4 0.0
K 0.4 0.0
S 0.3 0.0
Powered by Tru-Q®
cps/eV
keV

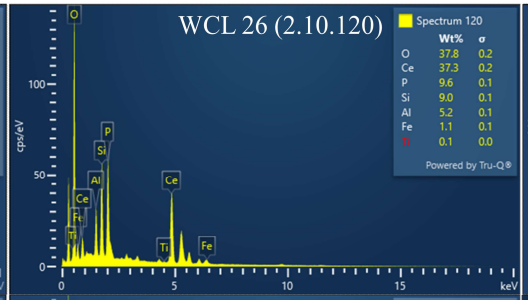

WCL 21 (3.23.83)
Spectrum 83
Wt% σ
Ce 44.5 0.1
O 33.0 0.1
P 11.2 0.1
Si 7.4 0.1
Al 2.8 0.0
Fe 0.7 0.1
K 0.3 0.0
Ti 0.1 0.0
Powered by Tru-Q®
cps/eV
keV

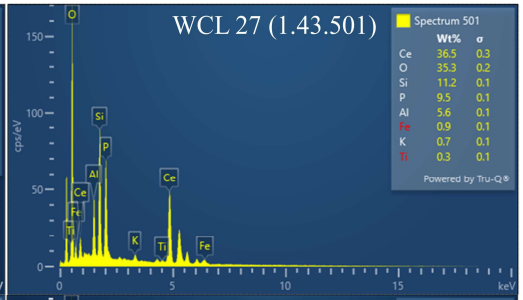

WCL 22 (2.51.1596)
Spectrum 1596
Wt% σ
Ce 42.2 0.1
O 23.9 0.1
Si 15.8 0.1
P 8.0 0.1
Al 6.7 0.1
Fe 2.2 0.1
K 0.8 0.0
Cl 0.3 0.0
Ti 0.2 0.0
Powered by Tru-Q®
cps/eV
keV

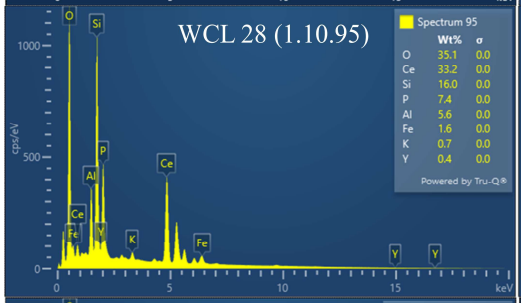

WCL 23 (1.54.646)
Spectrum 646
Wt% σ
Ce 39.9 0.3
O 34.2 0.2
P 10.4 0.1
Fe 6.8 0.2
Si 5.6 0.1
Al 2.7 0.1
K 0.4 0.0
Powered by Tru-Q®
cps/eV
keV

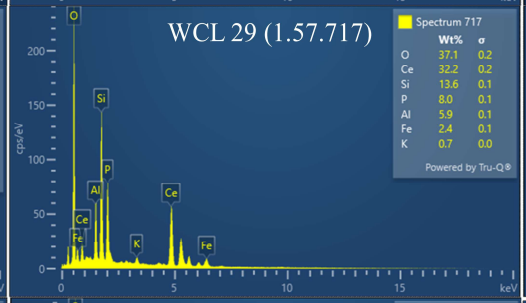

WCL 24 (1.8.106)
Spectrum 106
Wt% σ
Ce 39.7 0.1
O 31.9 0.1
Si 11.8 0.1
P 8.0 0.1
Al 5.2 0.1
Ti 1.8 0.0
Fe 1.0 0.1
K 0.5 0.0
Powered by Tru-Q®

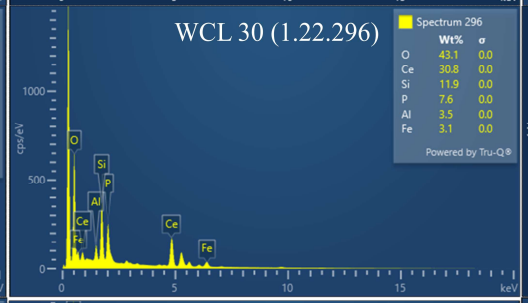

WCL 25 (2.7.831)
Spectrum 831
Wt% σ
Ce 38.4 0.3
O 30.5 0.2
Si 10.8 0.1
P 8.2 0.1
Fe 6.2 0.2
Al 5.3 0.1
K 0.6 0.1
Powered by Tru-Q®


WCL 26 (2.10.120)
Spectrum 120
Wt% σ
O 37.8 0.2
Ce 37.3 0.2
P 9.6 0.1
Si 9.0 0.1
Al 5.2 0.1
Fe 1.1 0.1
Ti 0.1 0.0
Powered by Tru-Q®

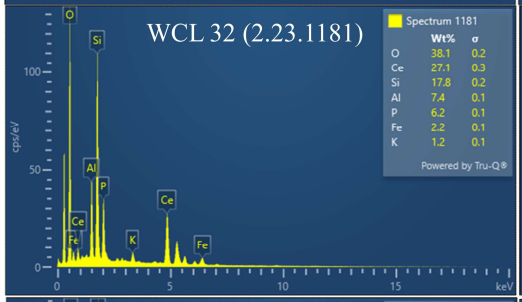

WCL 27 (1.43.501)
Spectrum 501
Wt% σ
Ce 36.5 0.3
O 35.3 0.2
Si 11.2 0.1
P 9.5 0.1
Al 5.6 0.1
Fe 0.9 0.1
K 0.7 0.1
Ti 0.3 0.1
Powered by Tru-Q®


WCL 28 (1.10.95)
Spectrum 95
Wt% σ
O 35.1 0.0
Ce 33.2 0.0
Si 16.0 0.0
P 7.4 0.0
Al 5.6 0.0
Fe 1.6 0.0
K 0.7 0.0
Y 0.4 0.0
Powered by Tru-Q®

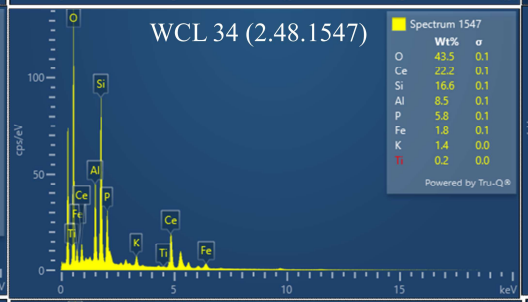

WCL 29 (1.57.717)
Spectrum 717
Wt% σ
O 37.1 0.2
Ce 32.2 0.2
Si 13.6 0.1
P 8.0 0.1
Al 5.9 0.1
Fe 2.4 0.1
K 0.7 0.0
Powered by Tru-Q®

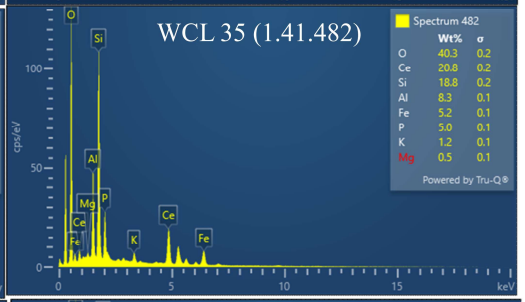

WCL 30 (1.22.296)
Spectrum 296
Wt% σ
O 43.1 0.0
Ce 30.8 0.0
Si 11.9 0.0
P 7.6 0.0
Al 3.5 0.0
Fe 3.1 0.0
Powered by Tru-Q®

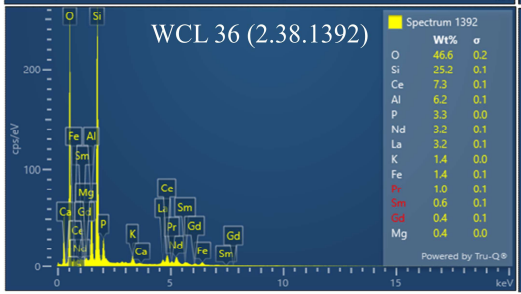

WCL 31 (1.12.69)
Spectrum 69
Wt% σ
O 37.7 0.2
Ce 28.6 0.2
Si 17.6 0.1
Al 7.2 0.1
P 5.5 0.1
Fe 2.3 0.1
K 0.8 0.0
Ti 0.3 0.0
Powered by Tru-Q®

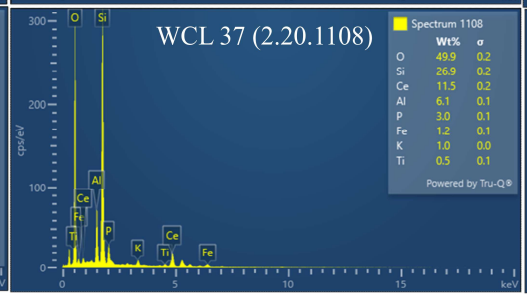

WCL 32 (2.23.1181)
Spectrum 1181
Wt% σ
O 38.1 0.2
Ce 27.1 0.3
Si 17.8 0.2
Al 7.4 0.1
P 6.2 0.1
Fe 2.2 0.1
K 1.2 0.1
Powered by Tru-Q®

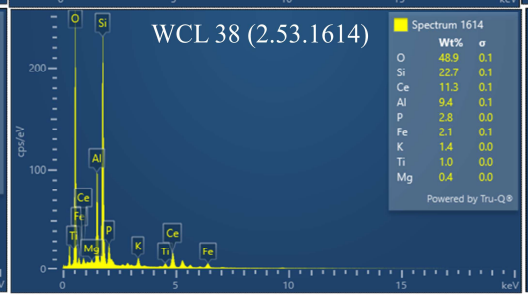

WCL 33 (1.44.511)
Spectrum 511
Wt% σ
O 40.1 0.3
Si 19.9 0.2
Ce 11.2 0.3
Al 9.2 0.1
La 5.5 0.2
P 5.2 0.1
Nd 4.5 0.3
Fe 1.9 0.1
Pr 1.1 0.2
K 1.1 0.1
Mg 0.3 0.1
Powered by Tru-Q®

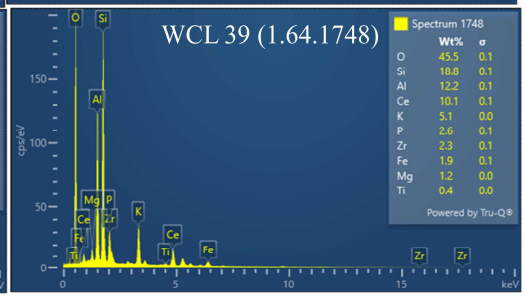

WCL 34 (2.48.1547)
Spectrum 1547
Wt% σ
O 43.5 0.1
Ce 22.2 0.1
Si 16.6 0.1
Al 8.5 0.1
P 5.8 0.1
Fe 1.8 0.1
K 1.4 0.0
Ti 0.2 0.0
Powered by Tru-Q®

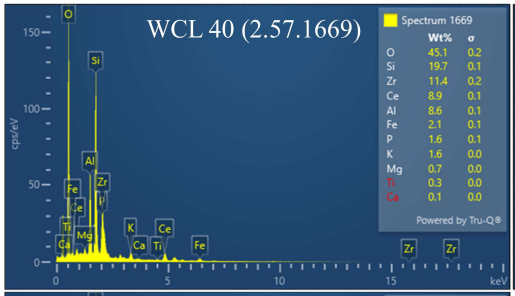

WCL 35 (1.41.482)
Spectrum 482
Wt% σ
O 40.3 0.2
Ce 20.8 0.2
Si 18.8 0.2
Al 8.3 0.1
Fe 5.2 0.1
P 5.0 0.1
K 1.2 0.1
Mg 0.5 0.1
Powered by Tru-Q®

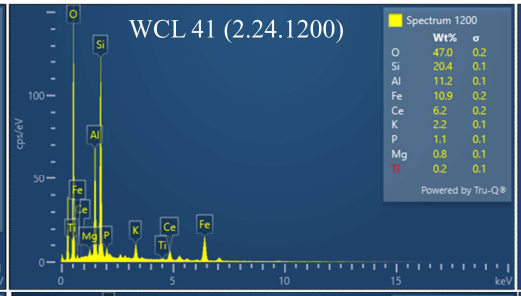

WCL 36 (2.38.1392)
Spectrum 1392
Wt% σ
O 46.6 0.2
Si 25.2 0.1
Ce 7.3 0.1
Al 6.2 0.1
P 3.3 0.0
Nd 3.2 0.1
La 3.2 0.1
K 1.4 0.0
Fe 1.4 0.1
Pr 1.0 0.1
Sm 0.6 0.1
Gd 0.4 0.1
Mg 0.4 0.0
Powered by Tru-Q®

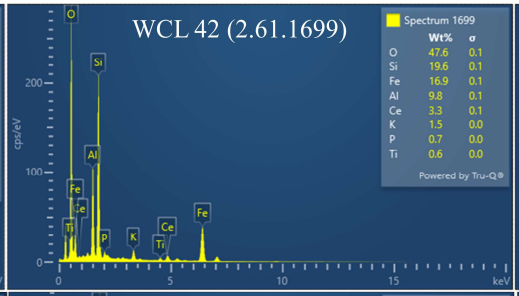

WCL 37 (2.20.1108)
Spectrum 1108
Wt% σ
O 49.9 0.2
Si 26.9 0.2
Ce 11.5 0.2
Al 6.1 0.1
P 3.0 0.1
Fe 1.2 0.1
K 1.0 0.0
Ti 0.5 0.1
Powered by Tru-Q®

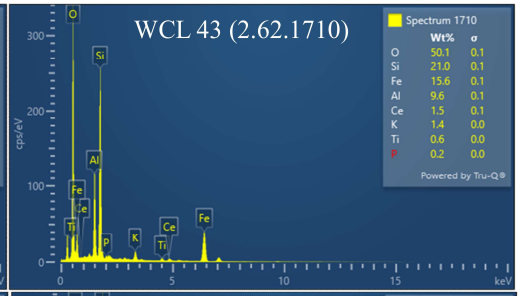

WCL 38 (2.53.1614)
Spectrum 1614
Wt% σ
O 48.9 0.1
Si 22.7 0.1
Ce 11.3 0.1
Al 9.4 0.1
P 2.8 0.0
Fe 2.1 0.1
K 1.4 0.0
Ti 1.0 0.0
Mg 0.4 0.0
Powered by Tru-Q®


WCL 39 (1.64.1748)
Spectrum 1748
Wt% σ
O 45.5 0.1
Si 18.8 0.1
Al 12.2 0.1
Ce 10.1 0.1
K 5.1 0.0
P 2.6 0.1
Zr 2.3 0.1
Fe 1.9 0.1
Mg 1.2 0.0
Ti 0.4 0.0
Powered by Tru-Q®

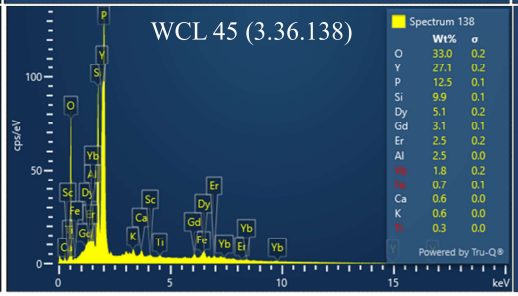

WCL 40 (2.57.1669)
Spectrum 1669
Wt% σ
O 45.1 0.2
Si 19.7 0.1
Zr 11.4 0.2
Ce 8.9 0.1
Al 8.6 0.1
Fe 2.1 0.1
P 1.6 0.1
K 1.6 0.0
Mg 0.7 0.0
Ti 0.3 0.0
Ca 0.1 0.0
Powered by Tru-Q®
cps/eV
keV

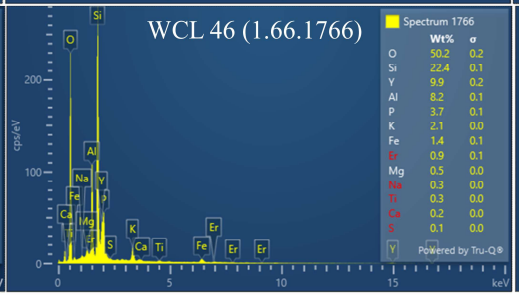

WCL 41 (2.24.1200)
Spectrum 1200
Wt% σ
O 47.0 0.2
Si 20.4 0.1
Al 11.2 0.1
Fe 10.9 0.2
Ce 6.2 0.2
K 2.2 0.1
P 1.1 0.1
Mg 0.8 0.1
Ti 0.2 0.1
Powered by Tru-Q®
cps/eV
keV


WCL 42 (2.61.1699)
Spectrum 1699
Wt% σ
O 47.6 0.1
Si 19.6 0.1
Fe 16.9 0.1
Al 9.8 0.1
Ce 3.3 0.1
K 1.5 0.0
P 0.7 0.0
Ti 0.6 0.0
Powered by Tru-Q®
cps/eV
keV


WCL 43 (2.62.1710)
Spectrum 1710
Wt% σ
O 50.1 0.1
Si 21.0 0.1
Fe 15.6 0.1
Al 9.6 0.1
Ce 1.5 0.1
K 1.4 0.0
Ti 0.6 0.0
P 0.2 0.0
Powered by Tru-Q®
cps/eV
keV


WCL 44 (1.20.276)
Spectrum 276
Wt% σ
O 53.7 0.0
Si 27.3 0.0
Al 16.3 0.0
Fe 1.3 0.0
K 1.1 0.0
Ce 0.2 0.0
P 0.1 0.0
Powered by Tru-Q®
cps/eV
keV


WCL 45 (3.36.138)
Spectrum 138
Wt% σ
O 33.0 0.2
Y 27.1 0.2
P 12.5 0.1
Si 9.9 0.1
Dy 5.1 0.2
Gd 3.1 0.1
Er 2.5 0.2
Al 2.5 0.0
Yb 1.8 0.2
Fe 0.7 0.1
Ca 0.6 0.0
K 0.6 0.0
Ti 0.3 0.0
Powered by Tru-Q®
cps/eV
keV


WCL 46 (1.66.1766)
Spectrum 1766
Wt% σ
O 50.2 0.2
Si 22.4 0.1
Y 9.9 0.2
Al 8.2 0.1
P 3.7 0.1
K 2.1 0.0
Fe 1.4 0.1
Er 0.9 0.1
Mg 0.5 0.0
Na 0.3 0.0
Ti 0.3 0.0
Ca 0.2 0.0
S 0.1 0.0
Powered by Tru-Q®
cps/eV
keV

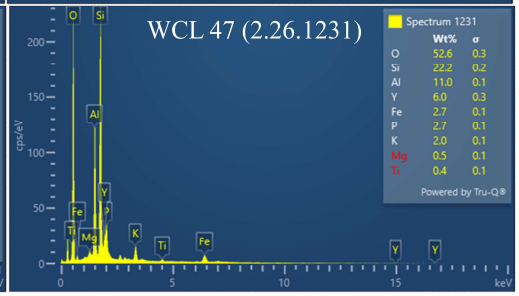
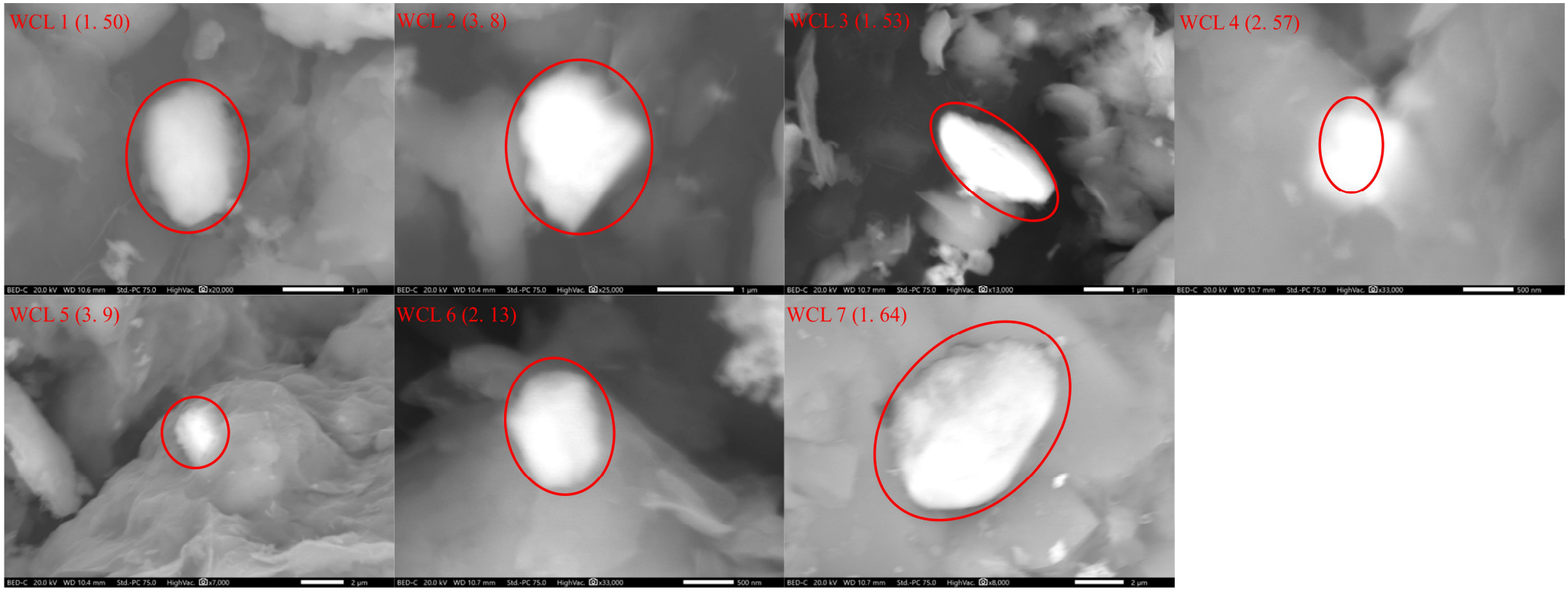
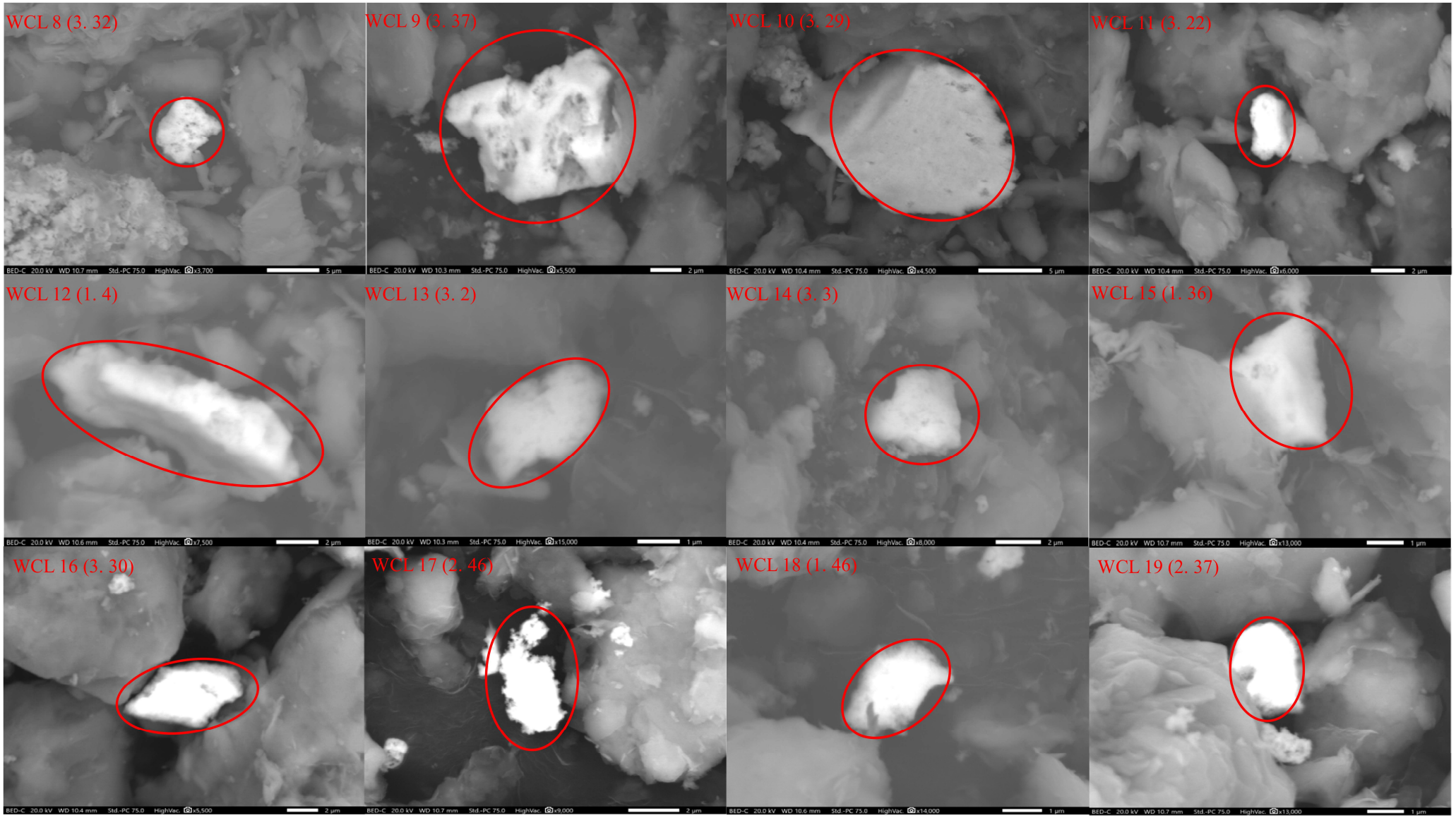
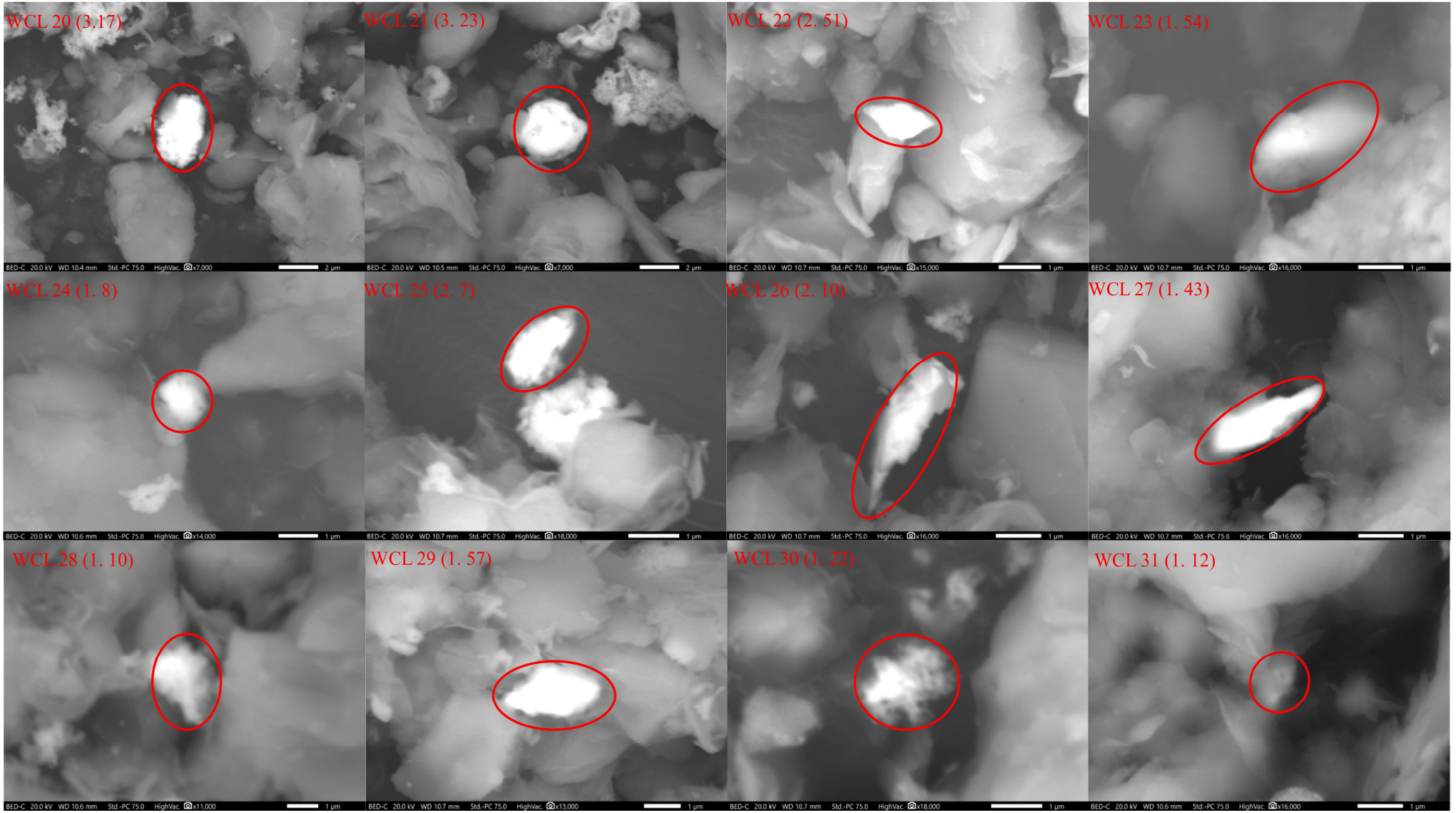

WCL 47 (2.26.1231)
Spectrum 1231
Wt% σ
O 52.6 0.3
Si 22.2 0.2
Al 11.0 0.1
Y 6.0 0.3
Fe 2.7 0.1
P 2.7 0.1
K 2.0 0.1
Mg 0.5 0.1
Ti 0.4 0.1
Powered by Tru-Q®
cps/eV
keV

Figure B.4 SEM images of the particles containing REEs found from the calcined Western Kentucky No. 13 (WK No. 13) coal waste leaching residue . (The images are labelled as WCL # (Specimen #. Site #))




WCL 8 (3. 32)
WCL 9 (3. 37)
WCL 10 (3. 29)
WCL 11 (3. 22)
WCL 12 (1. 4)
WCL 13 (3. 2)
WCL 14 (3. 3)
WCL 15 (1. 36)
WCL 16 (3. 30)
WCL 17 (2. 46)
WCL 18 (1. 46)
WCL 19 (2. 37)


WCL 20 (3.17)
WCL 21 (3. 23)
WCL 22 (2. 51)
WCL 23 (1. 54)
WCL 24 (1. 8)
WCL 25 (2. 7)
WCL 26 (2. 10)
WCL 27 (1. 43)
WCL 28 (1. 10)
WCL 29 (1. 57)
WCL 30 (1. 22)
WCL 31 (1. 12)

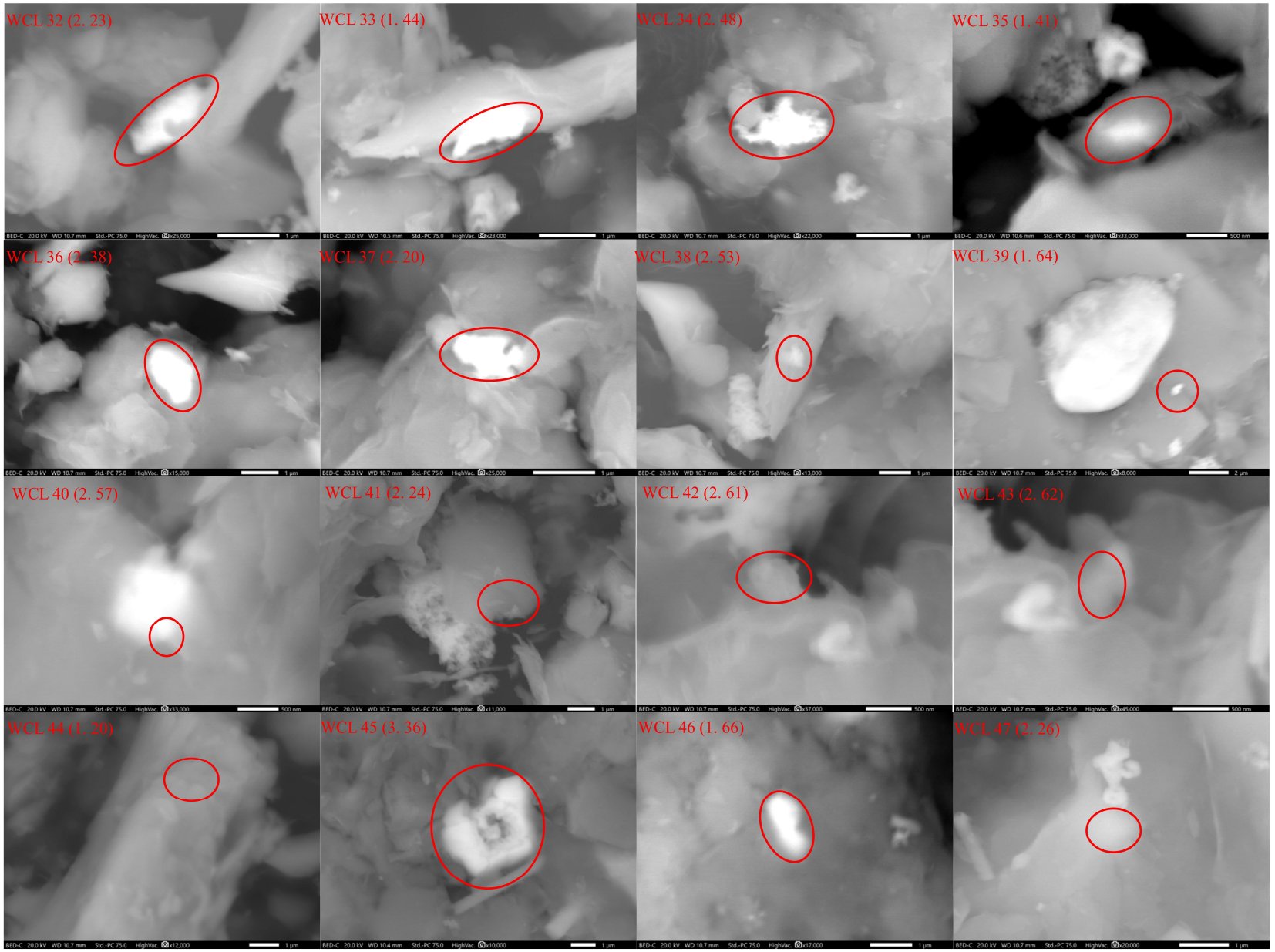
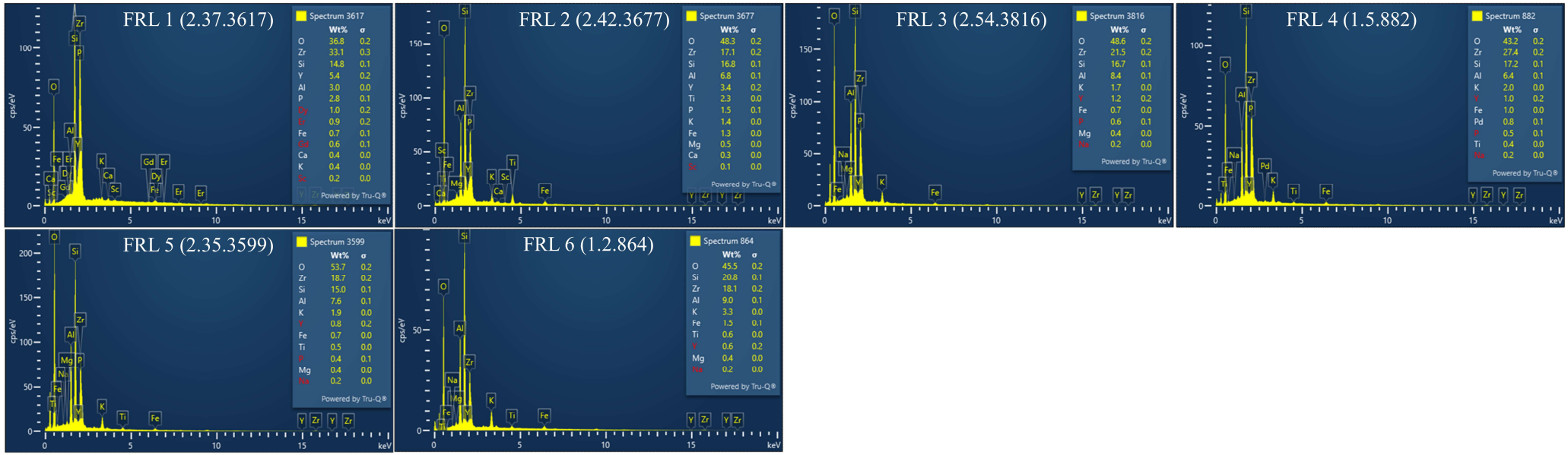
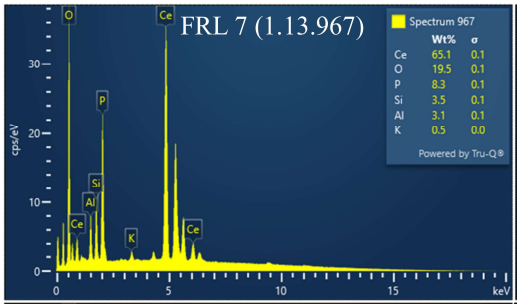

WCL 32 (2. 23)
WCL 33 (1. 44)
WCL 34 (2. 48)
WCL 35 (1. 41)
WCL 36 (2. 38)
WCL 37 (2. 20)
WCL 38 (2. 53)
WCL 39 (1. 64)
WCL 40 (2. 57)
WCL 41 (2. 24)
WCL 42 (2. 61)
WCL 43 (2. 62)
WCL 44 (1. 20)
WCL 45 (3. 36)
WCL 46 (1. 66)
WCL 47 (2. 26)

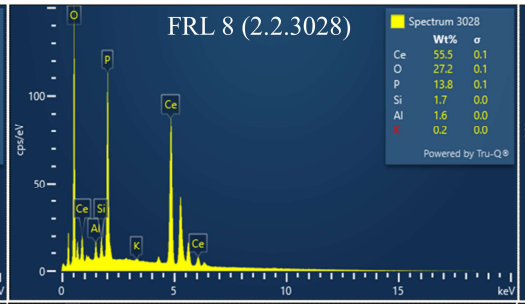
Table B.3 Elemental compositions of the particles containing REEs found from the raw Fire Clay (FC) coal waste leaching residue through SEM-EDS analysis.

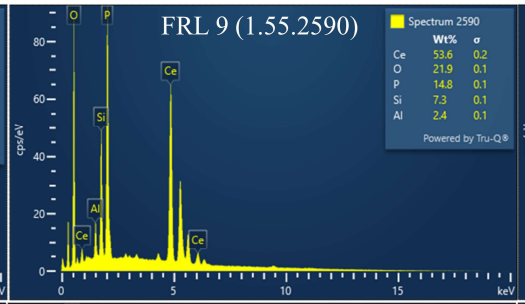
Particle #	Specimen #	Site #	Spectrum #	Mineral	Al (%)	Si (%)	O (%)	Ca (%)	P (%)	Fe (%)	K (%)	S (%)	Ba (%)	Mg (%)	Ti (%)	Na (%)	Sr (%)	F(%)	Zr (%)	Sc (%)	La (%)	Ce(%)	Pr (%)	Nd(%)	Sm (%)	Gd (%)	Y(%)	Dy (%)	Er (%)	Yb (%)	Ho (%)	Th(%)	U (%)	TREE (%)	Sum (%)	Al/Si	Al/P	TREE/P
FRL 1	2	37	3617	Zircon	3.0	14.8	36.8	0.4	2.8	0.7	0.4	0.0	0.0	0.0	0.0	0.0	0.0	0.0	33.1	0.2	0.0	0.0	0.0	0.0	0.0	0.6	5.4	1.0	0.9	0.0	0.0	0.0	0.0	8.1	100	0.20	1.07	2.89
FRL 2	2	42	3677	Zircon	6.8	16.8	48.3	0.3	1.5	1.3	1.4	0.0	0.0	0.5	2.3	0.0	0.0	0.0	17.1	0.1	0.0	0.0	0.0	0.0	0.0	0.0	3.4	0.0	0.0	0.0	0.0	0.0	0.0	3.5	100	0.40	4.53	2.33
FRL 3	2	54	3816	Zircon	8.4	16.7	48.6	0.0	0.6	0.7	1.7	0.0	0.0	0.4	0.0	0.2	0.0	0.0	21.5	0.0	0.0	0.0	0.0	0.0	0.0	0.0	1.2	0.0	0.0	0.0	0.0	0.0	0.0	1.2	100	0.50	14.00	2.00
FRL 4	1	5	882	Zircon	6.6	17.4	43.4	0.0	0.5	1.0	2.0	0.0	0.0	0.0	0.4	0.2	0.0	0.0	27.4	0.0	0.0	0.0	0.0	0.0	0.0	0.0	1.1	0.0	0.0	0.0	0.0	0.0	0.0	1.1	100	0.38	13.20	2.20
FRL 5	2	35	3599	Zircon	7.6	15.0	53.7	0.0	0.4	0.7	1.9	0.0	0.0	0.4	0.5	0.2	0.0	0.0	18.7	0.0	0.0	0.0	0.0	0.0	0.0	0.0	0.8	0.0	0.0	0.0	0.0	0.0	0.0	0.8	100	0.51	19.00	2.00
FRL 6	1	2	864	Zircon	9.0	20.8	45.5	0.0	0.0	1.5	3.3	0.0	0.0	0.4	0.6	0.2	0.0	0.0	18.1	0.0	0.0	0.0	0.0	0.0	0.0	0.0	0.6	0.0	0.0	0.0	0.0	0.0	0.0	0.6	100	0.43	N/A	N/A
FRL 7	1	13	967	Monazite	3.1	3.5	19.5	0.0	8.3	0.0	0.5	0.0	0.0	0.0	0.0	0.0	0.0	0.0	0.0	0.0	0.0	65.1	0.0	0.0	0.0	0.0	0.0	0.0	0.0	0.0	0.0	0.0	0.0	65.1	100	0.89	0.37	7.84
FRL 8	2	2	3028	Monazite	1.6	1.7	27.2	0.0	13.8	0.0	0.2	0.0	0.0	0.0	0.0	0.0	0.0	0.0	0.0	0.0	0.0	55.5	0.0	0.0	0.0	0.0	0.0	0.0	0.0	0.0	0.0	0.0	0.0	55.5	100	0.94	0.12	4.02
FRL 9	1	55	2590	Monazite	2.4	7.3	21.9	0.0	14.8	0.0	0.0	0.0	0.0	0.0	0.0	0.0	0.0	0.0	0.0	0.0	0.0	53.6	0.0	0.0	0.0	0.0	0.0	0.0	0.0	0.0	0.0	0.0	0.0	53.6	100	0.33	0.16	3.62
FRL 10	1	35	4196	Monazite	3.4	4.3	24.5	0.0	12.0	0.0	0.8	0.0	0.0	0.0	0.0	0.0	0.0	0.0	0.0	0.0	13.8	26.0	2.8	10.3	0.0	0.0	0.0	0.0	0.0	0.0	0.0	2.2	0.0	52.9	100	0.79	0.28	4.41
FRL 11	1	69	2894	Monazite	2.9	4.1	28.3	0.0	11.7	0.0	0.4	0.0	0.0	0.0	0.0	0.0	0.0	0.0	0.0	0.0	0.0	52.6	0.0	0.0	0.0	0.0	0.0	0.0	0.0	0.0	0.0	0.0	0.0	52.6	100	0.71	0.25	4.50
FRL 12	1	76	2972	Monazite	3.7	5.8	26.1	0.0	12.0	0.0	0.4	0.0	0.0	0.0	0.0	1.0	0.0	0.0	0.0	0.0	0.0	51.0	0.0	0.0	0.0	0.0	0.0	0.0	0.0	0.0	0.0	0.0	0.0	51.0	100	0.64	0.31	4.25
FRL 13	1	52	2565	Monazite	2.4	5.9	27.8	0.0	12.8	0.0	0.4	0.0	0.0	0.0	0.0	0.0	0.0	0.0	0.0	0.0	0.0	50.7	0.0	0.0	0.0	0.0	0.0	0.0	0.0	0.0	0.0	0.0	0.0	50.7	100	0.41	0.19	3.96
FRL 14	1	18	1052	Monazite	3.8	4.5	32.3	0.3	12.0	0.0	0.4	0.0	0.0	0.0	0.0	0.0	0.0	0.0	0.0	0.0	9.8	21.0	2.3	10.0	2.1	1.6	0.0	0.0	0.0	0.0	0.0	0.0	0.0	46.8	100	0.84	0.32	3.90
FRL 15	2	44	4279	Monazite	5.2	8.3	29.1	0.0	9.7	0.0	0.8	0.0	0.0	0.0	0.0	0.0	0.0	0.0	0.0	0.0	0.0	46.8	0.0	0.0	0.0	0.0	0.0	0.0	0.0	0.0	0.0	0.0	0.0	46.8	100	0.63	0.54	4.82
FRL 16	1	59	2660	Monazite	7.4	12.1	24.5	0.0	8.4	1.0	0.8	0.0	0.0	0.3	0.0	0.0	0.0	0.0	0.0	0.0	0.0	45.5	0.0	0.0	0.0	0.0	0.0	0.0	0.0	0.0	0.0	0.0	0.0	45.5	100	0.61	0.88	5.42
FRL 17	1	36	1430	Monazite	11.3	21.3	13.9	0.0	5.8	1.1	2.6	0.0	0.0	0.4	0.0	0.0	0.0	0.0	0.0	0.0	18.8	17.7	1.7	3.7	0.8	1.0	0.0	0.0	0.0	0.0	0.0	0.0	0.0	43.7	100	0.53	1.95	7.53
FRL 18	1	9	913	Monazite	4.6	6.5	34.1	0.0	11.0	0.3	0.7	0.0	0.0	0.0	0.0	0.0	0.0	0.0	0.0	0.0	0.0	42.7	0.0	0.0	0.0	0.0	0.0	0.0	0.0	0.0	0.0	0.0	0.0	42.7	100	0.71	0.42	3.88
FRL 19	1	21	1097	Monazite	4.3	7.9	33.8	0.0	12.0	0.3	0.7	0.0	0.0	0.0	0.0	0.0	0.0	0.0	0.0	0.0	0.0	41.0	0.0	0.0	0.0	0.0	0.0	0.0	0.0	0.0	0.0	0.0	0.0	41.0	100	0.54	0.36	3.42
FRL 20	2	14	3946	Monazite	4.2	9.5	36.0	0.0	10.4	0.0	0.9	0.0	0.0	0.0	0.0	0.0	0.0	0.0	0.0	0.0	0.0	39.1	0.0	0.0	0.0	0.0	0.0	0.0	0.0	0.0	0.0	0.0	0.0	39.1	100	0.44	0.40	3.76
FRL 21	1	40	4254	Monazite	5.6	10.3	32.8	0.0	9.6	1.7	0.7	0.5	0.0	0.0	0.0	0.0	0.0	0.0	0.0	0.0	0.0	38.8	0.0	0.0	0.0	0.0	0.0	0.0	0.0	0.0	0.0	0.0	0.0	38.8	100	0.54	0.58	4.04
FRL 22	2	38	3629	Monazite	8.3	15.1	31.2	0.0	8.0	0.6	1.6	0.0	0.0	0.5	0.2	0.0	0.0	0.0	0.0	0.0	6.9	16.6	1.7	7.7	1.1	0.6	0.0	0.0	0.0	0.0	0.0	0.0	0.0	34.6	100	0.55	1.04	4.33
FRL 23	2	33	3562	Monazite	7.6	12.9	43.9	0.0	8.9	0.3	1.5	0.0	0.0	0.0	0.0	0.0	0.0	0.0	0.0	0.0	0.0	24.8	0.0	0.0	0.0	0.0	0.0	0.0	0.0	0.0	0.0	0.0	0.0	24.8	100	0.59	0.85	2.79
FRL 24	2	51	3800	Monazite	5.1	16.9	39.0	0.0	11.2	0.4	1.0	0.0	0.0	0.0	1.8	0.0	0.0	0.0	0.0	0.0	0.0	24.6	0.0	0.0	0.0	0.0	0.0	0.0	0.0	0.0	0.0	0.0	0.0	24.6	100	0.30	0.46	2.20
FRL 25	2	5	3892	Monazite	11.2	14.9	41.0	0.0	6.2	0.8	1.2	0.0	0.0	0.6	0.2	0.5	0.0	0.0	0.0	0.0	0.0	23.3	0.0	0.0	0.0	0.0	0.0	0.0	0.0	0.0	0.0	0.0	0.0	23.3	100	0.75	1.81	3.76
FRL 26	2	4	3054	Monazite	9.0	15.0	44.3	0.0	5.7	1.0	2.5	0.0	0.0	0.8	0.0	0.0	0.0	0.0	0.0	0.0	0.0	21.7	0.0	0.0	0.0	0.0	0.0	0.0	0.0	0.0	0.0	0.0	0.0	21.7	100	0.60	1.58	3.81
FRL 27	2	29	4135	Monazite	4.0	24.8	44.5	0.0	5.6	0.2	0.6	0.0	0.0	0.2	0.0	0.0	0.0	0.0	0.0	0.0	0.0	20.0	0.0	0.0	0.0	0.0	0.0	0.0	0.0	0.0	0.0	0.0	0.0	20.0	100	0.16	0.71	3.57
FRL 28	1	6	888	Monazite	8.9	24.9	45.0	0.0	3.9	0.7	1.7	0.0	0.0	0.5	0.1	0.0	0.0	0.0	0.0	0.0	0.0	14.4	0.0	0.0	0.0	0.0	0.0	0.0	0.0	0.0	0.0	0.0	0.0	14.4	100	0.36	2.28	3.69
FRL 29	2	8	3101	Monazite	13.1	20.0	45.2	0.0	3.2	0.9	2.3	0.0	0.0	0.6	0.8	0.0	0.0	0.0	0.0	0.0	0.0	13.9	0.0	0.0	0.0	0.0	0.0	0.0	0.0	0.0	0.0	0.0	0.0	13.9	100	0.66	4.09	4.34
FRL 30	2	46	3761	Monazite	8.1	30.4	42.9	0.0	3.3	0.9	2.2	0.0	0.0	0.0	0.2	0.0	0.0	0.0	0.0	0.0	0.0	12.0	0.0	0.0	0.0	0.0	0.0	0.0	0.0	0.0	0.0	0.0	0.0	12.0	100	0.27	2.45	3.64
FRL 31	1	8	3912	Monazite	14.3	17.8	50.0	0.0	2.8	0.9	3.7	0.0	0.0	0.5	0.3	0.4	0.0	0.0	0.0	0.0	0.0	9.3	0.0	0.0	0.0	0.0	0.0	0.0	0.0	0.0	0.0	0.0	0.0	9.3	100	0.80	5.11	3.32
FRL 32	1	3	869	Xenotime	3.6	5.7	37.2	0.0	12.5	0.0	0.9	0.0	0.0	0.0	0.0	0.0	0.0	0.0	0.0	0.0	0.0	0.0	0.0	0.0	0.0	3.2	28.2	4.7	2.4	1.5	0.0	0.0	0.0	40.0	100	0.63	0.29	3.20
FRL 33	2	23	3368	Xenotime	5.2	7.2	42.6	0.0	9.9	0.0	0.5	0.0	0.0	0.0	3.5	0.0	0.0	0.0	0.0	0.0	0.0	0.0	0.0	0.0	0.0	1.6	22.6	3.0	2.2	1.7	0.0	0.0	0.0	31.1	100	0.72	0.53	3.14
FRL 34	1	19	4003	Xenotime	9.4	17.2	43.7	0.0	6.5	0.7	2.4	0.0	0.0	0.4	0.3	0.0	0.0	0.0	0.0	0.0	0.0	0.0	0.0	0.0	0.0	1.5	14.0	2.2	1.6	0.0	0.0	0.0	0.0	19.3	100	0.55	1.45	2.97
FRL 35	1	38	4229	Xenotime	13.8	22.3	39.2	0.0	4.9	2.1	3.9	0.0	0.0	0.6	0.3	0.0	0.0	0.0	0.0	0.0	0.0	0.0	0.0	0.0	0.0	1.3	9.0	2.6	0.0	0.0	0.0	0.0	0.0	12.9	100	0.62	2.82	2.63
FRL 36	1	72	2926	Crandallite	16.7	4.8	49.6	0.3	9.9	0.0	0.3	0.0	0.0	0.0	0.0	0.0	2.5	0.0	0.0	0.0	4.3	8.1	0.8	2.7	0.0	0.0	0.0	0.0	0.0	0.0	0.0	0.0	0.0	15.9	100	3.48	1.69	1.61
FRL 37	2	28	3450	Crandallite	18.7	17.1	30.3	0.7	8.8	0.6	1.9	1.4	0.0	0.3	0.0	0.0	4.7	0.0	0.0	0.0	3.6	8.1	0.8	3.2	0.0	0.0	0.0	0.0	0.0	0.0	0.0	0.0	0.0	15.7	100	1.09	2.13	1.78
FRL 38	2	40	3652	Crandallite	16.3	12.8	35.1	1.2	9.0	1.3	1.3	0.0	2.7	0.0	0.5	0.0	5.2	0.0	0.0	0.0	5.0	7.3	0.5	1.8	0.0	0.0	0.0	0.0	0.0	0.0	0.0	0.0	0.0	14.6	100	1.27	1.81	1.62
FRL 39	1	48	1599	Crandallite	15.8	12.2	51.7	0.0	5.7	0.5	2.0	0.0	0.0	0.0	0.6	0.0	1.3	0.0	0.0	0.0	2.2	5.1	0.6	2.2	0.0	0.0	0.0	0.0	0.0	0.0	0.0	0.0	0.0	10.1	100	1.30	2.77	1.77
FRL 40	1	77	2976	Crandallite	17.8	12.8	43.4	2.0	8.3	0.8	1.3	0.0	1.4	0.0	0.0	0.0	2.7	0.0	0.0	0.0	2.2	4.6	0.4	2.3	0.0	0.0	0.0	0.0	0.0	0.0	0.0	0.0	0.0	9.5	100	1.39	2.14	1.14
FRL 41	1	15	988	Crandallite	16.9	17.8	36.5	0.3	8.3	1.1	1.4	0.8	0.8	0.0	0.2	0.9	5.6	0.0	0.0	0.0	2.2	4.6	0.5	1.9	0.0	0.0	0.0	0.0	0.0	0.0	0.0	0.0	0.0	9.2	100	0.95	2.04	1.11
FRL 42	2	29	4132	Crandallite	16.7	11.0	50.9	0.9	7.0	0.6	1.1	0.0	0.0	0.4	0.0	0.0	3.0	0.0	0.0	0.0	3.9	2.7	0.0	1.8	0.0	0.0	0.0	0.0	0.0	0.0	0.0	0.0	0.0	8.4	100	1.52	2.39	1.20
FRL 43	1	61	2706	Crandallite	12.1	17.8	53.4	0.3	4.9	0.6	1.1	0.4	0.4	0.4	0.0	0.0	2.0	0.0	0.0	0.0	1.4	3.2	0.5	1.4	0.3	0.0	0.0	0.0	0.0	0.0	0.0	0.0	0.0	6.8	100	0.68	2.47	1.39
FRL 44	1	31	4153	Crandallite	14.1	12.8	53.7	0.3	5.9	0.3	0.9	0.5	0.0	0.0	0.0	1.6	3.1	0.0	0.0	0.0	1.9	3.7	0.0	1.2	0.0	0.0	0.0	0.0	0.0	0.0	0.0	0.0	0.0	6.8	100	1.10	2.39	1.15
FRL 45	2	25	3400	Crandallite	17.4	11.9	48.2	1.6	7.9	1.4	1.0	0.0	1.0	0.0	0.2	0.0	3.5	0.0	0.0	0.0	2.3	2.3	0.0	1.3	0.0	0.0	0.0	0.0	0.0	0.0	0.0	0.0	0.0	5.9	100	1.46	2.20	0.75
FRL 46	2	43	4276	Crandallite	12.9	18.0	48.2	0.2	6.5	0.8	1.1	1.3	0.5	0.0	0.0	0.0	4.6	0.0	0.0	0.0	1.4	3.0	0.0	1.4	0.0	0.0	0.0	0.0	0.0	0.0	0.0	0.0	0.0	5.8	100	0.72	1.98	0.89
FRL 47	1	28	4124	Crandallite	16.4	12.4	50.9	1.3	6.5	1.0	1.6	0.5	0.0	0.6	0.2	0.0	3.6	0.0	0.0	0.0	1.2	2.3	0.4	1.0	0.0	0.0	0.0	0.0	0.0	0.0	0.0	0.0	0.0	4.9	100	1.32	2.52	0.75
FRL 48	1	73	2940	Crandallite	15.0	15.0	50.8	0.6	4.8	1.1	0.7	1.6	0.6	0.5	0.2	0.0	4.5	0.0	0.0	0.0	1.2	2.5	0.0	0.9	0.0	0.0	0.0	0.0	0.0	0.0	0.0	0.0	0.0	4.6	100	1.00	3.13	0.96
FRL 49	2	47	3763	Crandallite	15.8	24.6	42.5	0.0	2.6	1.8	5.1	0.0	0.0	0.5	0.8	0.0	2.3	0.0	0.0	0.0	1.0	2.3	0.0	0.6	0.0	0.0	0.0	0.0	0.0	0.0	0.0	0.0	0.0	3.9	100	0.64	6.08	1.50
FRL 50	2	19	3267	Crandallite	16.0	18.0	49.2	0.0	4.8	1.0	4.0	0.0	0.0	0.5	0.0	0.0	2.8	0.0	0.0	0.0	0.0	2.7	0.0	1.0	0.0	0.0	0.0	0.0	0.0	0.0	0.0	0.0	0.0	3.7	100	0.89	3.33	0.77
FRL 51	1	33	1365	Crandallite	15.2	13.5	51.5	0.5	5.0	0.8	2.2	1.6	0.4	0.4	0.2	0.8	4.5	0.0	0.0	0.0	0.8	1.8	0.0	0.9	0.0	0.0	0.0	0.0	0.0	0.0	0.0	0.0	0.0	3.5	100	1.13	3.04	0.70
FRL 52	2	26	3410	Crandallite	18.4	16.6	52.4	0.2	3.8	0.5	1.0	0.0	0.6	0.0	0.2	0.0	2.9	0.0	0.0	0.0	1.4	1.5	0.0	0.4	0.0	0.0	0.0	0.0	0.0	0.0	0.0	0.0	0.0	3.3	100	1.11	4.84	0.87
FRL 53	2	12	3158	Crandallite	15.3	9.1	57.3	1.9	7.4	0.6	1.5	0.0	0.8	0.0	0.1	0.0	3.2	0.0	0.0	0.0	0.7	1.5	0.0	0.4	0.0	0.0	0.0	0.0	0.0	0.0	0.0	0.0	0.0	2.6	100	1.68	2.07	0.35
FRL 54	2	21	4018	Crandallite	17.5	19.4	47.7	0.4	3.4	3.4	4.1	0.6	0.0	1.0	0.3	0.0	0.0	0.0	0.0	0.0	0.9	1.4	0.0	0.0	0.0	0.0	0.0	0.0	0.0	0.0	0.0	0.0	0.0	2.3	100	0.90	5.15	0.68
FRL 55	1	44	1539	Crandallite	16.5	20.7	48.1	0.0	2.6	1.7	4.5	0.0	0.0	0.7	1.0	0.0	2.5	0.0	0.0	0.0	0.0	1.1	0.0	0.7	0.0	0.0	0.0	0.0	0.0	0.0	0.0	0.0	0.0	1.8	100	0.80	6.35	0.69
FRL 56	2	56	3831	Crandallite	19.9	25.5	46.0	0.0	0.9	2.1	2.6	0.0	0.0	0.7	0.6	0.0	0.0	0.0	0.0	0.0	0.4	0.8	0.0	0.4	0.0	0.0	0.0	0.0	0.0	0.0	0.0	0.0	0.0	1.6	100	0.78	22.11	1.78
FRL 57	2	11	3144	Crandallite	18.5	19.9	50.2	0.4	2.8	1.4	1.5	0.0	0.3	0.6	0.1	0.0	2.6	0.0	0.0	0.0	0.4	0.8	0.0	0.4	0.0	0.0	0.0	0.0	0.0	0.0	0.0	0.0	0.0	1.6	100	0.93	6.61	0.57
FRL 58	1	10	925	Crandallite	16.0	21.5	51.1	0.2	2.3	1.2	2.1	0.8	0.0	0.7	0.2	0.0	2.7	0.0	0.0	0.0	0.0	0.9	0.0	0.4	0.0	0.0	0.0	0.0	0.0	0.0	0.0	0.0	0.0	1.3	100	0.74	6.96	0.57
FRL 59	1	62	2714	Crandallite	15.6	21.3	52.0	0.0	2.2	1.5	3.1	0.0	0.0	1.0	0.0	0.0	2.3	0.0	0.0	0.0	0.0	0.9	0.0	0.0	0.0	0.0	0.0	0.0	0.0	0.0	0.0	0.0	0.0	0.9	100	0.73	7.09	0.41
FRL 60	2	17	3228	Crandallite	15.9	29.2	44.2	0.3	1.5	2.6	3.3	0.0	0.4	1.0	0.9	0.0	0.0	0.0	0.0	0.0	0.0	0.4	0.0	0.4	0.0	0.0	0.0	0.0	0.0	0.0	0.0	0.0	0.0	0.8	100	0.54	10.60	0.53
FRL 61	2	3	3874	Crandallite	17.6	22.3	52.0	0.0	1.4	1.0	3.8	0.3	0.0	0.8	0.0	0.0	0.0	0.0	0.0	0.0	0.0	0.5	0.0	0.3	0.0	0.0	0.0	0.0	0.0	0.0	0.0	0.0	0.0	0.8	100	0.79	12.57	0.57
FRL 62	1	68	2891	Crandallite	17.3	25.2	47.8	0.0	0.5	1.8	4.5	0.0	0.0	0.8	1.1	0.4	0.0	0.0	0.0	0.0	0.0	0.7	0.0	0.0	0.0	0.0	0.0	0.0	0.0	0.0	0.0	0.0	0.0	0.7	100	0.69	34.60	1.40
FRL 63	2	31	3513	Crandallite	16.3	23.5	53.2	0.0	0.3	1.1	4.0	0.0	0.0	0.7	0.1	0.4	0.0	0.0	0.0	0.0	0.0	0.5	0.0	0.0	0.0	0.0	0.0	0.0	0.0	0.0	0.0	0.0	0.0	0.5	100	0.69	54.33	1.67
FRL 64	1	79	3006	Crandallite	16.9	26.3	45.1	0.0	1.4	1.1	4.6	0.0	0.0	0.9	0.2	0.2	2.8	0.0	0.0	0.0	0.0	0.5	0.0	0.0	0.0	0.0	0.0	0.0	0.0	0.0	0.0	0.0	0.0	0.5	100	0.64	12.07	0.36

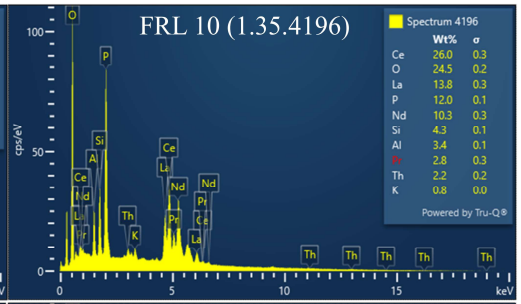
Figure B.5 EDS spectra of the particles containing REEs found from the the raw Fire Clay (FC) coal waste leaching residue. (The spectra are labelled as FRL # (Specimen #. Site #. Spectrum #))

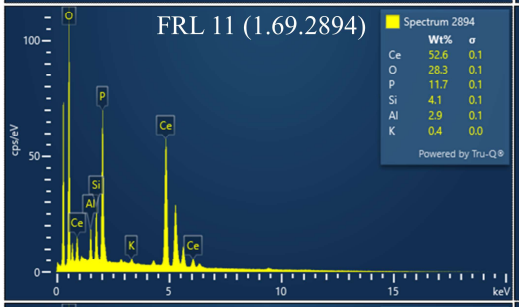


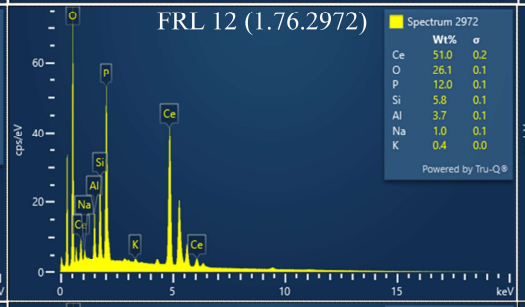

FRL 7 (1.13.967)
Spectrum 967
Wt% σ
Ce 65.1 0.1
O 19.5 0.1
P 8.3 0.1
Si 3.5 0.1
Al 3.1 0.1
K 0.5 0.0
Powered by Tru-Q®
cps/eV
keV

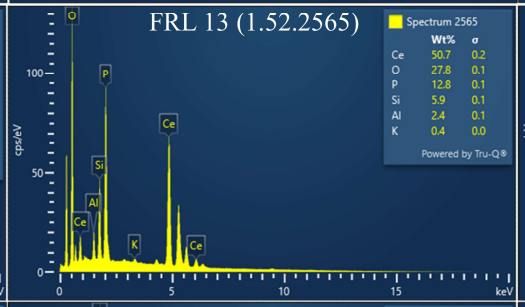

FRL 8 (2.2.3028)
Spectrum 3028
Wt% σ
Ce 55.5 0.1
O 27.2 0.1
P 13.8 0.1
Si 1.7 0.0
Al 1.6 0.0
K 0.2 0.0
Powered by Tru-Q®
cps/eV
keV

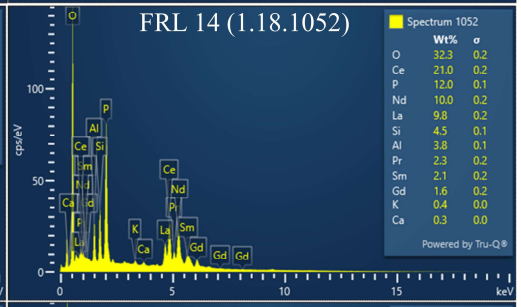

FRL 9 (1.55.2590)
Spectrum 2590
Wt% σ
Ce 53.6 0.2
O 21.9 0.1
P 14.8 0.1
Si 7.3 0.1
Al 2.4 0.1
Powered by Tru-Q®
cps/eV
keV

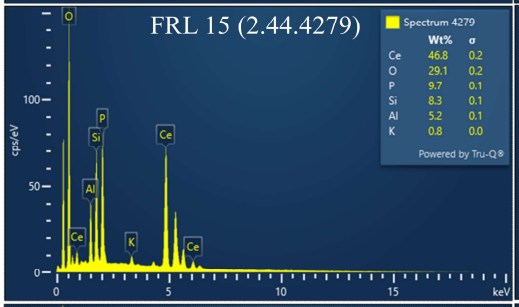

FRL 10 (1.35.4196)
Spectrum 4196
Wt% σ
Ce 26.0 0.3
O 24.5 0.2
La 13.8 0.3
P 12.0 0.1
Nd 10.3 0.3
Si 4.3 0.1
Al 3.4 0.1
Pr 2.8 0.3
Th 2.2 0.2
K 0.8 0.0
Powered by Tru-Q®
cps/eV
keV

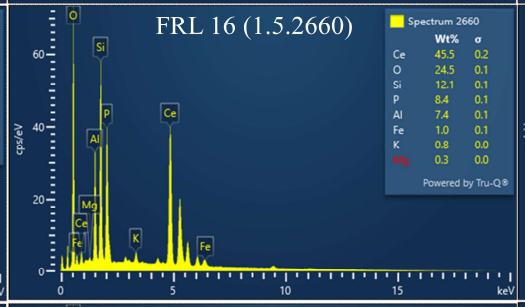

FRL 11 (1.69.2894)
Spectrum 2894
Wt% σ
Ce 52.6 0.1
O 28.3 0.1
P 11.7 0.1
Si 4.1 0.1
Al 2.9 0.1
K 0.4 0.0
Powered by Tru-Q®
cps/eV
keV

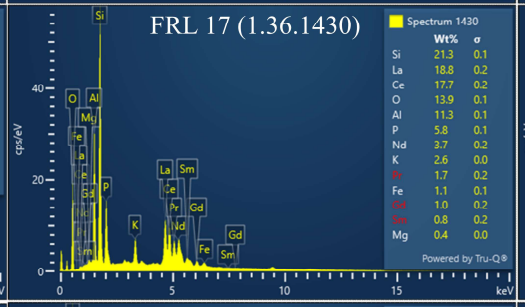

FRL 12 (1.76.2972)
Spectrum 2972
Wt% σ
Ce 51.0 0.2
O 26.1 0.1
P 12.0 0.1
Si 5.8 0.1
Al 3.7 0.1
Na 1.0 0.1
K 0.4 0.0
Powered by Tru-Q®
cps/eV
keV

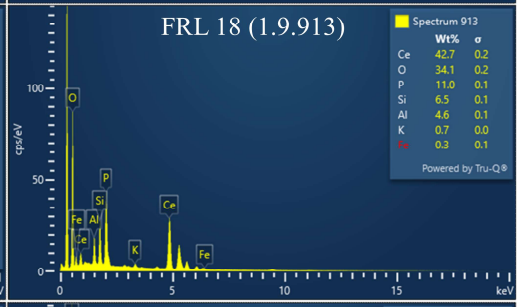

FRL 13 (1.52.2565)
Spectrum 2565
Wt% σ
Ce 50.7 0.2
O 27.8 0.1
P 12.8 0.1
Si 5.9 0.1
Al 2.4 0.1
K 0.4 0.0
Powered by Tru-Q®
cps/eV
keV

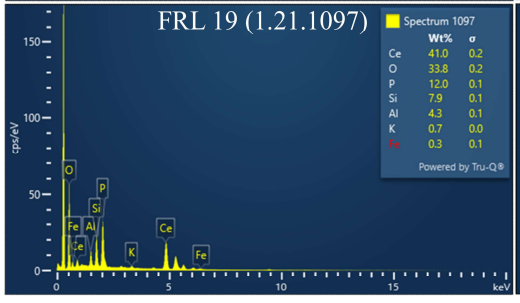

FRL 14 (1.18.1052)
Spectrum 1052
Wt% σ
O 32.3 0.2
Ce 21.0 0.2
P 12.0 0.1
Nd 10.0 0.2
La 9.8 0.2
Si 4.5 0.1
Al 3.8 0.1
Pr 2.3 0.2
Sm 2.1 0.2
Gd 1.6 0.2
K 0.4 0.0
Ca 0.3 0.0
Powered by Tru-Q®
cps/eV
keV

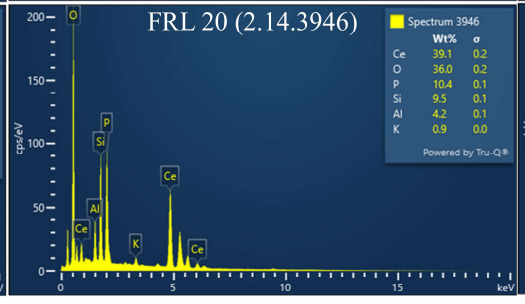

FRL 15 (2.44.4279)
Spectrum 4279
Wt% σ
Ce 46.8 0.2
O 29.1 0.2
P 9.7 0.1
Si 8.3 0.1
Al 5.2 0.1
K 0.8 0.0
Powered by Tru-Q®
cps/eV
keV

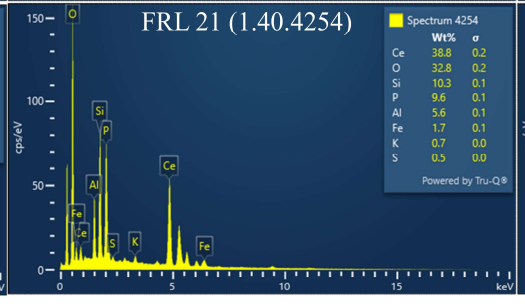

FRL 16 (1.5.2660)
Spectrum 2660
Wt% σ
Ce 45.5 0.2
O 24.5 0.1
Si 12.1 0.1
P 8.4 0.1
Al 7.4 0.1
Fe 1.0 0.1
K 0.8 0.0
Mg 0.3 0.0
Powered by Tru-Q®
cps/eV
keV

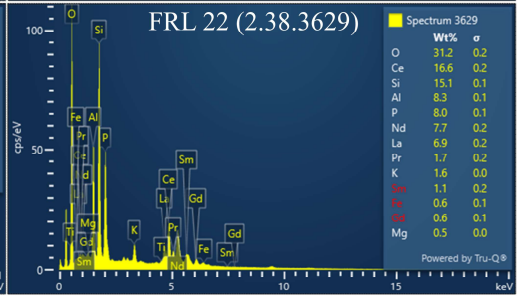

FRL 17 (1.36.1430)
Spectrum 1430
Wt% σ
Si 21.3 0.1
La 18.8 0.2
Ce 17.7 0.2
O 13.9 0.1
Al 11.3 0.1
P 5.8 0.1
Nd 3.7 0.2
K 2.6 0.0
Pr 1.7 0.2
Fe 1.1 0.1
Gd 1.0 0.2
Sm 0.8 0.2
Mg 0.4 0.0
Powered by Tru-Q®
cps/eV
keV

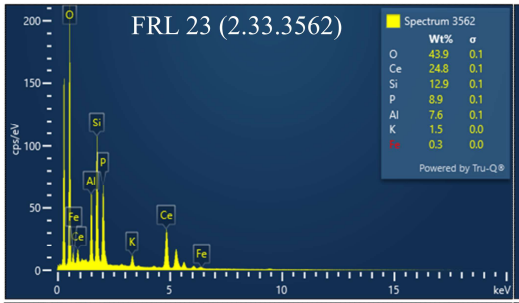

FRL 18 (1.9.913)
Spectrum 913
Wt% σ
Ce 42.7 0.2
O 34.1 0.2
P 11.0 0.1
Si 6.5 0.1
Al 4.6 0.1
K 0.7 0.0
Fe 0.3 0.1
Powered by Tru-Q®
cps/eV
keV

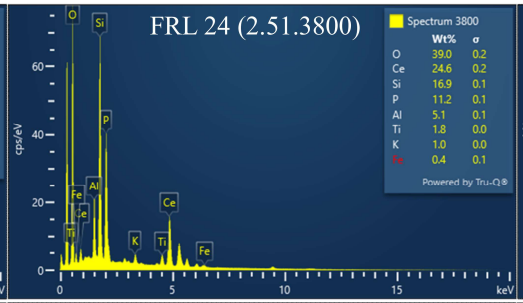

FRL 19 (1.21.1097)
Spectrum 1097
Wt% σ
Ce 41.0 0.2
O 33.8 0.2
P 12.0 0.1
Si 7.9 0.1
Al 4.3 0.1
K 0.7 0.0
Fe 0.3 0.1
Powered by Tru-Q®
cps/eV
keV

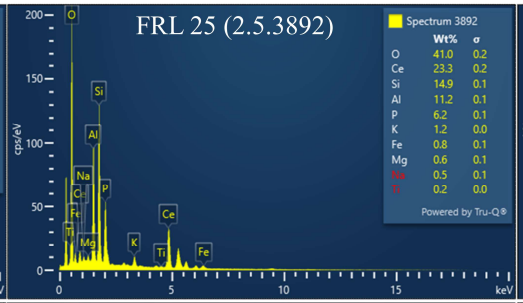

FRL 20 (2.14.3946)
Spectrum 3946
Wt% σ
Ce 39.1 0.2
O 36.0 0.2
P 10.4 0.1
Si 9.5 0.1
Al 4.2 0.1
K 0.9 0.0
Powered by Tru-Q®
cps/eV
keV

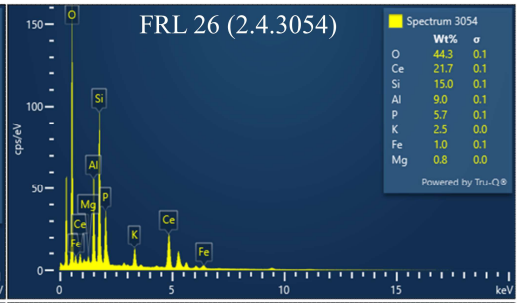

FRL 21 (1.40.4254)
Spectrum 4254
Wt% σ
Ce 38.8 0.2
O 32.8 0.2
Si 10.3 0.1
P 9.6 0.1
Al 5.6 0.1
Fe 1.7 0.1
K 0.7 0.0
S 0.5 0.0
Powered by Tru-Q®
cps/eV
keV

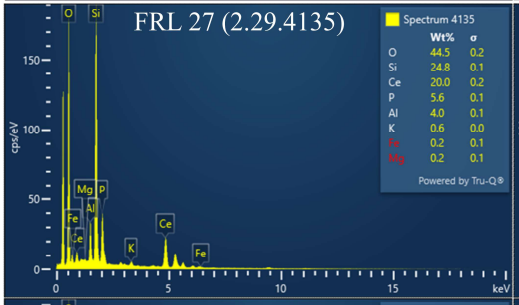

FRL 22 (2.38.3629)
Spectrum 3629
Wt% σ
O 31.2 0.2
Ce 16.6 0.2
Si 15.1 0.1
Al 8.3 0.1
P 8.0 0.1
Nd 7.7 0.2
La 6.9 0.2
Pr 1.7 0.2
K 1.6 0.0
Sm 1.1 0.2
Fe 0.6 0.1
Gd 0.6 0.1
Mg 0.5 0.0
Powered by Tru-Q®
cps/eV
keV

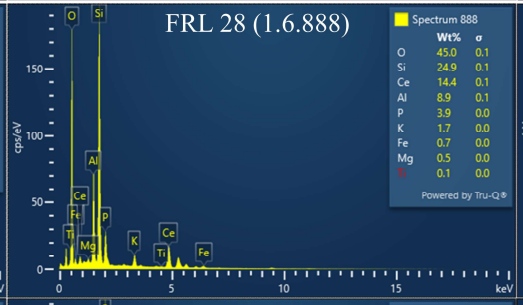

FRL 23 (2.33.3562)
Spectrum 3562
Wt% σ
O 43.9 0.1
Ce 24.8 0.1
Si 12.9 0.1
P 8.9 0.1
Al 7.6 0.1
K 1.5 0.0
Fe 0.3 0.0
Powered by Tru-Q®
cps/eV
keV

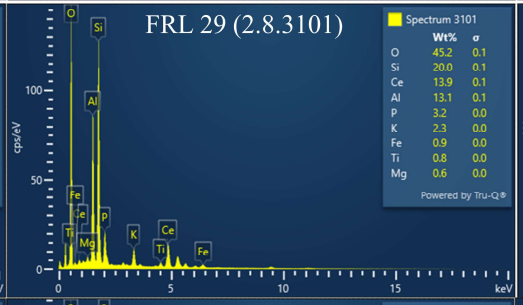

FRL 24 (2.51.3800)
Spectrum 3800
Wt% σ
O 39.0 0.2
Ce 24.6 0.2
Si 16.9 0.1
P 11.2 0.1
Al 5.1 0.1
Ti 1.8 0.0
K 1.0 0.0
Fe 0.4 0.1
Powered by Tru-Q®
cps/eV
keV

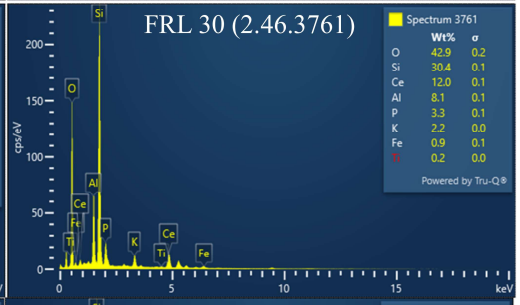

FRL 25 (2.5.3892)
Spectrum 3892
Wt% σ
O 41.0 0.2
Ce 23.3 0.2
Si 14.9 0.1
Al 11.2 0.1
P 6.2 0.1
K 1.2 0.0
Fe 0.8 0.1
Mg 0.6 0.1
Na 0.5 0.1
Ti 0.2 0.0
Powered by Tru-Q®
cps/eV
keV

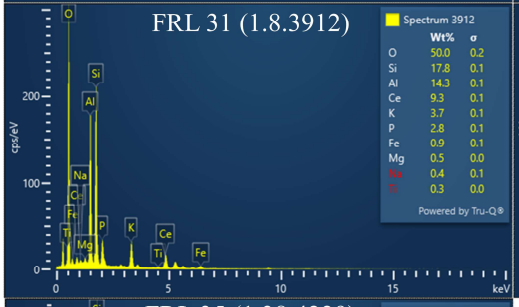

FRL 26 (2.4.3054)
Spectrum 3054
Wt% σ
O 44.3 0.1
Ce 21.7 0.1
Si 15.0 0.1
Al 9.0 0.1
P 5.7 0.1
K 2.5 0.0
Fe 1.0 0.1
Mg 0.8 0.0
Powered by Tru-Q®
cps/eV
keV

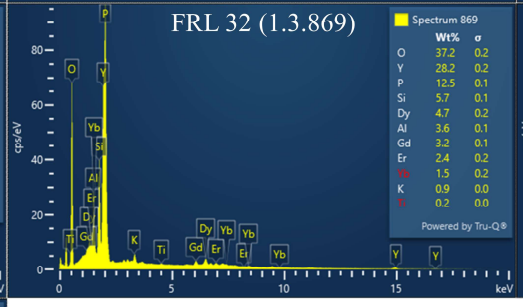

FRL 27 (2.29.4135)
Spectrum 4135
Wt% σ
O 44.5 0.2
Si 24.8 0.1
Ce 20.0 0.2
P 5.6 0.1
Al 4.0 0.1
K 0.6 0.0
Fe 0.2 0.1
Mg 0.2 0.1
Powered by Tru-Q®
cps/eV
keV

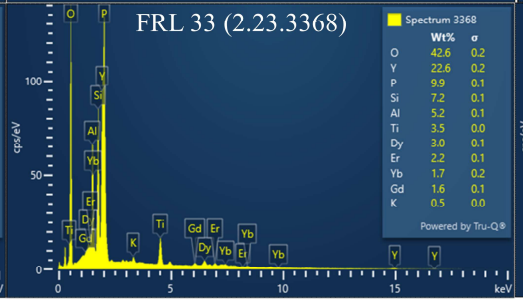

FRL 28 (1.6.888)
Spectrum 888
Wt% σ
O 45.0 0.1
Si 24.9 0.1
Ce 14.4 0.1
Al 8.9 0.1
P 3.9 0.0
K 1.7 0.0
Fe 0.7 0.0
Mg 0.5 0.0
Ti 0.1 0.0
Powered by Tru-Q®
cps/eV
keV

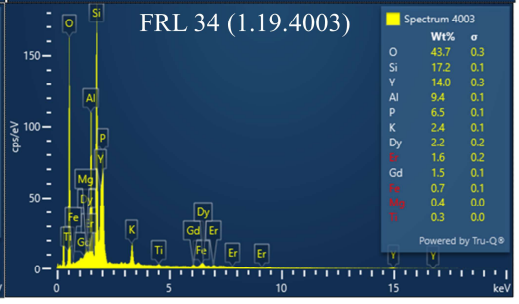

FRL 29 (2.8.3101)
Spectrum 3101
Wt% σ
O 45.2 0.1
Si 20.0 0.1
Ce 13.9 0.1
Al 13.1 0.1
P 3.2 0.0
K 2.3 0.0
Fe 0.9 0.0
Ti 0.8 0.0
Mg 0.6 0.0
Powered by Tru-Q®
cps/eV
keV

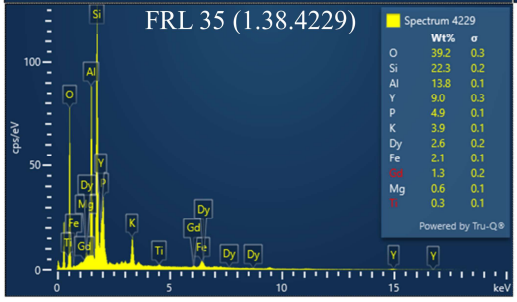

FRL 30 (2.46.3761)
Spectrum 3761
Wt% σ
O 42.9 0.2
Si 30.4 0.1
Ce 12.0 0.1
Al 8.1 0.1
P 3.3 0.1
K 2.2 0.0
Fe 0.9 0.1
Ti 0.2 0.0
Powered by Tru-Q®
cps/eV
keV

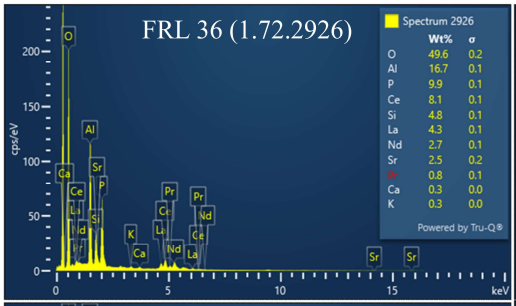

FRL 31 (1.8.3912)
Spectrum 3912
Wt% σ
O 50.0 0.2
Si 17.8 0.1
Al 14.3 0.1
Ce 9.3 0.1
K 3.7 0.1
P 2.8 0.1
Fe 0.9 0.1
Mg 0.5 0.0
Na 0.4 0.1
Ti 0.3 0.0
Powered by Tru-Q®
cps/eV
keV

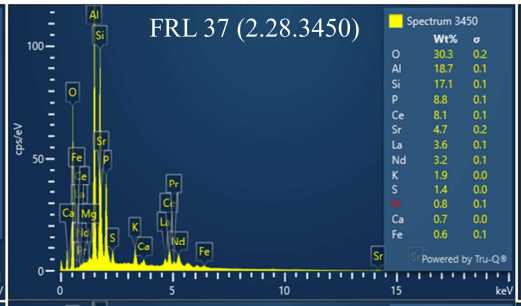

FRL 32 (1.3.869)
Spectrum 869
Wt% σ
O 37.2 0.2
Y 28.2 0.2
P 12.5 0.1
Si 5.7 0.1
Dy 4.7 0.2
Al 3.6 0.1
Gd 3.2 0.1
Er 2.4 0.2
Yb 1.5 0.2
K 0.9 0.0
Ti 0.2 0.0
Powered by Tru-Q®
cps/eV
keV

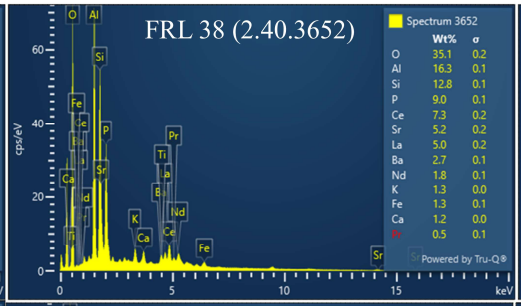

FRL 33 (2.23.3368)
Spectrum 3368
Wt% σ
O 42.6 0.2
Y 22.6 0.2
P 9.9 0.1
Si 7.2 0.1
Al 5.2 0.1
Ti 3.5 0.0
Dy 3.0 0.1
Er 2.2 0.1
Yb 1.7 0.2
Gd 1.6 0.1
K 0.5 0.0
Powered by Tru-Q®
cps/eV
keV

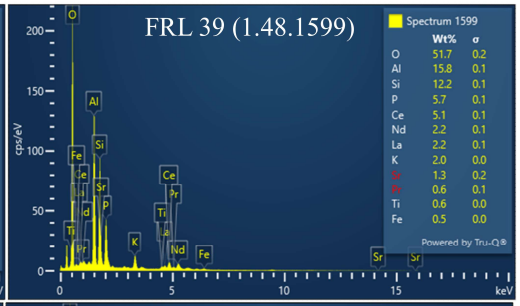

FRL 34 (1.19.4003)
Spectrum 4003
Wt% σ
O 43.7 0.3
Si 17.2 0.1
Y 14.0 0.3
Al 9.4 0.1
P 6.5 0.1
K 2.4 0.1
Dy 2.2 0.2
Er 1.6 0.2
Gd 1.5 0.1
Fe 0.7 0.1
Mg 0.4 0.0
Ti 0.3 0.0
Powered by Tru-Q®
cps/eV
keV

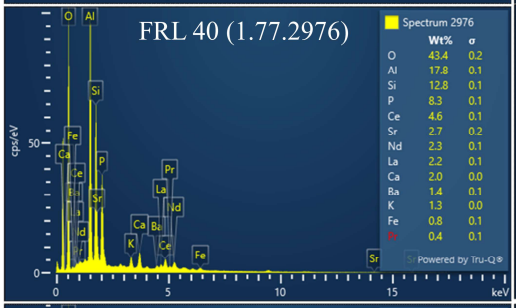

FRL 35 (1.38.4229)
Spectrum 4229
Wt% σ
O 39.2 0.3
Si 22.3 0.2
Al 13.8 0.1
Y 9.0 0.3
P 4.9 0.1
K 3.9 0.1
Dy 2.6 0.2
Fe 2.1 0.1
Gd 1.3 0.2
Mg 0.6 0.1
Ti 0.3 0.1
Powered by Tru-Q®
cps/eV
keV

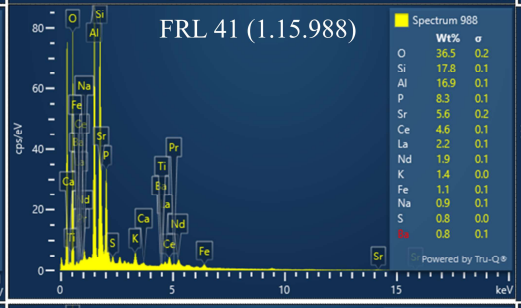

FRL 36 (1.72.2926)
Spectrum 2926
Wt% σ
O 49.6 0.2
Al 16.7 0.1
P 9.9 0.1
Ce 8.1 0.1
Si 4.8 0.1
La 4.3 0.1
Nd 2.7 0.1
Sr 2.5 0.2
Pr 0.8 0.1
Ca 0.3 0.0
K 0.3 0.0
Powered by Tru-Q®
cps/eV
keV

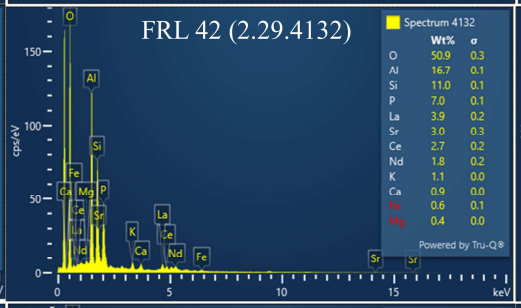

FRL 37 (2.28.3450)
Spectrum 3450
Wt% σ
O 30.3 0.2
Al 18.7 0.1
Si 17.1 0.1
P 8.8 0.1
Ce 8.1 0.1
Sr 4.7 0.2
La 3.6 0.1
Nd 3.2 0.1
K 1.9 0.0
S 1.4 0.0
Pr 0.8 0.1
Ca 0.7 0.0
Fe 0.6 0.1
Powered by Tru-Q®
cps/eV
keV

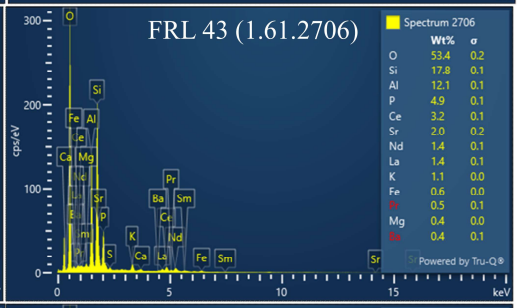

FRL 38 (2.40.3652)
Spectrum 3652
Wt% σ
O 35.1 0.2
Al 16.3 0.1
Si 12.8 0.1
P 9.0 0.1
Ce 7.3 0.2
Sr 5.2 0.2
La 5.0 0.2
Ba 2.7 0.1
Nd 1.8 0.1
K 1.3 0.0
Fe 1.3 0.1
Ca 1.2 0.0
Pr 0.5 0.1
Powered by Tru-Q®
cps/eV
keV

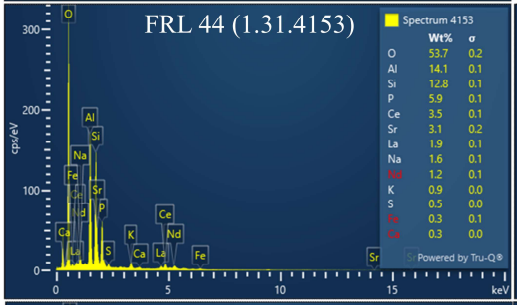

FRL 39 (1.48.1599)
Spectrum 1599
Wt% σ
O 51.7 0.2
Al 15.8 0.1
Si 12.2 0.1
P 5.7 0.1
Ce 5.1 0.1
Nd 2.2 0.1
La 2.2 0.1
K 2.0 0.0
Sr 1.3 0.2
Pr 0.6 0.1
Ti 0.6 0.0
Fe 0.5 0.0
Powered by Tru-Q®
cps/eV
keV

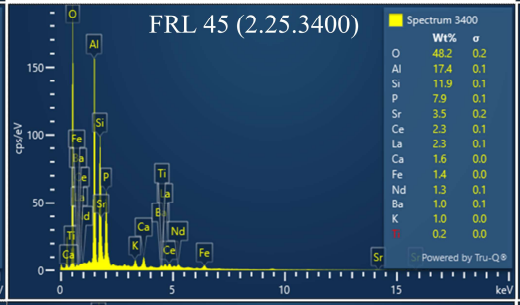

FRL 40 (1.77.2976)
Spectrum 2976
Wt% σ
O 43.4 0.2
Al 17.8 0.1
Si 12.8 0.1
P 8.3 0.1
Ce 4.6 0.1
Sr 2.7 0.2
Nd 2.3 0.1
La 2.2 0.1
Ca 2.0 0.0
Ba 1.4 0.1
K 1.3 0.0
Fe 0.8 0.1
Pr 0.4 0.1
Powered by Tru-Q®
cps/eV
keV

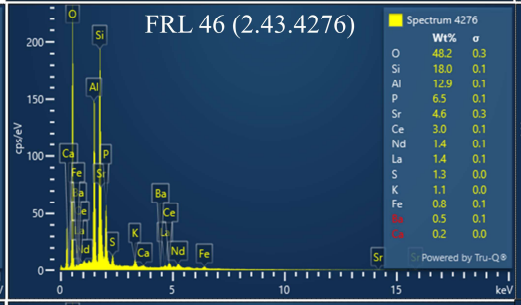

FRL 41 (1.15.988)
Spectrum 988
Wt% σ
O 36.5 0.2
Si 17.8 0.1
Al 16.9 0.1
P 8.3 0.1
Sr 5.6 0.2
Ce 4.6 0.1
La 2.2 0.1
Nd 1.9 0.1
K 1.4 0.0
Fe 1.1 0.1
Na 0.9 0.1
S 0.8 0.0
Ba 0.8 0.1
Powered by Tru-Q®
cps/eV
keV

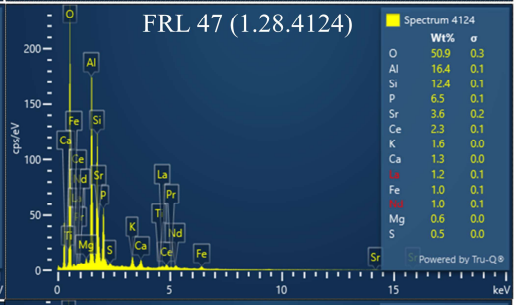

FRL 42 (2.29.4132)
Spectrum 4132
Wt% σ
O 50.9 0.3
Al 16.7 0.1
Si 11.0 0.1
P 7.0 0.1
La 3.9 0.2
Sr 3.0 0.3
Ce 2.7 0.2
Nd 1.8 0.2
K 1.1 0.0
Ca 0.9 0.0
Pr 0.6 0.1
Mg 0.4 0.0
Powered by Tru-Q®
cps/eV
keV

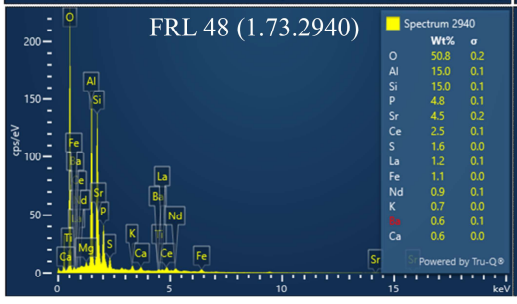

FRL 43 (1.61.2706)
Spectrum 2706
Wt% σ
O 53.4 0.2
Si 17.8 0.1
Al 12.1 0.1
P 4.9 0.1
Ce 3.2 0.1
Sr 2.0 0.2
Nd 1.4 0.1
La 1.4 0.1
K 1.1 0.0
Fe 0.6 0.0
Pr 0.5 0.1
Mg 0.4 0.0
Ba 0.4 0.1
Powered by Tru-Q®
cps/eV
keV

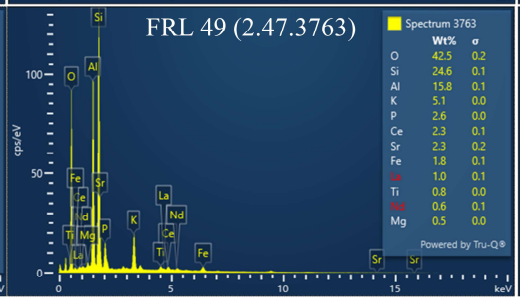

FRL 44 (1.31.4153)
Spectrum 4153
Wt% σ
O 53.7 0.2
Al 14.1 0.1
Si 12.8 0.1
P 5.9 0.1
Ce 3.5 0.1
Sr 3.1 0.2
La 1.9 0.1
Na 1.6 0.1
Nd 1.2 0.1
K 0.9 0.0
S 0.5 0.0
Pr 0.3 0.1
Ca 0.3 0.0
Powered by Tru-Q®
cps/eV
keV

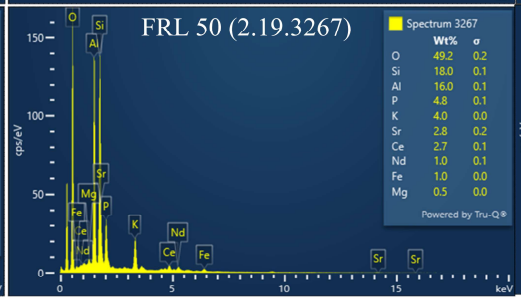

FRL 45 (2.25.3400)
Spectrum 3400
Wt% σ
O 48.2 0.2
Al 17.4 0.1
Si 11.9 0.1
P 7.9 0.1
Sr 3.5 0.2
Ce 2.3 0.1
La 2.3 0.1
Ca 1.6 0.0
Fe 1.4 0.0
Nd 1.3 0.1
Ba 1.0 0.1
K 1.0 0.0
Ti 0.2 0.0
Powered by Tru-Q®
cps/eV
keV

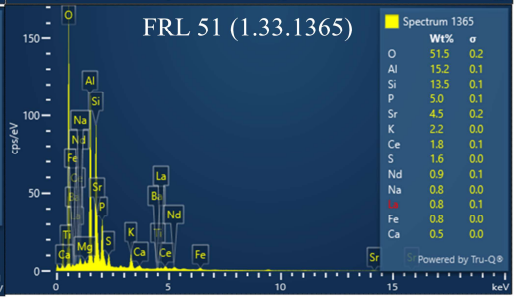

FRL 46 (2.43.4276)
Spectrum 4276
Wt% σ
O 48.2 0.3
Si 18.0 0.1
Al 12.9 0.1
P 6.5 0.1
Sr 4.6 0.3
Ce 3.0 0.1
Nd 1.4 0.1
La 1.4 0.1
S 1.3 0.0
K 1.1 0.0
Fe 0.8 0.1
Ba 0.5 0.1
Ca 0.2 0.0
Powered by Tru-Q®
cps/eV
keV

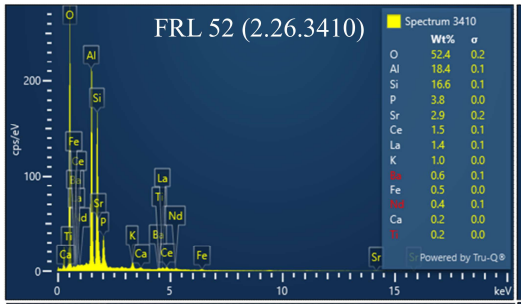

FRL 47 (1.28.4124)
Spectrum 4124
Wt% σ
O 50.9 0.3
Al 16.4 0.1
Si 12.4 0.1
P 6.5 0.1
Sr 3.6 0.2
Ce 2.3 0.1
K 1.6 0.0
Ca 1.3 0.0
La 1.2 0.1
Fe 1.0 0.1
Nd 1.0 0.1
Mg 0.6 0.0
S 0.5 0.0
Powered by Tru-Q®
cps/eV
keV

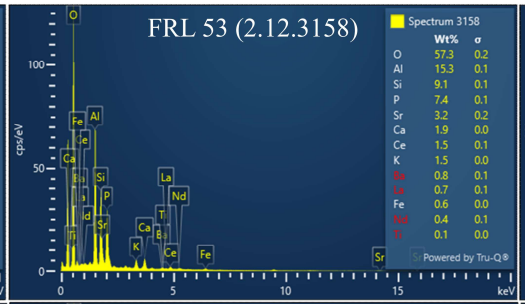

FRL 48 (1.73.2940)
Spectrum 2940
Wt% σ
O 50.8 0.2
Al 15.0 0.1
Si 15.0 0.1
P 4.8 0.1
Sr 4.5 0.2
Ce 2.5 0.1
S 1.6 0.0
La 1.2 0.1
Fe 1.1 0.0
Nd 0.9 0.1
K 0.7 0.0
Ba 0.6 0.1
Ca 0.6 0.0
Powered by Tru-Q®
cps/eV
keV

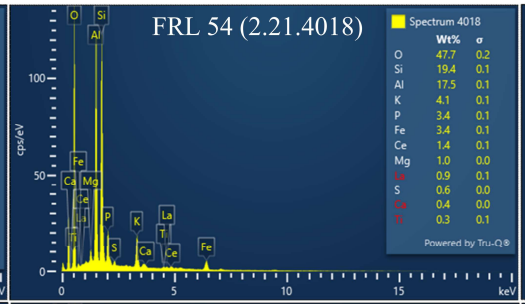

FRL 49 (2.47.3763)
Spectrum 3763
Wt% σ
O 42.5 0.2
Si 24.6 0.1
Al 15.8 0.1
K 5.1 0.0
P 2.6 0.0
Ce 2.3 0.1
Sr 2.3 0.2
Fe 1.8 0.1
La 1.0 0.1
Ti 0.8 0.0
Nd 0.6 0.1
Mg 0.5 0.0
Powered by Tru-Q®
cps/eV
keV

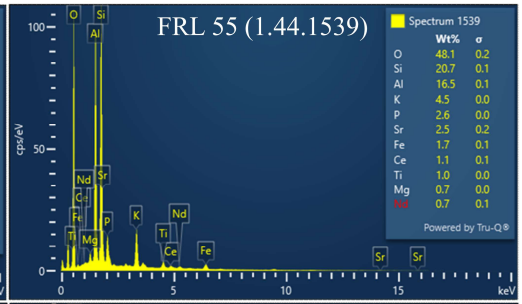

FRL 50 (2.19.3267)
Spectrum 3267
Wt% σ
O 49.2 0.2
Si 18.0 0.1
Al 16.0 0.1
P 4.8 0.1
K 4.0 0.0
Sr 2.8 0.2
Ce 2.7 0.1
Nd 1.0 0.1
Fe 1.0 0.0
Mg 0.5 0.0
Powered by Tru-Q®
cps/eV
keV

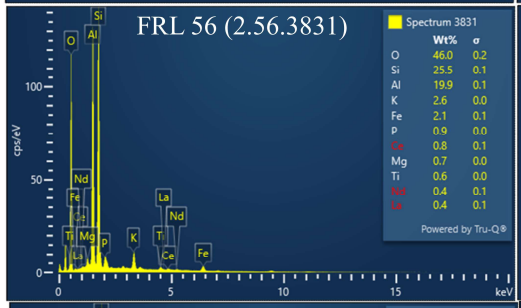

FRL 51 (1.33.1365)
Spectrum 1365
Wt% σ
O 51.5 0.2
Al 15.2 0.1
Si 13.5 0.1
P 5.0 0.1
Sr 4.5 0.2
K 2.2 0.0
Ce 1.8 0.1
S 1.6 0.0
Nd 0.9 0.1
Na 0.8 0.0
La 0.8 0.1
Fe 0.8 0.0
Ca 0.5 0.0
Powered by Tru-Q®
cps/eV
keV

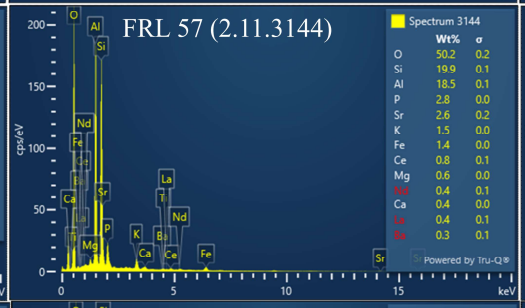

FRL 52 (2.26.3410)
Spectrum 3410
Wt% σ
O 52.4 0.2
Al 18.4 0.1
Si 16.6 0.1
P 3.8 0.0
Sr 2.9 0.2
Ce 1.5 0.1
La 1.4 0.1
K 1.0 0.0
Ba 0.6 0.1
Fe 0.5 0.0
Nd 0.4 0.1
Ca 0.2 0.0
Ti 0.2 0.0
Powered by Tru-Q®
cps/eV
keV

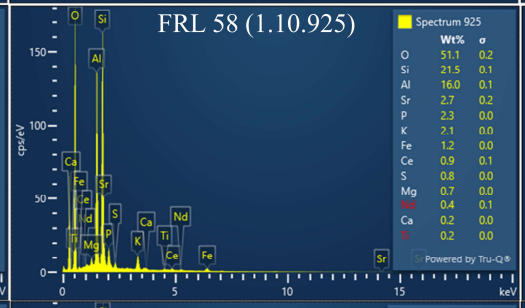

FRL 53 (2.12.3158)
Spectrum 3158
Wt% σ
O 57.3 0.2
Al 15.3 0.1
Si 9.1 0.1
P 7.4 0.1
Sr 3.2 0.2
Ca 1.9 0.0
Ce 1.5 0.1
K 1.5 0.0
Ba 0.8 0.1
La 0.7 0.1
Fe 0.6 0.0
Nd 0.4 0.1
Ti 0.1 0.0
Powered by Tru-Q®
cps/eV
keV

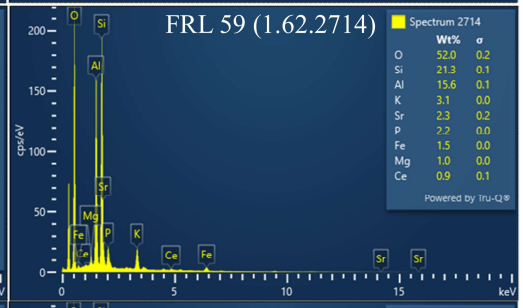

FRL 54 (2.21.4018)
Spectrum 4018
Wt% σ
O 47.7 0.2
Si 19.4 0.1
Al 17.5 0.1
K 4.1 0.1
P 3.4 0.1
Fe 3.4 0.1
Ce 1.4 0.1
Mg 1.0 0.0
La 0.9 0.1
S 0.6 0.0
Ca 0.4 0.0
Ti 0.3 0.1
Powered by Tru-Q®
cps/eV
keV

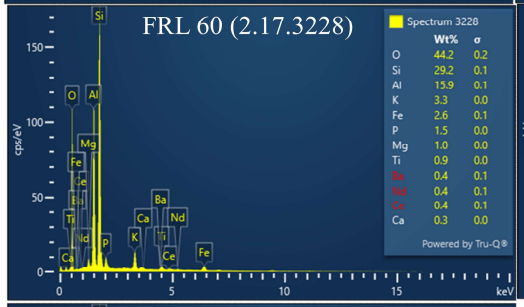

FRL 55 (1.44.1539)
Spectrum 1539
Wt% σ
O 48.1 0.2
Si 20.7 0.1
Al 16.5 0.1
K 4.5 0.0
P 2.6 0.0
Sr 2.5 0.2
Fe 1.7 0.1
Ce 1.1 0.1
Ti 1.0 0.0
Mg 0.7 0.0
Nd 0.7 0.1
Powered by Tru-Q®
cps/eV
keV

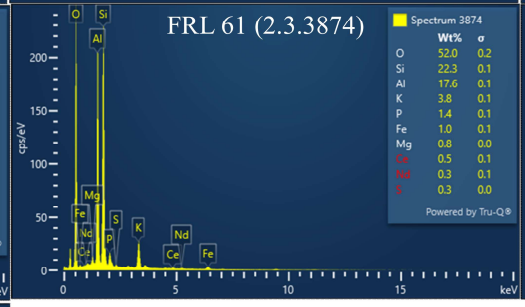

FRL 56 (2.56.3831)
Spectrum 3831
Wt% σ
O 46.0 0.2
Si 25.5 0.1
Al 19.9 0.1
K 2.6 0.0
Fe 2.1 0.1
P 0.9 0.0
Ce 0.8 0.1
Mg 0.7 0.0
Ti 0.6 0.0
Nd 0.4 0.1
La 0.4 0.1
Powered by Tru-Q®
cps/eV
keV

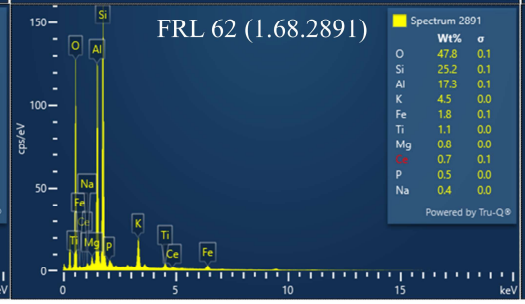

FRL 57 (2.11.3144)
Spectrum 3144
Wt% σ
O 50.2 0.2
Si 19.9 0.1
Al 18.5 0.1
P 2.8 0.0
Sr 2.6 0.2
K 1.5 0.0
Fe 1.4 0.0
Ce 0.8 0.1
Mg 0.6 0.0
Nd 0.4 0.1
Ca 0.4 0.0
La 0.4 0.1
Ba 0.3 0.1
Powered by Tru-Q®
cps/eV
keV

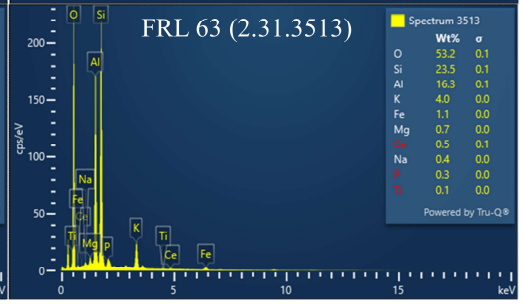

FRL 58 (1.10.925)
Spectrum 925
Wt% σ
O 51.1 0.2
Si 21.5 0.1
Al 16.0 0.1
Sr 2.7 0.2
P 2.3 0.0
K 2.1 0.0
Fe 1.2 0.0
Ce 0.9 0.1
S 0.8 0.0
Mg 0.7 0.0
Nd 0.4 0.1
Ca 0.2 0.0
Ti 0.2 0.0
Powered by Tru-Q®
cps/eV
keV


FRL 59 (1.62.2714)
Spectrum 2714
Wt% σ
O 52.0 0.2
Si 21.3 0.1
Al 15.6 0.1
K 3.1 0.0
Sr 2.3 0.2
P 2.2 0.0
Fe 1.5 0.0
Mg 1.0 0.0
Ce 0.9 0.1
Powered by Tru-Q®
cps/eV
keV


FRL 60 (2.17.3228)
Spectrum 3228
Wt% σ
O 44.2 0.2
Si 29.2 0.1
Al 15.9 0.1
K 3.3 0.0
Fe 2.6 0.1
P 1.5 0.0
Mg 1.0 0.0
Ti 0.9 0.0
Ba 0.4 0.1
Nd 0.4 0.1
Ce 0.4 0.1
Ca 0.3 0.0
Powered by Tru-Q®
cps/eV
keV


FRL 61 (2.3.3874)
Spectrum 3874
Wt% σ
O 52.0 0.2
Si 22.3 0.1
Al 17.6 0.1
K 3.8 0.1
P 1.4 0.1
Fe 1.0 0.1
Mg 0.8 0.0
Ce 0.5 0.1
Nd 0.3 0.1
S 0.3 0.0
Powered by Tru-Q®
cps/eV
keV


FRL 62 (1.68.2891)
Spectrum 2891
Wt% σ
O 47.8 0.1
Si 25.2 0.1
Al 17.3 0.1
K 4.5 0.0
Fe 1.8 0.1
Ti 1.1 0.0
Mg 0.8 0.0
Ce 0.7 0.1
P 0.5 0.0
Na 0.4 0.0
Powered by Tru-Q®
cps/eV
keV


FRL 63 (2.31.3513)
Spectrum 3513
Wt% σ
O 53.2 0.1
Si 23.5 0.1
Al 16.3 0.1
K 4.0 0.0
Fe 1.1 0.0
Mg 0.7 0.0
Ce 0.5 0.1
Na 0.4 0.0
P 0.3 0.0
Ti 0.1 0.0
Powered by Tru-Q®
cps/eV
keV

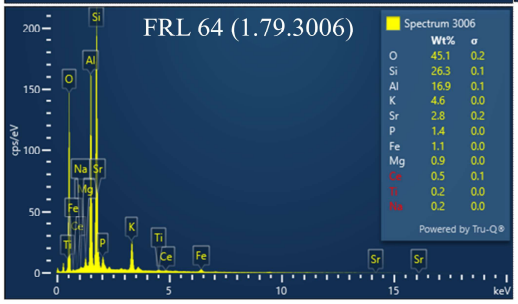
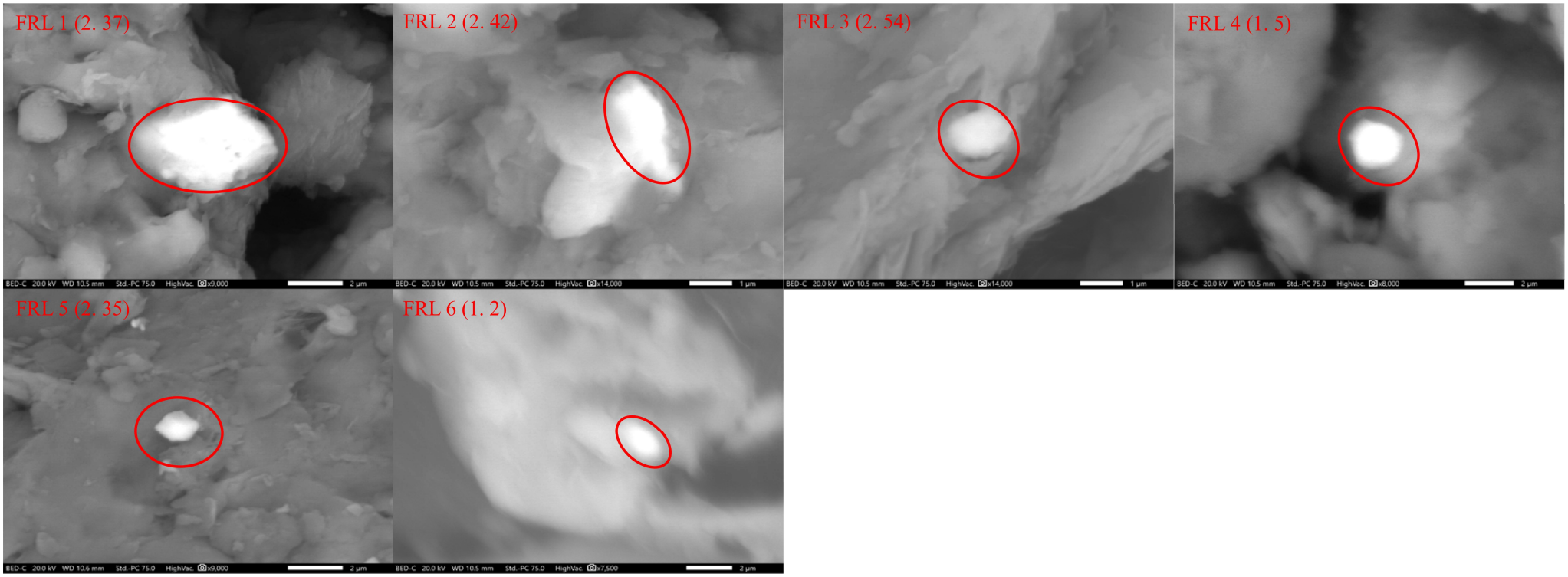
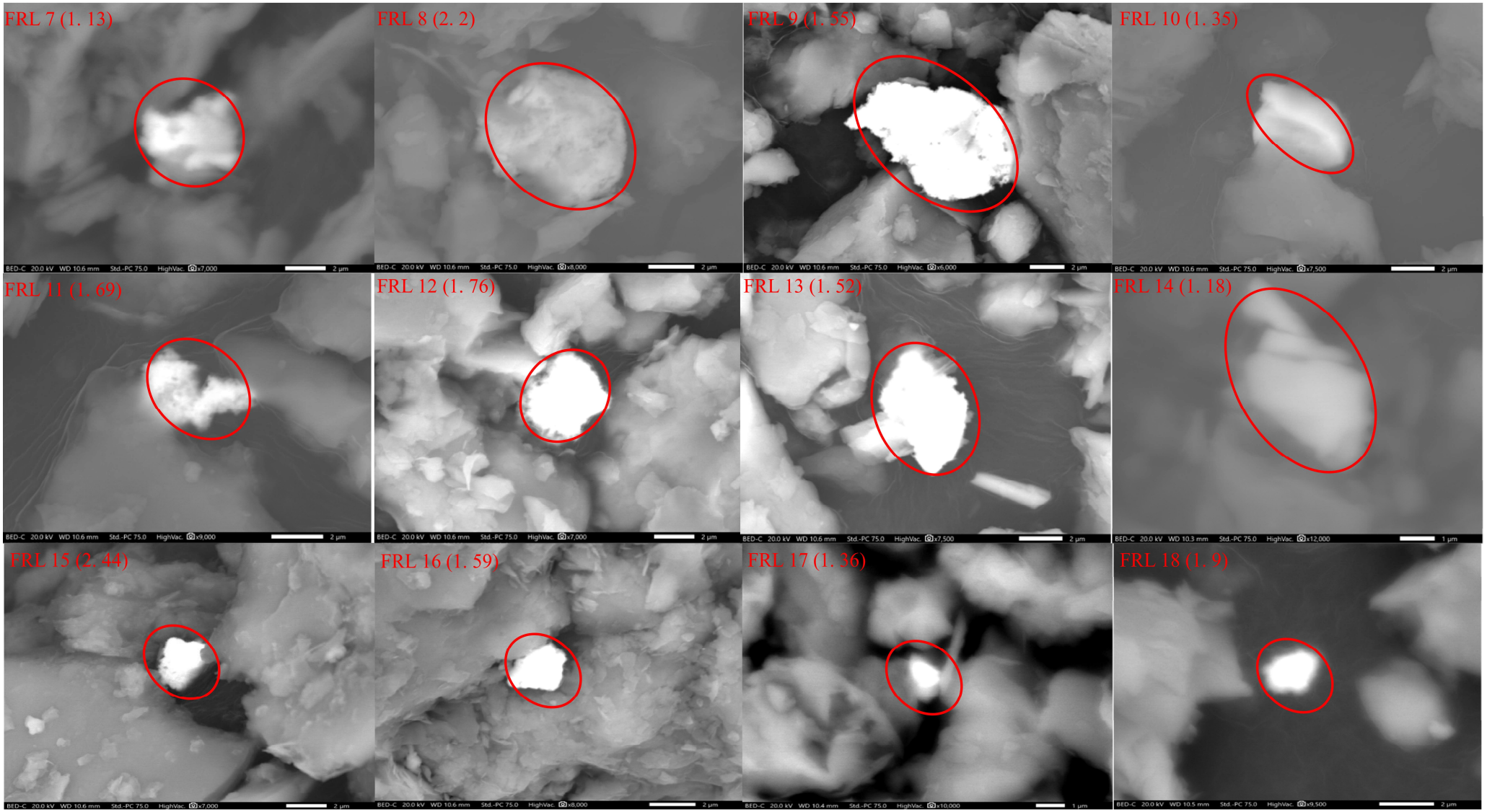
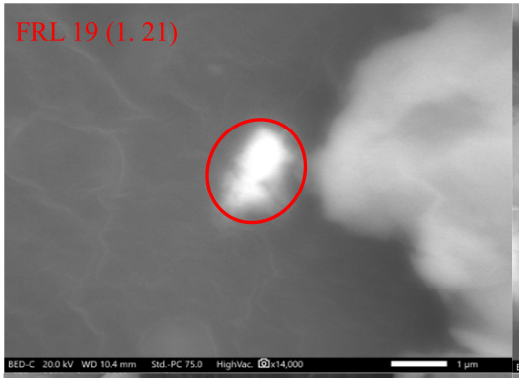
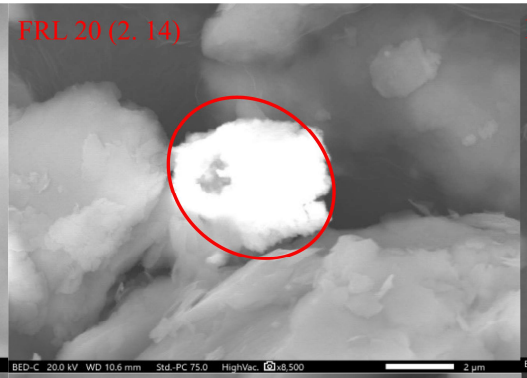

FRL 64 (1.79.3006)
Spectrum 3006
Wt% σ
O 45.1 0.2
Si 26.3 0.1
Al 16.9 0.1
K 4.6 0.0
Sr 2.8 0.2
P 1.4 0.0
Fe 1.1 0.0
Mg 0.9 0.0
Ce 0.5 0.1
Ti 0.2 0.0
Na 0.2 0.0
Powered by Tru-Q®
cps/eV
keV

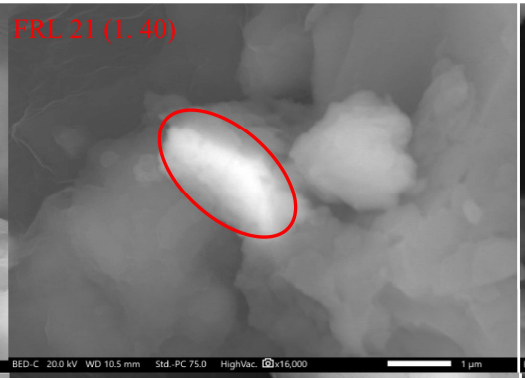
Figure B.6 SEM images of the particles containing REEs found from the the raw Fire Clay (FC) coal waste leaching residue. (The images are labelled as FRL # (Specimen #. Site #))




FRL 7 (1. 13)
FRL 8 (2. 2)
FRL 9 (1. 55)
FRL 10 (1. 35)
FRL 11 (1. 69)
FRL 12 (1. 76)
FRL 13 (1. 52)
FRL 14 (1. 18)
FRL 15 (2. 44)
FRL 16 (1. 59)
FRL 17 (1. 36)
FRL 18 (1. 9)


FRL 19 (1. 21)
BED-C 20.0 kV WD 10.4 mm Std.-PC 75.0 HighVac. x14,000 1 µm


FRL 20 (2. 14)
BED-C 20.0 kV WD 10.6 mm Std.-PC 75.0 HighVac. x8,500 2 µm


FRL 21 (1. 40)
BED-C 20.0 kV WD 10.5 mm Std.-PC 75.0 HighVac. x16,000 1 µm

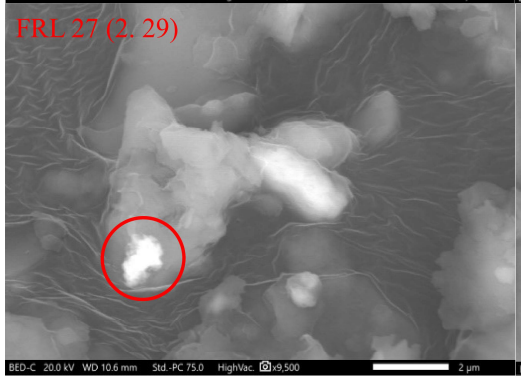

FRL 22 (2. 38)
BED-C 20.0 kV WD 10.5 mm Std.-PC 75.0 HighVac. x11,000 1 µm


FRL 23 (2. 33)
BED-C 20.0 kV WD 10.6 mm Std.-PC 75.0 HighVac. x10,000 1 µm


FRL 24 (2. 51)
BED-C 20.0 kV WD 10.5 mm Std.-PC 75.0 HighVac. x13,000 1 µm

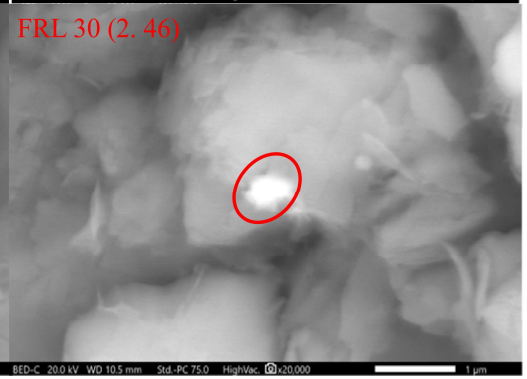

FRL 25 (2. 5)
BED-C 20.0 kV WD 10.6 mm Std.-PC 75.0 HighVac. x16,000 1 µm

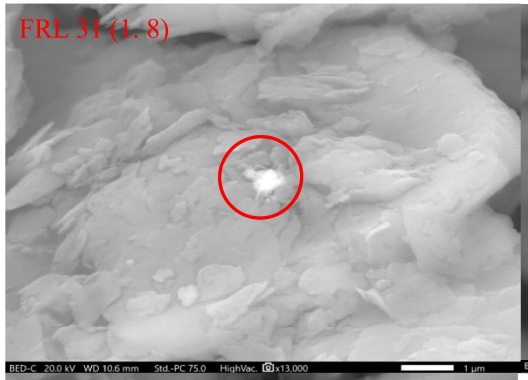

FRL 26 (2. 4)
BED-C 20.0 kV WD 10.6 mm Std.-PC 75.0 HighVac. x3,300 5 µm


FRL 27 (2. 29)
BED-C 20.0 kV WD 10.6 mm Std.-PC 75.0 HighVac. x9,500 2 µm


FRL 28 (1. 6)
BED-C 20.0 kV WD 10.5 mm Std.-PC 75.0 HighVac. x7,500 2 µm

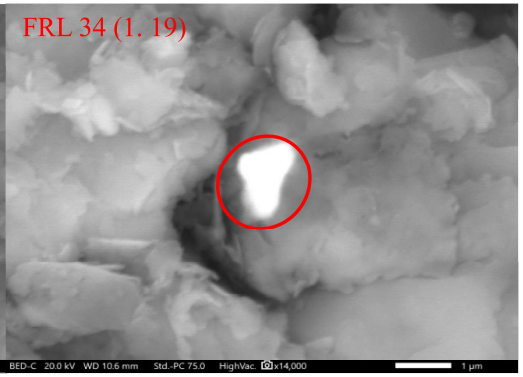

FRL 29 (2. 8)
BED-C 20.0 kV WD 10.6 mm Std.-PC 75.0 HighVac. x23,000 1 µm


FRL 30 (2. 46)
BED-C 20.0 kV WD 10.5 mm Std.-PC 75.0 HighVac. x20,000 1 µm

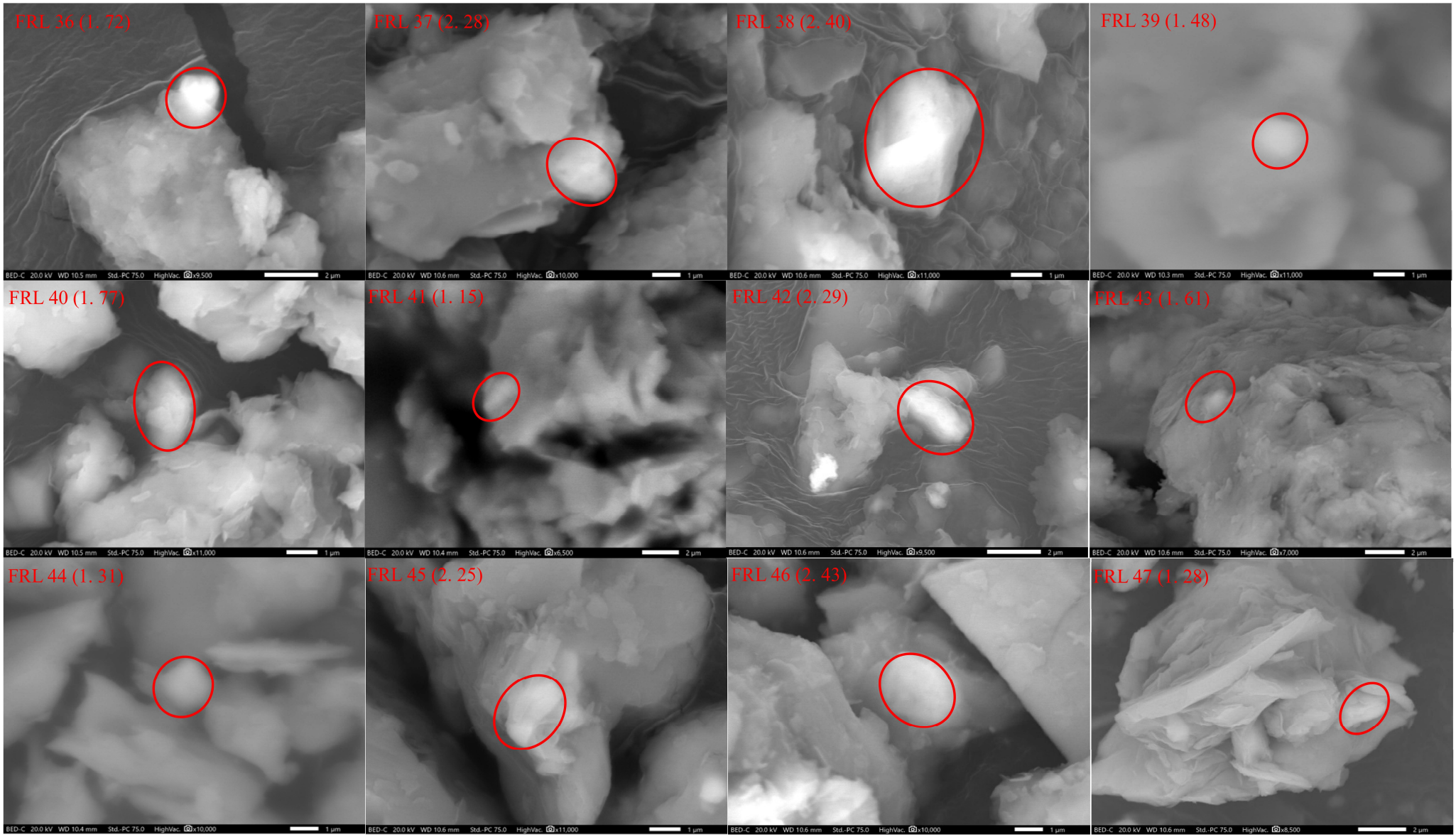

FRL 31 (1. 8)
BED-C 20.0 kV WD 10.6 mm Std.-PC 75.0 HighVac. x13,000 1 µm

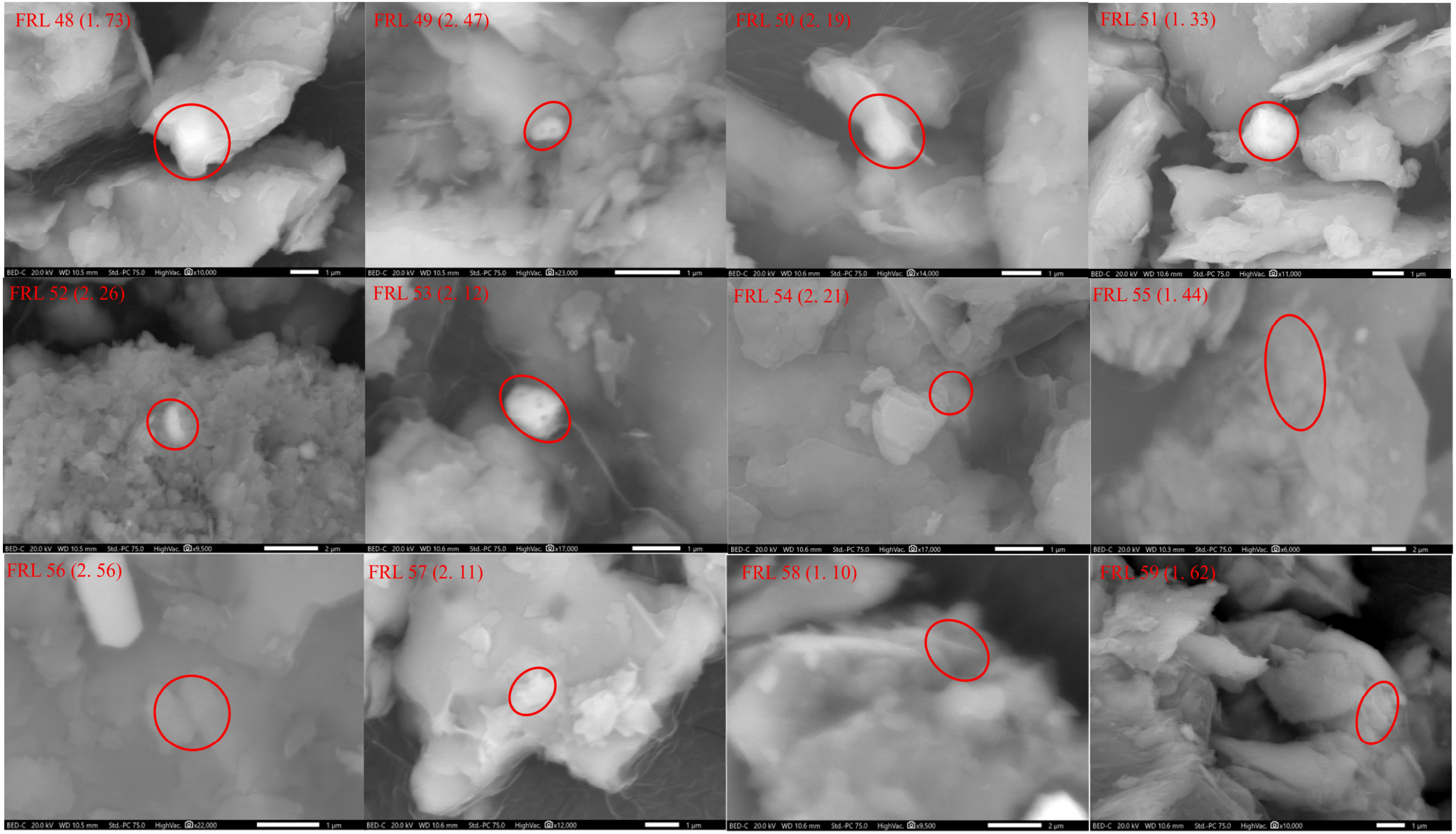

FRL 32 (1. 3)
BED-C 20.0 kV WD 10.5 mm Std.-PC 75.0 HighVac. x8,000 2 µm

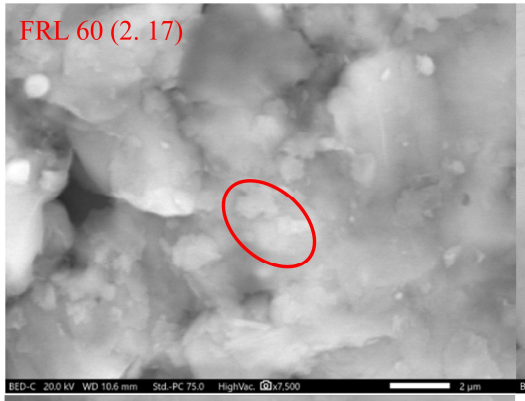

FRL 33 (2. 23)
BED-C 20.0 kV WD 10.6 mm Std.-PC 75.0 HighVac. x9,000 2 µm

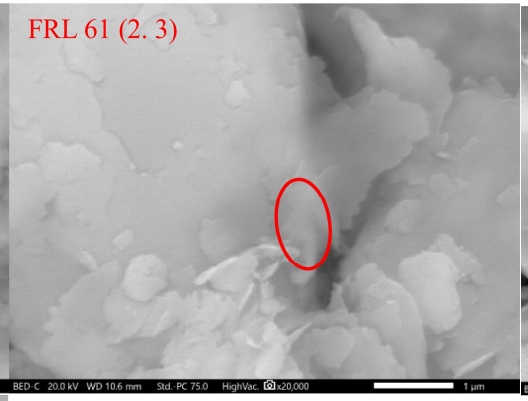

FRL 34 (1. 19)
BED-C 20.0 kV WD 10.6 mm Std.-PC 75.0 HighVac. x14,000 1 µm

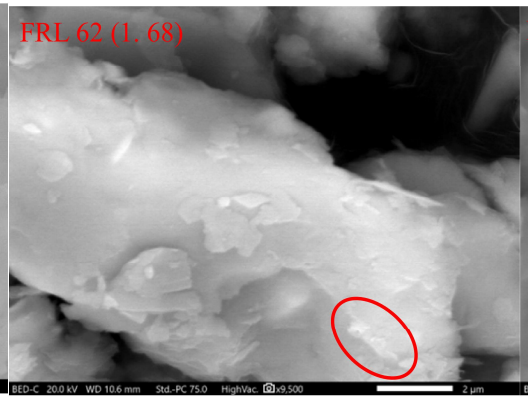

FRL 35 (1. 38)
BED-C 20.0 kV WD 10.5 mm Std.-PC 75.0 HighVac. x9,000 2 µm

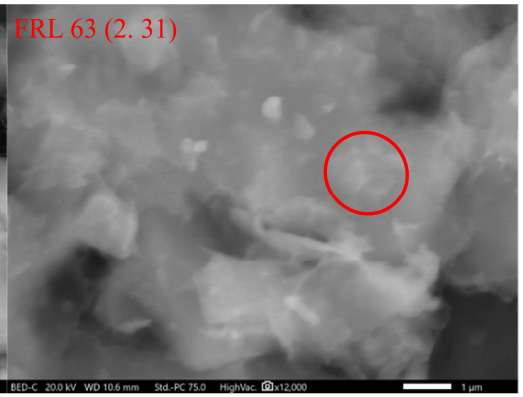

FRL 36 (1. 72)
FRL 37 (2. 28)
FRL 38 (2. 40)
FRL 39 (1. 48)
FRL 40 (1. 77)
FRL 41 (1. 15)
FRL 42 (2. 29)
FRL 43 (1. 61)
FRL 44 (1. 31)
FRL 45 (2. 25)
FRL 46 (2. 43)
FRL 47 (1. 28)


FRL 48 (1. 73)
FRL 49 (2. 47)
FRL 50 (2. 19)
FRL 51 (1. 33)
FRL 52 (2. 26)
FRL 53 (2. 12)
FRL 54 (2. 21)
FRL 55 (1. 44)
FRL 56 (2. 56)
FRL 57 (2. 11)
FRL 58 (1. 10)
FRL 59 (1. 62)


FRL 60 (2. 17)
BED-C 20.0 kV WD 10.6 mm Std.-PC 75.0 HighVac. x7,500 2 µm


FRL 61 (2. 3)
BED-C 20.0 kV WD 10.6 mm Std.-PC 75.0 HighVac. x20,000 1 µm


FRL 62 (1. 68)
BED-C 20.0 kV WD 10.6 mm Std.-PC 75.0 HighVac. x9,500 2 µm


FRL 63 (2. 31)
BED-C 20.0 kV WD 10.6 mm Std.-PC 75.0 HighVac. x12,000 1 µm

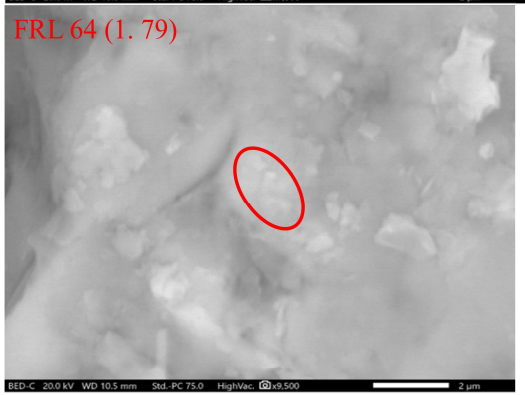
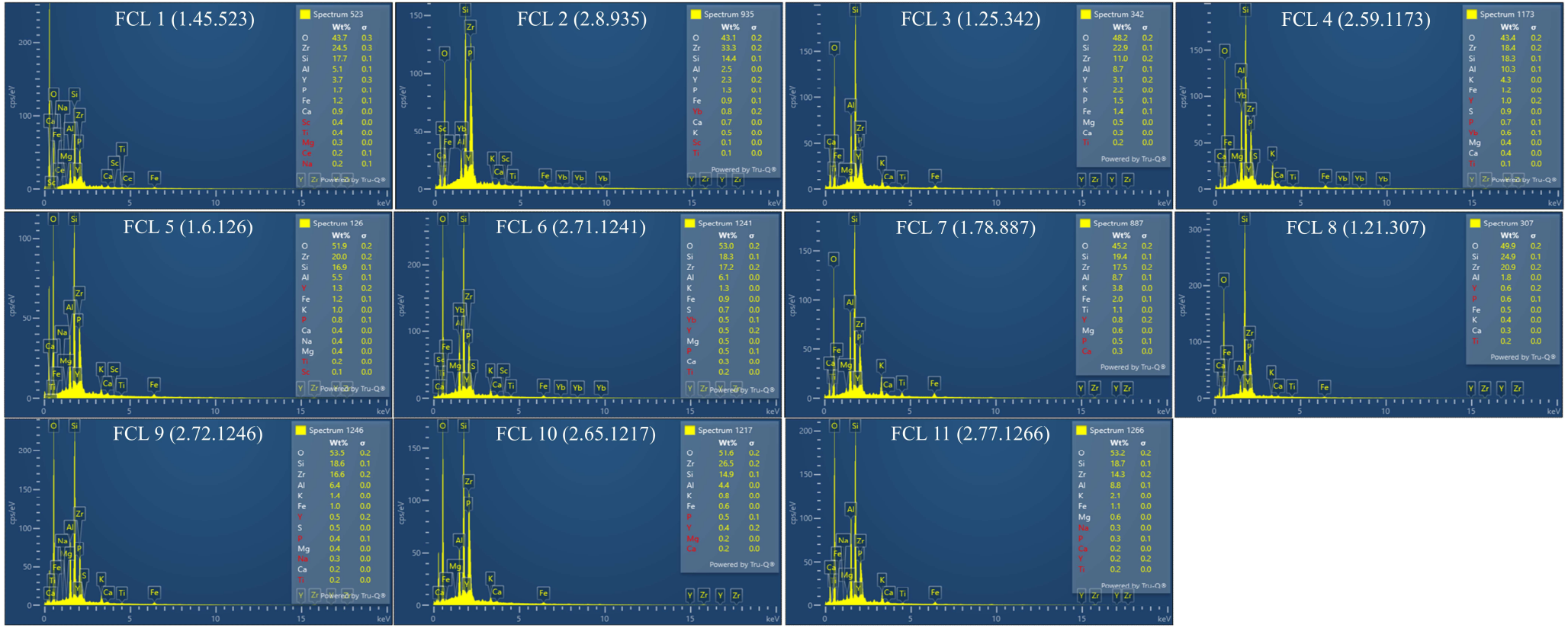
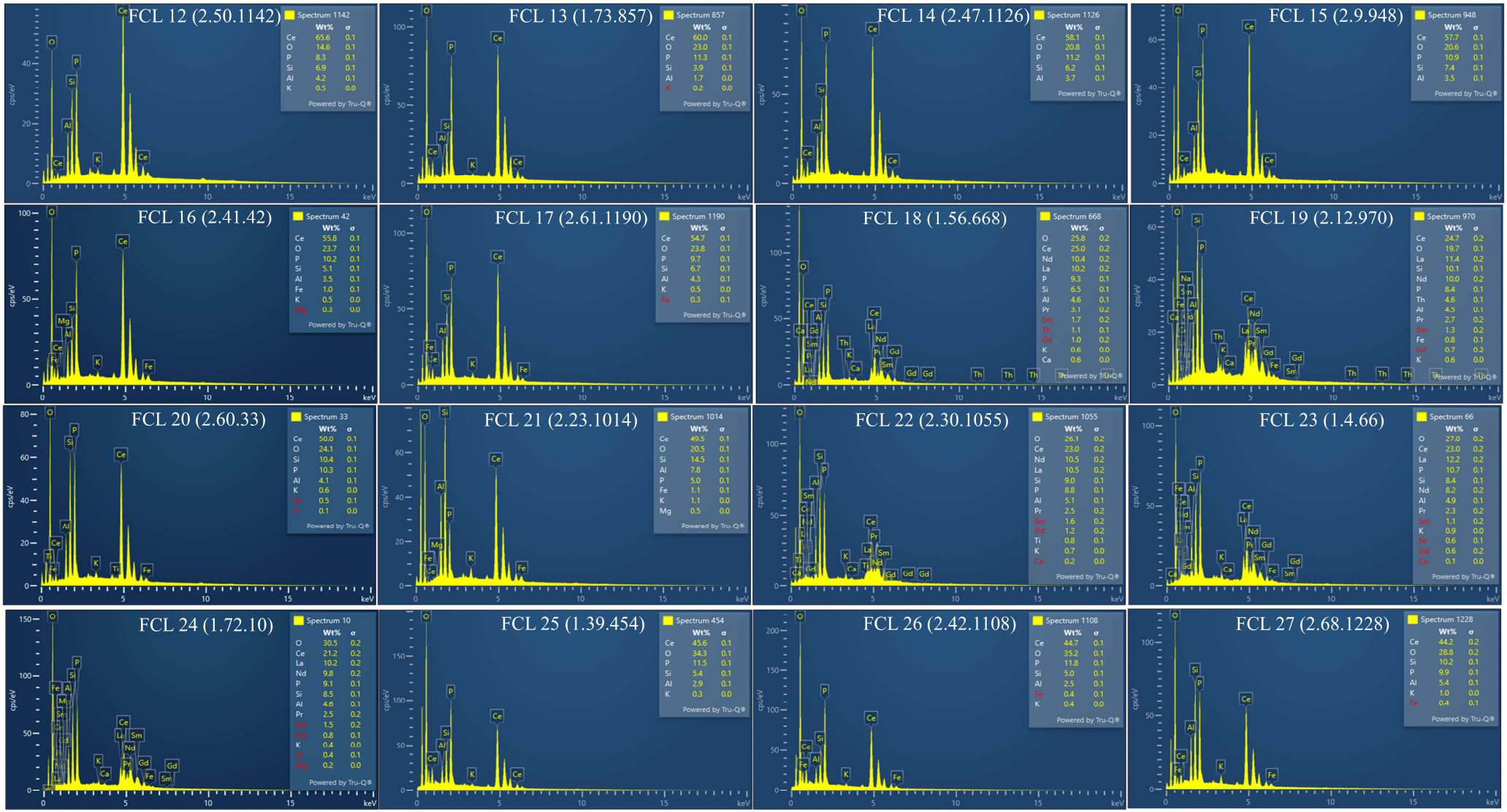

FRL 64 (1. 79)
BED-C 20.0 kV WD 10.5 mm Std.-PC 75.0 HighVac. x9,500 2 µm

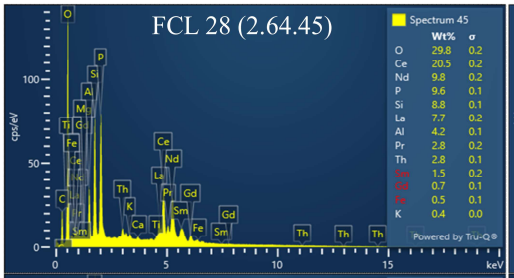
Table B.4 Elemental compositions of the particles containing REEs found from the calcined Fire Clay (FC) coal waste leaching residue through SEM-EDS analysis.

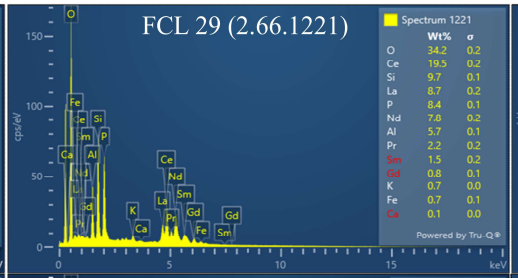
Particle #	Specimen #	Site #	Spectrum #	Mineral	Al (%)	Si (%)	O (%)	Ca (%)	P (%)	Fe (%)	K (%)	S (%)	Ba (%)	Mg (%)	Ti (%)	Na (%)	Sr (%)	F(%)	Zr (%)	Sc (%)	La (%)	Ce(%)	Pr (%)	Nd(%)	Sm (%)	Gd (%)	Dy (%)	Y(%)	Ho (%)	Er (%)	Yb (%)	Th(%)	U (%)	TREE (%	Sum (%)	Al/Si	Al/P	TREE/P
FCL 1	1	45	523	Zircon	5.1	17.7	43.7	0.9	1.7	1.2	0.0	0.0	0.0	0.3	0.4	0.2	0.0	0.0	24.5	0.4	0.0	0.2	0.0	0.0	0.0	0.0	0.0	3.7	0.0	0.0	0.0	0.0	0.0	4.3	100	0.29	3.00	2.53
FCL 2	2	8	935	Zircon	2.5	14.4	43.1	0.7	1.3	0.9	0.5	0.0	0.0	0.0	0.1	0.0	0.0	0.0	33.3	0.1	0.0	0.0	0.0	0.0	0.0	0.0	0.0	2.3	0.0	0.0	0.8	0.0	0.0	3.2	100	0.17	1.92	2.46
FCL 3	1	25	342	Zircon	8.7	22.9	48.2	0.3	1.5	1.4	2.2	0.0	0.0	0.5	0.2	0.0	0.0	0.0	11.0	0.0	0.0	0.0	0.0	0.0	0.0	0.0	0.0	3.1	0.0	0.0	0.0	0.0	0.0	3.1	100	0.38	5.80	2.07
FCL 4	2	59	1173	Zircon	10.3	18.3	43.4	0.4	0.7	1.2	4.3	0.9	0.0	0.4	0.1	0.0	0.0	0.0	18.4	0.0	0.0	0.0	0.0	0.0	0.0	0.0	0.0	1.0	0.0	0.0	0.6	0.0	0.0	1.6	100	0.56	14.71	2.29
FCL 5	1	6	126	Zircon	5.5	16.9	51.9	0.4	0.8	1.2	1.0	0.0	0.0	0.4	0.2	0.4	0.0	0.0	20.0	0.1	0.0	0.0	0.0	0.0	0.0	0.0	0.0	1.3	0.0	0.0	0.0	0.0	0.0	1.4	100	0.33	6.88	1.75
FCL 6	2	71	1241	Zircon	6.1	18.3	53.0	0.3	0.5	0.9	1.3	0.7	0.0	0.5	0.2	0.0	0.0	0.0	17.2	0.0	0.0	0.0	0.0	0.0	0.0	0.0	0.0	0.5	0.0	0.0	0.5	0.0	0.0	1.0	100	0.33	12.20	2.00
FCL 7	1	78	887	Zircon	8.7	19.4	45.2	0.3	0.5	2.0	3.8	0.0	0.0	0.6	1.1	0.0	0.0	0.0	17.5	0.0	0.0	0.0	0.0	0.0	0.0	0.0	0.0	0.8	0.0	0.0	0.0	0.0	0.0	0.8	100	0.45	17.40	1.60
FCL 8	1	21	307	Zircon	1.8	24.9	49.9	0.3	0.6	0.5	0.4	0.0	0.0	0.0	0.2	0.0	0.0	0.0	20.9	0.0	0.0	0.0	0.0	0.0	0.0	0.0	0.0	0.6	0.0	0.0	0.0	0.0	0.0	0.6	100	0.07	3.00	1.00
FCL 9	2	72	1246	Zircon	6.4	18.6	53.5	0.2	0.4	1.0	1.4	0.5	0.0	0.4	0.2	0.3	0.0	0.0	16.6	0.0	0.0	0.0	0.0	0.0	0.0	0.0	0.0	0.5	0.0	0.0	0.0	0.0	0.0	0.5	100	0.34	16.00	1.25
FCL 10	2	65	1217	Zircon	4.4	14.9	51.6	0.2	0.5	0.6	0.8	0.0	0.0	0.2	0.0	0.0	0.0	0.0	26.5	0.0	0.0	0.0	0.0	0.0	0.0	0.0	0.0	0.4	0.0	0.0	0.0	0.0	0.0	0.4	100	0.30	8.80	0.80
FCL 11	2	77	1266	Zircon	8.8	18.7	53.2	0.2	0.3	1.1	2.1	0.0	0.0	0.6	0.2	0.3	0.0	0.0	14.3	0.0	0.0	0.0	0.0	0.0	0.0	0.0	0.0	0.2	0.0	0.0	0.0	0.0	0.0	0.2	100	0.47	29.33	0.67
FCL 12	2	50	1142	Monazite	4.2	6.9	14.6	0.0	8.3	0.0	0.5	0.0	0.0	0.0	0.0	0.0	0.0	0.0	0.0	0.0	0.0	65.6	0.0	0.0	0.0	0.0	0.0	0.0	0.0	0.0	0.0	0.0	0.0	65.6	100	0.61	0.51	7.90
FCL 13	1	73	857	Monazite	1.7	3.9	23.0	0.0	11.3	0.0	0.2	0.0	0.0	0.0	0.0	0.0	0.0	0.0	0.0	0.0	0.0	60.0	0.0	0.0	0.0	0.0	0.0	0.0	0.0	0.0	0.0	0.0	0.0	60.0	100	0.44	0.15	5.31
FCL 14	2	47	1126	Monazite	3.7	6.2	20.8	0.0	11.2	0.0	0.0	0.0	0.0	0.0	0.0	0.0	0.0	0.0	0.0	0.0	0.0	58.1	0.0	0.0	0.0	0.0	0.0	0.0	0.0	0.0	0.0	0.0	0.0	58.1	100	0.60	0.33	5.19
FCL 15	2	9	948	Monazite	3.5	7.4	20.6	0.0	10.9	0.0	0.0	0.0	0.0	0.0	0.0	0.0	0.0	0.0	0.0	0.0	0.0	57.7	0.0	0.0	0.0	0.0	0.0	0.0	0.0	0.0	0.0	0.0	0.0	57.7	100	0.47	0.32	5.29
FCL 16	2	41	42	Monazite	3.5	5.1	23.7	0.0	10.2	1.0	0.5	0.0	0.0	0.3	0.0	0.0	0.0	0.0	0.0	0.0	0.0	55.8	0.0	0.0	0.0	0.0	0.0	0.0	0.0	0.0	0.0	0.0	0.0	55.8	100	0.69	0.34	5.47
FCL 17	2	61	1190	Monazite	4.3	6.7	23.8	0.0	9.7	0.3	0.5	0.0	0.0	0.0	0.0	0.0	0.0	0.0	0.0	0.0	0.0	54.7	0.0	0.0	0.0	0.0	0.0	0.0	0.0	0.0	0.0	0.0	0.0	54.7	100	0.64	0.44	5.64
FCL 18	1	56	668	Monazite	4.6	6.5	25.8	0.6	9.3	0.0	0.6	0.0	0.0	0.0	0.0	0.0	0.0	0.0	0.0	0.0	10.2	25.0	3.1	10.4	1.7	1.0	0.0	0.0	0.0	0.0	0.0	1.1	0.0	51.4	100	0.71	0.49	5.53
FCL 19	2	12	970	Monazite	4.5	10.1	19.7	0.3	8.4	0.8	0.6	0.0	0.0	0.0	0.0	0.3	0.0	0.0	0.0	0.0	11.4	24.7	2.7	10.0	1.3	0.7	0.0	0.0	0.0	0.0	0.0	4.6	0.0	50.8	100	0.45	0.54	6.05
FCL 20	2	60	33	Monazite	4.1	10.4	24.1	0.0	10.3	0.5	0.6	0.0	0.0	0.0	0.1	0.0	0.0	0.0	0.0	0.0	0.0	50.0	0.0	0.0	0.0	0.0	0.0	0.0	0.0	0.0	0.0	0.0	0.0	50.0	100	0.39	0.40	4.85
FCL 21	2	23	1014	Monazite	7.8	14.5	20.5	0.0	5.0	1.1	1.1	0.0	0.0	0.5	0.0	0.0	0.0	0.0	0.0	0.0	0.0	49.5	0.0	0.0	0.0	0.0	0.0	0.0	0.0	0.0	0.0	0.0	0.0	49.5	100	0.54	1.56	9.90
FCL 22	2	30	1055	Monazite	5.1	9.0	26.1	0.2	8.8	0.0	0.7	0.0	0.0	0.0	0.8	0.0	0.0	0.0	0.0	0.0	10.5	23.0	2.5	10.5	1.6	1.2	0.0	0.0	0.0	0.0	0.0	0.0	0.0	49.3	100	0.57	0.58	5.60
FCL 23	1	4	66	Monazite	4.9	8.4	27.0	0.1	10.7	0.6	0.9	0.0	0.0	0.0	0.0	0.0	0.0	0.0	0.0	0.0	12.2	23.0	2.3	8.2	1.1	0.6	0.0	0.0	0.0	0.0	0.0	0.0	0.0	47.4	100	0.58	0.46	4.43
FCL 24	1	72	10	Monazite	4.6	8.5	30.5	0.2	9.1	0.4	0.4	0.0	0.0	0.2	0.0	0.0	0.0	0.0	0.0	0.0	10.2	21.2	2.5	9.8	1.5	0.8	0.0	0.0	0.0	0.0	0.0	0.0	0.0	46.0	100	0.54	0.51	5.05
FCL 25	1	39	454	Monazite	2.9	5.4	34.3	0.0	11.5	0.0	0.3	0.0	0.0	0.0	0.0	0.0	0.0	0.0	0.0	0.0	0.0	45.6	0.0	0.0	0.0	0.0	0.0	0.0	0.0	0.0	0.0	0.0	0.0	45.6	100	0.54	0.25	3.97
FCL 26	2	42	1108	Monazite	2.5	5.0	35.2	0.0	11.8	0.4	0.4	0.0	0.0	0.0	0.0	0.0	0.0	0.0	0.0	0.0	0.0	44.7	0.0	0.0	0.0	0.0	0.0	0.0	0.0	0.0	0.0	0.0	0.0	44.7	100	0.50	0.21	3.79
FCL 27	2	68	1228	Monazite	5.4	10.2	28.8	0.0	9.9	0.4	1.0	0.0	0.0	0.0	0.0	0.0	0.0	0.0	0.0	0.0	0.0	44.2	0.0	0.0	0.0	0.0	0.0	0.0	0.0	0.0	0.0	0.0	0.0	44.2	100	0.53	0.55	4.46
FCL 28	2	64	45	Monazite	4.2	8.8	29.8	0.3	9.6	0.5	0.4	0.0	0.0	0.3	0.4	0.0	0.0	0.0	0.0	0.0	7.7	20.5	2.8	9.8	1.5	0.7	0.0	0.0	0.0	0.0	0.0	2.8	0.0	43.0	100	0.48	0.44	4.48
FCL 29	2	66	1221	Monazite	5.7	9.7	34.2	0.1	8.4	0.7	0.7	0.0	0.0	0.0	0.0	0.0	0.0	0.0	0.0	0.0	8.7	19.5	2.2	7.8	1.5	0.8	0.0	0.0	0.0	0.0	0.0	0.0	0.0	40.5	100	0.59	0.68	4.82
FCL 30	1	79	892	Monazite	6.0	8.1	36.6	0.5	8.8	0.4	0.9	0.0	0.0	0.4	0.0	0.0	0.0	0.0	0.0	0.0	9.3	18.0	2.0	7.2	1.1	0.7	0.0	0.0	0.0	0.0	0.0	0.0	0.0	38.3	100	0.74	0.68	4.35
FCL 31	2	40	1096	Monazite	6.8	7.4	39.6	0.1	8.4	0.7	0.0	0.0	0.0	0.0	0.0	0.0	0.0	0.0	0.0	0.0	0.0	37.1	0.0	0.0	0.0	0.0	0.0	0.0	0.0	0.0	0.0	0.0	0.0	37.1	100	0.92	0.81	4.42
FCL 32	2	74	52	Monazite	11.7	19.5	23.0	0.3	4.5	1.1	2.4	0.0	0.0	0.5	0.3	0.0	0.0	0.0	0.0	0.0	7.3	18.9	0.0	10.6	0.0	0.0	0.0	0.0	0.0	0.0	0.0	0.0	0.0	36.8	100	0.60	2.60	8.18
FCL 33	1	71	11	Monazite	4.7	9.2	39.6	0.2	8.8	0.4	0.8	0.0	0.0	0.2	0.0	0.0	0.0	0.0	0.0	0.0	8.5	16.6	1.8	6.7	1.1	0.4	0.0	0.0	0.0	0.0	0.0	0.0	0.8	35.1	100	0.51	0.53	3.99
FCL 34	2	25	1021	Monazite	6.3	12.1	37.1	0.0	8.5	0.4	0.9	0.0	0.0	0.0	0.2	0.0	0.0	0.0	0.0	0.0	0.0	34.5	0.0	0.0	0.0	0.0	0.0	0.0	0.0	0.0	0.0	0.0	0.0	34.5	100	0.52	0.74	4.06
FCL 35	2	32	1070	Monazite	4.2	13.6	39.2	0.3	7.5	0.8	0.8	0.0	0.0	0.0	0.0	0.0	0.0	0.0	0.0	0.0	7.6	15.3	1.9	7.2	1.3	0.5	0.0	0.0	0.0	0.0	0.0	0.0	0.0	33.8	100	0.31	0.56	4.51
FCL 36	1	75	875	Monazite	5.8	9.2	40.4	0.1	8.5	0.4	0.9	0.0	0.0	0.0	0.0	0.0	0.0	0.0	0.0	0.0	8.4	16.0	1.5	6.3	0.7	0.5	0.0	0.0	0.0	0.0	0.0	1.2	0.0	33.4	100	0.63	0.68	3.93
FCL 37	2	69	1233	Monazite	9.8	15.9	33.7	0.1	5.2	0.9	2.1	0.0	0.0	0.6	0.0	0.0	0.0	0.0	0.0	0.0	5.1	14.9	2.1	6.8	1.7	1.1	0.0	0.0	0.0	0.0	0.0	0.0	0.0	31.7	100	0.62	1.88	6.10
FCL 38	1	13	221	Monazite	7.1	15.9	36.0	0.0	6.8	0.6	1.2	0.0	0.0	0.5	0.2	0.0	0.0	0.0	0.0	0.0	0.0	31.7	0.0	0.0	0.0	0.0	0.0	0.0	0.0	0.0	0.0	0.0	0.0	31.7	100	0.45	1.04	4.66
FCL 39	1	67	1	Monazite	6.8	17.1	40.0	0.0	5.9	0.6	1.1	0.0	0.0	0.4	0.1	0.0	0.0	0.0	0.0	0.0	6.3	13.5	1.4	5.9	0.8	0.0	0.0	0.0	0.0	0.0	0.0	0.0	0.0	27.9	100	0.40	1.15	4.73
FCL 40	1	2	22	Monazite	9.7	19.6	33.5	0.0	4.9	0.9	1.8	0.0	0.0	0.7	0.9	0.5	0.0	0.0	0.0	0.0	0.0	27.7	0.0	0.0	0.0	0.0	0.0	0.0	0.0	0.0	0.0	0.0	0.0	27.7	100	0.49	1.98	5.65
FCL 41	1	16	251	Monazite	11.6	21.2	31.6	0.0	3.4	1.7	3.9	0.0	0.0	0.8	0.3	0.8	0.0	0.0	0.0	0.0	0.0	24.6	0.0	0.0	0.0	0.0	0.0	0.0	0.0	0.0	0.0	0.0	0.0	24.6	100	0.55	3.41	7.24
FCL 42	2	56	1162	Monazite	11.8	21.0	37.9	0.0	4.1	0.8	2.2	0.0	0.0	0.6	0.0	0.0	0.0	0.0	0.0	0.0	4.7	10.4	1.0	4.3	0.8	0.5	0.0	0.0	0.0	0.0	0.0	0.0	0.0	21.7	100	0.56	2.88	5.29
FCL 43	1	9	173	Monazite	8.6	16.0	43.5	0.0	4.1	1.3	1.7	0.0	0.0	0.5	0.1	0.0	0.0	0.0	0.0	0.0	0.0	19.2	0.0	0.0	0.0	0.0	0.0	0.0	0.0	0.0	0.0	0.0	0.0	19.2	100	0.54	2.10	4.68
FCL 44	2	26	1029	Monazite	8.9	16.8	47.3	0.1	5.0	1.0	1.5	0.0	0.0	0.6	0.0	0.0	0.0	0.0	0.0	0.0	4.2	8.7	0.9	3.7	0.8	0.5	0.0	0.0	0.0	0.0	0.0	0.0	0.0	18.8	100	0.53	1.78	3.76
FCL 45	1	59	710	Monazite	7.8	20.6	41.7	0.2	4.1	1.3	1.1	0.0	0.0	0.7	4.7	0.0	0.0	0.0	0.0	0.0	3.3	7.8	0.9	3.9	0.8	0.7	0.0	0.0	0.0	0.0	0.0	0.0	0.0	17.4	100	0.38	1.90	4.24
FCL 46	2	21	1003	Monazite	2.2	29.1	47.8	0.1	4.1	0.3	0.4	0.0	0.0	0.0	0.0	0.0	0.0	0.0	0.0	0.0	3.9	8.8	0.7	2.7	0.0	0.0	0.0	0.0	0.0	0.0	0.0	0.0	0.0	16.1	100	0.08	0.54	3.93
FCL 47	2	67	1224	Monazite	8.8	20.0	48.4	0.0	3.2	1.1	1.5	0.0	0.0	0.5	0.4	0.2	0.0	0.0	0.0	0.0	0.0	15.9	0.0	0.0	0.0	0.0	0.0	0.0	0.0	0.0	0.0	0.0	0.0	15.9	100	0.44	2.75	4.97
FCL 48	1	32	390	Monazite	7.7	31.4	43.5	0.0	2.7	1.2	2.2	0.0	0.0	0.4	0.2	0.0	0.0	0.0	0.0	0.0	0.0	10.7	0.0	0.0	0.0	0.0	0.0	0.0	0.0	0.0	0.0	0.0	0.0	10.7	100	0.25	2.85	3.96
FCL 49	2	73	1252	Monazite	5.4	34.7	45.1	0.1	2.3	0.5	0.9	0.0	0.0	0.3	0.5	0.0	0.0	0.0	0.0	0.0	2.2	4.7	0.5	2.1	0.4	0.4	0.0	0.0	0.0	0.0	0.0	0.0	0.0	10.3	100	0.16	2.35	4.48
FCL 50	1	13	218	Monazite	12.5	21.1	51.3	0.0	1.3	1.6	4.1	0.0	0.0	1.1	0.2	0.0	0.0	0.0	0.0	0.0	0.0	6.5	0.0	0.0	0.0	0.0	0.0	0.0	0.0	0.0	0.0	0.0	0.0	6.5	100	0.59	9.62	5.00
FCL 51	1	17	261	Monazite	6.5	29.1	54.6	0.0	1.6	0.8	1.3	0.0	0.0	0.4	0.0	0.0	0.0	0.0	0.0	0.0	1.2	3.2	0.0	1.4	0.0	0.0	0.0	0.0	0.0	0.0	0.0	0.0	0.0	5.8	100	0.22	4.06	3.63
FCL 52	2	48	17	Xenotime	4.8	10.3	28.8	0.2	10.5	0.5	0.8	0.0	0.0	0.0	0.2	0.0	0.0	0.0	0.0	0.0	0.0	0.0	0.0	0.0	1.1	6.2	7.5	21.2	1.7	3.8	2.5	0.0	0.0	44.0	100	0.47	0.46	4.19
FCL 53	1	61	721	Xenotime	3.3	7.8	34.3	0.2	11.6	0.5	0.7	0.0	0.0	0.0	0.1	0.0	0.0	0.0	0.0	0.0	0.0	0.1	0.0	0.0	0.0	0.9	4.4	27.0	1.2	4.1	3.6	0.0	0.0	41.3	100	0.42	0.28	3.56
FCL 54	2	1	53	Xenotime	2.5	6.5	47.5	0.1	9.1	0.1	0.3	0.0	0.0	0.0	0.0	0.0	0.0	0.0	2.2	0.0	0.0	0.0	0.0	0.0	0.0	2.2	3.6	21.5	0.8	2.1	1.4	0.0	0.0	31.6	100	0.38	0.27	3.47
FCL 55	2	44	1114	Xenotime	4.2	8.4	45.5	0.4	9.4	0.0	1.7	0.0	0.0	0.0	0.0	0.0	0.0	0.0	0.0	0.1	0.0	0.0	0.0	0.0	0.0	2.1	3.3	22.5	0.0	2.3	0.0	0.0	0.0	30.3	100	0.50	0.45	3.22
FCL 56	2	63	1200	Xenotime	5.5	10.6	43.6	0.0	8.7	0.5	1.4	0.0	0.0	0.4	0.2	0.0	0.0	0.0	0.0	0.0	0.0	0.0	0.0	0.0	0.0	0.9	2.3	22.3	0.0	2.0	1.5	0.0	0.0	29.0	100	0.52	0.63	3.33
FCL 57	2	54	1153	Xenotime	4.5	14.5	44.4	0.3	8.2	0.0	0.9	0.0	0.0	0.3	0.2	0.0	0.0	0.0	0.0	0.0	0.0	0.0	0.0	0.0	0.0	2.2	3.2	19.1	0.0	2.3	0.0	0.0	0.0	26.8	100	0.31	0.55	3.27
FCL 58	1	30	377	Xenotime	5.4	10.1	47.2	0.1	7.8	0.7	1.6	0.0	0.0	0.4	0.1	0.0	0.0	0.0	0.0	0.0	0.0	0.0	0.0	0.4	0.4	1.3	2.1	18.4	0.0	1.5	2.6	0.0	0.0	26.7	100	0.53	0.69	3.42
FCL 59	2	15	62	Xenotime	5.7	13.6	46.7	0.0	7.0	0.5	1.7	0.0	0.0	0.0	0.3	0.0	0.0	0.0	0.0	0.0	0.0	0.0	0.0	0.0	0.0	1.3	2.4	16.4	0.0	2.0	2.4	0.0	0.0	24.5	100	0.42	0.81	3.50
FCL 60	2	28	1039	Xenotime	9.9	19.4	33.3	0.2	3.2	2.1	2.8	0.0	0.0	0.0	8.9	0.0	0.0	0.0	0.0	0.0	0.0	0.0	0.0	0.0	0.0	2.2	5.7	5.5	1.2	3.3	2.4	0.0	0.0	20.3	100	0.51	3.09	6.34
FCL 61	1	23	322	Xenotime	7.3	15.8	54.8	0.3	4.3	0.9	1.6	0.0	0.0	0.5	0.4	0.2	0.0	0.0	0.0	0.0	0.0	0.0	0.0	0.0	0.0	1.1	1.5	9.8	0.0	1.0	0.0	0.5	0.0	13.4	100	0.46	1.70	3.12
FCL 62	1	34	414	Crandallite	17.2	11.8	43.3	0.2	7.1	0.7	0.9	1.0	0.0	0.3	0.6	0.0	3.6	0.0	0.0	0.0	2.1	6.2	0.8	3.6	0.4	0.0	0.0	0.3	0.0	0.0	0.0	0.0	0.0	13.4	100	1.46	2.42	1.89

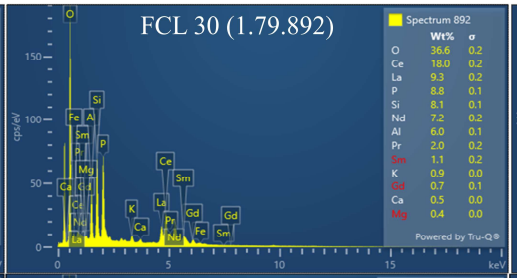
Figure B.7 EDS spectra of the particles containing REEs found from the the calcined Fire Clay (FC) coal waste leaching residue. (The spectra are labelled as FCL # (Specimen #. Site #. Spectrum #))

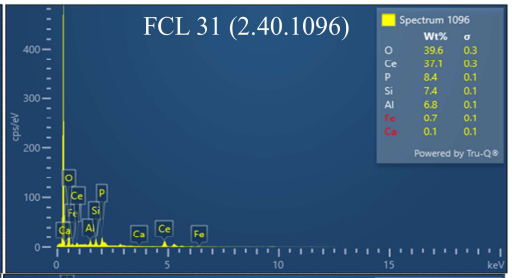


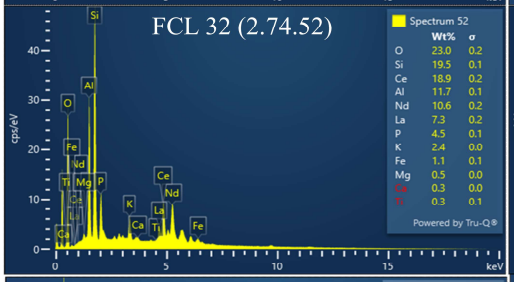

FCL 12 (2.50.1142)
Spectrum 1142
Wt% σ
Ce 65.6 0.1
O 14.6 0.1
P 8.3 0.1
Si 6.9 0.1
Al 4.2 0.1
K 0.5 0.0
Powered by Tru-Q®
FCL 13 (1.73.857)
Spectrum 857
Wt% σ
Ce 60.0 0.1
O 23.0 0.1
P 11.3 0.1
Si 3.9 0.1
Al 1.7 0.0
K 0.2 0.0
Powered by Tru-Q®
FCL 14 (2.47.1126)
Spectrum 1126
Wt% σ
Ce 58.1 0.1
O 20.8 0.1
P 11.2 0.1
Si 6.2 0.1
Al 3.7 0.1
Powered by Tru-Q®
FCL 15 (2.9.948)
Spectrum 948
Wt% σ
Ce 57.7 0.1
O 20.6 0.1
P 10.9 0.1
Si 7.4 0.1
Al 3.5 0.1
Powered by Tru-Q®
FCL 16 (2.41.42)
Spectrum 42
Wt% σ
Ce 55.8 0.1
O 23.7 0.1
P 10.2 0.1
Si 5.1 0.1
Al 3.5 0.1
Fe 1.0 0.1
K 0.5 0.0
Mg 0.3 0.0
Powered by Tru-Q®
FCL 17 (2.61.1190)
Spectrum 1190
Wt% σ
Ce 54.7 0.1
O 23.8 0.1
P 9.7 0.1
Si 6.7 0.1
Al 4.3 0.1
K 0.5 0.0
Fe 0.3 0.1
Powered by Tru-Q®
FCL 18 (1.56.668)
Spectrum 668
Wt% σ
O 25.8 0.2
Ce 25.0 0.2
Nd 10.4 0.2
La 10.2 0.2
P 9.3 0.1
Si 6.5 0.1
Al 4.6 0.1
Pr 3.1 0.2
Sm 1.7 0.2
Th 1.1 0.1
Gd 1.0 0.2
K 0.6 0.0
Ca 0.6 0.0
Powered by Tru-Q®
FCL 19 (2.12.970)
Spectrum 970
Wt% σ
Ce 24.7 0.2
O 19.7 0.1
La 11.4 0.2
Si 10.1 0.1
Nd 10.0 0.2
P 8.4 0.1
Th 4.6 0.1
Al 4.5 0.1
Pr 2.7 0.2
Sm 1.3 0.2
Fe 0.8 0.1
Gd 0.7 0.2
K 0.6 0.0
Powered by Tru-Q®
FCL 20 (2.60.33)
Spectrum 33
Wt% σ
Ce 50.0 0.1
O 24.1 0.1
Si 10.4 0.1
P 10.3 0.1
Al 4.1 0.1
K 0.6 0.0
Fe 0.5 0.1
Ti 0.1 0.0
Powered by Tru-Q®
FCL 21 (2.23.1014)
Spectrum 1014
Wt% σ
Ce 49.5 0.1
O 20.5 0.1
Si 14.5 0.1
Al 7.8 0.1
P 5.0 0.1
Fe 1.1 0.1
K 1.1 0.0
Mg 0.5 0.0
Powered by Tru-Q®
FCL 22 (2.30.1055)
Spectrum 1055
Wt% σ
O 26.1 0.2
Ce 23.0 0.2
Nd 10.5 0.2
La 10.5 0.2
Si 9.0 0.1
P 8.8 0.1
Al 5.1 0.1
Pr 2.5 0.2
Sm 1.6 0.2
Gd 1.2 0.2
Ti 0.8 0.1
K 0.7 0.0
Ca 0.2 0.0
Powered by Tru-Q®
FCL 23 (1.4.66)
Spectrum 66
Wt% σ
O 27.0 0.2
Ce 23.0 0.2
La 12.2 0.2
P 10.7 0.1
Si 8.4 0.1
Nd 8.2 0.2
Al 4.9 0.1
Pr 2.3 0.2
Sm 1.1 0.2
K 0.9 0.0
Fe 0.6 0.1
Gd 0.6 0.2
Ca 0.1 0.0
Powered by Tru-Q®
FCL 24 (1.72.10)
Spectrum 10
Wt% σ
O 30.5 0.2
Ce 21.2 0.2
La 10.2 0.2
Nd 9.8 0.2
P 9.1 0.1
Si 8.5 0.1
Al 4.6 0.1
Pr 2.5 0.2
Sm 1.5 0.2
Gd 0.8 0.1
K 0.4 0.0
Fe 0.4 0.1
Mg 0.2 0.0
Powered by Tru-Q®
FCL 25 (1.39.454)
Spectrum 454
Wt% σ
Ce 45.6 0.1
O 34.3 0.1
P 11.5 0.1
Si 5.4 0.1
Al 2.9 0.1
K 0.3 0.0
Powered by Tru-Q®
FCL 26 (2.42.1108)
Spectrum 1108
Wt% σ
Ce 44.7 0.1
O 35.2 0.1
P 11.8 0.1
Si 5.0 0.1
Al 2.5 0.1
Fe 0.4 0.1
K 0.4 0.0
Powered by Tru-Q®
FCL 27 (2.68.1228)
Spectrum 1228
Wt% σ
Ce 44.2 0.2
O 28.8 0.2
Si 10.2 0.1
P 9.9 0.1
Al 5.4 0.1
K 1.0 0.0
Fe 0.4 0.1
Powered by Tru-Q®

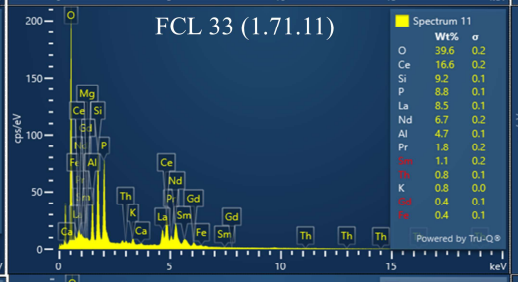

FCL 28 (2.64.45)
Spectrum 45
Wt% σ
O 29.8 0.2
Ce 20.5 0.2
Nd 9.8 0.2
P 9.6 0.1
Si 8.8 0.1
La 7.7 0.2
Al 4.2 0.1
Pr 2.8 0.2
Th 2.8 0.1
Sm 1.5 0.2
Gd 0.7 0.1
Fe 0.5 0.1
K 0.4 0.0
Powered by Tru-Q®
cps/eV
keV

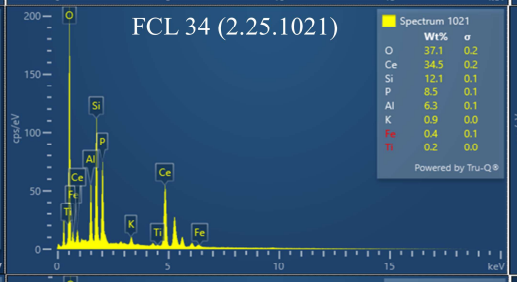

FCL 29 (2.66.1221)
Spectrum 1221
Wt% σ
O 34.2 0.2
Ce 19.5 0.2
Si 9.7 0.1
La 8.7 0.2
P 8.4 0.1
Nd 7.0 0.2
Al 5.7 0.1
Pr 2.2 0.2
Sm 1.5 0.2
Gd 0.8 0.1
K 0.7 0.0
Fe 0.7 0.1
Ca 0.1 0.0
Powered by Tru-Q®
cps/eV
keV

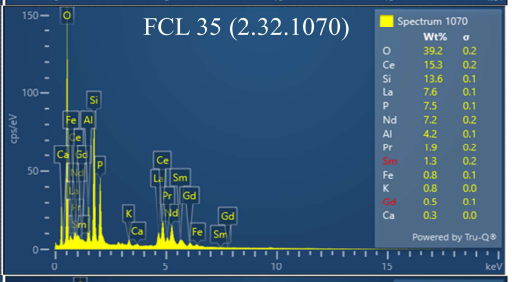

FCL 30 (1.79.892)
Spectrum 892
Wt% σ
O 36.6 0.2
Ce 18.0 0.2
La 9.3 0.2
P 8.8 0.1
Si 8.1 0.1
Nd 7.2 0.2
Al 6.0 0.1
Pr 2.0 0.2
Sm 1.1 0.2
K 0.9 0.0
Gd 0.7 0.1
Ca 0.5 0.0
Mg 0.4 0.0
Powered by Tru-Q®
cps/eV
keV

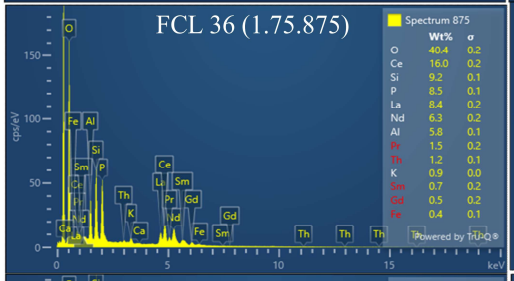

FCL 31 (2.40.1096)
Spectrum 1096
Wt% σ
O 39.6 0.3
Ce 37.1 0.3
P 8.4 0.1
Si 7.4 0.1
Al 6.8 0.1
Fe 0.7 0.1
Ca 0.1 0.1
Powered by Tru-Q®
cps/eV
keV

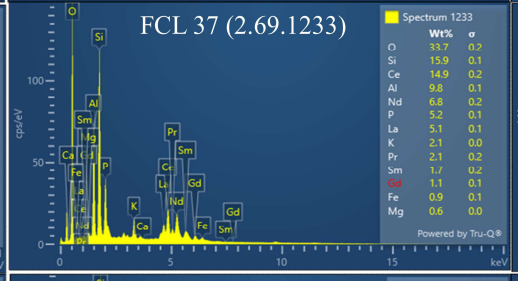

FCL 32 (2.74.52)
Spectrum 52
Wt% σ
O 23.0 0.2
Si 19.5 0.1
Ce 18.9 0.2
Al 11.7 0.1
Nd 10.6 0.2
La 7.3 0.2
P 4.5 0.1
K 2.4 0.0
Fe 1.1 0.1
Mg 0.5 0.0
Ca 0.3 0.0
Ti 0.3 0.1
Powered by Tru-Q®
cps/eV
keV

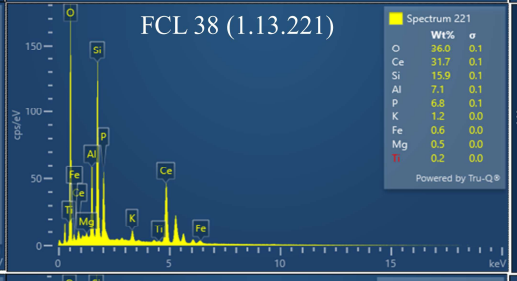

FCL 33 (1.71.11)
Spectrum 11
Wt% σ
O 39.6 0.2
Ce 16.6 0.2
Si 9.2 0.1
P 8.8 0.1
La 8.5 0.1
Nd 6.7 0.2
Al 4.7 0.1
Pr 1.8 0.2
Sm 1.1 0.2
Th 0.8 0.1
K 0.8 0.0
Gd 0.4 0.1
Fe 0.4 0.1
Powered by Tru-Q®
cps/eV
keV

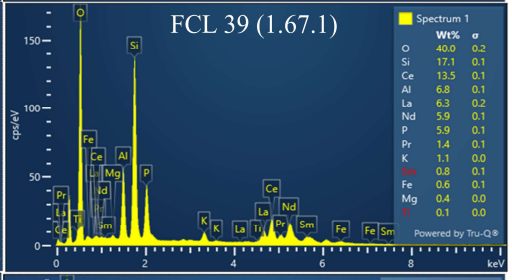

FCL 34 (2.25.1021)
Spectrum 1021
Wt% σ
O 37.1 0.2
Ce 34.5 0.2
Si 12.1 0.1
P 8.5 0.1
Al 6.3 0.1
K 0.9 0.0
Fe 0.4 0.1
Ti 0.2 0.0
Powered by Tru-Q®
cps/eV
keV

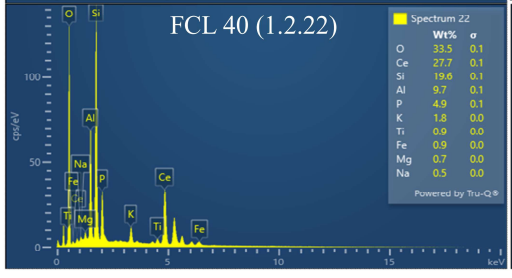

FCL 35 (2.32.1070)
Spectrum 1070
Wt% σ
O 39.2 0.2
Ce 15.3 0.2
Si 13.6 0.1
La 7.6 0.1
P 7.5 0.1
Nd 7.2 0.2
Al 4.2 0.1
Pr 1.9 0.2
Sm 1.3 0.2
Fe 0.8 0.1
K 0.8 0.0
Gd 0.5 0.1
Ca 0.3 0.0
Powered by Tru-Q®
cps/eV
keV

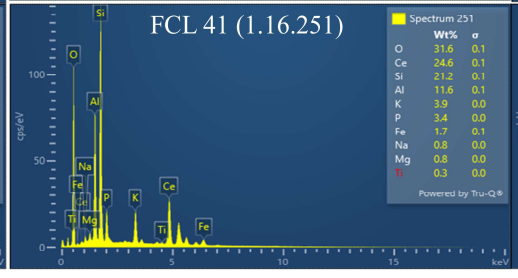

FCL 36 (1.75.875)
Spectrum 875
Wt% σ
O 40.4 0.2
Ce 16.0 0.2
Si 9.2 0.1
P 8.5 0.1
La 8.4 0.2
Nd 6.3 0.2
Al 5.8 0.1
Pr 1.5 0.2
Th 1.2 0.1
K 0.9 0.0
Sm 0.7 0.2
Gd 0.5 0.2
Fe 0.4 0.1
Powered by Tru-Q®
cps/eV
keV

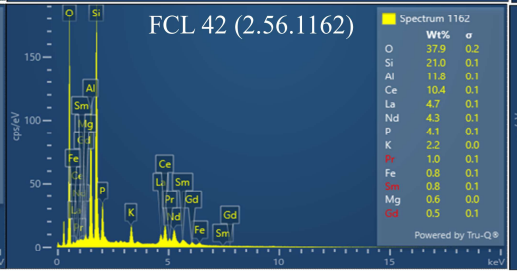

FCL 37 (2.69.1233)
Spectrum 1233
Wt% σ
O 33.7 0.2
Si 15.9 0.1
Ce 14.9 0.2
Al 9.8 0.1
Nd 6.8 0.2
P 5.2 0.1
La 5.1 0.1
K 2.1 0.0
Pr 2.1 0.2
Sm 1.7 0.2
Gd 1.1 0.1
Fe 0.9 0.1
Mg 0.6 0.0
Powered by Tru-Q®
cps/eV
keV

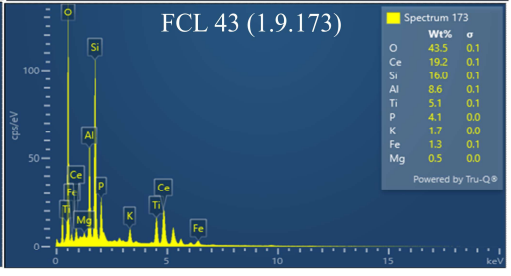

FCL 38 (1.13.221)
Spectrum 221
Wt% σ
O 36.0 0.1
Ce 31.7 0.1
Si 15.9 0.1
Al 7.1 0.1
P 6.8 0.1
K 1.2 0.0
Fe 0.6 0.0
Mg 0.5 0.0
Ti 0.2 0.0
Powered by Tru-Q®
cps/eV
keV


FCL 39 (1.67.1)
Spectrum 1
Wt% σ
O 40.0 0.2
Si 17.1 0.1
Ce 13.5 0.1
Al 6.8 0.1
La 6.3 0.2
Nd 5.9 0.1
P 5.9 0.1
Pr 1.4 0.1
K 1.1 0.0
Sm 0.8 0.1
Fe 0.6 0.1
Mg 0.4 0.0
Ti 0.1 0.0
Powered by Tru-Q®
cps/eV
keV


FCL 40 (1.2.22)
Spectrum 22
Wt% σ
O 33.5 0.1
Ce 27.7 0.1
Si 19.6 0.1
Al 9.7 0.1
P 4.9 0.1
K 1.8 0.0
Ti 0.9 0.0
Fe 0.9 0.0
Mg 0.7 0.0
Na 0.5 0.0
Powered by Tru-Q®
cps/eV
keV


FCL 41 (1.16.251)
Spectrum 251
Wt% σ
O 31.6 0.1
Ce 24.6 0.1
Si 21.2 0.1
Al 11.6 0.1
K 3.9 0.0
P 3.4 0.0
Fe 1.7 0.1
Na 0.8 0.0
Mg 0.8 0.0
Ti 0.3 0.0
Powered by Tru-Q®
cps/eV
keV


FCL 42 (2.56.1162)
Spectrum 1162
Wt% σ
O 37.9 0.2
Si 21.0 0.1
Al 11.8 0.1
Ce 10.4 0.1
La 4.7 0.1
Nd 4.3 0.1
P 4.1 0.1
K 2.2 0.0
Pr 1.0 0.1
Fe 0.8 0.1
Sm 0.8 0.1
Mg 0.6 0.0
Gd 0.5 0.1
Powered by Tru-Q®
cps/eV
keV


FCL 43 (1.9.173)
Spectrum 173
Wt% σ
O 43.5 0.1
Ce 19.2 0.1
Si 16.0 0.1
Al 8.6 0.1
Ti 5.1 0.1
P 4.1 0.0
K 1.7 0.0
Fe 1.3 0.1
Mg 0.5 0.0
Powered by Tru-Q®
cps/eV
keV

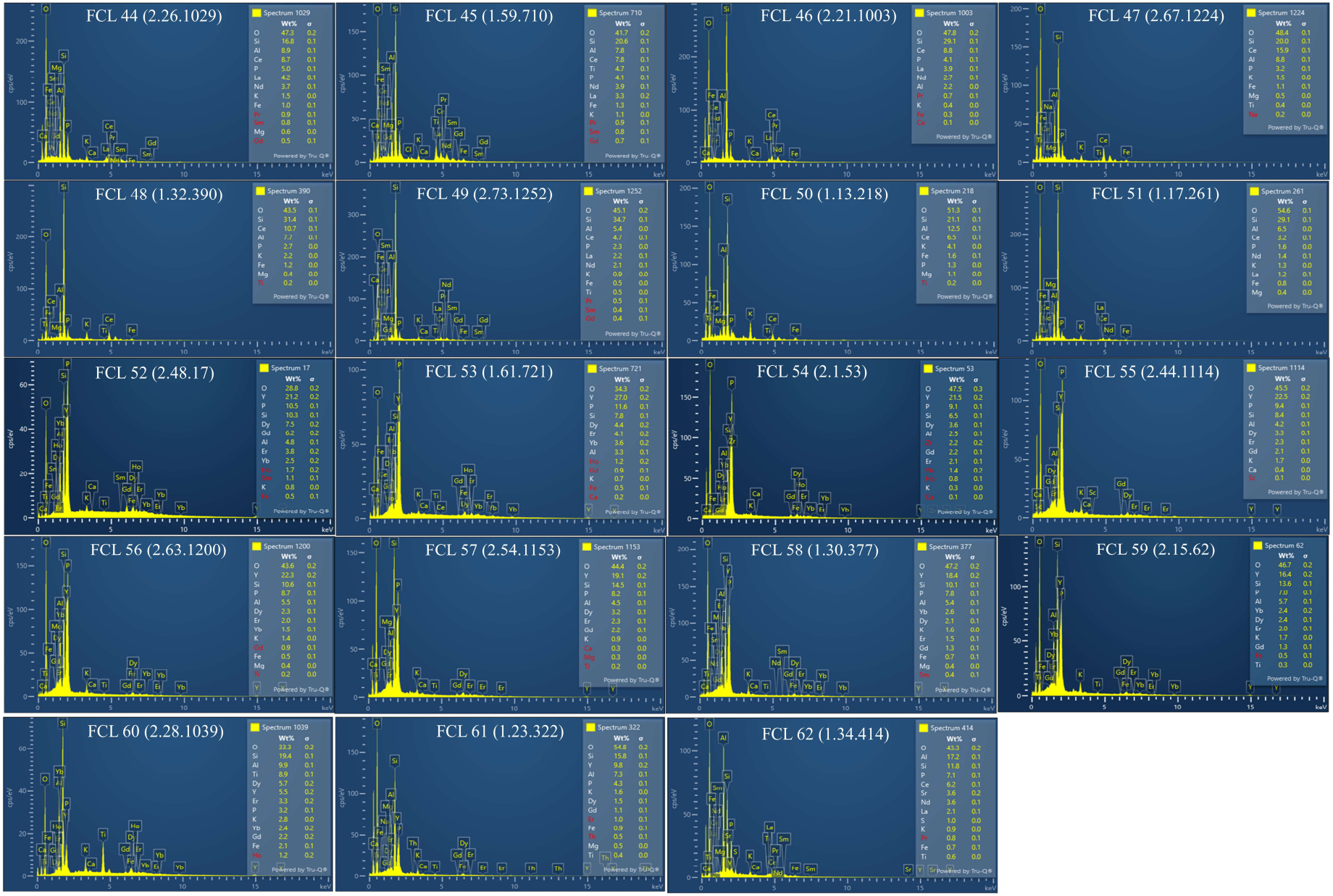
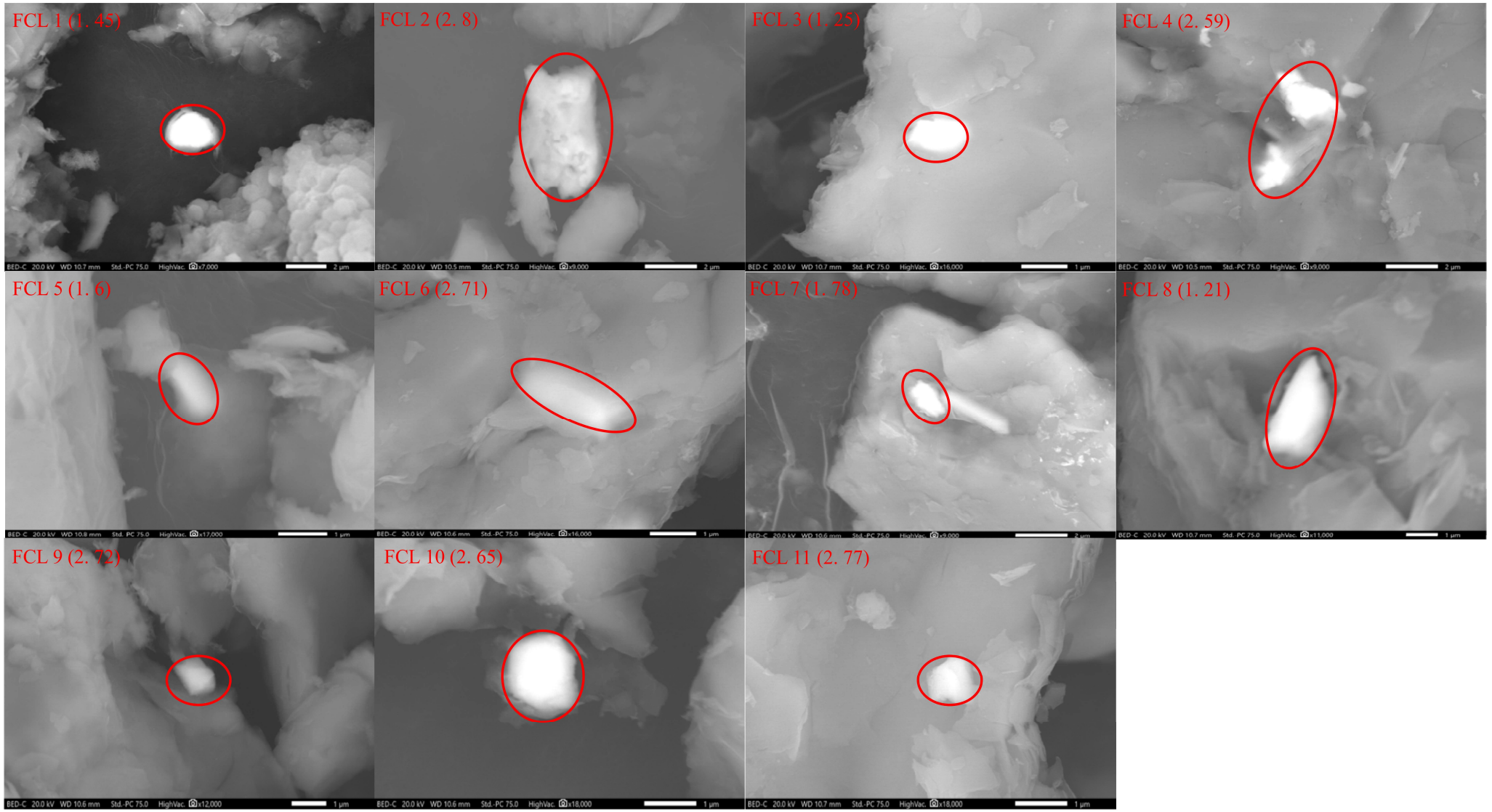
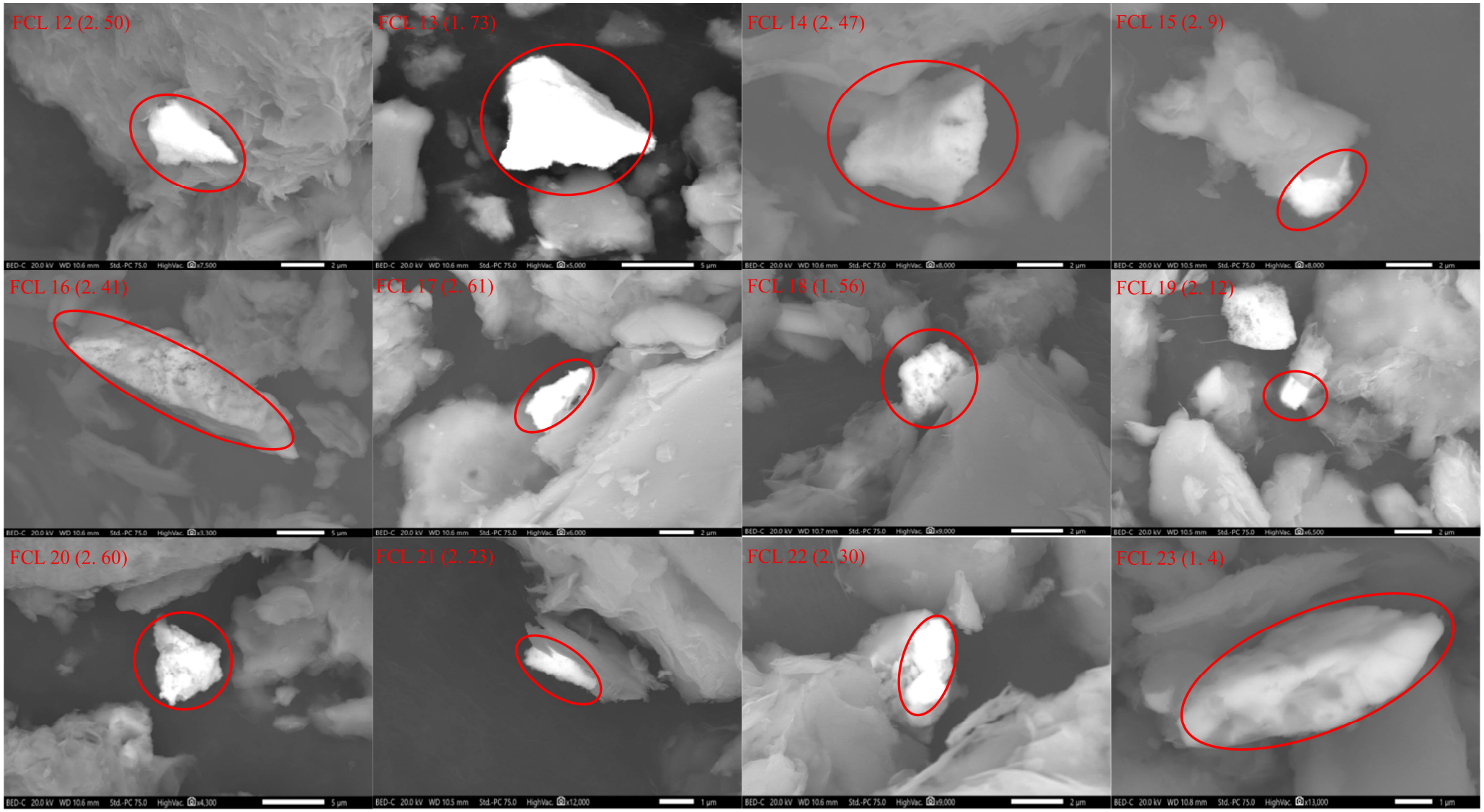
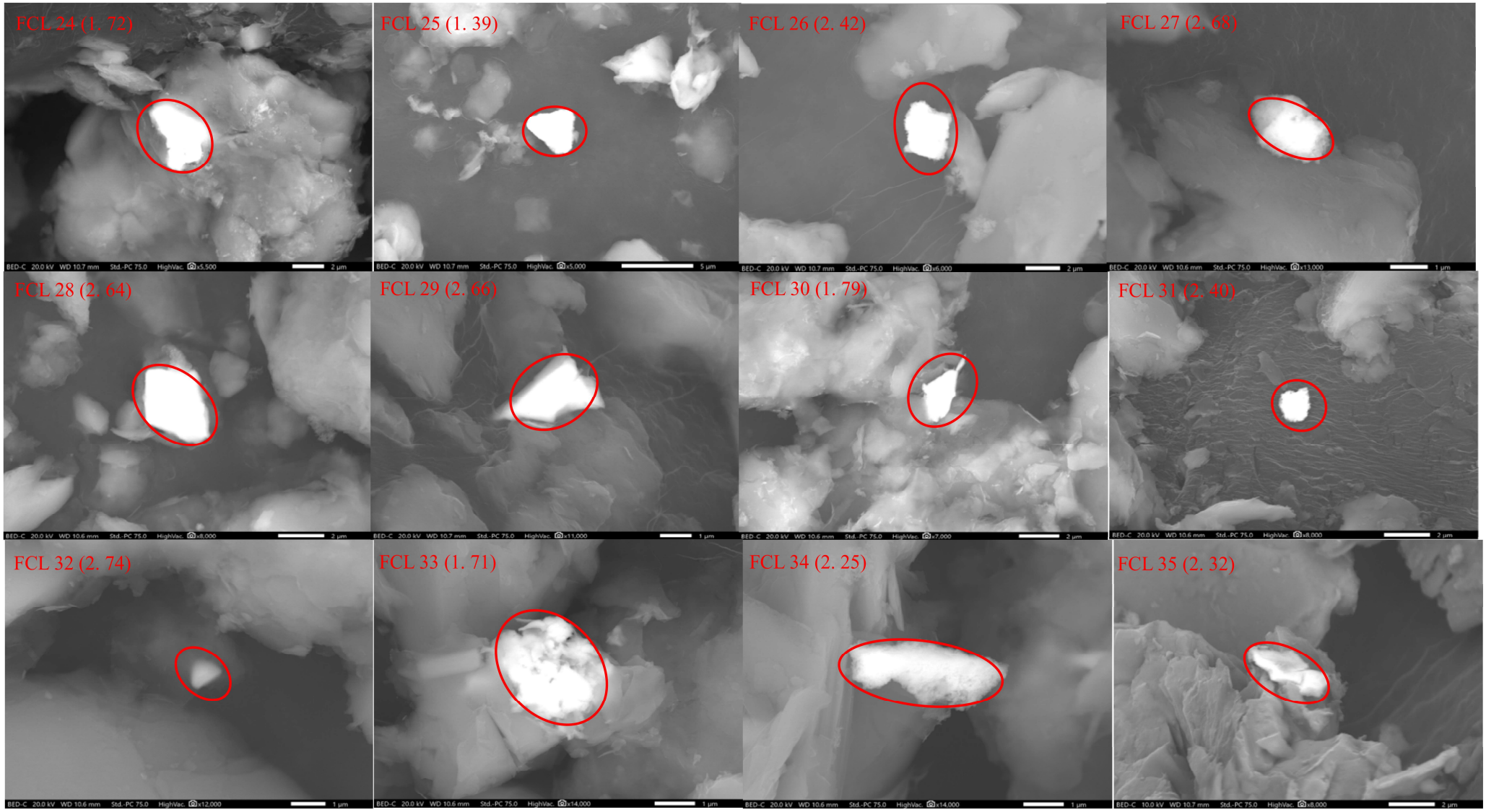
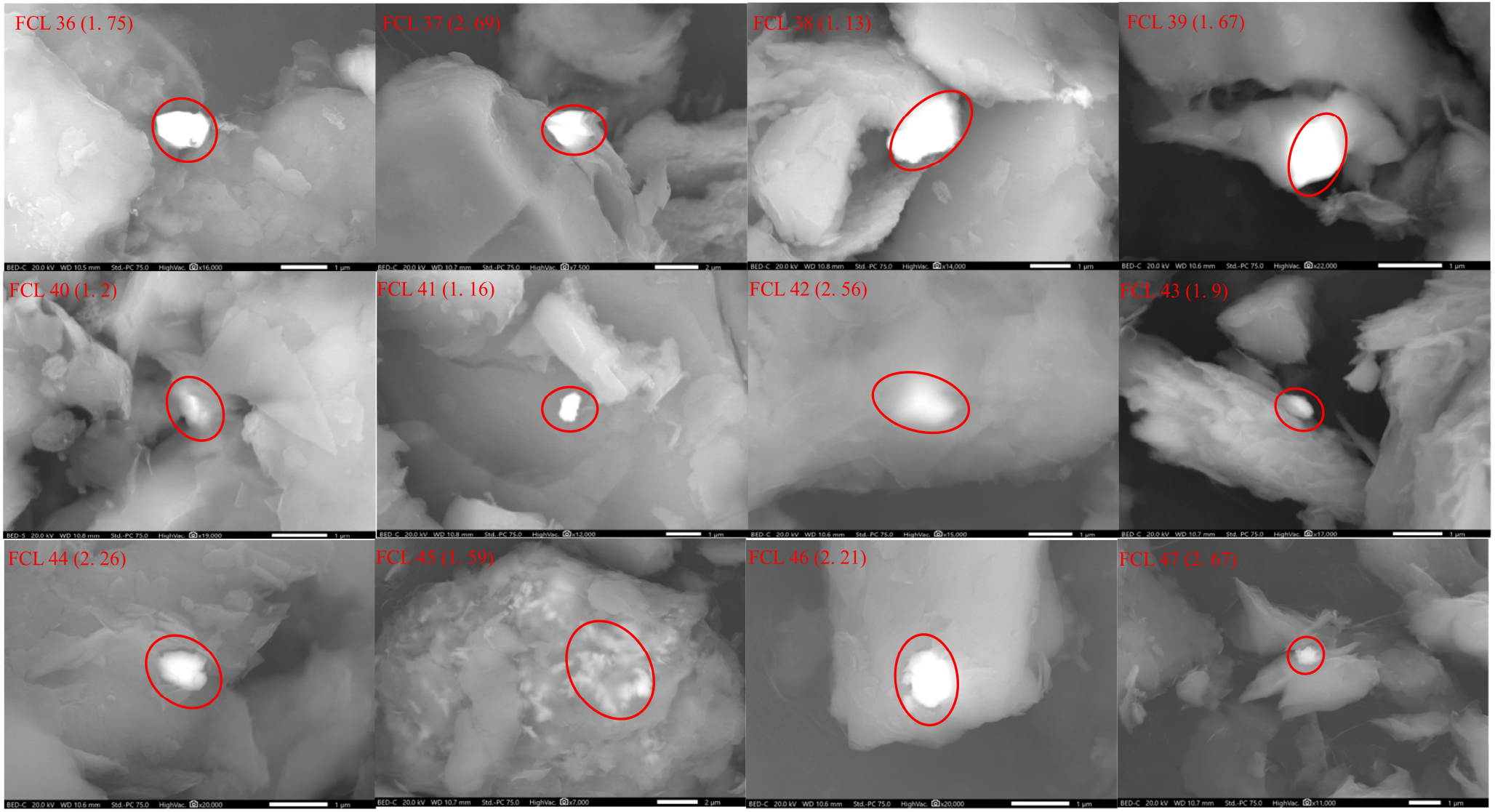

FCL 44 (2.26.1029)
Spectrum 1029
Wt% σ
O 47.3 0.2
Si 16.8 0.1
Al 8.9 0.1
Ce 8.7 0.1
P 5.0 0.1
La 4.2 0.1
Nd 3.7 0.1
K 1.5 0.0
Fe 1.0 0.1
Pr 0.9 0.1
Sm 0.8 0.1
Mg 0.6 0.0
Gd 0.5 0.1
Powered by Tru-Q®
FCL 45 (1.59.710)
Spectrum 710
Wt% σ
O 41.7 0.2
Si 20.6 0.1
Al 7.8 0.1
Ce 7.8 0.1
Ti 4.7 0.1
P 4.1 0.1
Nd 3.9 0.1
La 3.3 0.2
Fe 1.3 0.1
K 1.1 0.0
Pr 0.9 0.1
Sm 0.8 0.1
Gd 0.7 0.1
Powered by Tru-Q®
FCL 46 (2.21.1003)
Spectrum 1003
Wt% σ
O 47.8 0.2
Si 29.1 0.1
Ce 8.8 0.1
P 4.1 0.1
La 3.9 0.1
Nd 2.7 0.1
Al 2.2 0.0
Pr 0.7 0.1
K 0.4 0.0
Fe 0.3 0.0
Ca 0.1 0.0
Powered by Tru-Q®
FCL 47 (2.67.1224)
Spectrum 1224
Wt% σ
O 48.4 0.1
Si 20.0 0.1
Ce 15.9 0.1
Al 8.8 0.1
P 3.2 0.1
K 1.5 0.0
Fe 1.1 0.1
Mg 0.5 0.0
Ti 0.4 0.0
Na 0.2 0.0
Powered by Tru-Q®
FCL 48 (1.32.390)
Spectrum 390
Wt% σ
O 43.5 0.1
Si 31.4 0.1
Ce 10.7 0.1
Al 7.7 0.1
P 2.7 0.0
K 2.2 0.0
Fe 1.2 0.0
Mg 0.4 0.0
Ti 0.2 0.0
Powered by Tru-Q®
FCL 49 (2.73.1252)
Spectrum 1252
Wt% σ
O 45.1 0.2
Si 34.7 0.1
Al 5.4 0.0
Ce 4.7 0.1
P 2.3 0.0
La 2.2 0.1
Nd 2.1 0.1
K 0.9 0.0
Fe 0.5 0.0
Ti 0.5 0.0
Pr 0.5 0.1
Sm 0.4 0.1
Gd 0.4 0.1
Powered by Tru-Q®
FCL 50 (1.13.218)
Spectrum 218
Wt% σ
O 51.3 0.1
Si 21.1 0.1
Al 12.5 0.1
Ce 6.5 0.1
K 4.1 0.0
Fe 1.6 0.1
P 1.3 0.0
Mg 1.1 0.0
Ti 0.2 0.0
Powered by Tru-Q®
FCL 51 (1.17.261)
Spectrum 261
Wt% σ
O 54.6 0.1
Si 29.1 0.1
Al 6.5 0.0
Ce 3.2 0.1
P 1.6 0.0
Nd 1.4 0.1
K 1.3 0.0
La 1.2 0.1
Fe 0.8 0.0
Mg 0.4 0.0
Powered by Tru-Q®
FCL 52 (2.48.17)
Spectrum 17
Wt% σ
O 28.8 0.2
Y 21.2 0.2
P 10.5 0.1
Si 10.3 0.1
Dy 7.5 0.2
Gd 6.2 0.2
Al 4.8 0.1
Er 3.8 0.2
Yb 2.5 0.2
Ho 1.7 0.2
Sm 1.1 0.1
K 0.8 0.0
Fe 0.5 0.1
Powered by Tru-Q®
FCL 53 (1.61.721)
Spectrum 721
Wt% σ
O 34.3 0.2
Y 27.0 0.2
P 11.6 0.1
Si 7.8 0.1
Dy 4.4 0.2
Er 4.1 0.2
Yb 3.6 0.2
Al 3.3 0.1
Ho 1.2 0.2
Gd 0.9 0.1
K 0.7 0.0
Fe 0.5 0.1
Ca 0.2 0.0
Powered by Tru-Q®
FCL 54 (2.1.53)
Spectrum 53
Wt% σ
O 47.5 0.3
Y 21.5 0.2
P 9.1 0.1
Si 6.5 0.1
Dy 3.6 0.1
Al 2.5 0.1
Er 2.2 0.2
Gd 2.2 0.1
Er 2.1 0.1
Ho 1.4 0.2
Pm 0.8 0.1
K 0.3 0.0
Ca 0.1 0.0
Powered by Tru-Q®
FCL 55 (2.44.1114)
Spectrum 1114
Wt% σ
O 45.5 0.2
Y 22.5 0.2
P 9.4 0.1
Si 8.4 0.1
Al 4.2 0.1
Dy 3.3 0.1
Er 2.3 0.1
Gd 2.1 0.1
K 1.7 0.0
Ca 0.4 0.0
Sc 0.1 0.0
Powered by Tru-Q®
FCL 56 (2.63.1200)
Spectrum 1200
Wt% σ
O 43.6 0.2
Y 22.3 0.2
Si 10.6 0.1
P 8.7 0.1
Al 5.5 0.1
Dy 2.3 0.1
Er 2.0 0.1
Yb 1.5 0.1
K 1.4 0.0
Ho 0.9 0.1
Fe 0.5 0.1
Mg 0.4 0.0
Ti 0.2 0.0
Powered by Tru-Q®
FCL 57 (2.54.1153)
Spectrum 1153
Wt% σ
O 44.4 0.2
Y 19.1 0.2
Si 14.5 0.1
P 8.2 0.1
Al 4.5 0.1
Dy 3.2 0.1
Er 2.3 0.1
Gd 2.2 0.1
K 0.9 0.0
Ca 0.3 0.0
Mg 0.3 0.0
Ti 0.2 0.0
Powered by Tru-Q®
FCL 58 (1.30.377)
Spectrum 377
Wt% σ
O 47.2 0.2
Y 18.4 0.2
Si 10.1 0.1
P 7.8 0.1
Al 5.4 0.1
Yb 2.6 0.1
Dy 2.1 0.1
K 1.6 0.0
Er 1.5 0.1
Gd 1.3 0.1
Fe 0.7 0.1
Mg 0.4 0.0
Pm 0.4 0.1
Powered by Tru-Q®
FCL 59 (2.15.62)
Spectrum 62
Wt% σ
O 46.7 0.2
Y 16.4 0.2
Si 13.6 0.1
P 7.0 0.1
Al 5.7 0.1
Yb 2.4 0.2
Dy 2.4 0.1
Er 2.0 0.1
K 1.7 0.0
Gd 1.3 0.1
Na 0.5 0.1
Ti 0.3 0.0
Powered by Tru-Q®
FCL 60 (2.28.1039)
Spectrum 1039
Wt% σ
O 33.3 0.2
Si 19.4 0.1
Al 9.9 0.1
Ti 8.9 0.1
Dy 5.7 0.2
Y 5.5 0.2
Er 3.3 0.2
P 3.2 0.1
K 2.8 0.0
Yb 2.4 0.2
Gd 2.2 0.2
Fe 2.1 0.1
Ho 1.2 0.2
Powered by Tru-Q®
FCL 61 (1.23.322)
Spectrum 322
Wt% σ
O 54.8 0.2
Si 15.8 0.1
Y 9.8 0.2
Al 7.3 0.1
P 4.3 0.1
K 1.6 0.0
Dy 1.5 0.1
Gd 1.1 0.1
Er 1.0 0.1
Fe 0.9 0.1
Th 0.5 0.1
Mg 0.5 0.0
Ti 0.4 0.0
Powered by Tru-Q®
FCL 62 (1.34.414)
Spectrum 414
Wt% σ
O 43.3 0.2
Al 17.2 0.1
Si 11.8 0.1
P 7.1 0.1
Ce 6.2 0.1
Sr 3.6 0.2
Nd 3.6 0.1
La 2.1 0.1
S 1.0 0.0
K 0.9 0.0
Pr 0.8 0.1
Fe 0.7 0.1
Ti 0.6 0.0
Powered by Tru-Q®

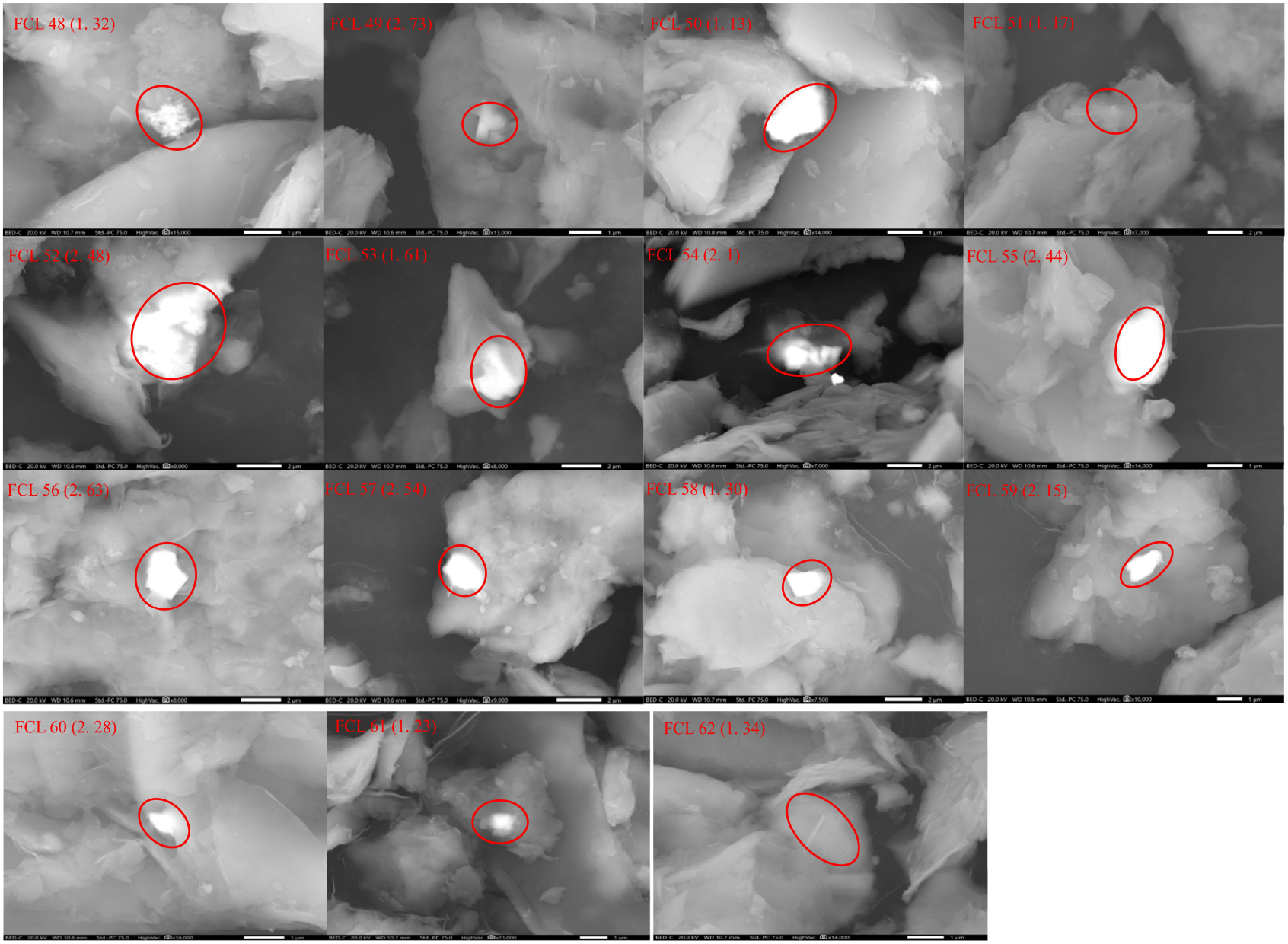
Figure B.8 SEM images of the particles containing REEs found from the the calcined Fire Clay (FC) coal waste leaching residue . (The images are labelled as FCL # (Specimen #. Site #))



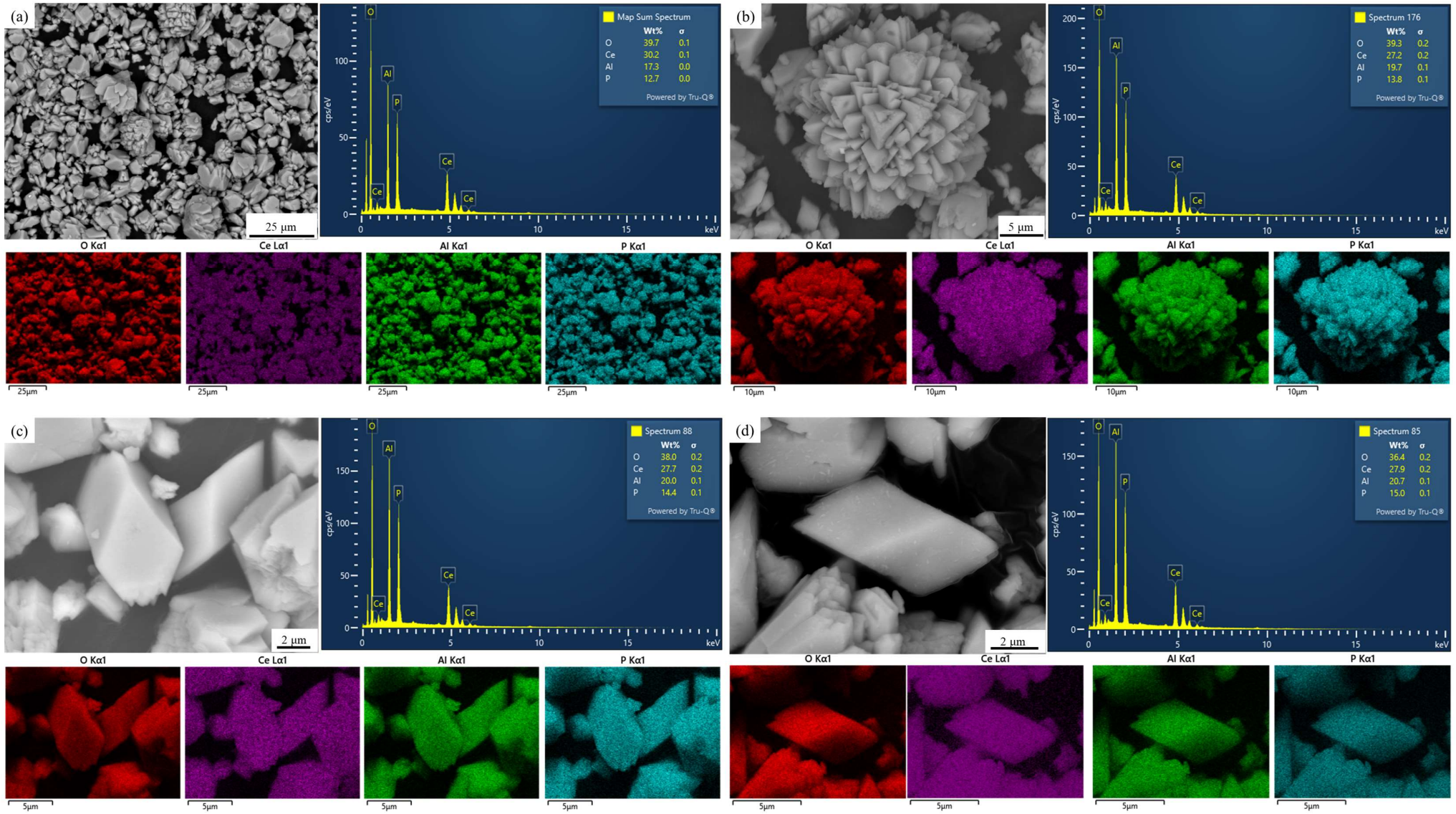

FCL 12 (2. 50)
FCL 13 (1. 73)
FCL 14 (2. 47)
FCL 15 (2. 9)
FCL 16 (2. 41)
FCL 17 (2. 61)
FCL 18 (1. 56)
FCL 19 (2. 12)
FCL 20 (2. 60)
FCL 21 (2. 23)
FCL 22 (2. 30)
FCL 23 (1. 4)


FCL 24 (1. 72)
FCL 25 (1. 39)
FCL 26 (2. 42)
FCL 27 (2. 68)
FCL 28 (2. 64)
FCL 29 (2. 66)
FCL 30 (1. 79)
FCL 31 (2. 40)
FCL 32 (2. 74)
FCL 33 (1. 71)
FCL 34 (2. 25)
FCL 35 (2. 32)


FCL 36 (1. 75)
FCL 37 (2. 69)
FCL 38 (1. 13)
FCL 39 (1. 67)
FCL 40 (1. 2)
FCL 41 (1. 16)
FCL 42 (2. 56)
FCL 43 (1. 9)
FCL 44 (2. 26)
FCL 45 (1. 59)
FCL 46 (2. 21)
FCL 47 (2. 67)


FCL 48 (1. 32)
FCL 49 (2. 73)
FCL 50 (1. 13)
FCL 51 (1. 17)
FCL 52 (2. 48)
FCL 53 (1. 61)
FCL 54 (2. 1)
FCL 55 (2. 44)
FCL 56 (2. 63)
FCL 57 (2. 54)
FCL 58 (1. 30)
FCL 59 (2. 15)
FCL 60 (2. 28)
FCL 61 (1. 23)
FCL 62 (1. 34)

Appendix C Supporting materials for Chapter 4



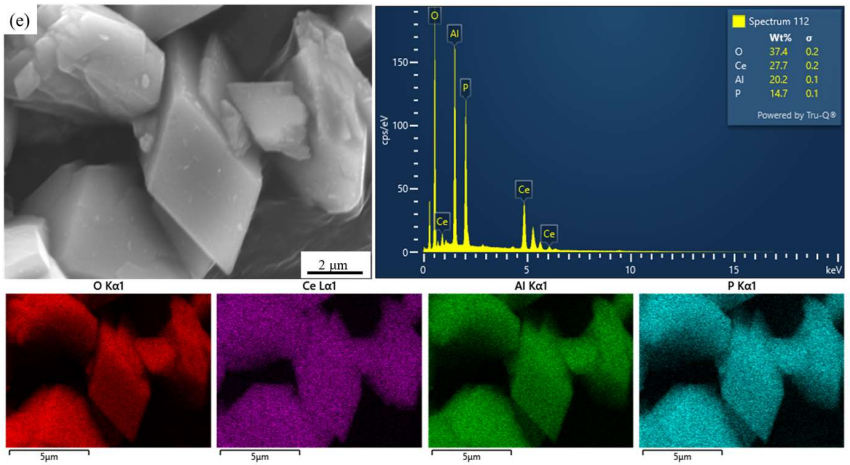


Figure C.1 SEM images, EDS spectra, and elemental mapping of the synthesized florencite-(Ce) under various magnifications.

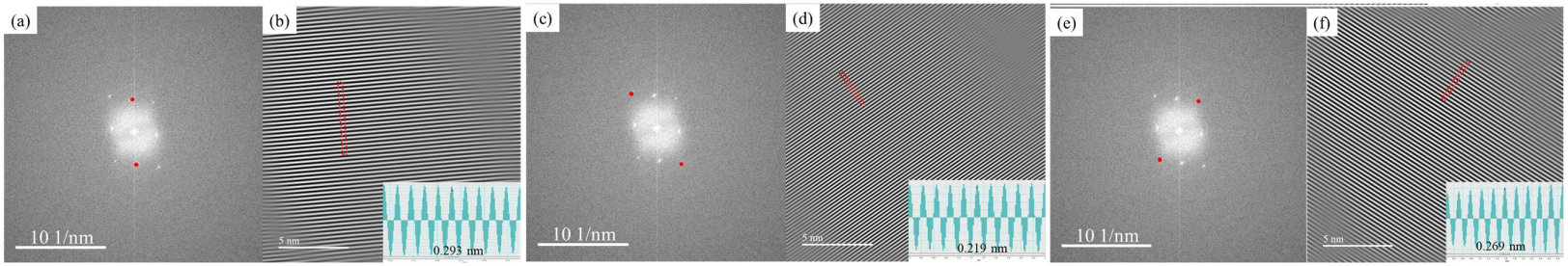


Figure C.2 The FFT patterns of selected symmetrical diffraction spots in red color (a)(c)(e), and the corresponding IFFT images (b)(d)(f).

Table C.1 The chemical composition of the completely recrystallized product.

Compounds	Concentration / %
$CePO_4$	51.21
$AlPO_4$	26.56
Al_2O_3	22.21